U.S. DEPARTMENT OF COMMERCE
National Technical Information Service
PB-274 017

Proceedings: Particulate Collection Problems Using ESP's in the Metallurgical Industry

Southern Research Inst, Birmingham, Ala

Prepared for

Industrial Environmental Research Lab, Research Triangle Park, N C

Oct 77

PB 274 017

EPA-600/2-77-208
October 1977

Environmental Protection Technology Series

UNITED STATES ENVIRONMENTAL PROTECTION AGENCY

REPRODUCED BY
NATIONAL TECHNICAL
INFORMATION SERVICE
U. S. DEPARTMENT OF COMMERCE
SPRINGFIELD, VA. 22161

RESEARCH REPORTING SERIES

Research reports of the Office of Research and Development, U.S. Environmental Protection Agency, have been grouped into nine series. These nine broad categories were established to facilitate further development and application of environmental technology. Elimination of traditional grouping was consciously planned to foster technology transfer and a maximum interface in related fields. The nine series are:

1. Environmental Health Effects Research
2. Environmental Protection Technology
3. Ecological Research
4. Environmental Monitoring
5. Socioeconomic Environmental Studies
6. Scientific and Technical Assessment Reports (STAR)
7. Interagency Energy-Environment Research and Development
8. "Special" Reports
9. Miscellaneous Reports

This report has been assigned to the ENVIRONMENTAL PROTECTION TECHNOLOGY series. This series describes research performed to develop and demonstrate instrumentation, equipment, and methodology to repair or prevent environmental degradation from point and non-point sources of pollution. This work provides the new or improved technology required for the control and treatment of pollution sources to meet environmental quality standards.

REVIEW NOTICE

This report has been reviewed by the participating Federal Agencies, and approved for publication. Approval does not signify that the contents necessarily reflect the views and policies of the Government, nor does mention of trade names or commercial products constitute endorsement or recommendation for use.

This document is available to the public through the National Technical Information Service, Springfield, Virginia 22161.

TECHNICAL REPORT DATA
(Please read Instructions on the reverse before completing)

1. REPORT NO. EPA-600/2-77-208	2.	3. RECIPIENT'S ACCESSION NO. PB274017
4. TITLE AND SUBTITLE Proceedings: Particulate Collection Problems Using ESP's in the Metallurgical Industry		5. REPORT DATE October 1977 6. PERFORMING ORGANIZATION CODE
7. AUTHOR(S) C.E. Feazel, Editor		8. PERFORMING ORGANIZATION REPORT NO.
9. PERFORMING ORGANIZATION NAME AND ADDRESS Southern Research Institute 2000 Ninth Avenue, South Birmingham, Alabama 35205		10. PROGRAM ELEMENT NO. 1AB012; ROAP 21ADL-034 11. CONTRACT/GRANT NO. 68-02-2114
12. SPONSORING AGENCY NAME AND ADDRESS EPA, Office of Research and Development Industrial Environmental Research Laboratory Research Triangle Park, NC 27711		13. TYPE OF REPORT AND PERIOD COVERED Proceedings; 11/76-8/77 14. SPONSORING AGENCY CODE EPA/600/13

15. SUPPLEMENTARY NOTES IERL-RTP project officer for these proceedings is Dennis C. Drehmel, Mail Drop 61, 919/541-2925.

16. ABSTRACT The proceedings contain 13 papers on topics selected to present to the metals industry the most recent developments in electrostatic precipitator (ESP) technology. Subjects include the application of ESP's to the collection of fumes from operations in the iron and steel industry: production of mineral wool from blast furnace slag, hot scarfing of steel billets, sintering of blast furnace feed, and steel production in electric arc furnaces. The behavior of ferrous sinter dust in a laboratory scale ESP was discussed. Data were presented on a wet ESP collecting fumes from aluminum reduction cells. Preliminary results on the performance of ESP's in collecting fume from a copper smelter were compared with values obtained using a mathematical model of ESP action that calculates collection efficiency as a function of particle size and operating conditions. Performance test results were presented on a hot-side ESP in a power plant burning medium-sulfur coal. Design details were given for a mobile ESP unit. Other papers dealt with techniques of optimizing rapping schedules; interpreting voltage/current curves; and interference by reverse corona in the process of particle charging. Some advanced concepts for electrostatic collection of particulate matter were compared: two-stage ESP's, electrically augmented scrubbers, charged droplet scrubbers and ESP's, and electrostatic fiber and fabric filters.

17. KEY WORDS AND DOCUMENT ANALYSIS

a. DESCRIPTORS		b. IDENTIFIERS/OPEN ENDED TERMS	c. COSATI Field/Group	
Air Pollution	Iron and Steel Industry	Air Pollution Control	13B	
Electrostatic Precipitators	Fumes	Stationary Sources		
Dust	Mineral Wool	Particulate		
Metallurgical Engineering	Blast Furnaces	Mobile ESP's	11G	11E
	Slags	Charged Droplets	11F	

18. DISTRIBUTION STATEMENT Unlimited	19. SECURITY CLASS *(This Report)* Unclassified	21. NO. OF PAGES 261
	20. SECURITY CLASS *(This page)* Unclassified	22. PRICE PC A12 / MF A01

EPA Form 2220-1 (9-73)

EPA-600/2-77-208
October 1977

PROCEEDINGS: PARTICULATE COLLECTION PROBLEMS USING ESP'S IN THE METALLURGICAL INDUSTRY

C.E. Feazel, Editor

Southern Research Institute
2000 Ninth Avenue, South
Birmingham, Alabama 35205

Contract No. 68-02-2114
ROAP No. 21ADL-034
Program Element No. 1AB012

EPA Project Officer: Dennis C. Drehmel

Industrial Environmental Research Laboratory
Office of Energy, Minerals, and Industry
Research Triangle Park, N.C. 27711

Prepared for

U.S. ENVIRONMENTAL PROTECTION AGENCY
Office of Research and Development
Washington, D.C. 20460

ABSTRACT

These proceedings contain 13 papers on topics which were selected to present to the metals industry the most recent developments in electrostatic precipitator technology. The subjects include the application of precipitators to the collection of fumes from operations in the iron and steel industry: production of mineral wool from blast furnace slag, hot scarfing of steel billets, sintering of blast furnace feed, and steel production in electric arc furnaces. The behavior of ferrous sinter dust in a laboratory-scale precipitator was discussed. Data were presented on a wet electrostatic precipitator collecting fumes from aluminum reduction cells. Preliminary results on the performance of precipitators in collecting fume from a copper smelter were compared with values obtained by means of a mathematical model of precipitator action that calculates collection efficiency as a function of particle size and operating conditions. Performance test results on a hot-side precipitator installed in a power plant burning coal with a medium sulfur content were presented. Design details were given for a mobile unit electrostatic precipitator. Other papers dealt with techniques of optimizing rapping schedules; interpreting voltage-current curves; and interference by reverse corona in the process of particle charging. A comparison was given of some advanced concepts for electrostatic collection of particulate matter: two-stage precipitators, electrically augmented scrubbers, charged droplet scrubbers and precipitators, and electrostatic fiber and fabric filters.

ACKNOWLEDGEMENTS

Chairman of the conference was Dennis C. Drehmel, of the Environmental Protection Agency. The program chairman was Grady B. Nichols, of Southern Research Institute. E.L. Plyler (Environmental Protection Agency) opened the conference and served as chairman of the first session. Ivor E. Campbell (Clyde Williams and Co.), Sidney R. Orem (Industrial Gas Cleaning Institute), and Norman Plaks (Environmental Protection Agency) also served as session chairmen, and as moderators for panel discussions. James H. Abbott (Environmental Protection Agency) delivered closing remarks. Meeting arrangements were made by James H. Strickland (Southern Research Institute), with the help of Marilyn Bailey and Bettye Smith.

CONTENTS

Abstract iii

Acknowledgements iv

Paper 1. The Application of Wet Electrostatic Precipitators for the Control of Emissions From Three Metallurgical Processes
S.A. Jaasund and M.R. Mazer. 1

Paper 2. Design and Operating Experience With Electrostatic Precipitators on Electric Arc Furnaces
Clifford Whitehead 23

Paper 3. Test of University of Washington Electrostatic Scrubber at an Electric Arc Steel Furnace
Michael J. Pilat, G.A. Raemhild, and Dale L. Harmon. 40

Paper 4. Laboratory Electrostatic Precipitator Studies Relating to the Steel Industry
J.C. Steelhammer, D.R. Nogash, and D.M. Polizzotti 54

Paper 5. A Precipitator Performance Model:Application To the Nonferrous Metals Industry
Jack R. McDonald and Leslie E. Sparks. 72

Paper 6. Studies of Particle Reentrainment Resulting From Electrode Rapping
John P. Gooch and Walter Piulle 103

Paper 7. Voltage-Current Data From Electrostatic Precipitators Under Normal and Abnormal Conditions
Sherman M. Banks, Jack R. McDonald, and Leslie E. Sparks . . . 129

Paper 8. Particle Charging in an Electrical Corona and Associated Problems
Duane H. Pontius, Wallace B. Smith, and James H. Abbott. . . . 154

Paper 9. Advanced Electrostatic Collection Concepts
Dennis C Drehmel 167

Paper 10. Performance of a Wet Electrostatic Precipitator in an Aluminum Processing Facility
John P. Gooch, Joseph D. McCain, and Leslie E. Sparks. 176

Paper 11. Design and Fabrication of a Mobile Electrostatic Precipitator
Joseph L. Brumfield, Fred Crowson, and Dale L. Harmon. 205

Paper 12. Field Test of a Hot-Side Electrostatic Precipitator
Dennis C. Drehmel and Charles H. Gooding. 223

Paper 13. Experience With Electrostatic Precipitators as Applied to the Primary Copper Smelting Reverberatory Furnace
George S. Thompson, Jr. and Grady B. Nichols. 234

PAPER 1

THE APPLICATION OF WET ELECTROSTATIC PRECIPITATORS FOR THE CONTROL OF EMISSIONS FROM THREE METALLURGICAL PROCESSES

S. A. JAASUND
M. R. MAZER
BETHLEHEM STEEL CORPORATION

INTRODUCTION

Increasing public and governmental pressure to reduce air pollution particulate emissions has been brought to bear on the steel industry. Traditional emission control technology is limited in application and has often been found to be inadequate for the attainment of existing stringent environmental goals. While highly efficient on dry particulate emissions, dry collection systems, including electrostatic precipitators and fabric filters, are unable to capture condensible emissions. Wet scrubbers can achieve satisfactory control of both dry and condensible emissions but often require high levels of energy consumption. Consequently, the need for new high-efficiency, low-energy control technology capable of wide application is evident.

Unique features of the wet electrostatic precipitator (WESP) make it an attractive candidate solution to these emission control problems. For example, recently developed WESP systems combine the low energy requirements of dry ESPs with the ability of wet scrubbers to control condensible hydrocarbon emissions. Furthermore, unlike fabric filters, WESPs are relatively insensitive to gas temperatures and dew point effects. Finally, because the collecting electrodes are continuously flushed with water, the dust resistivity problems of the dry ESPs are avoided.

Application of WESP systems for the control of emissions from coke oven pushing, Soderberg aluminum reduction[1], and anode baking operations associated with aluminum production[2] have demonstrated their potential. However, since the WESP still represent an emerging technology, each new application requires testing, and where required, specifically tailored design.

This paper describes Bethlehem Steel Corporation's test and development programs to adapt wet electrostatic precipitators for the control of particulate emissions from:

- Mineral wool production at the Bethlehem Plant
- Hot scarfing at the Lackawanna Plant
- Sintering operations at the Lackawanna and Johnstown Plants.

These programs included the evaluation of pilot-scale WESPs for the control of emissions from all three sources and the operation of full-scale WESPs at the Bethlehem mineral wool plant and the Johnstown sinter plant. Test and developmental work over a period of two years culminated in operating procedures and design modifications to counter problems with: (a) solid and liquid depositions on high-voltage components, (b) plugging of the water supply system, and (c) operation in the restricted-blowdown, recirculated-water mode. With the incorporation of these modifications, it was demonstrated that WESP systems can operate reliably while providing excellent control of emissions.

MINERAL WOOL

Bethlehem Steel utilizes blast furnace slag from ironmaking facilities to manufacture mineral wool in two hot-blast cupolas at its mineral wool plant located in Bethlehem, Pennsylvania. Shortly after plant start-up in 1972 it was found that the original venturi scrubbers were not reducing the cupola top gas particulate concentrations to desired levels. Stack tests showed that operation at a 22 in. WG* pressure drop seldom reduced the emission concentration to less than 0.2 gr/scfd. This poor performance was due principally to the nature of the emissions generated in the process of making mineral wool from blast furnace slag, coke and silica stone. Particle size analyses of this high-alkali, high-silica fume showed 80% of it to be less than one micron in diameter. Pilot-scale tests with a high-energy venturi scrubber demonstrated that a very high pressure drop, 90-100 in. WG, was required to meet the state outlet criterion of 0.04 gr/scfd total particulate. On the basis of the experience of other mineral wool manufacturers,[3] a pilot-scale baghouse was installed and evaluated as an alternative to the energy-intensive venturi scrubber. Baghouse tests showed that fabric filtration was successful only if the operating temperature was rigorously maintained to prevent either low-temperature dew point problems or high-temperature sublimation of elemental sulfur.

---

* Some of the papers in these proceedings use nonmetric units for convenience. Readers are asked to use table of conversion factors on page 253.

Given its low-energy, high-efficiency operation and relative insensitivity to temperature problems, the wet electrostatic precipitator presented itself as a logical alternative to both venturi scrubbing and fabric filtration. In January 1975 a 1200-cfm pilot-scale WESP was obtained from Fluid-Ionic Systems, Division of Dart Industries, Inc. This patented WESP design[4] utilizes an integral tangential prescrubbing inlet chamber followed by a vertical wetted-wall concentric-ring electrostatic precipitator (Figure 1). The unique feature of this design is its all-corrosion-resistant construction. Its fiberglass collection cylinders and 316L stainless steel or titanium discharge electrodes make this device particularly suitable for use on corrosive gases such as those generated by mineral wool cupolas.

The pilot-plant test unit was operated using a sidestream takeoff from the main exhaust duct of one of the plant's two cupolas. Figure 2 is a schematic diagram of the cupola and the test WESP arrangement.

The test program was conducted in two phases: in Phase I, which lasted from January to early April 1975, the gas flow rate was set at 700-800 acfm, corresponding to full-scale design velocities of 8.8-10.1 fps, respectively. However, the equipment proved to be inoperable for periods of extended duration at these high gas flow rates. Therefore, in Phase II, April to early June, the gas flow rate was set at about half the original rate.

Results of emission testing for Phase I are summarized in Table 1. The initial test results were encouraging, with outlet dry particulate concentrations averaging 0.002 gr/scfd, while inlet concentrations averaged 0.31 gr/scf. However, when inlet concentrations consistently exceeded 0.5 gr/scfd, the WESP could not be made to operate continuously for greater than about 48 hours. Also, the WESP would not operate properly during periods when charging was stopped (burndown). During these periods, high temperatures were experienced and the inlet loading exceeded 2 gr/scfd. Under these severe conditions, the WESP could not function for even one hour. Precipitator shutdown resulted from short-circuiting of the high voltage system whenever a reduction in particulate removal efficiency allowed the deposition of solids on the normally "clean-side" components of the WESP. This type of efficiency reduction is caused by the space-charge corona-suppression effect that occurs in electrostatic precipitators when a heavy concentration of finely divided particulate matter is introduced into the zone between the high-energy discharge electrode and the collection electrode.

Because of this unreliable performance, the gas flow rate was reduced to 350 acfm, which corresponds to a design velocity of 4.4 fps. Although the initial results at this condition were encouraging,

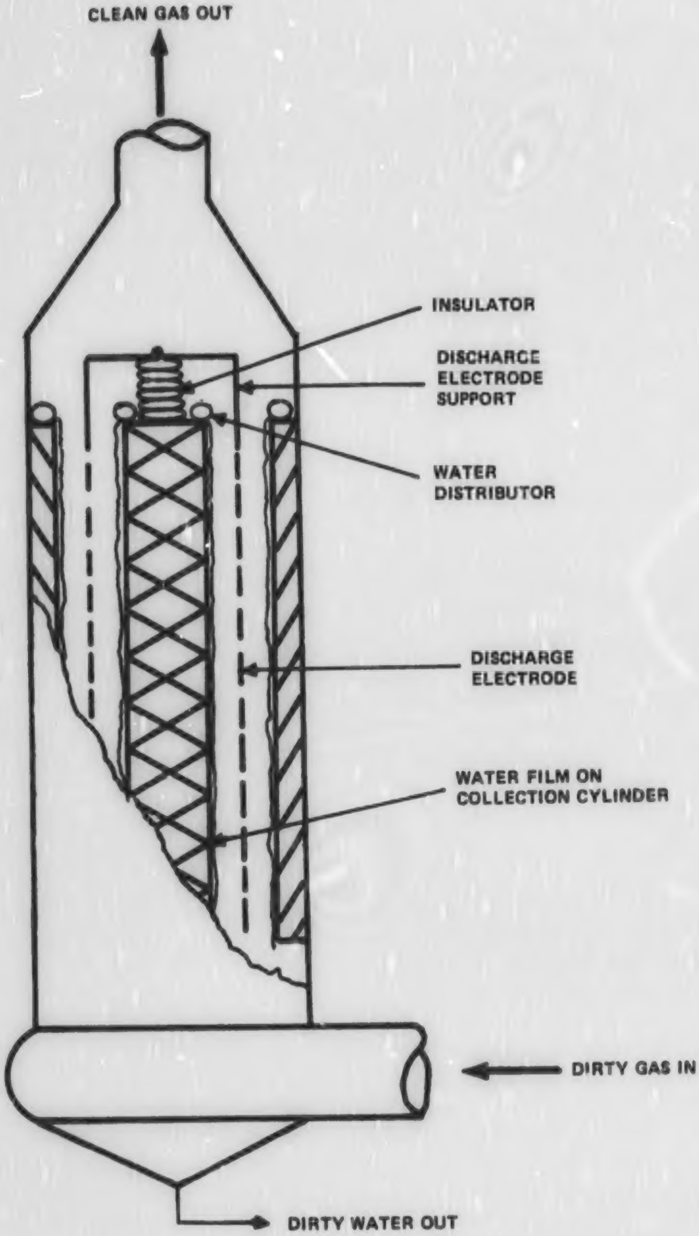
CLEAN GAS OUT
INSULATOR
DISCHARGE ELECTRODE SUPPORT
WATER DISTRIBUTOR
DISCHARGE ELECTRODE
WATER FILM ON COLLECTION CYLINDER
DIRTY GAS IN
DIRTY WATER OUT

Figure 1. Schematic of Fluid-Ionic pilot WESP.

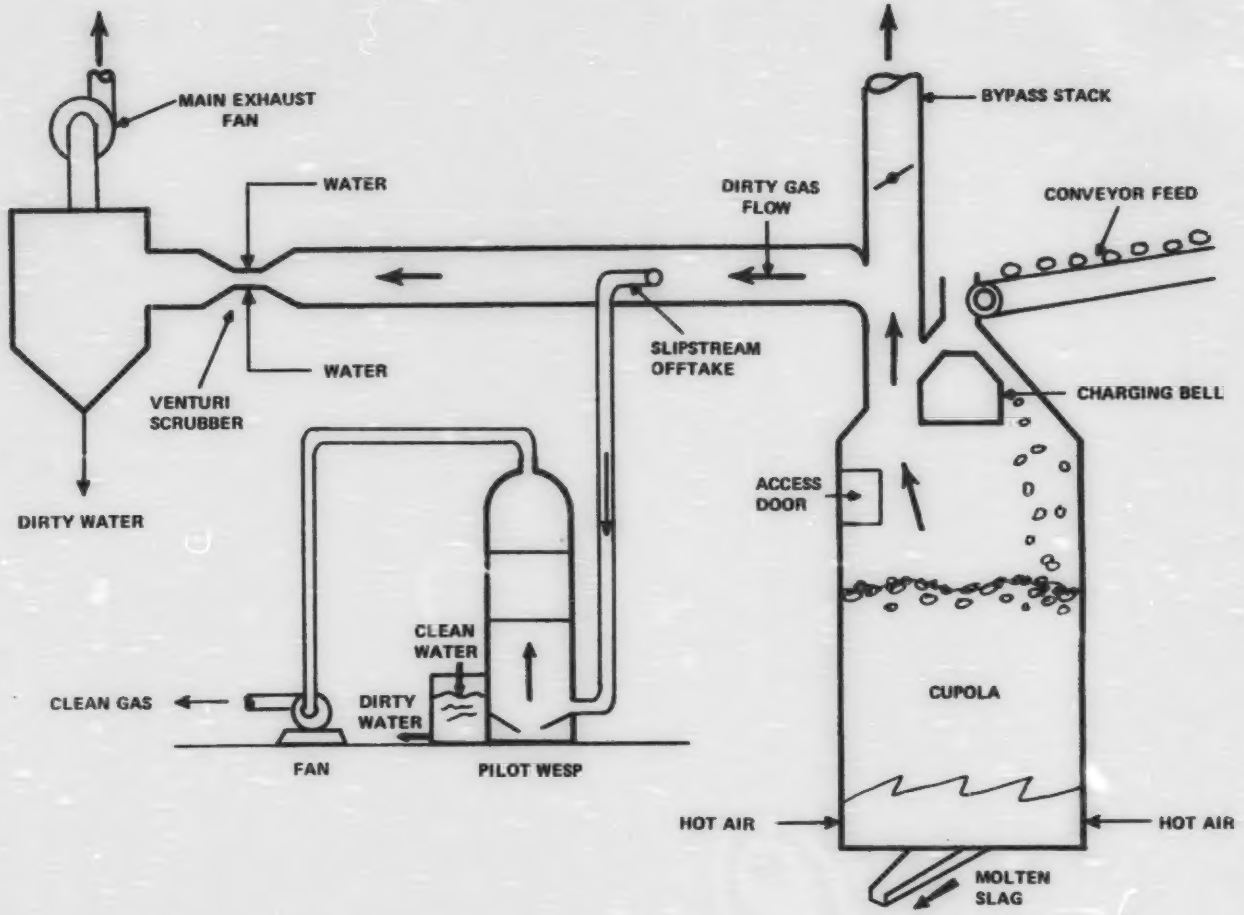
MAIN EXHAUST FAN
WATER
WATER
VENTURI SCRUBBER
DIRTY WATER
DIRTY GAS FLOW
SLIPSTREAM OFFTAKE
BYPASS STACK
CONVEYOR FEED
CHARGING BELL
ACCESS DOOR
CUPOLA
CLEAN WATER
DIRTY WATER
CLEAN GAS
FAN
PILOT WESP
HOT AIR
HOT AIR
MOLTEN SLAG

Figure 2. *Cupola and pilot WESP arrangement at the mineral wool plant.*

TABLE 1. MINERAL WOOL PLANT PILOT WESP EMISSION TEST RESULTS

Test No.	Cupola operating mode	Inlet flow, acfm	Inlet temperature, °F	Inlet dry particulate, gr/scfd	Outlet dry particulate, gr/scfd
			PHASE I - OLD UNIT		
1	Normal	556	116-180	0.3020	0.0016
2	Normal	726	128	0.5310	0.0062
3	Normal	707	112	0.3290	0.0016
4	Normal	707	128	0.1981	0.0018
5	Normal	702	130	0.2549	0.0016
6	Normal	702	130	0.2611	0.0024
7	Normal	683	136	0.2634	0.0023
8	Normal	874	175	0.9172	0.0535
9	Normal	795	150	0.6708	0.0955
10	Normal	795	150-280	0.7407	0.1163
11	Normal	764	110	0.7213	0.0751
12	Normal	764	110-140	0.9432	0.1434
13	Normal	678	110	0.3731	0.0015
14	Burndown	350	400-900	1.174	0.0980
15	Normal	350	110	1.280	0.0019
16	Normal	350	110	1.709	0.0035
			PHASE II - NEW UNIT		
17	Normal	350	110	0.6446	0.0014
18	Normal	350	110	0.4161	0.00097
19	Normal	350	110	0.4401	0.00075
20	Normal	350	110	0.3837	0.00034
21	Burndown	350	280-400	0.8075	0.0014
22	Normal	350	150	-	0.0020
23	Burndown	350	-	-	0.0054

the unit was destroyed by a fire before it could be operated for a satisfactory period of time. The fire was probably caused by a combustible mixture of cupola top gas being ignited by normal precipitator sparking.

Phase II of the test program began with the installation of a new pilot-scale WESP which was run at the 350 acfm gas flow rate. The new unit was like the first, except that it had a recessed insulator with a purge-air system designed to prevent the accumulation of solids and moisture on the insulator surface.

Table 1 includes the results of emission testing during Phase II. The gas-cleaning effectiveness of this new WESP was excellent under conditions of continuous operation. The WESP was able to clean the cupola gas to an average outlet concentration of 0.002 gr/scfd from an average inlet concentration of 0.47 gr/scfd dry particulate, which was a considerable higher inlet loading than that in Phase I. The buildup of solids on the clean-side components that was experienced in Phase I did not occur, and the unit operated for 300 hours of normal operation and through eight burndowns before any maintenance was required.

Once-through water operation of a full-scale WESP installation at the mineral wool plant would have exceeded the available amount of municipal fresh water. It was therefore decided to pilot-test a recirculated water system at a restricted blowdown of 25%. The precipitator ran at this blowdown rate for over 100 hours without any noticable deposition or scaling on the wetted surfaces.

On the basis of the successful operation of the pilot-scale WESP, a full-scale installation was designed and installed. The full-scale system was designed to handle the approximately 20,000 scfm of cupola top gas. It included an eight-cylinder WESP (Figure 3) similar to the pilot unit, plus the necessary water recirculation and blowdown treatment facilities.

Operation of this integrated air and water pollution control facility was begun in March 1976. The initial performance was good; stack tests conducted according to EPA Method 5 showed outlet front-half particulate loadings of less than 0.01 gr/scfd. The recirculated wastewater system also functioned well.

The operation of the WESP was smooth until June 1976, when problems with the wastewater treatment system developed. The principal difficulty was the unacceptably high chemical oxygen demand in the 70 gpm of wastewater being discharged. To solve this problem the recirculation rate was increased from 25% to 95%. Thus, the only liquid discharge was contained in the approximately 10 gpm of thickened sludge removed from the clarifier.

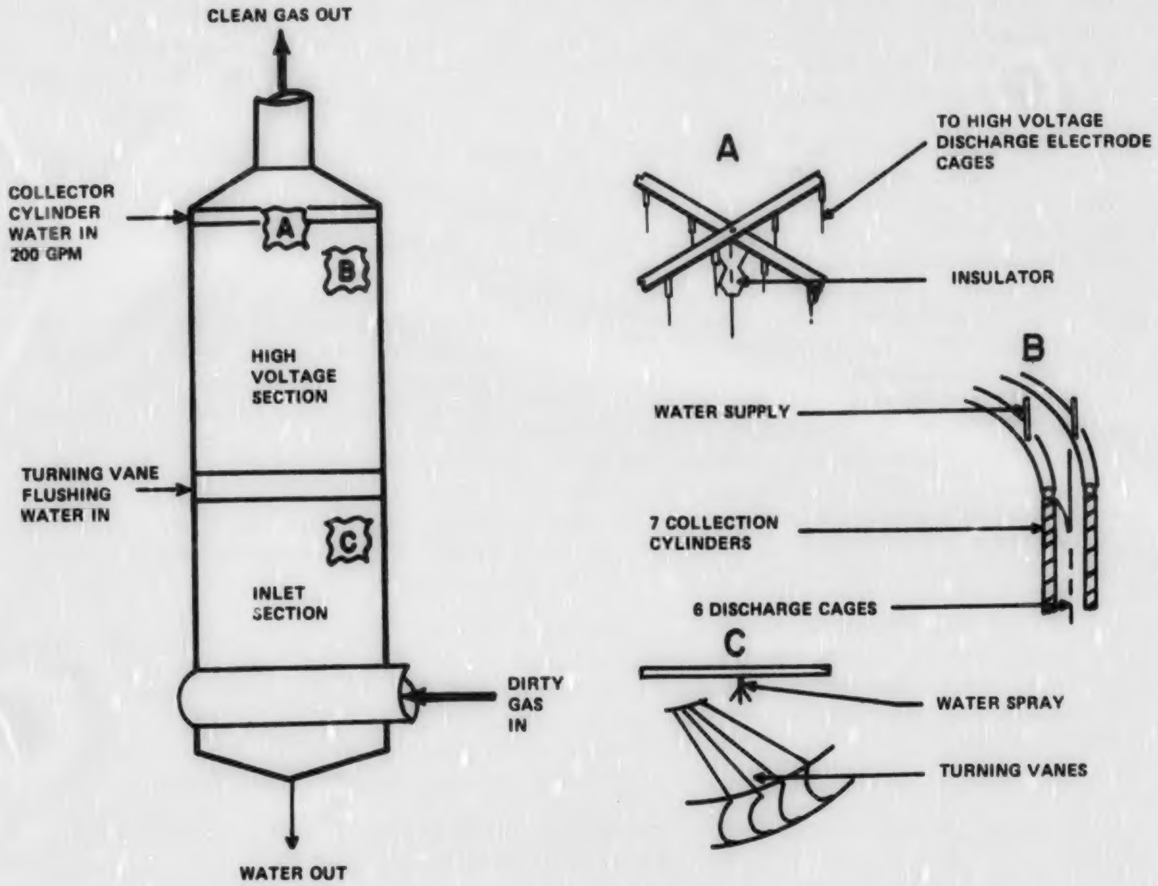
CLEAN GAS OUT
COLLECTOR CYLINDER WATER IN 200 GPM
A
B
HIGH VOLTAGE SECTION
TURNING VANE FLUSHING WATER IN
C
INLET SECTION
DIRTY GAS IN
WATER OUT
A
TO HIGH VOLTAGE DISCHARGE ELECTRODE CAGES
INSULATOR
B
WATER SUPPLY
7 COLLECTION CYLINDERS
6 DISCHARGE CAGES
C
WATER SPRAY
TURNING VANES

Figure 3. Schematic of full scale WESP at mineral wool plant.

Although this modification solved the wastewater problem and the system operated well until July 1976, two new problems arose. First, an explosion occurred due to an unusually high concentration of combustible constituents in the cupola gas. The explosion caused relatively minor damage, and repairs were quickly made. The second problem was discovered during repairs of the damage. The fiberglass collection cylinders were found to be cracked and blistered from chemical attack on the epoxy resin by the warm, acidic recirculated liquor. This damage to the collection cylinders was sufficient to disturb the flushing liquor film, thus significantly reducing the precipitator power input. The vendor had experienced similar problems with epoxy-resin cylinders at other installations and therefore made arrangements to subsequently replace the existing set of collection cylinders with cylinders made from a chemically resistant vinyl ester-based resin fiberglass. Industrial experience with this new material had demonstrated its ability to withstand similar environments.[5]

In the July-November 1976 interim before installation of the new collection cylinders, the plant was forced to operate the precipitator on reduced power because of the defective cylinders. Nevertheless, even at reduced power the WESP met the 0.04 gr/scfd total particulate outlet criterion. In November 1976 another explosion occurred that again caused relatively minor damage. After repair of the explosion damage and installation of a system that would provide enough dilution air to prevent future explosions, the WESP was shut down for replacement of the collection cylinders, as had been planned by the vendor. The WESP was started up again in early March 1977.

With the wastewater-treatment and explosion problems solved, and the new chemically resistant cylinders installed, the system has provided reliable service and effective gas cleaning at outlet particulate concentrations well within the Pennsylvania criterion. Operation with the extremely "tight" water circuit, i.e., less than 10% blowdown, has also been satisfactory.

Maintenance on the system is required on a regular schedule, but such activities, including inspection and cleaning of the insulator and water distributors, are performed in less than four manhours during the plant's biweekly maintenance down-shifts.

SCARFER

Bethlehem operates an automatic hot scarfer at the 44-inch rolling mill at its Lackawanna, New York, plant. Oxygen and natural gas are used in this operation to flame-scarf newly-rolled hot billets and slabs, a practice which results in the generation of a dense iron oxide fume. The particulate emissions from this operation are controlled in an underground tunnel by water sprays that contact the waste gas as it is transported to the exhaust fan. Stack tests have shown that this method of fume control results in compliance with the particulate mass emission codes of Erie County and New York State. However, the plume produced has an opacity somewhat greater than the 20% criterion established by these agencies for scarfing operations.

To evaluate methods for reduction of the opacity, a pilot venturi scrubber was tested in December 1973 and January 1974. However, even at a 60-in. WG pressure drop, the pilot plant outlet plume still exceeded 20% opacity. As an alternative approach, it was decided to test two continuously-irrigated WESPs because a similar type, the traditional intermittently flushed tube-type wet precipitator, had demonstrated effectiveness in emission reduction at various hot-scarfing facilities in the industry.[6]

The program for testing the effectiveness of continuously-irrigated precipitators involved pilot-scale units from Fluid-Ionic

Systems and MikroPul Corporation. The MikroPul unit is a horizontal-flow plate-type wet electrostatic precipitator that is continuously flushed by sprays directed at both the inlet baffle and the vertical collection plates (Figure 4). The Fluid-Ionic pilot-scale WESP was the same one that had been tested at the Mineral Wool Plant. The two WESPs were installed to handle slipstreams from the six-foot diameter scarfer waste gas stack, as shown in Figure 5, and were tested simultaneously.

The sampling program consisted of 12 tests, during which particulate samples were drawn at the outlet of both pilot WESPs. Since initial samples taken simultaneously at the inlets to both units showed that the inlet concentrations were at about the same level, a single inlet sample sufficed throughout the testing. Each test consisted of 15 to 30 scarfs. The pilot units were operated during daylight shifts only.

The results of the gas-cleaning tests (Table 2) show that both WESPs did an excellent job of cleaning the scarfer fume. The outlet dry-particulate loadings were less than 0.01 gr/scfd for all but one test. Because the object of the test program was to reduce the opacity of the plumes, visible emissions from the pilot stacks and the main stack were observed and quantified for each scarf. The average of these observed opacities are shown in Table 2. The Beer-Lambert Law, which relates opacity to optical path length, was used to translate the observed opacities from the one-foot-diameter pilot stacks to the opacity expected at the larger stack of a full-scale installation. According to this relationship, a 5% opacity in a one-foot pilot stack would mean an opacity of 27% in the six-foot full-scale stack. From this analysis it follows that to meet the opacity limitation of 20% from a full-scale installation, the requirement would be a particulate loading corresponding to a nearly invisible pilot stack plume, i.e., 0.001 gr/scfd or less, such as was observed in Test 11, Table 2.

SINTERING PLANTS

Stricter environmental controls and economic considerations have necessitated the recycling of many by-products of steel production that were formerly regarded as waste materials. Most of these recycled, or revert, materials must be agglomerated before they are returned to the ironmaking process. Almost without exception, the reverts are blended and sintered at sintering plants before being recycled to the blast furnace. Unfortunately, the addition of these reverts to other sintering strand constituents usually results in the formation of a harder-to-clean aerosol in the windbox exhaust. Because of this increased gas-cleaning difficulty and the lower discharge criteria associated with current stringent air pollution regulations, the collection of sintering windbox emissions has become one of the most difficult pollution abatement tasks in the steel industry.

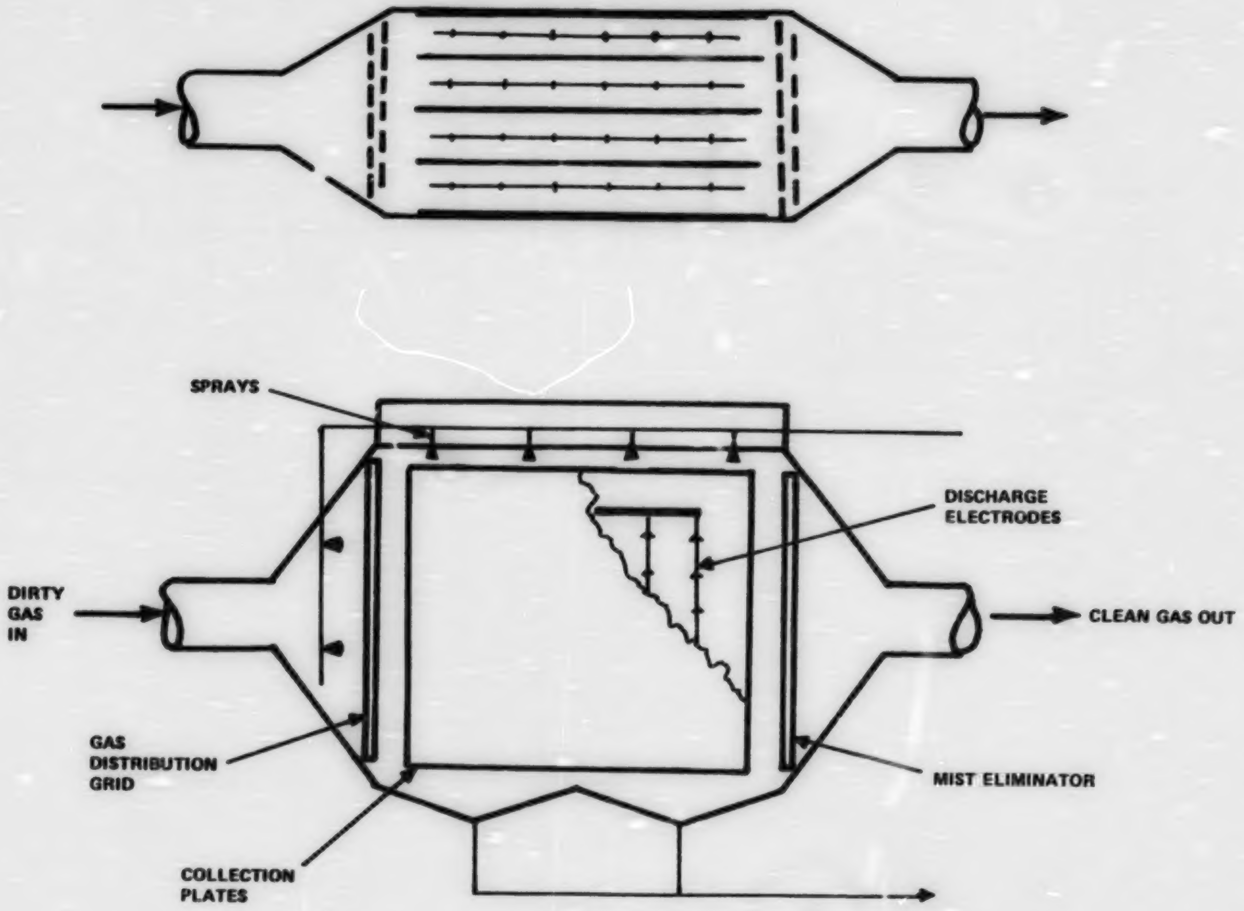
SPRAYS
DISCHARGE ELECTRODES
DIRTY GAS IN
CLEAN GAS OUT
GAS DISTRIBUTION GRID
MIST ELIMINATOR
COLLECTION PLATES

Figure 4. Schematic of Mikropul Pilot WESP.

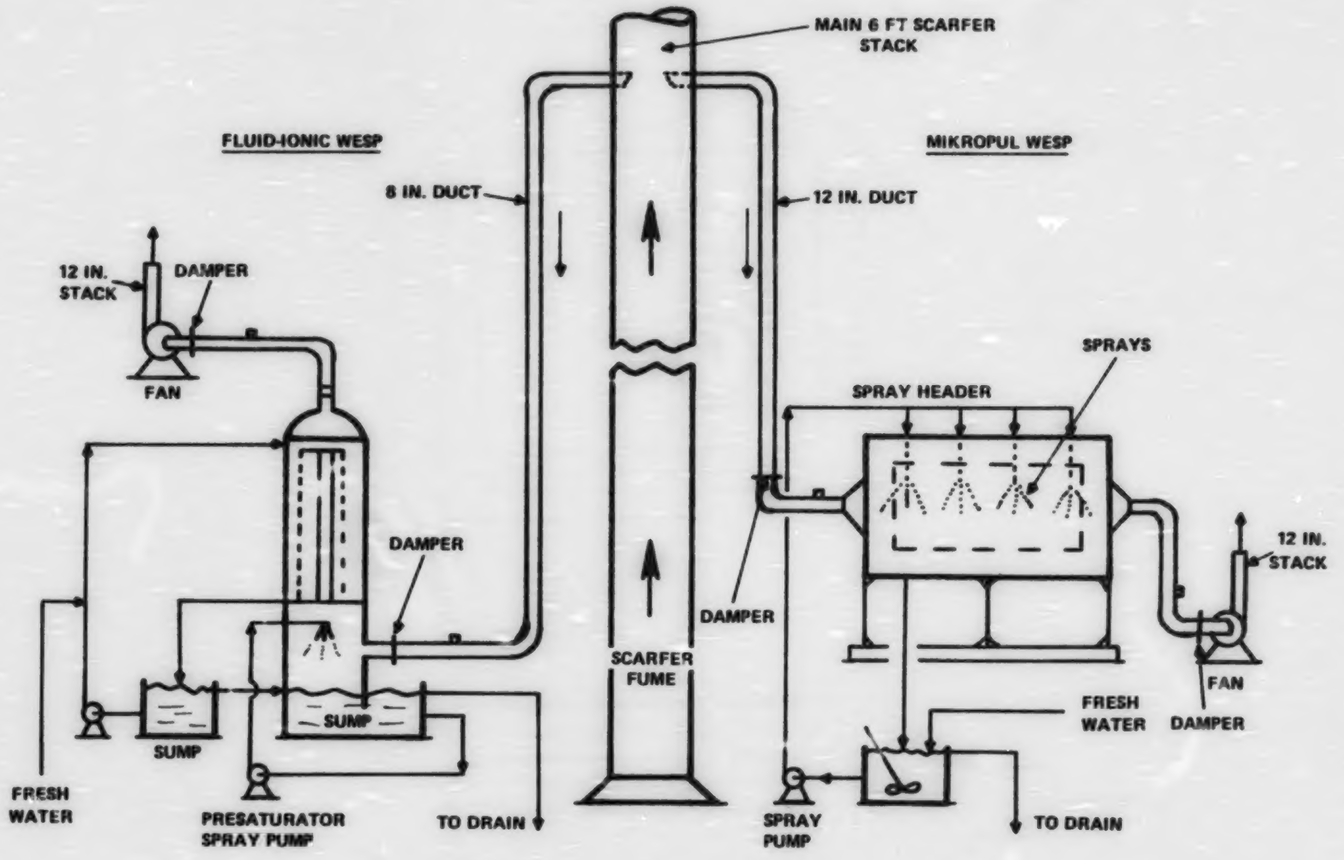
MAIN 6 FT SCARFER STACK
FLUID-IONIC WESP
MIKROPUL WESP
8 IN. DUCT
12 IN. DUCT
12 IN. STACK
DAMPER
FAN
SPRAYS
SPRAY HEADER
DAMPER
DAMPER
SCARFER FUME
12 IN. STACK
FAN
FRESH WATER
DAMPER
SUMP
SUMP
FRESH WATER
PRESATURATOR SPRAY PUMP
TO DRAIN
SPRAY PUMP
TO DRAIN

Figure 5. Schematic of pilot WESP arrangement at the Lackawanna 44 in. mill scarfer.

TABLE 2. RESULTS OF SIMULTANEOUS PARTICULATE TESTS ON MIKROPUL AND FLUID-IONIC SYSTEMS WESPS AT THE LACKAWANNA 44-IN. MILL SCARFER

Test No. and Main Stack Plume Density[a]	MikroPul WESP					Fluid-Ionic WESP				
	Inlet, gr/scfd	Outlet, gr/scfd	Efficiency, %	Average opacity, %	Inlet flow, scfmw	Inlet, gr/scfd	Outlet, gr/scfd	Efficiency, %	Average opacity %	Inlet flow, scfmw
1 - -	0.0570	-	-	-	-	0.0552	-	-	-	-
2 Heavy	0.1326	0.0023	98.26	12	1850	0.1326	0.0013	99.01	6	800
3 Heavy	0.1228	0.0023	98.12	9	1850	0.1228	0.0007	99.43	6	800
4 Moderate	0.0673	0.0016	97.62	9	1850	0.0673	0.0016	97.62	3	800
5 Moderate	0.0377	0.0016	95.76	6	1500	0.0377	0.0025	93.36	9	1000
6 Heavy	0.0758	0.0015	98.02	8	1500	0.0758	0.0023	96.96	10	1000
7 Moderate-Heavy	0.1260	0.0039	96.90	12	1500	0.1260	0.0030	97.62	14	1000
8 Moderate	0.0989	0.0056	94.33	20	2200	0.0989	0.0076	92.31	19	1200
9 Moderate	0.1031	0.0072	93.02	17	2200	0.1031	0.0108	89.52	18	1200
10 Moderate-Light	0.0880	0.0050	94.32	15	2200	0.0880	0.0089	89.88	17	1200
11 Light	0.0305	0.0013	95.73	4	1500	0.0305	0.0009	97.05	2	750
12 Very Light	0.0633	0.0034	94.63	14	2200	0.0633	0.0081	87.20	20	1400
13 Very Heavy	0.2688	0.0084	96.87	29	2200	0.2688	0.0258	90.40	39	1400

[a] All main stack opacities were in excess of 100%; therefore a qualitative assessment of the opacity is listed

Originally, sinter plants were equipped with dry mechanical collectors for windbox emission control. By the early 1970s electrostatic precipitators were the predominant control technology,[7] although high-energy venturi scrubbers were also being pilot-tested and installed in some plants.[8] At least two plants have also tried fabric filtration for windbox emission control. As for the new WESP technology, experience with its capability for sinter plants is still quite limited. The experience of others had shown that while the WESP approach has a potential for good gas-cleaning performance, operating problems, particularly with corrosion,[9] had prevented successful full-scale application.

Generally, Bethlehem's experience with windbox emission control has paralleled that of the steel industry. By 1970 the installation of mechanical collectors and dry electrostatic precipitators at three sintering plants had considerably reduced the emission of particulate matter in the windbox stack gases. However, at the Johnstown and Lackawanna plants, the performance of these systems was found to be marginal at first and later unsatisfactory. Attempts to upgrade the dry ESP performance by the addition of flue gas conditioners, such as ammonium sulfate, or by changing the rapping practice, met with limited success.

Medium- to high-energy wet scrubbing was evaluated as a possible retrofit or replacement of the dry ESPs. A pilot-scale scrubber was tested at the Lackawanna Plant for applicability as an add-on to the dry ESPs. The results showed that scrubber pressure drops of up to 45 in. WG were required to reduce dry particulate outlet loadings to less than the 0.03 gr/scfd outlet criterion. From an economics standpoint, this high energy requirement represented a decided disadvantage. It became evident that if Bethlehem wanted to achieve environmental goals at reasonable levels of energy consumption, more sophisticated air pollution technology such as wet electrostatic precipitators would have to be evaluated and adapted for windbox emission control. To this end, a program at the Lackawanna sinter plant was initiated in the spring of 1975 to pilot-test a MikroPul WESP, which, incidentally, was subsequently used in the test program at the Lackawanna 44-in. mill scarfer.

As part of the evaluation of the WESP approach, careful attention was paid to the variations in the strand mix that are known to affect windbox gas-cleaning difficulty. Of primary concern were: (a) the percentage and composition of revert materials such as rolling-mill scale and blast furnace flue dust, and (b) the ratio of (CaO + MgO) to (SiO_2 + Al_2O_3) in the sinter, commonly called the base-to-acid ratio (B/A). Results of previous sinter plant tests had shown that oily rolling-mill scales could contribute to the condensible-hydrocarbon loading in the windbox gases. Also, it was found that the high-alkali blast furnace flue dust could add to the stack-gas concentration of hard-to-remove potassium and sodium chloride fume. Furthermore, it was shown that the quantity of this alkaline-chloride fume in the stack gas depends on the B/A of the sinter mix and is particularly high at high values of B/A. For these reasons, high-basicity sinter mixes containing reverts present a very difficult gas-cleaning job. In general, the WESP was evaluated at strand-mix conditions which yielded typically hard-to-clean windbox gas.

Figure 6 is a schematic diagram of the MikroPul WESP setup. Gas-cleaning tests were conducted with once-through clean water and later with recirculated acidic and recirculated neutralized water. To assess the potential long-term problems of the WESP design when operating in a minimum wastewater discharge mode, tests with recirculated water were conducted on an around-the-clock basis for periods of up to ten days.

Table 3 summarizes the gas-cleaning performance test results, pilot-plant operating conditions, and strand mixes for this WESP evaluation. Overall, the gas-cleaning performance was excellent. Dry-particulate outlet loadings were generally less than 0.01 gr/scfd. Deliberate efforts were made to exceed the capacity of the pilot plant by increasing the gas flow rate and revert percentage. Although the performance of the pilot WESP was thereby slightly impaired, it was still adequate, as evidenced by the fact that dry-particulate loadings were not in excess of the 0.03 gr/scfd discharge criterion.

Potentially serious problems arose during the tests with recirculated water. Tests and observations made while operating in the acidic recycled mode showed the potential for serious corrosion problems. Analyses of the recirculating liquor (pH 3; 500 ppm chloride

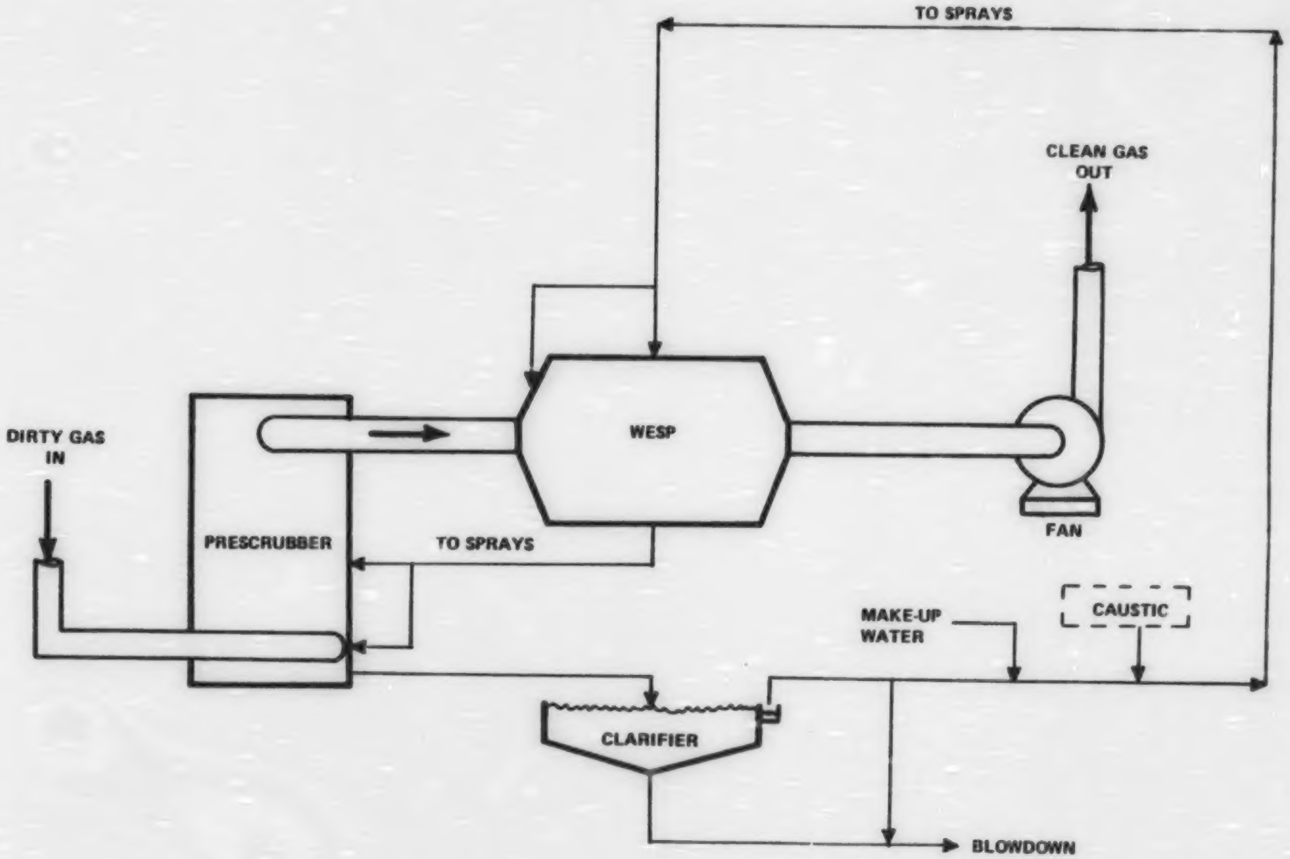
TO SPRAYS
CLEAN GAS OUT
DIRTY GAS IN
WESP
PRESCRUBBER
TO SPRAYS
FAN
CAUSTIC
MAKE-UP WATER
CLARIFIER
BLOWDOWN

Figure 6. Mikropul Pilot WESP test setup at the Lackawanna Sinter Plant.

TABLE 3. RESULTS OF PARTICULATE TESTS ON THE PILOT MIKROPUL WESP AT THE LACKAWANNA SINTER PLANT

No. of Tests	Water System	Inlet gas flow, scfmd	Strand Mix[a]		Inlet loading average,[c] gr/scfd		Outlet loading average, gr/scfd		Outlet loading range, gr/scfd	
			scale	flue dust	particulate	hydrocarbon[b]	particulate	hydrocarbon[b]	particulate	hydrocarbon[b]
1	Once-through	1870	High	Low	0.437	0.004	0.002	0.001	-	-
4	Once-through	3100	High	Low	0.319	0.009	0.009	0.003	0.014	0.006
5	Recirculated acid	2170	High	Low	0.250	0.017	0.005	0.006	0.003-0.006	0.002-0.013
3	Recirculated acid	2420	Moderate	Low	0.352	0.016	0.008	0.002	0.007-0.010	0.002-0.003
1	Recirculated acid	2420	High	Low	0.265	0.013	0.009	0.007	-	-
1	Recirculated acid	3100	Low	Moderate	0.407	0.013	0.017	0.004	-	-
2	Recirculated acid	3100	Moderate	Moderate	0.315	0.008	0.020	0.004	0.017-0.023	0.004-0.005
2	Recirculated pH control	1740	High	Low	0.293	0.015	0.002	0.004	0.001-0.004	0.002-0.005
1	Recirculated pH control	2150	Low	Low	0.185	0.016	0.002	0.001	-	-
5	Recirculated pH control	2150	High	Low	0.294	0.019	0.002	0.004	0.002-0.003	0.002-0.006
6	Recirculated pH control	2660	High	Low	0.320	0.025	0.008	0.007	0.003-0.014	0.004-0.011

[a] Strand Mix Designation:
High: Concentration greater than 8% of strand mix.
Low: Concentration less than 6% of strand mix.
Moderate: Concentration mid-range 6-8% of strand mix.

[b] Extracted with chloroform.

[c] Measured at inlet of prescrubber; see Figure 6.

concentration) showed that it would be extremely corrosive to the more reasonably-priced corrosion-resistant alloys, such as 316L stainless steel, that are adequate for less rigorous service. Tests conducted in the pH-controlled recirculated mode also resulted in problems. By metering caustic into the water to maintain a pH of 7.0 or greater in the WESP, the absorption of CO_2 from the windbox gas increased, and a resultant calcium and magnesium carbonate scale was deposited on the spray nozzles and other critical components of the WESP, thereby rendering it inoperable. It was concluded that operation of any WESP system for sinter plant windbox gas-cleaning duty would have to be in the acidic mode and that the materials of construction would have to be chosen accordingly. To this end a test program involving the Fluid-Ionic Systems corrosion-resistant WESP was begun in late 1975. The pilot-scale WESP was installed at the Lackawanna sinter plant in an arrangement as shown in Figure 7. The system was fitted with a titanium discharge electrode to provide corrosion resistance appropriate for the environment.[10]

The initial phase of the performance evaluation involved testing at various gas flow rates to establish design parameters for a possible full-scale installation. As before, the sinter strand mix was carefully monitored and adjusted to give a windbox emission that would be hard to clean. Table 4 summarizes the gas-cleaning data generated during these tests. As with the previous system, this WESP design gave excellent gas cleaning. Dry-particulate outlet loadings averaged 0.007 gr/scfd, and none greater than 0.02 gr/scfd were measured. Also, chloroform extractable condensible hydrocarbons were reduced from an average inlet loading of 0.004 gr/scfd to an average outlet loading of 0.002 gr/scfd. However, water distributor

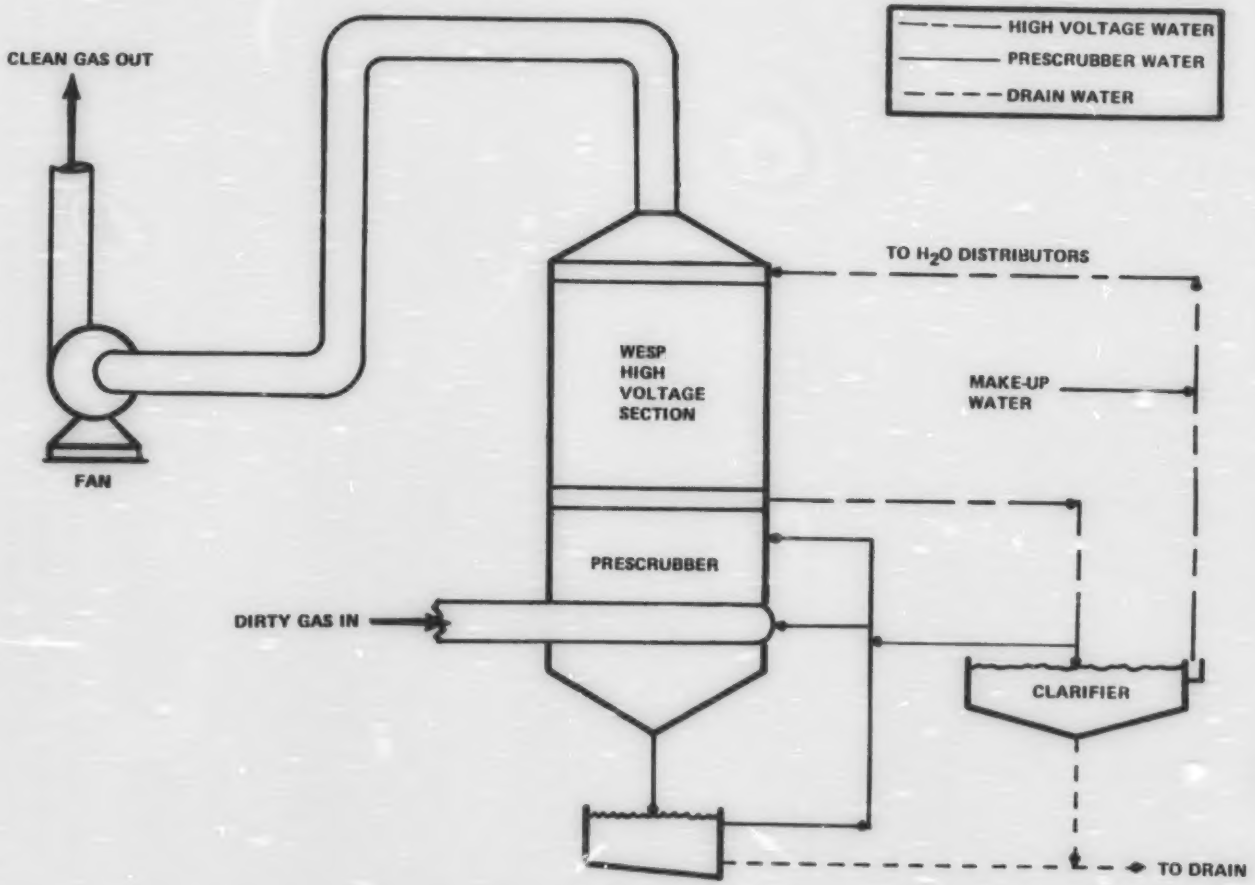
HIGH VOLTAGE WATER
PRESCRUBBER WATER
DRAIN WATER
CLEAN GAS OUT
FAN
WESP
HIGH
VOLTAGE
SECTION
PRESCRUBBER
DIRTY GAS IN
TO H_2O DISTRIBUTORS
MAKE-UP
WATER
CLARIFIER
TO DRAIN

Figure 7. Fluid-Ionic Pilot WESP test setup at the Lackawanna Sinter Plant.

TABLE 4. SUMMARY OF RESULTS OF PARTICULATE TESTS ON THE PILOT FLUID-IONIC SYSTEMS WESP AT THE LACKAWANNA SINTER PLANT

No. of Tests	Inlet gas flow, acfm	Strand Mix[a] scale	Strand Mix[a] flue dust	Outlet particulate loading, gr/scfd range	Outlet particulate loading, gr/scfd average
10	1060	High	Moderate	0.001-0.006	0.003
1	1200	High	Moderate	-	0.005
5	1430	High	Moderate	0.004-0.009	0.006
5	1600	High	Moderate	0.005-0.017	0.010

[a] Strand Mix Designation:

High: Concentration greater than 8% of strand mix.
Low: Concentration less than 6% of strand mix.
Moderate: Concentration mid-range 6-8% of strand mix.

plugging and solids deposition that resulted from the recirculation of the acidic solids-laden liquor were problems remaining to be resolved.

The pilot facility was modified to include an eight-foot diameter clarifier for solids removal from recycled water and a pulse air system to prevent water distributor plugging. The WESP was then operated on an around-the-clock basis in an endurance test to define and solve operational difficulties that might emerge from the system, which now incorporated both air pollution control and water treatment.

The system ran well during the three ten-day periods of the endurance test. In general, it was possible to operate the WESP on recirculated water and with minimum blowdown for periods of up to seven days before maintenance cleaning had to be performed.

Encouraged by the progress being made on the adaptation of the WESP for windbox emission control, Bethlehem decided to fund a full-scale WESP demonstration system at the Johnstown sinter plant. Construction of the full-scale system, with associated water treatment equipment, was begun in April 1976 and completed in June 1976. A schematic diagram of the major components of the system is shown in Figure 8. The exhaust gas conveyance equipment of the demonstration system was capable of handling slightly less than one-quarter of the total 300,000 acfm of windbox gas generated by the plant.

Table 5 summarizes the results of gas-cleaning tests conducted with the WESP demonstration system. Within limits, most of the tests were made at baseline operating conditions that paralleled the expected operating conditions of the full-scale WESP installation at the Johnstown sinter plant. These conditions were: sinter B/A = 0.85, average gas flow = 68,600 acfm at 250°F (47,000 scfmd), and operation of the existing dry electrostatic precipitator ahead of the WESP. Some tests were also conducted to establish the effect of higher B/A on the gas-cleaning performance of the WESP. Finally, three brief tests of about one-half hour each were conducted with the existing dry ESPs de-energized to find out whether a gas precleaning step is needed prior to treatment in the WESP system.

The tests conducted under baseline conditions showed outlet dry-particulate loadings ranging from 0.003 to 0.022 gr/scfd with an average of 0.010 gr/scfd. Only one test exceeded 0.020 gr/scfd and that one corresponded to an abnormally high inlet particulate loading. The total particulate loading for the baseline case averaged 0.012 gr/scfd, which included filterable and chloroform extractable hydrocarbons from the back-half impingers.

The tests at increased B/A showed a significant increase in the outlet loading. At a B/A of 1.50 the filterable and back-half chloroform extractable particulate loading averaged 0.018 gr/scfd.

As part of the evaluation of increased B/A, a series of tests was conducted with the existing dry electrostatic precipitator de-energized. Inlet dry-particulate loadings at this condition increased to greater than 2.50 gr/scfd, resulting in a corresponding increase in outlet loadings to as much as 0.037 gr/scfd. These tests pointed up the inability of the WESP to adequately clean high concentrations of particulate emissions without some precleaning by an auxiliary system.

For every operating condition the opacity of the plume from the demonstration stack was less than that of the main stack. However, when viewed against the contrasting background of a clear sky, the opacities were commonly judged to be 20% to 40% during times when outlet loadings were known to be less than 0.02 gr/scfd.

The operability and reliability of the WESP system was generally satisfactory for the three-month period in which it was operated. Required maintenance was performed during the weekly eight-hour sinter plant downturn. With the exception of a few problems with equipment not specifically related to normal WESP operation, the weekly maintenance on the WESP itself, which included a general

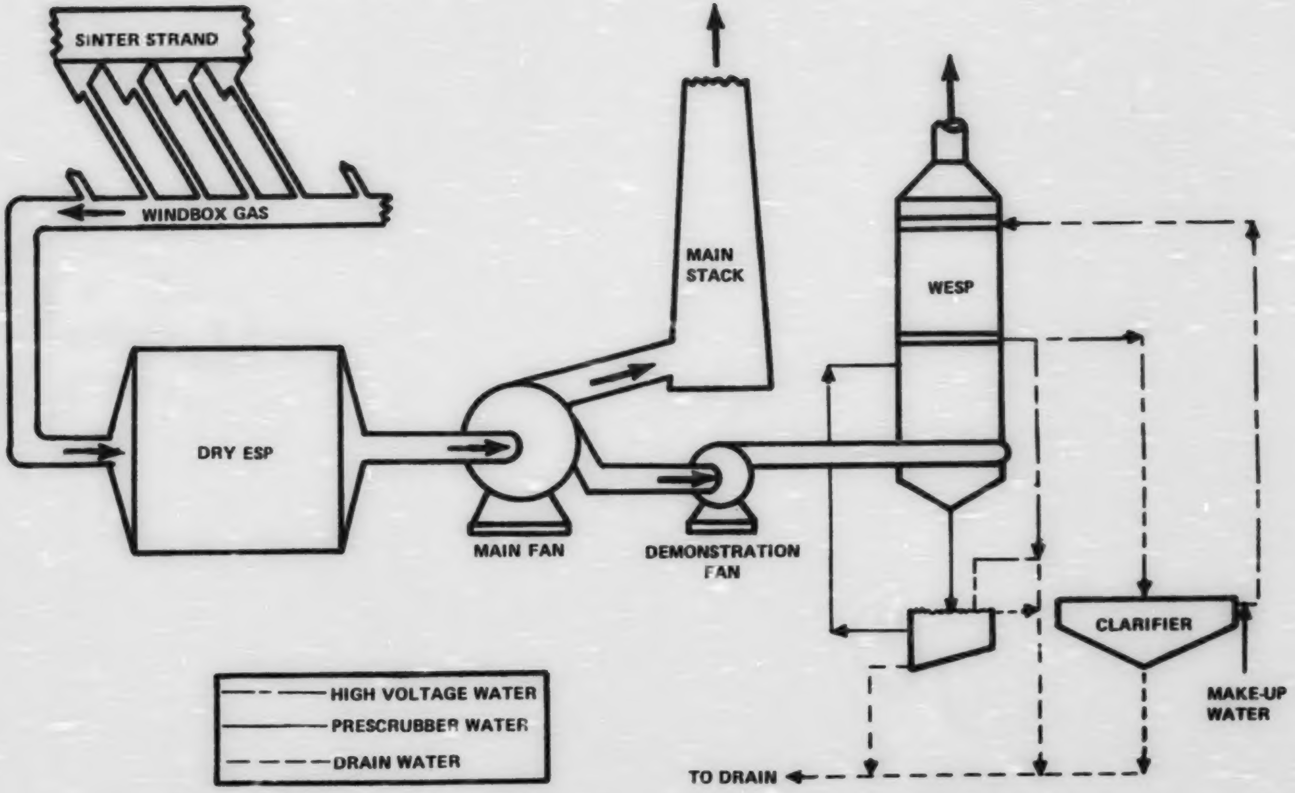
SINTER STRAND
WINDBOX GAS
DRY ESP
MAIN FAN
MAIN STACK
DEMONSTRATION FAN
WESP
CLARIFIER
MAKE-UP WATER
TO DRAIN
HIGH VOLTAGE WATER
PRESCRUBBER WATER
DRAIN WATER

Figure 8. Full scale WESP demonstration setup at Johnston Sinter Plant.

TABLE 5. SUMMARY OF WESP DEMONSTRATION SYSTEM GAS-CLEANING TEST RESULTS AT THE JOHNSTON SINTER PLANT

			Demonstration System Inlet Loadings[a]						Demonstration System Outlet Loadings[a]					
			Particulate (Total filter catch)			Hydrocarbon (Extracted condensibles)			Particulate (Total filter catch)			Hydrocarbon (Extracted condensibles)		
Operating Condition	B/A	Gas flow av., scfmd	Av., gr/scfd	Range, gr/scfd	No. of Tests	Av., gr/scfd	Range, gr/scfd	No. of Tests	Av., gr/scfd	Range, gr/scfd	No. of Tests	Av., gr/scfd	Range, gr/scfd	No. of Tests
Baseline	0.85	49,600	0.393	0.196-1.140	19	0.004	0.003-0.008	5	0.010	0.003-0.022	38	0.002	nil-0.004	18
Reduced Flow	0.85	22,000	0.231	0.172-0.295	3	—	—	—	0.004	0.004-0.004	3	—	-	
High Basicity	1.50	42,500	0.342	0.119-0.526	8	0.002	0.001-0.003	5	0.013	0.008-0.018	8	0.005	0.003-0.009	5
High Basicity + Oil	1.50	44,200	0.336	0.230-0.419	3	0.002	0.002-0.003	3	0.014	0.013-0.014	2	0.004	0.002-0.006	2
High Basicity, Dry ESP Off	1.50	45,600	2.568	—	1	0.005	—	1	0.032	-	1	0.005	-	1

[a] Total gas-stream grain loadings would include impinger condensibles not extractable with chloroform. They averaged 0.010 gr/scfd at the inlet for 15 tests and 0.008 gr/scfd at the outlet for 35 tests.

cleaning and inspection, usually took less than eight man-hours. The operation of the recirculated water system was also found to be satisfactory although a fair amount of attention was needed to maintain the strict water-quality requirements for successful WESP operation.

CONCLUSIONS

On the basis of Bethlehem Steel Corporation tests and operating experience with two commercially-available wet electrostatic precipitators, it was concluded that:

- WESP systems can be successfully adapted for the control of hard-to-clean particulate emissions from metallurgical processes.
- WESP systems can perform satisfactorily when operating with minimum blowdown of recirculated acidic water. The minimum achievable blowdown rate for a particular application must be determined by testing the specific system.
- Routine maintenance should be provided for WESP devices to ensure continued effective performance. In some cases, such maintenance can be scheduled to coincide with a plant's normal downturn.
- The main goals of reducing particulate emissions to below regulatory criteria were achieved. However, the test work thus far gives no basis for concluding that compliance with visible emissions standards is feasible by use of WESP technology.

REFERENCES

1. Bakke, E. Wet Electrostatic Precipitators for Control of Submicron Particles. J. Air Pollut. Contr. Assoc. 46(2):163, 1975.

2. Lunde, D.C. Control of Bake Oven Exhaust Fumes With a Wet Electrostatic Precipitator. Presented at AIME Convention, Atlanta, March, 1977.

3. Danielson, J.A. Air Pollution Engineering Manual. U. S. Department of Health, Education and Welfare, Cincinnati, 1967. pp. 342-349.

4. deSeversky, A.P. U. S. Patent 3,315,445 (April 25, 1967).

5. Chemical Processing. April, 1976, p. 70.

6. Haaland, H. H. and J. L. Ma. Corrosion Problems in Wet Precipitator Design. Resolving Corrosion Problems in Air Pollution Control Equipment. National Association of Corrosion Engineers, Houston, Texas, 1976. pp. 87-88.

7. Oglesby, S., Jr., and G.B. Nichols. A Manual of Electrostatic Precipitator Technology Part II - Application Areas. APTD 0611, National Air Pollution Control Administration, Cincinnati, OH, 1970. NTIS PB 196381. 875 pp.

8. Harris, E.R., and F.R. Beiser. Cleaning Sinter Plant Gas With Venturi Scrubbers. J. Air Pollut. Contr. Assoc., 15(2):46, 1965.

9. Stewart, A.D., Algoma Steel Corp., Sault Ste. Marie, Canada, personal communication, 1977.

10. Metals Handbook. Vol. 1, 1961, American Society for Metals. pp. 568-573, 1147-1153.

PAPER 2

DESIGN AND OPERATING EXPERIENCE WITH ELECTROSTATIC PRECIPITATORS ON ELECTRIC ARC FURNACES

CLIFFORD WHITEHEAD
LODGE-COTTRELL/DRESSER
DRESSER INDUSTRIES, INC.

SUMMARY

This paper covers the design of the gas cleaning plant associated with "K" electric arc furnace at the British Steel Corporation's Aldwarke Works at Rotherham, its operation and the results obtained. The probable future development of electric arc fume extraction and gas cleaning plants is also discussed.

INTRODUCTION

The problems associated with fume extraction from an arc furnace are basically:

(1) the containment of the fume and its carrier gas within a duct,

(2) the separation of the fume from the carrier gas, and

(3) the disposal of the collected fume.

There are two main methods of containment, firstly by positioning large hoods over the furnace roof and the various furnace openings and relying on thermal lift to carry the fume into the hoods, and secondly, by direct extraction from the furnace under slight suction through a hole in the furnace roof.

It is on the latter method that the Aldwarke plant was designed. It should be noted that the notation ncfm relates to normal conditions measured at 0°C.

SPECIFICATION

The specification issued by the British Steel Corporation was for a direct fume extraction system for a furnace of 175 tons capacity. This furnace, originally one of six built during the 1961-1964 period at Templeborough, at that time the largest melting shop in the world, was to be taken down and re-erected at Aldwarke. Because of this history, it was anticipated that accurate data would be available for the design of the gas cleaning plant. However, there was the possibility that British Steel would at some future date install continuous feeding systems. Also, British Steel had in mind the possibility of installing a larger transformer. Allowances were made in the specified design data for these possible changes.

The British Steel Corporation used their own design of combustion chamber with the result that the gas cleaning plant contract started at the exit from the combustion chamber, and terminated at the stack outlet, and included the gas cooling tower, the electrostatic precipitator and its energizing equipment, the I.D. fan, the stack, the interconnecting ductwork and the dust disposal plant.

Details given in the specification included:

Furnace capacity	175 tons per melt
Oxygen blowing rate	2,300 ncfm
Volume of exhaust gases leaving the furnace elbow	10,000 ncfm
Temperature of gases leaving furnace elbow	1,500°C maximum
Analysis of gases leaving furnace elbow	CO - 63% H_2 - 4% N_2 - 31% CO_2 - 2%

COMBUSTION CHAMBER

This was designed and erected by the British Steel Corporation and consisted of a horizontal cylinder split into two sections, the object being to provide facilities for rapid replacement of the inlet section, as it was anticipated that slagging would occur in this part. This provision has been fully justified and the section is changed approximately every two months; it is then cleaned and held in readiness for its reinstallation at a later date. The outlet half is cleaned out annually. The two sections are fabricated in mild steel and refractory lined. The combustion chamber was equipped with a forced draft combustion air fan and burner to ensure combustion.

Gas conditions leaving the combustion chamber were given as follows:

Combusted gas volume at outlet of combustion chamber including combustion air both induced at the elbow slice and forced air	49,750 ncfm
Gas temperature	1,230°C maximum
Analysis of gas (by volume) at the outlet	CO_2 - 13% N_2 - 75.5% O_2 - 11.5%

GAS CLEANING PLANT

The general layout of the gas cleaning plant installed to meet the above requirements is given in Figure 1, which illustrates an upflow evaporative cooling tower followed by an electrostatic precipitator, an induced draft fan and stack.

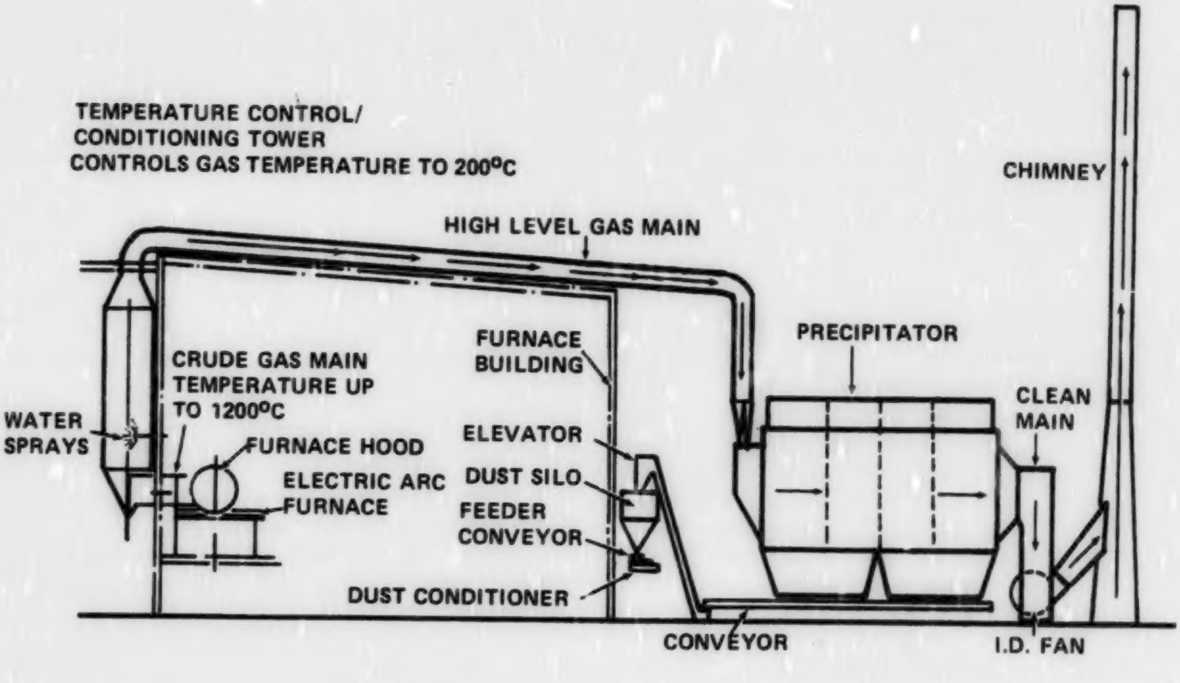
TEMPERATURE CONTROL/
CONDITIONING TOWER
CONTROLS GAS TEMPERATURE TO 200°C
CHIMNEY
HIGH LEVEL GAS MAIN
PRECIPITATOR
FURNACE BUILDING
CRUDE GAS MAIN TEMPERATURE UP TO 1200°C
CLEAN MAIN
WATER SPRAYS
FURNACE HOOD
ELEVATOR
ELECTRIC ARC FURNACE
DUST SILO
FEEDER CONVEYOR
DUST CONDITIONER
CONVEYOR
I.D. FAN

Figure 1. Electric arc furnace gas cleaning plant.

COOLING TOWER (See Figure 2)

The waste gases — 49,750 scfm — leave the combustion chamber at a maximum temperature of 1,230°C and enter an upflow tower located between the main steelwork of two adjacent bays. Aldwarke was an existing shop; therefore the location of the tower and its geometry were determined by existing steelwork cranes, etc. This resulted in a design which did not conform to the preferred parameters, the ratio, height to diameter, was smaller than our experience has shown to be desirable and the contact time for the evaporation of the spray water was on the low side. Further there was difficulty with the entry to the tower, the only possible arrangement being into the side of the hopper cone and hence, gas distribution within the tower was not as good as one would wish. However, the tower was modelled and reasonable results were achieved, but flow patterns were not as stable as would have been achieved with a lower inlet gas velocity. Normally a horizontal side entry into the vertical side of a circular tower giving opposed circumferential flows would have been used. This is a standard Lodge-Cottrell entry, developed especially for very high temperature conditions where gas distribution devices cannot be used, and excellent flow patterns have invariably been achieved with this proprietary arrangement.

In order to get the necessary contact time within the tower, after making allowance for an anticipated mal-distribution, the tower was built with the maximum possible diameter of 16 ft O.D. Calculations showed that an evaporation rate of up to 190 gal./min was necessary to reduce the gas temperature from 1230° to 160°C. To get the contact time necessary with full spray coverage, two rings of sprays were necessary and the largest standard spillback sprays were required. There are certain disadvantages with large sprays of this nature, the main one being that the mean droplet size tends to increase with orifice size. This increases the time to complete evaporation and also makes it difficult to cover the entire tower cross section without impingement on the walls, especially as the spray cone angle increases on turndown. Dust build-ups occur on the wetted wall surfaces so these must be minimized.

There was an appreciation of the difficulties involved in the design of the tower when it was installed. Although some initial teething problems were experienced with build-up and a completely dry bottom was not initially obtained, the operation has proved acceptable, putting no limitations on the furnace operation and controlling the conditions at the precipitator inlet within the required limits.

WATER CONTROL SYSTEM (See Figure 3)

Ten conditioning sprays arranged in two banks of five sprays each, giving a potential 190 gallons per minute were installed

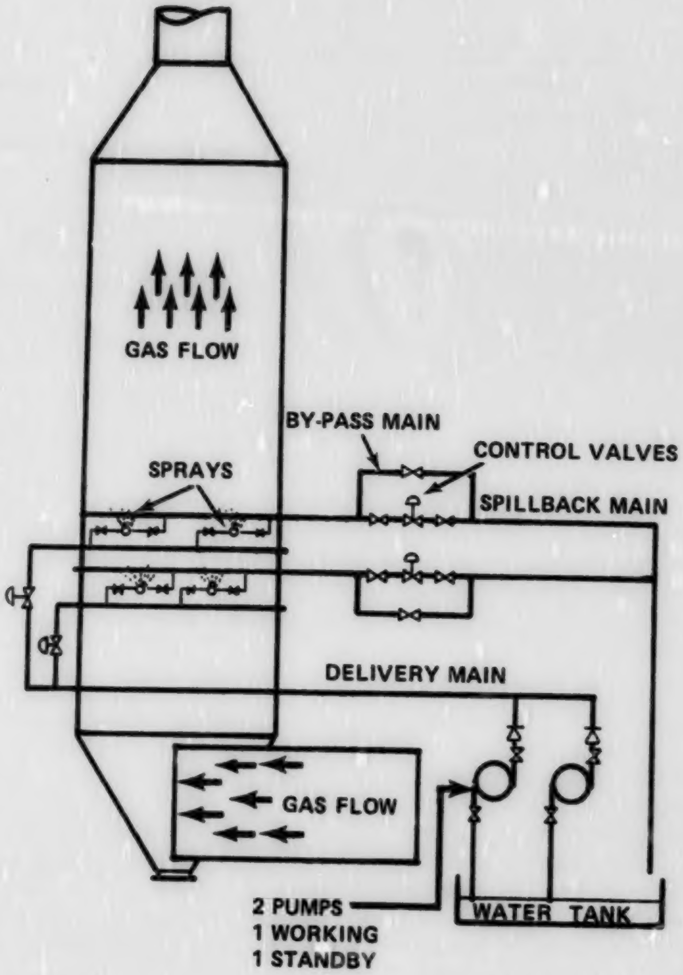
GAS FLOW
BY-PASS MAIN
CONTROL VALVES
SPRAYS
SPILLBACK MAIN
DELIVERY MAIN
GAS FLOW
2 PUMPS
1 WORKING
1 STANDBY
WATER TANK

Figure 2. Gas cooling tower.

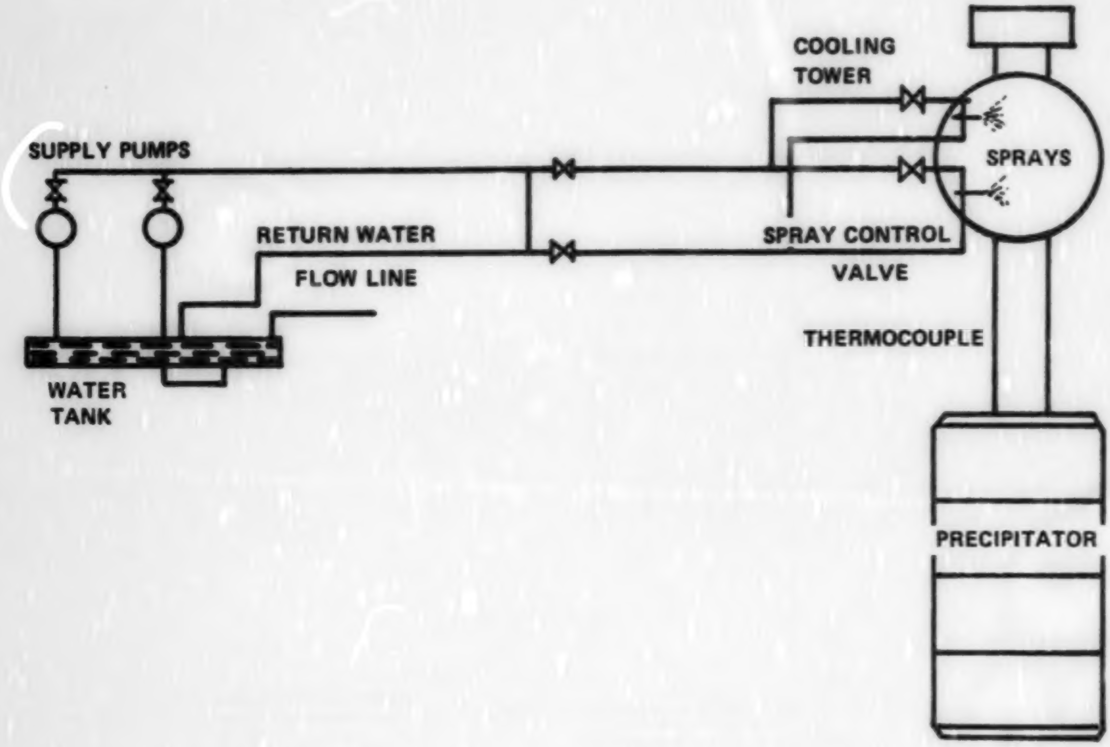
COOLING TOWER
SUPPLY PUMPS
SPRAYS
RETURN WATER
FLOW LINE
SPRAY CONTROL VALVE
THERMOCOUPLE
WATER TANK
PRECIPITATOR

Figure 3. Water control system.

with the facility to isolate any spray. Water flow to the sprays is initiated by a thermocouple monitoring the waste gas temperature at the tower outlet. As the gas temperature rises, a further thermocouple, also situated in the tower outlet, activates the electro-pneumatic control system. The resultant change of valve position modifies the water flow to the sprays, hence closely controlling the exit gas temperature. As the waste gases are cooled, water flow is accordingly reduced until a predetermined level is reached, when the main feed valve is closed and the by-pass valve opens. Water is then diverted from the spray system through the by-pass line and back to the water supply tank.

The spray water system is set to the following:

main valve open - by-pass closed	170°C
main control valve set position	250°C
instrument full scale	500°C with control over a 20% band.

this proportional band is	-70°C to +30°C of the set point
i.e., control valve operates	180°C - 280°C

Tower details:

diameter	16 ft
side wall height	49 ft
spray system	two banks of five sprays giving a total of up to 190 gal./min
materials of construction	mild steel, refractory lined
inlet volume	274,000 acfm
inlet temperature	1,230°C maximum
outlet volume	147,200 acfm
outlet temperature	160°C

PRECIPITATOR (See Figure 4)

The cooled gases pass over the roof of the shop in a 6-ft diameter duct constructed in mild steel and enter a 4-field, horizontal flow, precipitator located at ground level via a typical Lodge-Cottrell top entry mouthpiece. Good gas distribution with no risk of build-up is ensured by means of the triangulated splitter system followed by half round vertical distributors. The position of both the triangular splitters and vertical distributors was determined using a quarter scale model test carried out at Lodge-Cottrell's Birmingham Works. This is standard Lodge-Cottrell practice.

The precipitator itself is a standard Lodge horizontal flow unit with the exception that explosion facilities were installed at the request of the Government Safety Inspector as a precaution against an explosive mixture passing from the combustion chamber. The explosion relief per volumetric capacity ratio of the precipitator chamber and mouthpieces is one square foot of explosion relief to every 50 cubic foot capacity.

The collectors are of the standard Lodge catch space type consisting of flat sheets supported by specially shaped vertical channels, these channels forming a baffled zone which prevents scouring of the sheets and thus minimizes the problem of dust re-entrainment. Each collector is 15 ft long in the direction

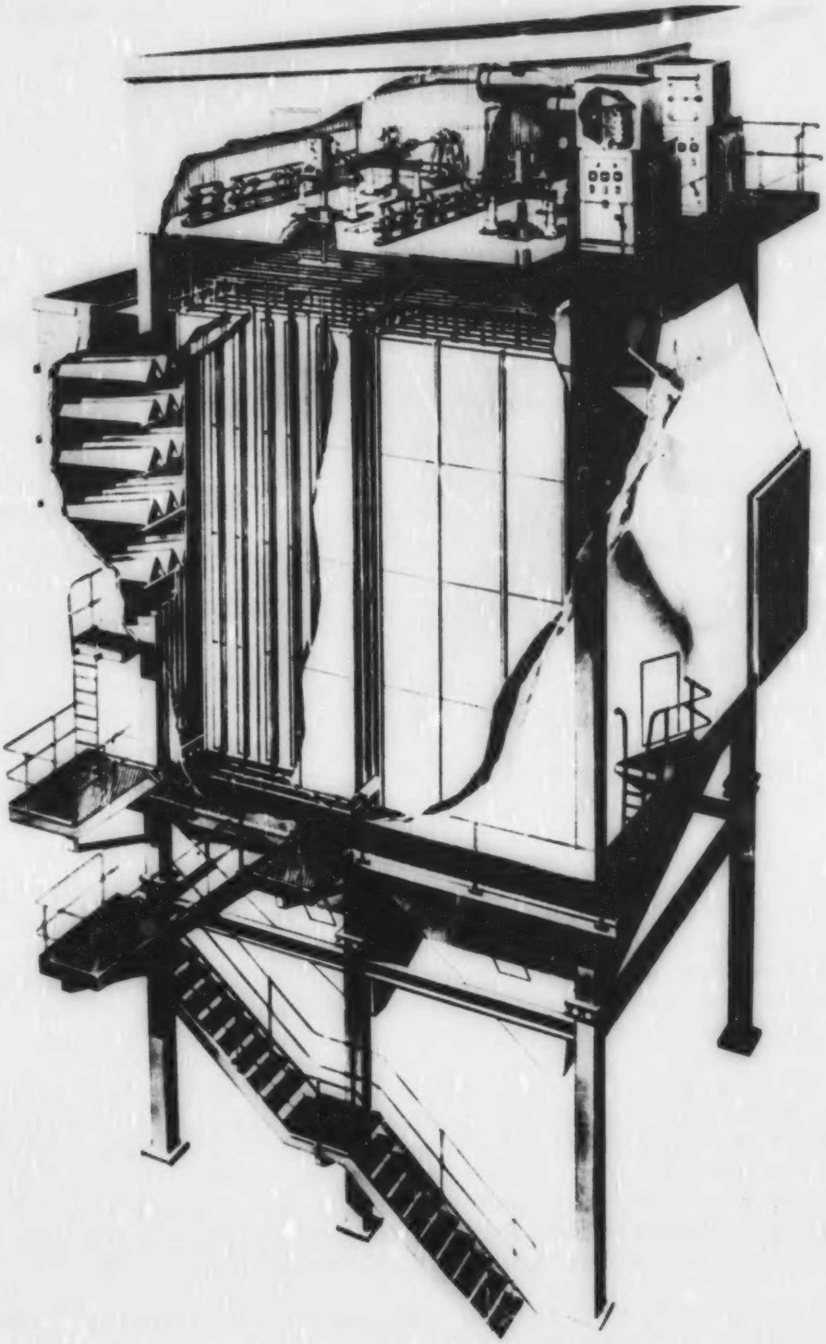

Figure 4. Typical Lodge-Cottrell electrostatic precipitator.

of gas flow by 30 ft high and is suspended from the collector casing by spring-cushioned suspension bolts.

The discharge elements are of the Lodge mast type — see Figure 5 — with the actual discharge elements on the inlet and second stage being of the serrated strip type while plain strip elements are used on Nos. 3 and 4 banks. Owing to the extremely fine fume particle sizing and the heavy dust burden anticipated, a tendency for corona suppression was expected on the inlet zones and hence the installation of high emission electrodes in these fields. Rigidity of the Lodge mast, the heavy rigid top frame with heavy lower spacing frames, ensures excellent alignment, freedom from breakage and the elimination of frame swing, any of which would have serious effects on precipitator efficiency.

The collectors are rapped at the top by a series of mechanically operated drop hammers arranged so that the rapping effort is staggered throughout the electrode zones, thus avoiding "puffs". The rates vary throughout the unit, being set at the optimum value for effective cleaning of the plates with minimum re-entrainment. The discharge elements are rapped in a similar manner via an insulated drive but at a much higher rate, as it is more important to keep the electrode discharge elements clean and re-entrainment is not a significant problem. The whole of the drives are located outside the gas chamber. Each bank of the plant is energized by a 60KV/600MA silicon rectifier complete with automatic control.

PRECIPITATOR DESIGN DATA

gas volume	147,200 cfm
gas temperature	180°C
dust burden	up to 15 gr/scf
particle size	85% between 0.1 and 1.0 μm
number of fields	4
ducts per field	21
size of collector	15 ft x 30 ft
outlet burden	not to exceed 0.04 gr/ft^3 stp

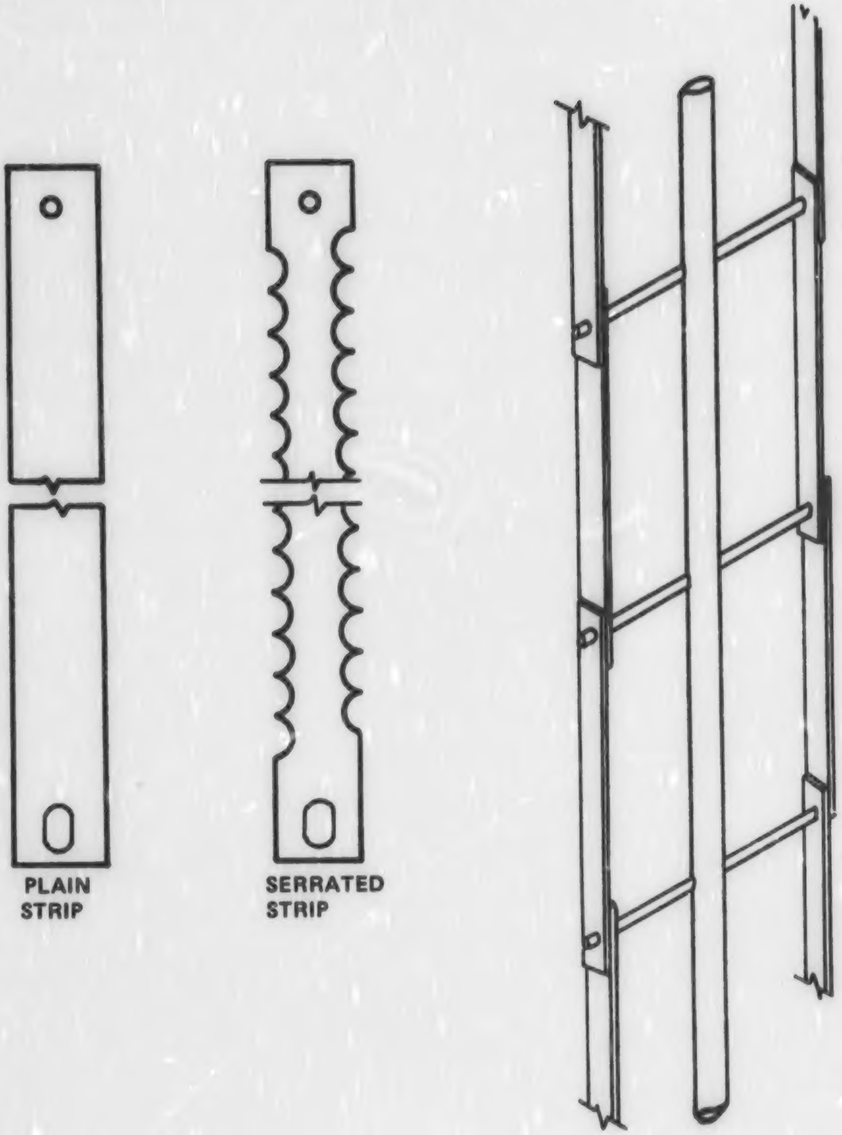
PLAIN STRIP
SERRATED STRIP

Figure 5. Typical Lodge-Cottrell high emission discharge electrodes.

DUST EXTRACTION

Drag link conveyors located beneath each hopper discharge the dust into an inclined double strand chain and bucket elevator discharging into a heated silo. Dust from the silo passes to a dust conditioner, consisting of a double worm screw with water conditioning sprays. Dust removal from the precipitators to the silo is continuous, the silo being emptied as required into skips or vehicles during the day shift only.

FAN

The fan is of the backward bladed type fitted with radial vane control and powered by a 285 hp motor. Calculations have shown that the maximum pressure drop throughout the system would not exceed 7 in. WG and in practice has been well within this figure.

The plant was ordered at the end of 1972 and was commissioned in early 1974.

OPERATING EXPERIENCE

During the three years that the plant has been in operation, gas conditions at the entry to the gas cleaning plant in general have been well below the maximum specified on which the plant was designed.

As both the volume and temperature of the gases have tended to be lower than anticipated, the total heat in the gases entering the cooling tower has been lower than expected, and this initially caused some problems with the turndown ratio of the sprays. The result was that a certain amount of wetting of the walls occurred with resultant build-up and at times a wet effluent was discharged from the tower hopper. However, the isolation of certain sprays, the re-positioning of others, and the improvement in gas flow patterns due to the installation of a number of refractory arches in the base of the tower have resulted in considerable improvements and the installation is now acceptable to the British Steel Corporation.

The precipitator itself has operated well, no electrode failures have been reported, the rapping gear has worked well with no significant build-up occurring on either discharge or collecting electrodes, and consequently maintenance costs have been low.

No dust build-up has been experienced in the inlet and outlet mouthpieces and dust extraction has proceeded without problems. The dust conditioning plant has worked so well that the system has been adopted on other plants.

In recent weeks, suction on the furnace has been increased, resulting in even less fume escape from the various openings, without any adverse effect on the gas cleaning plant performance.

Throughout the entire period, during all phases of furnace operation, the stack appearance has been excellent with no visible discharge.

Typical power consumption figures in kW:

	Installed	Operation
cooling tower (includes pumping supply, etc.) (kW)	75	55
precipitator (energizing, rapping, etc.) (kW)	210	150
exhaust fan (kW)	225	160
dust extraction and conditioning (kW)	55	10 (continuous) 45 (intermittent)
	560 kW	420 kW

PERFORMANCE TESTS

Due to the mode of operation of an electric arc furnace it is not possible to carry out tests under the normally accepted test procedure as laid down in Britain by BSS.893 or in America by the A.S.M.E. Power Test Code 27-1957.

PROCEDURE

A modified test procedure was accordingly drawn up by the British Steel Corporation in the light of their experience on such plants, and the following was adopted:

Simultaneous inlet and outlet samples were taken at each of the following times during the furnace cycle:

A. 5 minutes after power on the first scrap charge for a sampling period of 10 minutes.

B. 5 minutes after power on second scrap charge for a sampling period of 10 minutes.

C. During the pre-melt blow (oxygen blowing rate 2,300 cfm) for a period of 10 minutes towards the end of the blow.

D. During the oxygen refining period (fully melted).

The eight samples were taken during the furnace cycle and it was agreed that six complete furnace cycles would constitute the full performance test. As difficulty would be experienced in producing inlet conditions to match those specified, a series of curves based on varying inlet conditions was agreed upon as the basis for the guarantee.

RESULTS

The plant was operated as near to the original design conditions as possible with the following results:

	Specification	Test Figures
gas volume, acfm	147,200	139,200
gas temperature, °C	180	212
emissions, gr/ncf dry	0.04	0.026

The average emissions on all tests carried out during the various stages of the furnace cycle were:

1st scrap charge	0.018 gr/ncf dry
2nd scrap charge	0.01 gr/ncf dry
pre-blow	0.0283 gr/ncf dry
refining stage	0.0346 gr/ncf dry

As the average operating conditions are well below the maximum specified and on which the plant was designed, a further guarantee was given with only 3 of the 4 fields of the precipitator energized. With the plant operating on a lower gas volume, the guarantees and the actual results obtained under these conditions were:

	Specification	Test Figures
gas volume, acfm	101,000	109,700
gas temperature, °C	180	207
emissions, gr/ncf dry	0.035	0.015

The average emissions on all tests carried out during the various stages of the furnace cycle were:

1st scrap charge	0.0115 gr/ncf dry
2nd scrap charge	0.0063 gr/ncf dry
pre-blow	0.0116 gr/ncf dry
refining stage	0.0336 gr/ncf dry

PROBABLE FUTURE GAS CLEANING SYSTEMS

An arc furnace direct extraction system will at best only collect approximately 96% of the total fume generated during the steel making cycle. The system is not in operation while the furnace is charging or pouring and it has been shown that at least 60% of all the fume which escapes the extraction system is generated during this period. Hence, unless some form of secondary extraction is provided, fume discharge from the shop roof is inevitable and the working area around the furnace will not be kept clean of fume.

It is of course possible to treat these two sources separately, and this has been done in the past, but it is an expensive method, not only on capital cost but also on operating costs and so the obvious way is to combine the two flows and treat finally as one effluent. The choice of final gas cleaning plant lies mainly between bag filters and electrostatic precipitators. Scrubbers are not generally favored due to the water requirements, the capital and operating costs of the water treatment plant, the high pressure drop resulting in high power consumption, and the wet plume discharged from the stack.

Bag filters are limited by temperature considerations, as the materials from which the bags are made have distinct upper temperature limits. Any cooling of gases to reduce the temperature below this level is normally achieved by air infiltration. Cooling by water evaporation risks water carry over with the consequent wetting and blocking of the bags. In order to cool the hot exhaust gases leaving the combustion chamber in the direct extraction line (these at temperatures ranging from 900°C to 1200°C), it is usually necessary to mix with large volumes from the roof extraction system — see Figure 6. The pressure drop through the direct extraction system including the combustion chamber, the bag filter, the ducting and stack, is of the order of 10 - 14 in. WG, dependent on layout. As the direct extraction route could well be the deciding factor it would then be necessary to locate some restriction in the roof extraction line to balance the system. The result is that a main extraction fan, placed on the dirty side of the bag filter, is operating on about 10 - 14 in. WG on a considerably

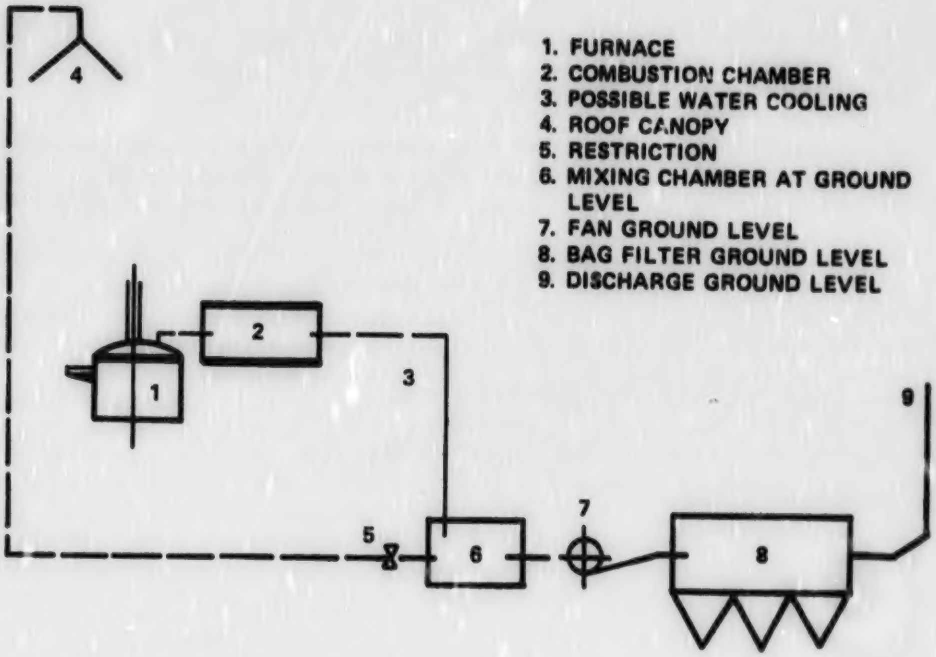
1. FURNACE
2. COMBUSTION CHAMBER
3. POSSIBLE WATER COOLING
4. ROOF CANOPY
5. RESTRICTION
6. MIXING CHAMBER AT GROUND LEVEL
7. FAN GROUND LEVEL
8. BAG FILTER GROUND LEVEL
9. DISCHARGE GROUND LEVEL
1
2
3
4
5
6
7
8
9

Figure 6. Combined system using bag filters.

increased gas volume, and consequently power consumption tends to be in the order of megawatts rather than kilowatts. In certain circumstances the volume could be reduced by indirect water cooling in the duct carrying the direct extraction gases from the combustion chamber to the mixing vessel. Normally this would need to be of excessive length and thus extremely costly, and hence is rarely considered.

The five main advantages of using precipitators in place of bag filters are that:

1. Precipitator size is reduced as the required collecting efficiency is lowered. This is in contrast to the bag filter, the size of which remains constant and hence cannot take advantage of low inlet dust burdens.

2. A precipitator is less readily damaged by heat. Temperatures up to 400°C can be accepted without damage, whereas bag filters have a considerably lower temperature range even when using special fabrics.

3. The pressure drop is low, up to 0.5 in. WG across the precipitator inlet and outlet flanges, against approximately 4 in. WG over the bag filter.

4. Precipitator pressure drop does not vary significantly whereas the bag filter can "blind" causing some reduction in gas flow and increased pressure drop.

5. Maintenance costs of a precipitator are lower; life is ten years plus, apart from a few minor wearing parts, whereas in contrast a bag life of 3 to 4 years would be considered good.

When using precipitators on this combined system - Figure 7 - the direct extraction system following the offtake elbow consists as usual ot a combustion chamber, a cooling tower, and a low efficiency precipitator, this being purely to protect the fan, which itself discharges into a mixing duct already carrying the exhaust gases from the roof extraction system. The suction across the direct extraction line would be of the order of 5-7 in. WG, but the gas volume handled would be only a fraction, 30% to 40%, of the combined flows. With a proper design of canopy utilizing the thermal lift, the suction required in the roof extraction line would be of the order of 1 in. WG; hence, as the direct extraction line would discharge into the duct the suction on the combined gases would be of the order of 1 in. WG.

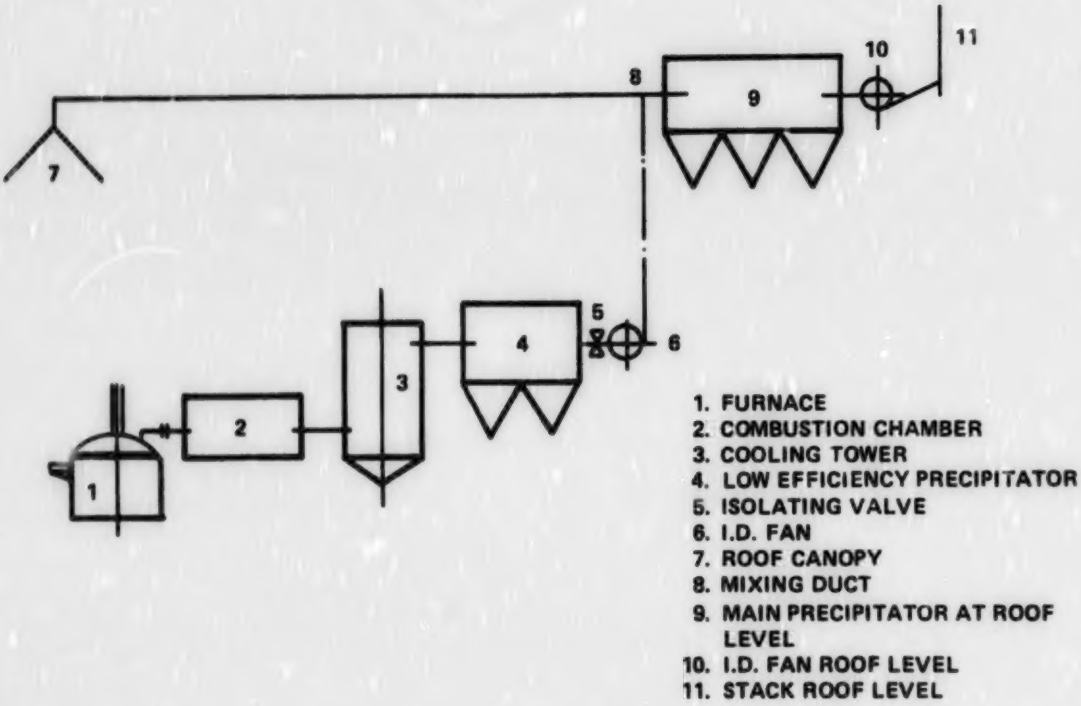
11
10
8
9
7
5
6
4
3
2
1
1. FURNACE
2. COMBUSTION CHAMBER
3. COOLING TOWER
4. LOW EFFICIENCY PRECIPITATOR
5. ISOLATING VALVE
6. I.D. FAN
7. ROOF CANOPY
8. MIXING DUCT
9. MAIN PRECIPITATOR AT ROOF LEVEL
10. I.D. FAN ROOF LEVEL
11. STACK ROOF LEVEL

Figure 7. Combined system using electrostatic precipitators.

The dust burden in the combined gases leaving the mixing chamber is of the order of 0.5 gr/ft^3. Hence a relatively low efficiency precipitator, correspondingly sized, is installed. With a high efficiency fan located downstream of the precipitator and being of low duty operating on clean gas, an axial fan can be used.

The great asset of this system is that when charging or pouring or when the furnace roof is moved the entire gas volume is extracted from the roof canopy, these incidentally being the periods of highest fume escape. During these periods the I.D. fan operating on the direct extraction line is isolated but is kept running at full speed by use of simple dampers tied into the furnace operating control and hence is immediately available when required.

The use of a system of this type keeps fan power down to a minimum, precipitator size as small as possible and ensures correct distribution and extraction at all times. Further, with the precipitator and fan mounted on a trestle at roof level not only is the pressure drop reduced but the ducting costs are kept to a minimum. The capital costs of the entire plant are at least comparable with that of a bag filter installation, and the differential in fan HP must offer a significant economic advantage in annual operating costs.

PAPER 3

TEST OF UNIVERSITY OF WASHINGTON ELECTROSTATIC SCRUBBER AT AN ELECTRIC ARC STEEL FURNACE

MICHAEL J. PILAT
G. A. RAEMHILD
UNIVERSITY OF WASHINGTON

AND

DALE L. HARMON
INDUSTRIAL ENVIRONMENTAL RESEARCH LABORATORY-RTP
U.S. ENVIRONMENTAL PROTECTION AGENCY

ABSTRACT

The UW Electrostatic Scrubber portable pilot plant has been tested for the collection of fine particulate emissions from an electric arc steel furnace. The UW Electrostatic Scrubber involves the use of electrostatically charged liquid droplets to collect air pollutant particles charged to a polarity opposite to that of the droplets. The tests illustrated the system's capability for high efficiency fine particle collection at a relatively low energy consumption (about 1 inch gas pressure drop, liquor flow of zero to 23 gal./1,000 acf at 57 psig, and about 300 watts/1,000 acf for electrical power for the high voltage power supplies). Tabular and graphical data are presented illustrating the effects of specific plate area (SCA), liquor-to-gas-flow rate (L/G) ratios, voltage magnitudes, and electrostatic polarities on overall particle collection efficiency and on particle collection efficiency as a function of particle size. Measured overall particle collection efficiencies ranged from 79.7% to 99.6% depending on electrostatic scrubber operating conditions and upon the inlet particle size distribution.

INTRODUCTION

Objectives of Research Project

The objectives of this on-going research project are to demonstrate the effectiveness of the UW Electrostatic Scrubber for controlling the emissions of fine particulates, to use the portable 1,000 acfm pilot plant in a 40 ft trailer to obtain the data needed to design larger electrostatic scrubber systems, and to perform preliminary design and economic analyses of full-scale electrostatic scrubber systems.

Review of Previous Work

Penney (1944)[1] patented an electrified liquid spray test precipitator involving particle charging by corona discharge and droplet charging by either ion impaction or induction. Penney's system consisted of a spray scrubber with electrostatically charged water droplets collecting aerosol particles charged to the opposite polarity. Kraemer and Johnstone (1955)[2] reported theoretically calculated single droplet (50 micron diameter droplet charged negatively to 5,000 volts) collection efficiencies of 332,000% for 0.05 micron diameter particles (4 electron unit positive charges per particle). Pilat, Jaasund, and Sparks (1974)[3] reported on theoretical calculation results and laboratory tests with an electrostatic spray scrubber apparatus. Pilat (1975)[4] reported on field testing during 1973-1974 with a 1,000 acfm UW Electrostatic Scrubber (Mark 1P model) funded by the Northwest Pulp and Paper Association. Pilat and Meyer (1976)[5] reported on the design and testing of a newer 1,000 acfm UW Electrostatic Scrubber (Mark 2P model) portable pilot plant. Pilat, Raemhild, and Harmon (1977)[6] reported on tests of the UW Electrostatic Scrubber pilot plant (Mark 2P model) on collecting laboratory generated DOP aerosols and emissions from a coal-fired boiler and an electric arc steel furnace. The UW Electrostatic Scrubber (patent pending) has been licensed to the Pollution Control Systems Corporation (of Renton and Seattle, Washington) for production and sales.

UW Electrostatic Scrubber

The UW (Pilat) Electrostatic Scrubber involves the use of electrostatically charged water droplets to collect air pollutant particles electrostatically charged to a polarity opposite to that of the droplets. A schematic illustration of the UW Electrostatic Scrubber system is presented in Figure 1. The particles are electrostatically charged (negative polarity) in the corona section.

From the corona section the gases and charged particles flow into a scrubber chamber into which electrostatically charged water droplets (positive polarity) are sprayed. The gases and some entrained

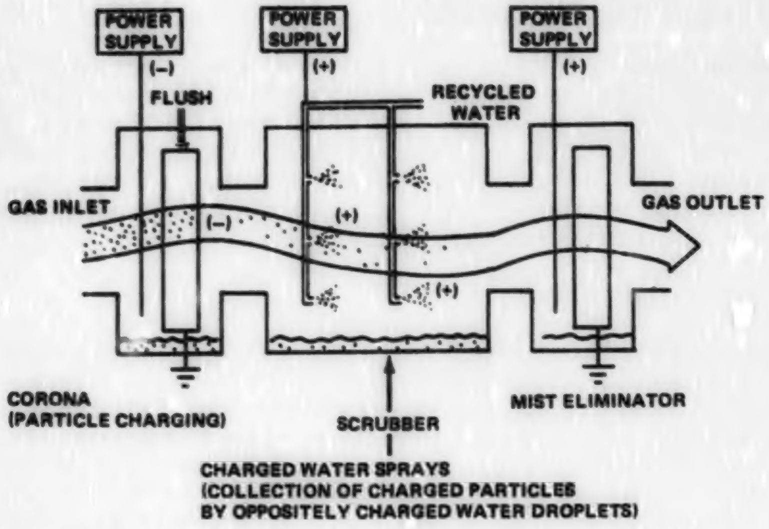
POWER SUPPLY
(–)
POWER SUPPLY
(+)
POWER SUPPLY
(+)
FLUSH
RECYCLED WATER
GAS INLET
(–)
(+)
(+)
GAS OUTLET
CORONA (PARTICLE CHARGING)
SCRUBBER
MIST ELIMINATOR
CHARGED WATER SPRAYS (COLLECTION OF CHARGED PARTICLES BY OPPOSITELY CHARGED WATER DROPLETS)

Figure 1. UW electrostatic scrubber.

water droplets flow out of the spray chamber into a mist eliminator consisting of a positively charged corona section in which the positively charged water droplets are removed from the gaseous stream.

EXPERIMENTAL METHOD

UW Electrostatic Scrubber Pilot Plant

The general layout of the UW Electrostatic Scrubber pilot plant (Mark 2P model) is shown in Figure 2. The system (in the direction of gas flow) includes a gas cooling tower, an inlet test duct with sampling port, a particle charging corona section (corona No. 1), a charged water spray tower (tower No. 1), a particle charging corona section (corona No. 2), a charged water spray tower (tower No. 2), a positively charged corona section (mist eliminator) to collect the positively charged water droplets, an outlet test duct with sampling port, and a fan. The pilot plant is housed in a 40 ft long trailer and can be easily transported to emission sources. Figure 3 is a photo of the pilot plant (Mark 2P model) located at a steel plant.

Test Methods

The particle size distribution and mass concentration were simultaneously measured at the inlet and outlet test ducts using

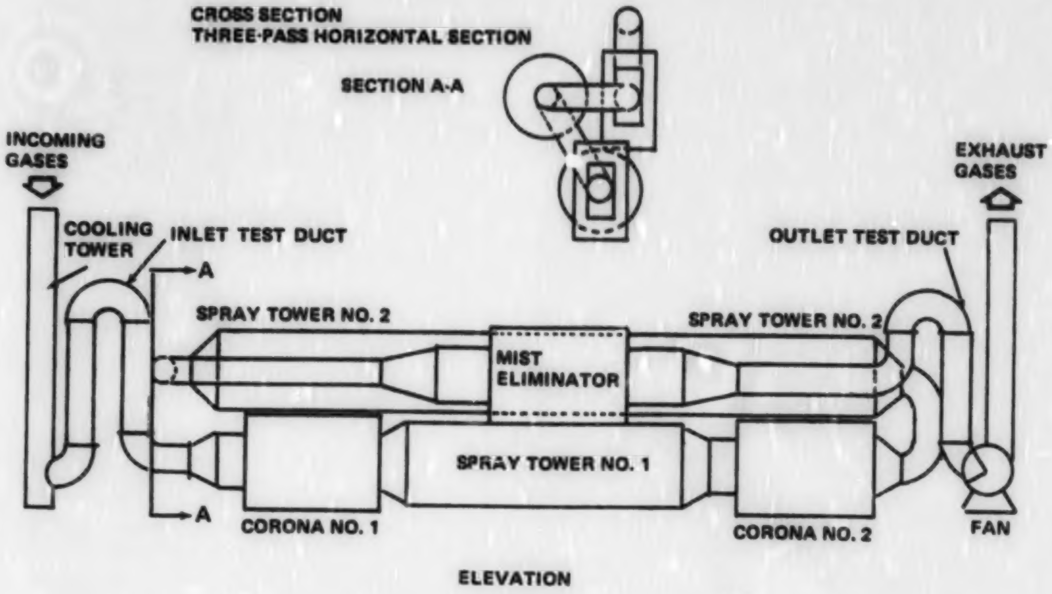
CROSS SECTION
THREE-PASS HORIZONTAL SECTION
SECTION A-A
INCOMING GASES
EXHAUST GASES
COOLING TOWER
INLET TEST DUCT
OUTLET TEST DUCT
A
SPRAY TOWER NO. 2
SPRAY TOWER NO. 2
MIST ELIMINATOR
SPRAY TOWER NO. 1
A
CORONA NO. 1
CORONA NO. 2
FAN
ELEVATION

Figure 2. General layout of electrostatic scrubber pilot plant. (Mark 2P Model)

UW Mark 3 and UW Mark 5 Source Test Cascade Impactors. During some tests the water charge/mass and aerosol charge/mass were measured. The test parameter measurement techniques are presented in Table 1.

RESULTS

The UW Electrostatic Scrubber pilot plant was connected to a duct exhausting from two electric arc steel furnaces. This source was selected for the tests because a large portion of the emission particles are in the submicron size range. This particular industrial plant has a very successful particulate emission control system involving filter baghouses, one of which is shown behind the pilot plant trailer in Figure 3.

The test results presented in Table 2 were obtained during tests conducted from January to June 1977. These are the first tests of the portable pilot plant with the new liquor recycle system. Some problems occurred during the earlier tests. During tests 1 through 16, particles were re-entraining from the duct downstream of the mist eliminator. This caused the overall particle collection efficiency to be less than expected for these tests.

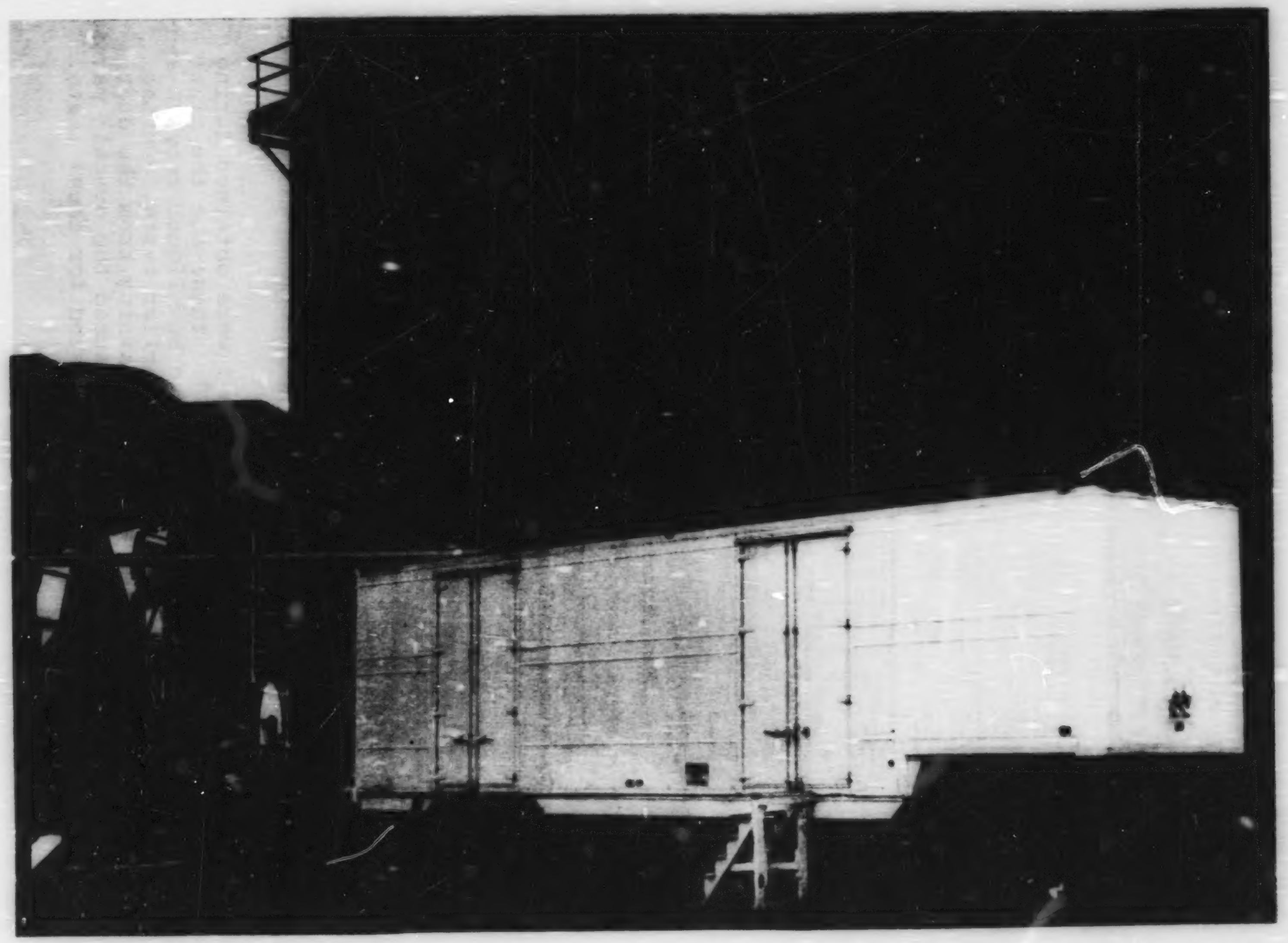

Figure 3. UW electrostatic scrubber pilot plant at steel plant.

TABLE 1. SOURCE TEST PARAMETER MEASUREMENT TECHNIQUES

Parameter	Equipment
1. Air	
a. velocity and volume	S-type pitot tube with draft gauge
b. temperature	thermometer
c. moisture	wet and dry bulb thermometer and checked by volume of condensate
d. atmospheric pressure	barometer
e. static pressure	Magnehelic* gauge
2. Water Spray Towers	
a. water flow	rotameters
b. water charge to mass ratio	digital multimeter
3. Aerosol	
a. mass concentration	UW Mark 3 or 5 Cascade Impactor
b. size distribution	UW Mark 3 or 5 Cascade Impactor
c. aerosol charge to mass ratio	digital multimeter

*Magnehelic: Dwyer Instruments, Inc., P.O. Box 373-7, Michigan City, IN 46360.

The particle re-entrainment was detected by a test performed with clean (atmospheric) air which showed a higher outlet particulate concentration than at the system inlet (clean water was used as the scrubbing liquor). Washing down the duct downstream of the mist eliminator eliminated the re-entrainment. During tests 22 to 29, the liquor spray to tower No. 1 was shut off because it appeared that the spray was flooding the No. 2 corona section. After test No. 29, the pilot plant was shut down and the spray towers and corona sections were washed down thoroughly. Of the six nozzles in tower No. 1, the downstream nozzle fittings were plugged, and the other three nozzles were replaced with nozzles providing a fine mist (manufacturer data specifies 200 to 300 micron diameter droplets). A screen-type mist eliminator was installed at the outlet of tower No. 1 (inlet to corona No. 2). Also all the spray nozzles in tower

TABLE 2. RESULTS OF TESTS AT ELECTRIC ARC STEEL FURNACE

Test No.	Gas Flow at Outlet Duct (acfm)	Water to Outlet Gas Flow Ratio (gal./1000 acf)	Voltage (kV)				Collection Efficiency (%)	Outlet Conc. (gr/scf)
			Corona		Spray			
			No. 1	No. 2	No. 1	No. 2		
1	1,783	10.4	70	70	15	15	94.2	0.0057
2	1,484	12.1	35	35	15	15	94.0	0.0025
3	1,553	11.9	70	70	20	20	98.1	0.0024
4	1,032	17.0	70	70	0	0	95.3	0.0016
5	1,474	12.6	70	70	15	15	92.6	0.0395
6	1,428	17.5	70	70	10	10	97.4	0.0025
7	1,391	18.0	70	70	20	20	87.9	0.0075
8	1,281	19.5	50	50	0	0	89.0	0.0978
9	1,470	17.0	50	50	20	20	80.2	0.0750
10	1,214	20.6	50	50	10	10	81.0	0.0811
11	1,331	18.8	70	70	20	20	91.0	0.0430
12	1,281	19.5	70	70	0	0	85.6	0.0178
13	1,210	19.8	0	0	20	20	83.7	0.1042
14	1,225	19.6	0	0	0	0	80.4	0.16797
15	1,259	19.1	0	0	10	10	58.8	0.33031
16	1,225	0	70	70	0	0	87.9	0.07380
17	1,189	21.0	70	70	20	20	93	0.0441
18	1,174	21.3	68	68	10	10	97	0.0285
19	1,163	21.5	68	68	0	0	98	0.0269
20	1,175	21.3	70	70	10	10	98	0.0313
21	1,148	21.8	0	0	10	10	89	0.1151
22	1,221	17.2	70	70	0	10	98.6	0.0194

(continued)

TABLE 2 (continued)

Test No.	Gas Flow at Outlet Duct (acfm)	Water to Outlet Gas Flow Ratio (gal./1,000 acf)	Voltage (kV)				Collection Efficiency (%)	Outlet Conc. (gr/scf)
			Corona		Spray			
			No. 1	NO. 2	No. 1	No. 2		
23	1,247	16.8	70	70	0	10	96.4	0.0258
24	1,293	16.2	65	65	0	0	93.6	0.0315
25	1,184	17.7	70	70	0	0	98.1	0.0074
26	905	23.2	70	70	0	10	99.0	0.00344
27	953	22.0	70	70	0	10	98.9	0.00524
28	1,309	16.0	70	70	0	10	86.5	0.15362
29	1,338	15.7	70	70	0	10	83.7	0.10095
30	1,296	12.3	70	70	10	10	96.6	0.00678
31	1,302	11.5	70	70	2	2	98.6	0.0100
32	1,298	11.6	70	70	2	2	98.8	0.00992
33	1,122	13.4	70	70	2	2	99.6	0.00458
34	1,253	11.97	-70	-70	10	10	98.9	0.0157
35	1,227	12.22	-70	-70	0	0	97.5	0.0312
36	1,233	12.16	-70	-70	0	0	95.5	0.03403
37	1,263	11.88	0	0	10	10	82.1	0.1226
38	1,265	11.86	0	0	0	0	79.7	0.1567
39	1,228	12.21	-70	-70	- 2	- 2	97.9	0.0234
40	1,223	12.26	-70	-70	- 2	- 2	97.5	0.01749
41	1,212	12.38	-70	-70	- 2	- 2	97.8	0.0093
42	1,260	7.14	-70	-70	2	2	99.5	0.00741
45	1,285	7.00	-65	-65	2	2	97.8	0.0299
46	1,026	8.77	-70	-70	2	2	98.2	0.0282
51	1,290	6.98	-70	-70	2	2	96.5	0.0430

No. 2 were replaced with the finer droplet nozzles. Tests 30 through 41 were run with both spray towers in operation at a total liquor flow of about 15 gal./minute and a liquor pressure of about 56 psig.

After test 41 the total liquor flow rate was reduced to 9 gal./minute by reducing the number of nozzles in tower No. 2 (the liquor pressure was about 57 psig). Data for tests 43, 44, 47, 48, 49, and 50 were not included in the table because of problems occurring during these tests (corona power supply tripping off, etc.).

Figure 4 presents the particle collection efficiency as a function of particle size for a range of liquor-to-gas-flow-rate ratios (L/G) and of corona plate areas (SCA). The highest particle collection efficiencies occur with the SCA and L/G at higher magnitudes. Figure 5 illustrates the effect of the magnitude of the corona (particle charging) and liquor spray voltages on the particle collection efficiencies at relatively constant SCA and L/G. The highest particle collection efficiencies (and correspondingly, the lowest penetrations) occur at the highest corona voltage (-70 kV) and liquor spray voltage (+2 kV).

Figure 6 presents a comparison of the particle collection efficiencies measured with equal and opposite electrostatic polarities of the corona and liquor sprays. The arrangement with the opposite polarities provides the highest particle collection efficiencies. Operation with equal polarities is in general similar to that of the space charge electrostatic precipitator as described by Hanson and Wilke (1969).[7] The space charge precipitator operates on the principle of mutual repulsion of the electrostatically charged particles and liquid droplets to the grounded walls.

Figure 7 presents a comparison of the particle collection efficiency as a function of L/G at constant SCA. Increasing L/G from about 8.6 to 11.6 gal./1,000 cf decreased the overall particle penetration from about 2.9% to 1.3%.

CONCLUSIONS

The results of the tests of the UW Electrostatic Scrubber field portable pilot plant at an electric arc steel furnace in Seattle have demonstrated the system's capability for high efficiency fine particle collection at a relatively low gas pressure drop (about 1 inch of water) and over a range of L/G (zero to 23 gal./1,000 acf) and corona plate SCA magnitudes (0.038 to 0.082 ft^2/acfm). Graphs illustrating the effect of SCA, L/G, voltage magnitudes, and electrostatic polarities on the particle collection efficiency as a function of particle size are presented. Measured overall particle collection efficiencies ranged from 79.7% to 99.6% depending on the electrostatic scrubber operating conditions and the inlet particle size distributions.

Test No.	Corona V, kV	Spray V, kV	Overall Coll Eff, %	SCA, ft^2/cfm	L/G, gal./ 1000 cf
22	70	10	98.6	0.047	17.2
23	70	10	96.4	0.045	16.8
26	65	10	99.0	0.072	23.2
27	65	10	98.9	0.071	22.0
28	70	10	86.5	0.038	16.0
29	70	10	87.3	0.038	15.7

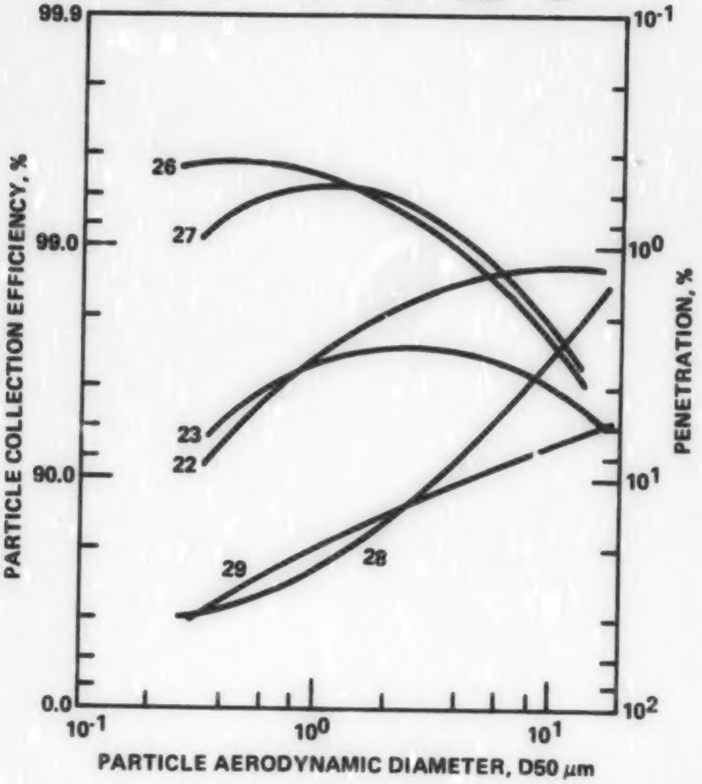

Figure 4. Influence of SCA and L/G on particle collection efficiencies.

Test No.	Corona V, kV	Spray V, kV	Overall Coll Eff, %	SCA, ft^2/cfm	L/G, gal./1000cf	Penetration, %
31	70	2	98.5	0.060	11.52	1.4
32	70	2	98.8	0.060	11.60	1.2
35	70	0	97.3	0.061	12.22	2.6
36	70	0	95.6	0.061	12.17	4.5
37	0	10	32.0	0.061	11.89	7.9
38	0	0	79.7	0.060	11.87	20.3

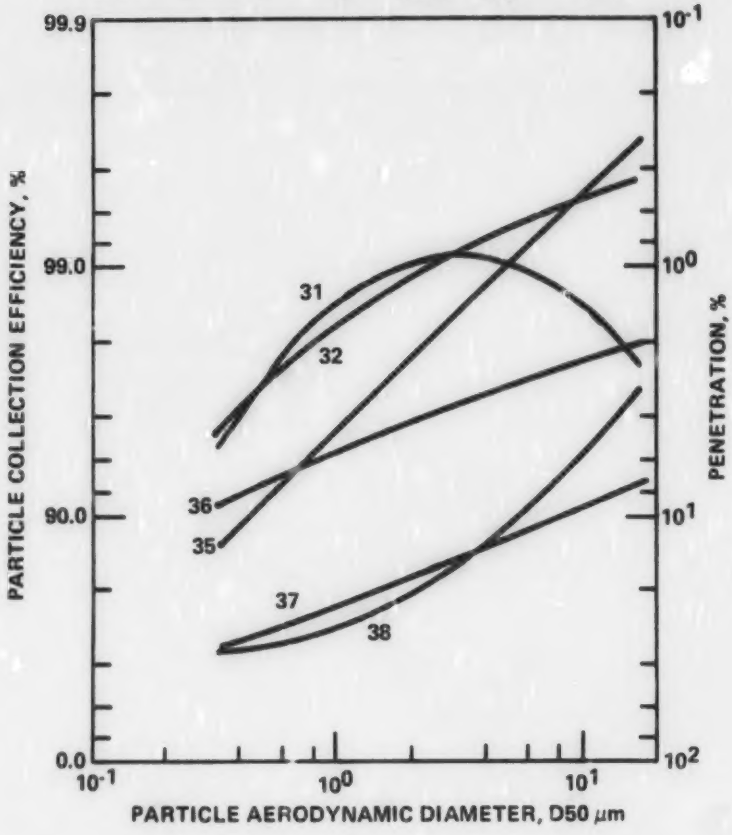

Figure 5. Effect of corona and spray voltages on particle collection efficiencies.

Test No.	Corona V, kV	Spray V, kV	Overall Coll Eff, %	SCA, ft^2/cfm	L/G, gal./1000cf	Penetration, %
31	70 (–)	2 (+)	98.6	0.060	11.52	1.4
32	70 (–)	2 (+)	98.8	0.060	11.60	1.2
39	70 (–)	2 (–)	98.0	0.061	12.21	2.1
41	70 (–)	2 (–)	97.8	0.062	12.38	2.5

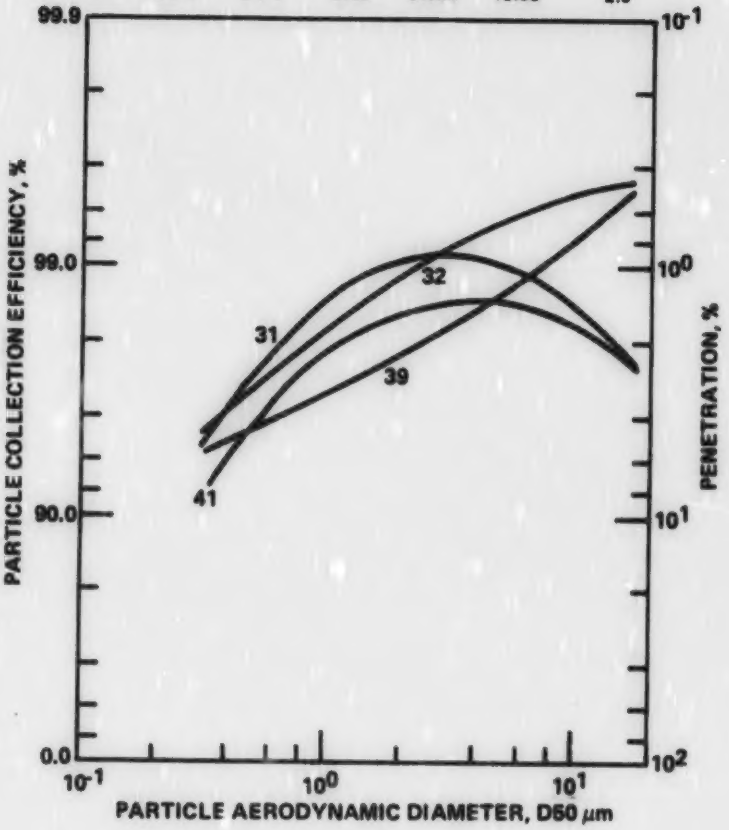

Figure 6. Particle collection efficiencies at equal and opposite polarities of corona and liquor sprays.

Test No.	Corona V, kV	Spray V, kV	Overall Coll Eff, %	SCA, ft^2/cfm	L/G, gal./1000cf	Penetration, %
31	70 (–)	2 (+)	98.6	0.060	11.52	1.4
32	70 (–)	2 (+)	98.8	0.060	11.60	1.2
45	70 (–)	2 (+)	97.8	0.060	8.7	2.2
51	70 (–)	2 (+)	96.5	0.060	8.5	3.6

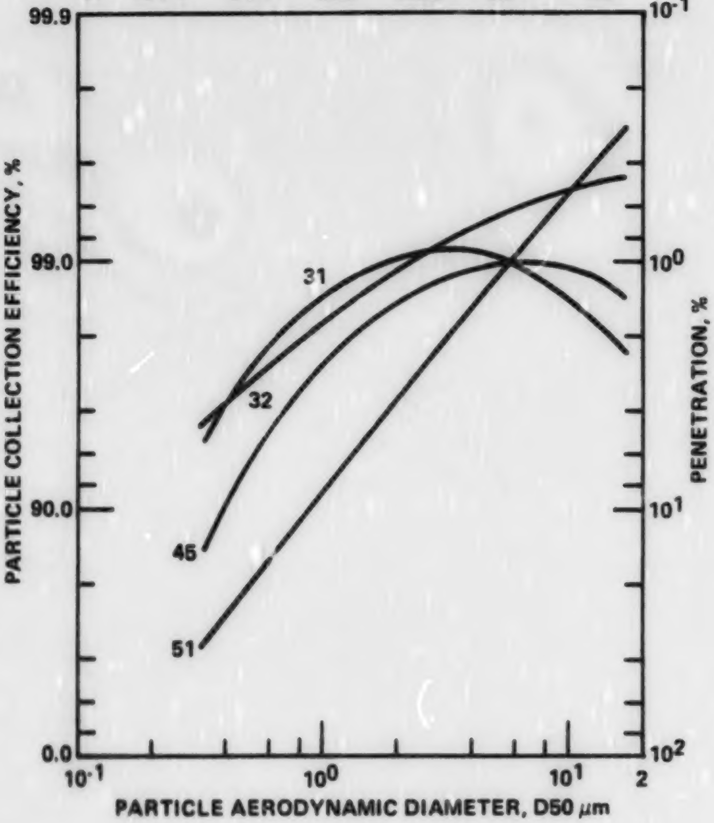

Figure 7. Effect of liquid-to-gas-flow-rate ratio on particle collection efficiencies.

ACKNOWLEDGEMENTS

This research was supported by EPA (IERL, RTP) Research Grant No. R803278. The assistance and cooperation of the Bethlehem Steel Corporation in Seattle is greatly appreciated.

REFERENCES

1. Penney, G.W. Electrified Liquid Spray Dust Precipitator. U.S. Patent 2,357,354, 1944.
2. Kraemer, H.F., and H.F. Johnstone. Collection of Aerosol Particles in the Presence of Electric Fields. Ind. Eng. Chem. 47:2426, 1955.
3. Pilat, M.J., S.A. Jaasund, and L.E. Sparks. Collection of Aerosol Particles by Electrostatic Droplet Spray Scrubbers. Environ. Sci. & Tech. 8:340-348, 1974.
4. Pilat, M.J. Collection of Aerosol Particles by Electrostatic Droplet Spray Scrubber. J. Air Pollut. Contr. Assoc. 25:176-178, 1975.
5. Pilat, M. J., and D. F. Meyer. University of Washington Electrostatic Spray Scrubber Evaluation. EPA-600/2-76-100, U.S. Environmental Protection Agency, Research Triangle Park, NC, April 1976. PB 252653/AS.
6. Pilat, M.J., G.A. Raemhild, and D.L. Harmon. Fine Particle Control with UW Electrostatic Scrubber. Presented at Second Fine Particle Scrubber Symposium, New Orleans, LA, 1977.
7. Hanson, D.N., and C.R. Wilke. Electrostatic Precipitator Analysis. Ind. & Eng. Chem. Process Des. Develop. 8:357-346, 1969.

PAPER 4

LABORATORY ELECTROSTATIC PRECIPITATOR STUDIES RELATING TO THE STEEL INDUSTRY

J. C. STEELHAMMER
D. R. NOGASH
D. M. POLIZZOTTI
BETZ LABORATORIES, INC.

INTRODUCTION

Although electrostatic precipitators are now and will continue to be the major particulate control device used in sinter plants, very little information exists in the literature about the performance of sinter plant electrostatic precipitators. This is understandable since most of the attention in the last few years has been given to fly ash electrostatic precipitators, especially those used in low sulfur coal applications.

This paper presents the results of various laboratory studies relative to sinter dust electrostatic precipitators. Briefly, sintering is a process for agglomerating iron-bearing fines (blast furnace flue dust, mill scale, and other metallurgical fines collected during the steel making process) to prevent their loss during reduction in the blast furnace. Raw materials used in the sintering process are iron-bearing fines, coke or coal dust, and fluxing materials such as limestone or dolomite.

CHARACTERIZATION OF SINTER DUST

Numerous sinter dusts were analyzed to determine the degree of variations in particle size, chemical composition, etc. that might be encountered. Microscopic analyses of these samples showed that they were all similar in appearance, regardless of their location. The sinter dusts were observed to be irregularly shaped with four prominent phases: (1) green-black (magnetite), (2) orange-red (hematite), (3) opaque-white (silicate), and (4) transparent (silica).

Table 1 shows the variation in bulk chemical composition observed for four different sinter dusts. The iron oxide present was determined to be primarily magnetite (Fe_3O_4) in all cases. It is interesting to note that there is extremely little variation in the iron oxide content of the sinter dusts. In fact, the largest variation observed was in the mean particle size of the sinter dusts, 12 μm to greater than 60 μm as determined by the Coulter Counter. This large variation in particle size was confirmed by dry sieve analyses of eight different sinter dusts (see Table 1).

TABLE 1. SINTER DUST CHARACTERIZATION[a]

Property	Range of Values
Bulk Composition, wt. %[a]	
LOI	1-2
Carbonate as CO_2	<1-4
Mg as MgO	1-6
Si as SiO_2	7-10
Ca as CaO	8-12
Fe as Fe_3O_4/Fe_2O_3	71-77[b]
S as SO_3	3-4
pH of 1% Slurry	10.8-11.2
Mean Particle Size (Coulter), μm	12 - >60
% < 400 mesh[c]	<1-100

[a] Based on 4 different sinter dusts sampled prior to any gas cleaning equipment.

[b] Chiefly magnetic.

[c] Based on 8 different sinter dusts sampled prior to any gas cleaning equipment.

Although the bulk chemical compositions given in Table 1 did not show any striking differences between various sinter dusts, chemical analyses of aqueous slurries did. Table 2 shows the chemical analyses of the supernatant from two sinter dust aqueous slurries. Note the large differences observed in the calcium ion concentration. One possible explanation for this is that the samples differ in the nature of the calcium salts present in the sinter dust. For example, the low calcium ion concentration of sinter dust sample SP-4 may be due to the fact that the calcium present is predominantly complexed in an insoluble calcium silicate (e.g., $CaSiO_3$). This is supported by the higher silica content present in the bulk chemical analysis. Conversely, the high concentration of calcium ion present in the filtrate of sample SP-3 indicates that much of the calcium may be complexed as a soluble salt ($CaSO_4$, $CaCl_2$, etc.).

TABLE 2. SLURRY ANALYSIS FOR SINTER DUSTS

Property	SP-3	SP-4
1% Slurry:		
pH	11.7	11.0
conductivity, 25°C, µ mho	2300	630
Ca^{2+}, ppm	208	46
SO_4^{2-}, ppm	48	16
Cl^-, ppm	10	2.5
SiO_2, ppm	<2	10
Solid - Bulk		
Ca as CaO	15	14
Si as SiO_2	4	10
carbonate as CO_2	7	--
mean particle size (Coulter), µm	50	12

Table 3 compares the bulk chemical composition of a sinter dust sampled on the process side with those sampled from the hoppers of the electrostatic precipitator. For this particular case, a mechanical collector existed prior to the electrostatic precipitator. Note that the iron content of the hopper samples is significantly lower than that in the process sample. Although the particle size distributions of the hopper samples were found to be less than that of the process sample, all samples were found by a Coulter Counter to have a mean particle size greater than 60 µm.

TABLE 3. SINTER DUST CHARACTERIZATION
PROCESS VS. PRECIPITATOR

Property	Process	Sampling Point ESP Inlet	ESP Outlet
LOI	3	6	8
Carbonate as CO_2	-	6	6
Chlorine, Cl^-		3	6
Si as SiO_2	12	9	6
Ca as CaO	11	15	12
Fe as (Fe_2O_3/Fe_3O_4)	73	56	55
% < 40 µm	-	25	36
pH of slurry	10.8	11.2	11.1
mean particle size, µm	>60	>60	>60

A BOF and sinter dust having approximately the same particle size distribution were selected for further study. Both samples were taken prior to any gas cleaning equipment. Microscopic analysis of the particle size fractions between 40 and 50 µm showed that the BOF dust was definitely spherical while the sinter dust was composed of particles of various shapes. The chemical analyses are given in Table 4.

The supernatant extract of pure samples of Fe_2O_3 and Fe_3O_4 were subjected to pH slurry analysis. The results indicated that these materials had a considerably lower pH (7.1 - 8.8) than either the sinter or BOF sample. This may well be a reflection of the fact that some of the surface constituents of the sinter/

BOF system are susceptible to hydrolysis. Such hydrolysis reactions may be of considerable importance in contribution to the particle surface conductivity.

TABLE 4. COMPARISON OF BOF AND SINTER DUSTS

Property	BOF	Sinter
Bulk analysis, wt. %		
LOI	1	1
Carbonate as CO_2	-	5
Mg as MgO	-	3
Si as SiO_2	2	10
Ca as CaO	2	7
Mn as MnO_2	3	-
Fe as (Fe_2O_3/Fe_3O_4)	92[a]	72[a]
1% Slurry analysis:		
pH	11.4	11.2
Ca^{2+}, ppm	142	97

[a] Chiefly magnetic.

SINTER DUST RESISTIVITY STUDIES

Resistivity measurements for several sinter dusts were made and the results are presented in Table 5. Also shown in Table 5 are measured resistivities for Fe_2O_3, Fe_3O_4, and two BOF dusts. The resistivities were determined with a resistivity apparatus manufactured according to specifications delineated in the ASME Power Test Code Manual No. 28. Resistivity measurements were made under ambient conditions.

As can be seen from Table 5, sinter dust resistivities were found to range between 1×10^7 to 4×10^8 ohm-cm at room temperature. Fe_3O_4 (magnetite), the primary constituent of sinter and BOF dust, had a resistivity less than 10^7 ohm-cm. The higher resistivity of the sinter dust is undoubtedly due to the flux material added during the sintering process.

TABLE 5. RESISTIVITY DATA

Sample	Resistivity, ohm-cm 25°C	110°C	120°C
Sinter - 1	3.8×10^7		3.0×10^6
Sinter - 2	1.0×10^7		
Sinter - 3	3.2×10^8		
Sinter - 3 Inlet Hopper/ESP	1.6×10^8		6.0×10^7
Sinter - 3 Outlet Hopper/ESP	8.5×10^7		2.1×10^8
Sinter - 3 < 45 μm	3.8×10^8		
Sinter - 3 < 149 μm	1.8×10^8		
BOF - 1	$<10^7$		
BOF - 2	$<10^7$	1.5×10^7	
Fe_3O_4	$<10^7$		
Fe_2O_3	3×10^9		
Fly Ash	$10^9 - 10^{11}$		

The presence of flux materials and process impurities in sinter and BOF dusts were reflected in the voltage/current characteristics of the dusts. Normally, an ohmic or slightly non-linear voltage/current response is obtained during a resistivity measurement. However, in some cases, interesting discontinuities in the current/voltage characteristics were obtained. These anomalies are schematically illustrated in Figure 1.

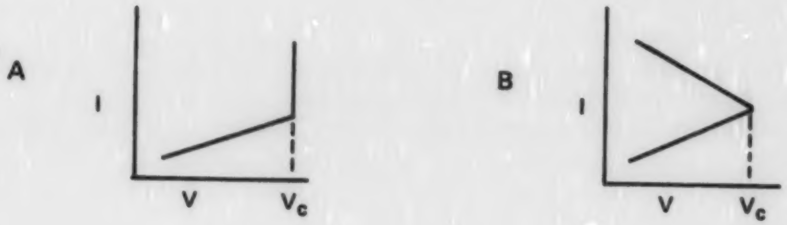

Figure 1. Voltage-current curves obtained in resistivity measurements.

In the case of Figure 1A, a rapid increase in current occurs at some critical voltage V_C. Such behavior is normally associated with semiconducting phenomena and may be the consequence of entrained impurities (CaO, etc.) in the dust matrix.

The case in Figure 1B is somewhat more difficult to interpret. However, it is clear that at the critical voltage V_C, some secondary process occurs which substantially reduces the resistance of the dust matrix. These critical potentials normally were observed at room temperature to be between 5000 and 8000 volts.

These phenomena may be of considerable importance to the operation of an electrostatic precipitator. It is well known that low resistivity dusts are difficult to collect and can lead to substantial reentrainment losses. The results of these resistivity measurements indicate that under certain conditions, not too dissimilar from those existing in an operating precipitator, sinter and BOF dusts can become very conductive leading to extremely rapid rates of capacitive discharge, once the ash layer contacts the collecting electrode. Resulting from these rapid rates of discharge, significant reentrainment losses may be expected—especially from the precipitator outlet fields. This suggests that inclusion of a dielectric material in the flue gas (i.e., clay or even a high resistivity fly ash) which is collected along with the metallic dust may enhance precipitator efficiency by reducing the conductivity of the collected dust layer.

DESCRIPTION OF THE BETZ LABORATORY PRECIPITATOR

Figure 2 shows a schematic of the Betz laboratory electrostatic precipitator. The system was designed and constructed by Bilrick, Inc. and is capable of simulating various systems (e.g., fly ash and sinter precipitators). As can be seen, the laboratory electrostatic precipitator system consists of four sections, namely, (1) the heater section, (2) the dust feeding section, (3) the precipitator proper, and (4) the exhaust section.

The heater section consists of an electric heater in series with an air aspirated oil burner. The electric heater alone is capable of heating the air up to a temperature of 400°F at 200 acfm. The heater unit is fitted with several injection ports permitting both the addition of chemical and the formulation of a synthetic flue gas (e.g., addition of SO_2, H_2O, etc.). Contained within the heater section is a damper used to moderate the air flow.

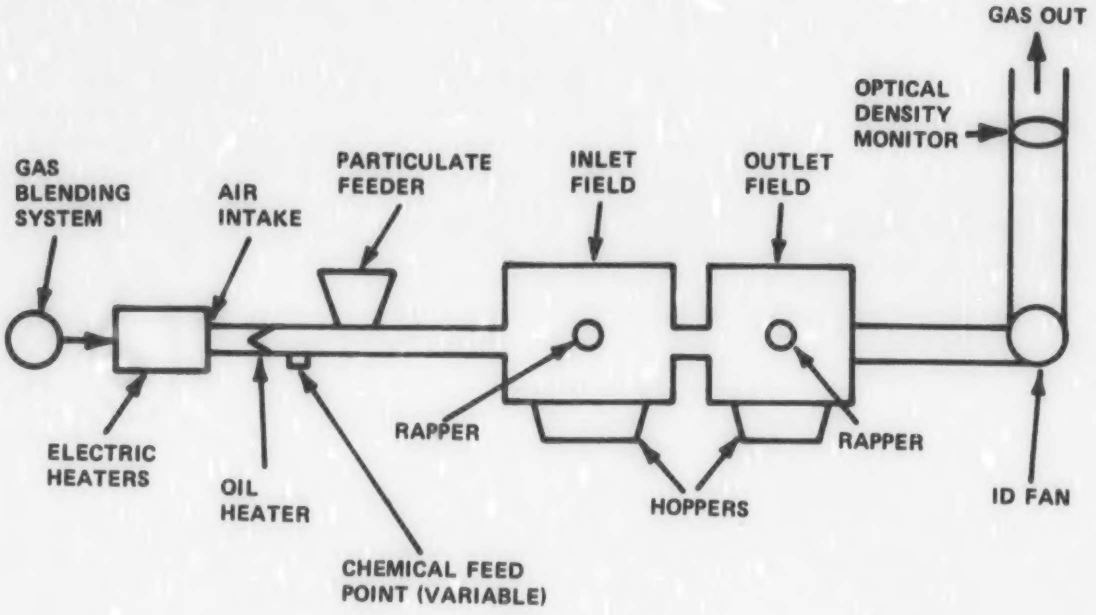
GAS OUT
OPTICAL DENSITY MONITOR
GAS BLENDING SYSTEM
AIR INTAKE
PARTICULATE FEEDER
INLET FIELD
OUTLET FIELD
RAPPER
RAPPER
ELECTRIC HEATERS
OIL HEATER
HOPPERS
ID FAN
CHEMICAL FEED POINT (VARIABLE)

Figure 2. Schematic of Betz Pilot Precipitator.

Following the heater assembly is the dust feeding section, which consists of a 10 ft. length of insulated duct work which leads into the precipitator proper. The dust used generally consists of samples taken from the hopper of an actual precipitator. The dust is fed into the gas via a vibrascrew particle feeder. Sampling ports, flow meters, and thermocouples also are located on this section of the duct.

The precipitator proper consists of two duct-type precipitators in series. Each precipitator (inlet and outlet) has its own set of controls for independent operation. All precipitator field variables can be operated in either a manual or automatic mode. Additionally, plate distances, rapper intensity, and rapper frequency can be varied. Particulate collected by the unit is deposited in hoppers located directly below the precipitator fields. Collected particulate is protected from reentrainment by suitably located baffles. View ports are located at the end of the outlet field and allow observation of the corona, sparking pattern, reentrainment, and deposition.

The exhaust section contains a variable speed induced draft fan which provides the air flow through the precipitator. Sampling ports are installed in the exit duct work in order to allow efficiency determinations by standard stack sampling methods. However, a Lear Siegler RM-41 opacity monitor located in the exit duct work is generally used to determine precipitator performance. Provided that the particle size distribution and other particulate properties (density, refractive index) do not change significantly with time, then optical density is directly proportional to grain loading.

Table 6 presents some of the basic design data for the Betz pilot precipitator.

TABLE 6. BASIC DESIGN PARAMETERS FOR BETZ PILOT PRECIPITATOR

Parameter	Range of Values for Betz Pilot Unit	Reported Ranges for Fly Ash Precipitators
Duct Spacing	6-12 in.	8-12 in.
Collection Surface	$\frac{200\text{-}500\ \mathrm{ft}^2}{1000\ \mathrm{cfm}}$	$\frac{100\text{-}800\ \mathrm{ft}^2}{1000\ \mathrm{cfm}}$
Gas Velocity	1.0-2.0 ft/sec	4-6 ft/sec
Aspect Ratio	1.33	0.5-1.5
No. H.T. Sections	2	2-8
No. of Corona Wires/H.T. Section	7	-
Corona Power	50-600 W/1000 cfm	50-500 W/1000 cfm
Corona Current	4-125 $\mu A/ft^2$	5-70 $\mu A/ft^2$
Efficiency	60-99.9+%	
Particulate Loading	1-15 gr/scf	
Temperature	Ambient - 450°F	

LABORATORY ELECTROSTATIC PRECIPITATOR STUDIES

This section presents the results of laboratory electrostatic precipitator studies of a sinter dust. For comparison purposes, results for a BOF dust are presented. Table 7 shows the optimum precipitator voltages found for these dusts. Also included are the results for Fe_2O_3 and Fe_3O_4. The voltages given in Table 7 represent the voltages at which sparkover occurs. Unless stated otherwise the moisture content of the gas in all the following studies was approximately 2%.

TABLE 7. OPTIMUM PRECIPITATOR VOLTAGES FOR VARIOUS DUSTS

Dust	Inlet Field, kV	Outlet Field, kV
Conditions: 270°F, 200 acfm, 4 gr/acf (132°C, 5.7 m^3/min, 9.2 g/m^3)		
Sinter	33	33
BOF	34	35
Fe_2O_3	28	--
Fe_3O_4	36	--

SINTER DUST

Actual sinter dust electrostatic precipitators generally operate over the following range of conditions:

Grain loading:	0.5-10 gr/scf (11.5 - 22.9 g/m^3)
Temperature:	230 - 340°F (110 - 171°C)
Moisture:	5 - 15%
Sulfur oxides:	25 - 500 ppm

Laboratory electrostatic precipitator studies on sinter dust were done in order to investigate the effect of some of the above variables on performance. The sinter dust used was obtained from the outlet hopper of an actual electrostatic precipitator and is characterized in Table 3 and Figure 3. The conditions used were: 2.5 gr/acf, 200 acfm, and 300°F (5.7 g/m^3, 5.7 m^3/min, 149°C)

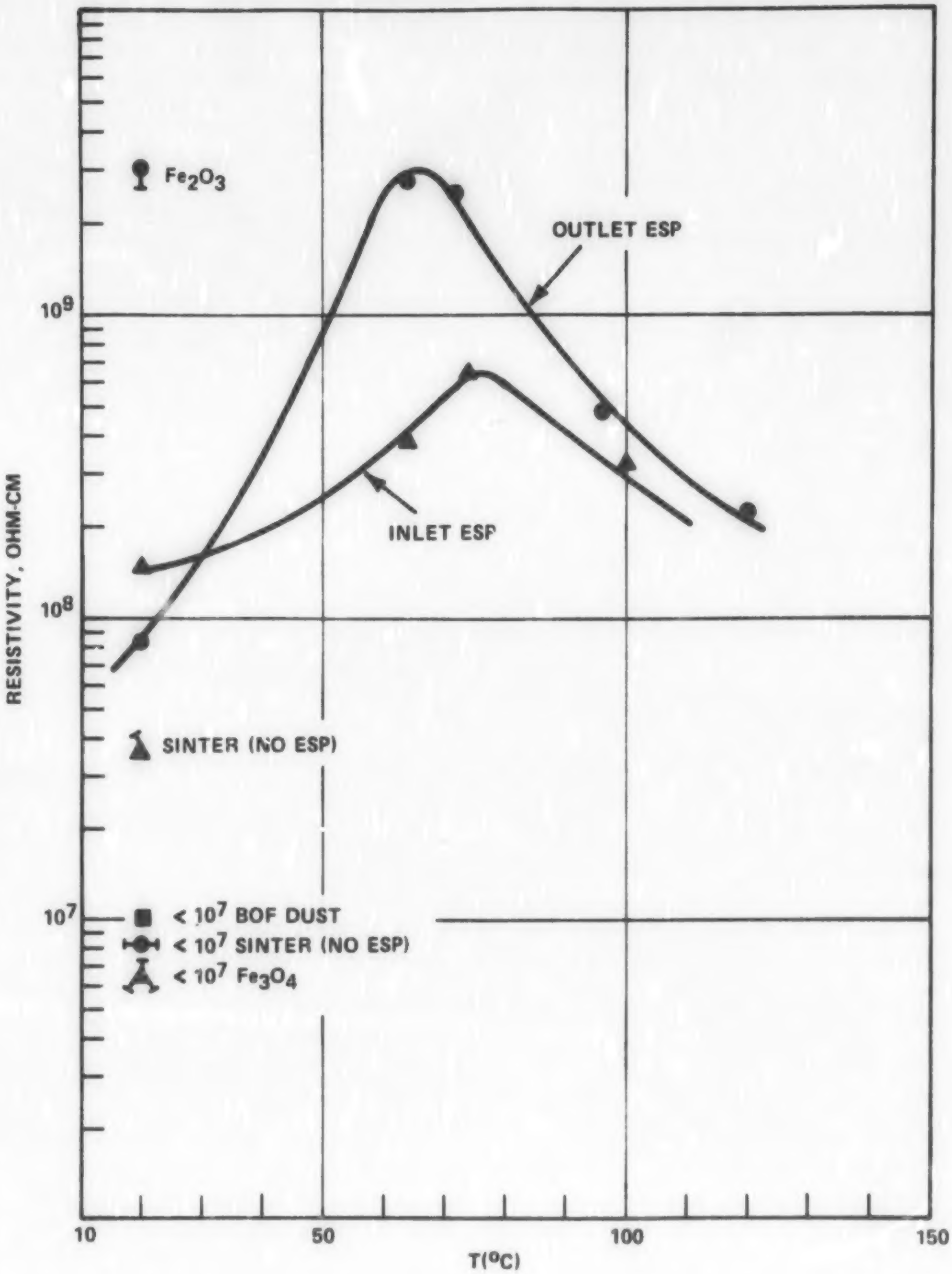

Figure 3. Resistivity vs. temperature, sinter dust.

(unless otherwise noted). In all cases, changes in optical density were used to indicate changes in efficiency. Briefly, the results are:

1. Effect of Moisture: No noticeable effect on the efficiency was observed when the moisture content was increased from 2% to 5%.

2. Effect of SO_2: The effect of SO_2 on the efficiency is shown in Figure 4. Note that there is only a small dependence, especially when compared to fly ash.

3. Effect of Temperature: The effect of temperature on precipitator performance is shown in Table 8. As can be seen, the temperature can have a large effect on the efficiency.

The temperature dependence of the collection efficiency can be interpreted in terms of the resistivity results cited earlier. From 105 to 138°C, the optical density declines indicating that the dust is being efficiently collected. However, a break occurs between 138 and 145°C and collection efficiency deteriorates past 178°C. Based on the results of the resistivity analysis, it is likely that this deterioration results from a change in the conductive nature of the sinter dust. That is, the thermal energy available at temperatures in excess of 138°C is sufficient to initiate transition, similar in nature to those observed earlier during the resistivity measurements.

TABLE 8. OPTICAL DENSITY VS. TEMPERATURE
SINTER DUST

Conditions: 2.5 gr/acf, 200 acfm

Temperature, °C	Optical Density
105	0.086
120	0.063
138	0.053
145	0.053
178	0.068

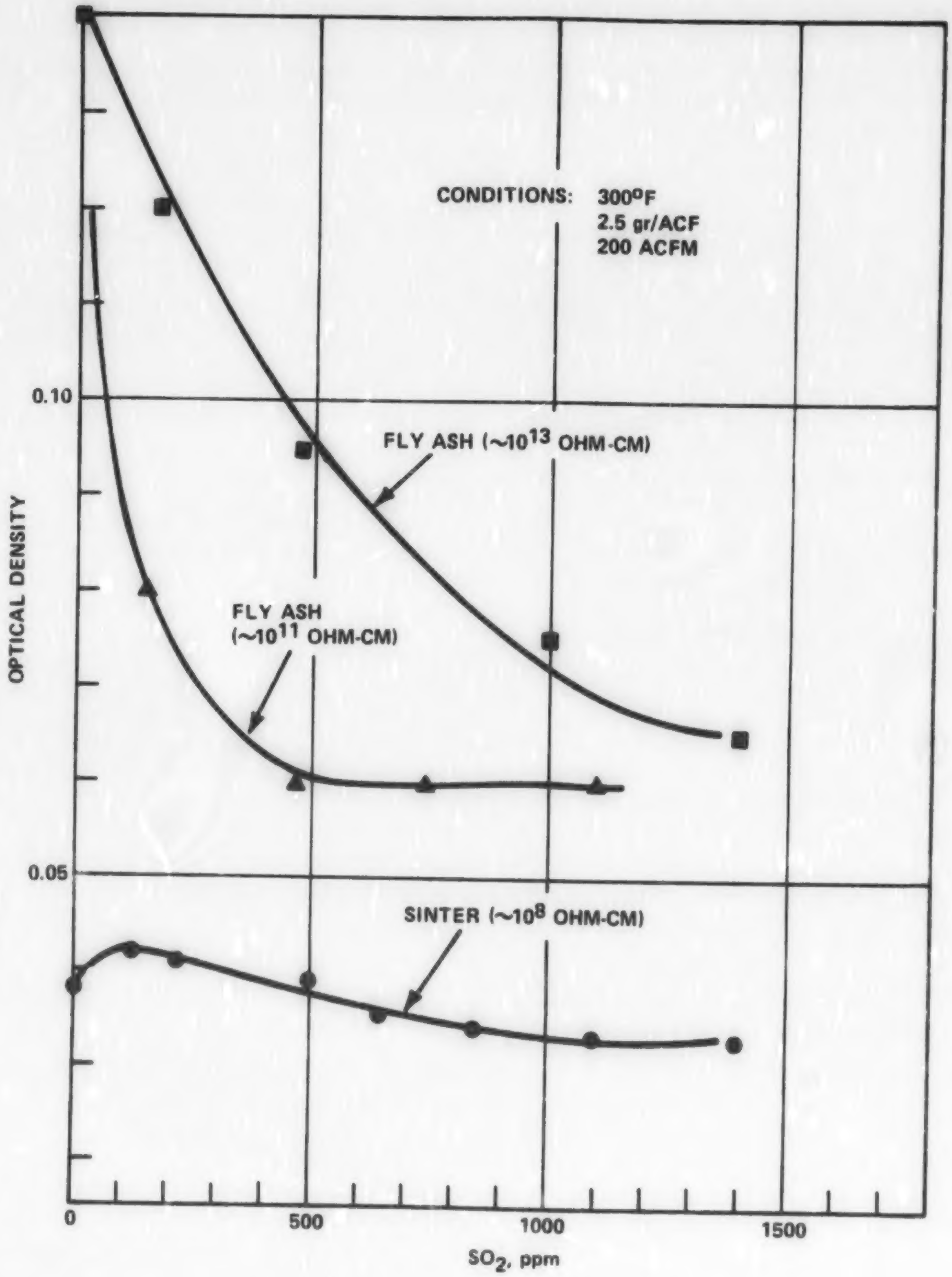

Figure 4. Effect of SO_2 on precipitator performance, sinter dust and fly ash.

The relative insensitivity of the sinter dust to varying SO_2 concentrations (especially when compared to fly ash) is difficult to understand. One possible factor which may be of significance is the fact that compared to fly ash, sinter is a better electrically conducting material.

Figures 5 - 7 show further studies on sinter dust under the following conditions: 4 gr/acf, 200 acfm, and 270°F (9.2 g/m^3, 5.7 m^3/min, 132°C). Figure 5 shows the relative influence of the inlet and outlet fields on the optical density. Note that the inlet field is more important in determining the overall efficiency. This is verified in Figure 6 which shows optical density versus voltage for the various combinations of inlet and outlet fields. It should also be noted in Figure 6 that more reentrainment losses result when only the outlet field is used (recall earlier comments). Figure 7 shows the operation of the precipitator with and without the rappers. Note that there is very little difference. At least for a short time period (2 hours), no noticeable deterioration occurs in the optical density when the rappers are off.

Table 9 shows the bulk chemical analyses for sinter dust samples taken from the hoppers of the pilot precipitator. Presented in this table are samples from the last inlet and last outlet hoppers. Note that a significant reduction in iron content results in going from the inlet to the outlet hopper. (This may be a reflection of physical separation — heavier particles "fall out" in the inlet field — lighter ones are carried on to the outlet field.)

BOF DUST

Figure 8 shows the results of investigating a BOF dust on the laboratory precipitator. This BOF dust was approximately 92% iron (chiefly magnetic) with a mean particle size of 15 μm, significantly lower than that for the sinter dust studied. Note that the BOF dust is significantly more sensitive to rapping than was the sinter dust. This could be a reflection of particle size, but undoubtedly the lower resistivity may also be important. Very little dependence of the efficiency on the SO_2 level was observed. However, it was noted that high SO_2 levels ($\sim$1000 ppm) resulted in a reduction in rapping reentrainment.

It should be mentioned that the studies in Figure 8 represent precipitator operation during an off blowing period. Generally during a blow, moisture in the flue gas approaches 25% due to water sprays used to cool the gas.

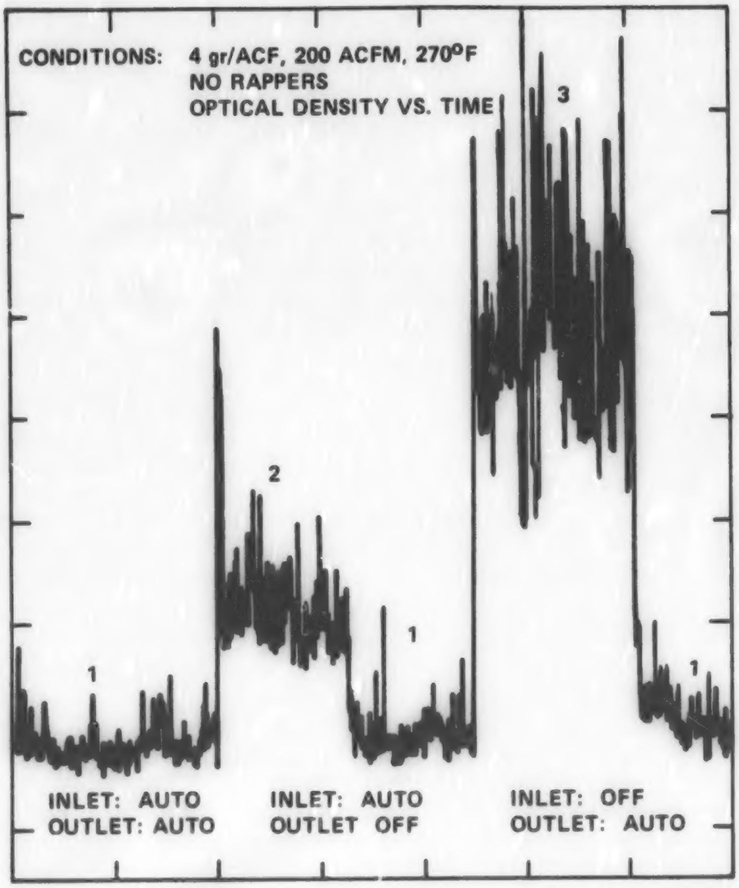

Figure 5. Sinter dust: influence of inlet and outlet fields on optical density.

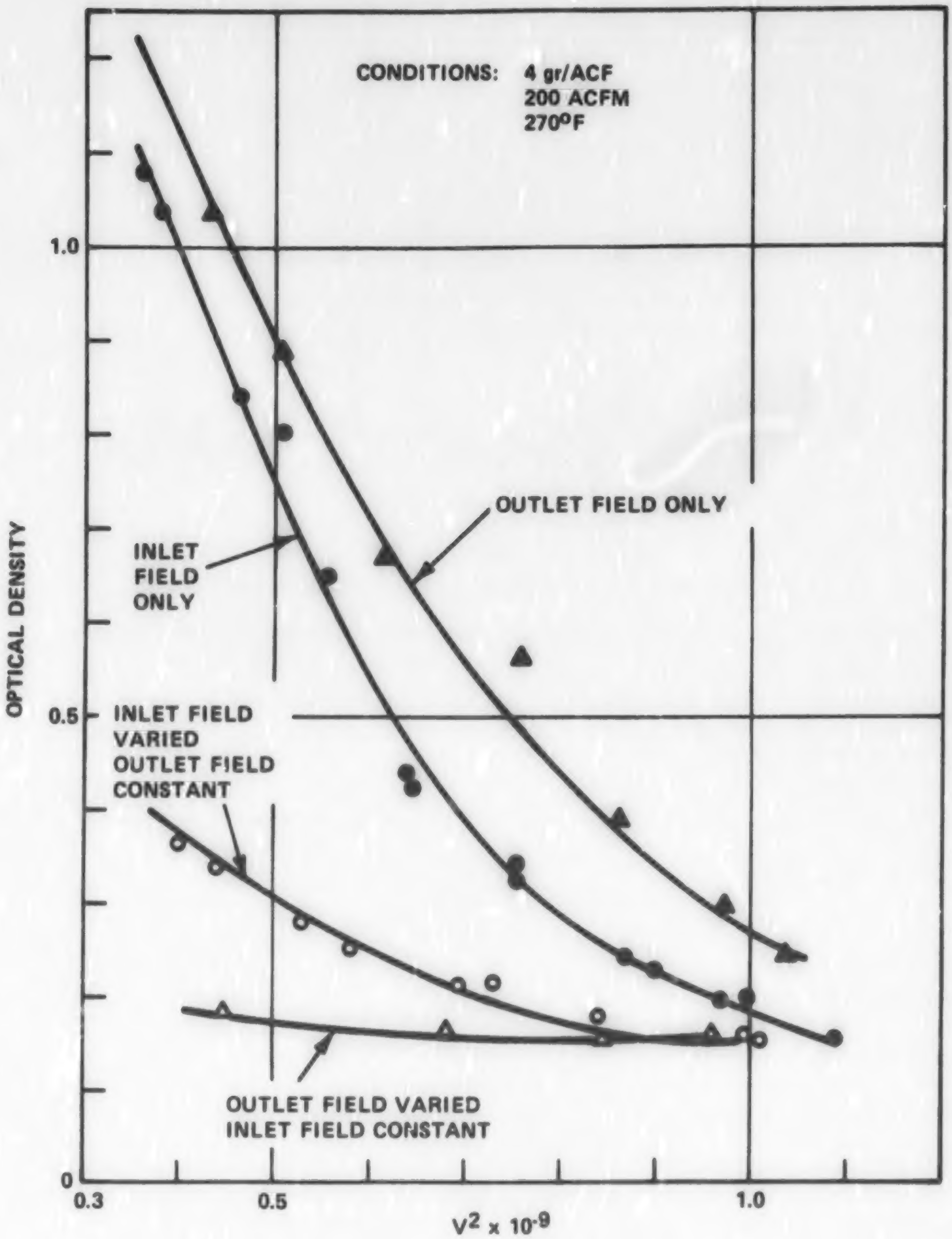

Figure 6. Sinter dust: optical density vs. voltage for various combinations of inlet and outlet fields.

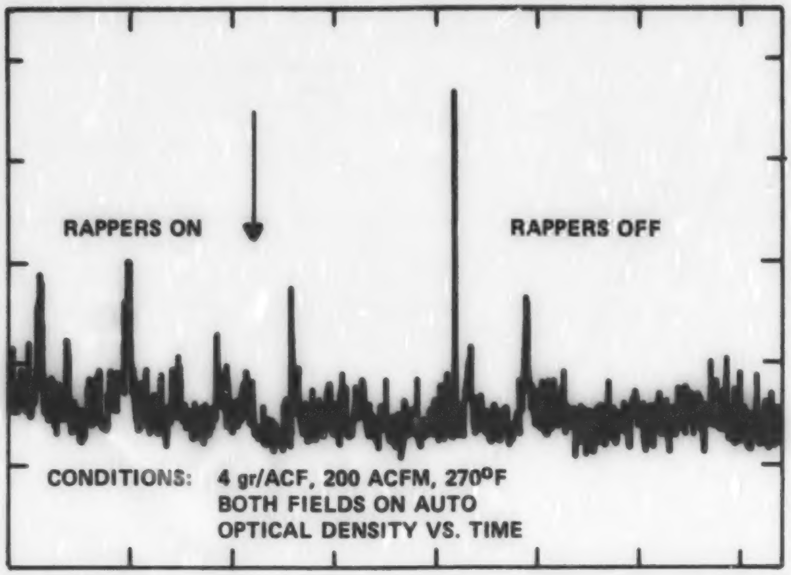

Figure 7. Sinter dust: operation of precipitator with and without rappers.

TABLE 9. CHARACTERIZATION OF PRECIPITATED SINTER DUST

	Hopper Sample	
Property	Last Inlet	Last Outlet
LOI	7	8
Carbonate as CO_2	6	5
Sulfur as SO_3	4	4
Al as Al_2O_3	-	3
Si as SiO_2	9	16
Ca as CaO	9	11
Fe as (Fe_2O_3/Fe_3O_4)	49[a]	31[a]
$CaCl_2$	11	16
Resistivity, ohm-cm at 115°C	$<10^7$	3×10^{10}
% < 38 μm	12	57

[a] Chiefly magnetic.

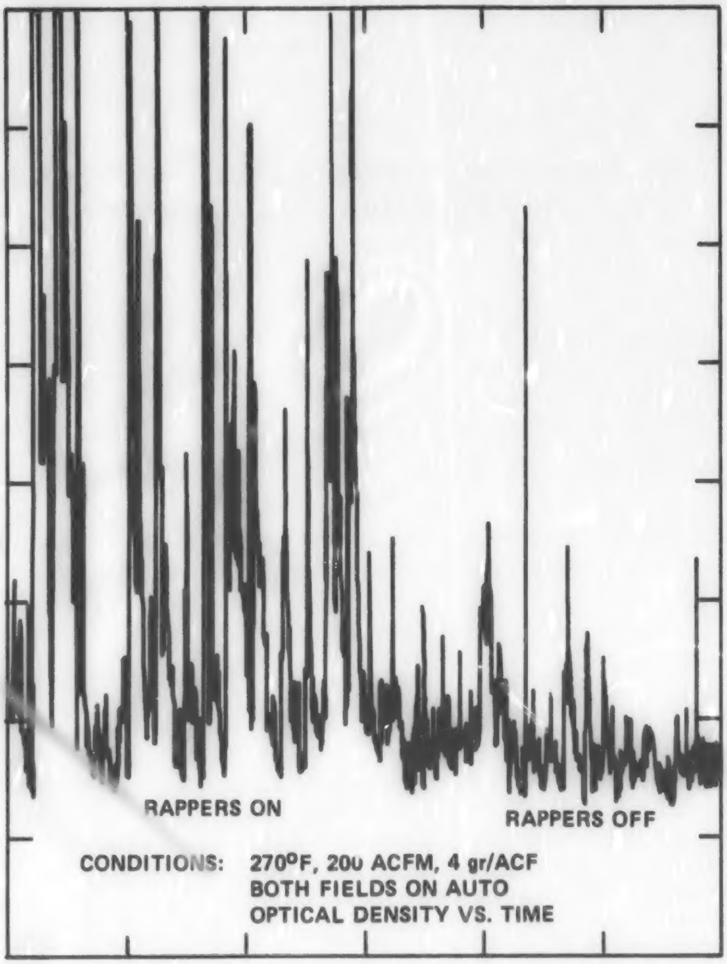

Figure 8. BOF dust: operation of precipitator with and without rappers.

PAPER 5

A PRECIPITATOR PERFORMANCE MODEL: APPLICATION TO THE NONFERROUS METALS INDUSTRY

JACK R. McDONALD
SOUTHERN RESEARCH INSTITUTE

AND

LESLIE E. SPARKS
INDUSTRIAL ENVIRONMENTAL RESEARCH LABORATORY-RTP
U. S. ENVIRONMENTAL PROTECTION AGENCY

ABSTRACT

The fundamental mechanisms involved in electrostatic precipitation are discussed and a mathematical model is described which calculates collection efficiency in an electrostatic precipitator as a function of particle size and operating conditions. The model determines the electric field, particle charge, and removal efficiency as functions of position along the length of the precipitator. Procedures for estimating collection efficiency losses caused by nonuniform gas velocity distributions, gas bypassage of electrified regions, and particle reentrainment are discussed. Those parameters which have the most significant effect on precipitator performance are analyzed using the model and experimental data from a precipitator installed on a copper reverberatory furnace. Model predictions of fractional collection efficiencies are compared with field data from three precipitators used to collect particulate emissions in the nonferrous metals industry.

INTRODUCTION

The separation of suspended particles from gases by an electrical process is referred to as electrostatic precipitation. Electrostatic precipitation can provide high-efficiency collection of dusts, fumes, and mists from industrial furnace and process gases. Reasons for using electrostatic precipitation are usually environmental or economic in nature or a combination of both. The electrostatic precipitation process has been employed with considerable success for air pollution control, recovery of valuable byproducts from primary processes, and removal of contaminants from gases which have a subsequent use.[1,2]

There are several characteristics of electrostatic precipitation which make its use desirable and its realm of application widespread.[3,4] The application of separation forces directly to the particles, instead of to the entire gas stream, results in modest power requirements and low resistance to gas flow characteristic. All particle sizes can be collected with relatively high efficiencies. Large quantities of gas can be treated at high temperatures. Corrosive atmospheres and particles can be handled successfully.

The electrostatic precipitation process involves several complicated and interrelated physical mechanisms: the creation of a nonuniform electric field and ionic current in a corona discharge; the ionic charging of particles moving in combined electro- and hydro-dynamic fields; and the turbulent transport of charged particles to a collection surface. In many practical applications the removal of the collected particles presents a serious problem since the removal procedures introduce collected material back into the gas stream and cause a reduction in collection efficiency. Other practical considerations which reduce the collection efficiency are nonuniform gas velocity distribution and bypassage of the electrified regions by particle-laden gas.

In recent years, increasing emphasis has been placed on developing theoretical relationships which accurately describe the individual physical mechanisms involved in the precipitation process and on incorporating these relationships into a complete model for electrostatic precipitation. From a practical standpoint, a reliable theoretical model for electrostatic precipitation would offer several valuable applications:

(1) Precipitator design could be easily and completely performed by calculation from theoretical principles.

(2) A theoretical model could be used in conjunction with a pilot plant study in order to design a full-scale precipitator.

(3) Precipitator bids submitted by various manufacturers could be evaluated by a purchaser with respect to meeting the design efficiency and related costs.

(4) The optimum operating efficiency of an existing precipitator could be established and the ability to meet particulate emissions standards could be ascertained.

(5) An existing precipitator performing below its optimum efficiency could be analyzed with respect to the different operating variables in a procedure to troubleshoot and diagnose problem areas.

The reliability of predictions obtained from a theoretical model is subject to the extent to which certain fundamental parameters are known, the degree to which the theoretical relationships describe precipitator operation, and the accuracy with which the factors that correct for nonideal conditions can be modeled and determined. At present, efficiency losses due to nonideal conditions can be accounted for only by estimation procedures in which assumed values of the descriptive parameters are normally used.

In this paper, the fundamental steps in the precipitation process are briefly discussed and a mathematical model[5,6,7] which incorporates these steps is outlined. Although the model has been applied with reasonable success to predict the performance of laboratory-scale precipitators[6] and full-scale precipitators collecting fly ash from coal-fired boilers,[5,7] it has not been applied to any extent to full-scale precipitators collecting particulate emissions from nonferrous metallurgical processes. The primary reason for the limited use of the precipitator performance model in the nonferrous metals industry has been the lack of data concerning precipitator operating conditions in these applications. As part of the present paper, experimental data obtained from full-scale precipitators collecting particulate emissions from two smelters and an aluminum reduction furnace are analyzed and the performance predictions of the precipitator model are compared with the experimental results.

FUNDAMENTAL STEPS IN THE COLLECTION PROCESS

Creation of an Electric Field and Corona Current

The first step in the precipitation process is the creation of an electric field and corona current. This is accomplished by applying a large potential difference between a small-radius electrode and a much larger radius electrode, where the two electrodes are separated by a region of space containing an insulating gas. For industrial applications, a large negative potential is applied at the small-radius electrode and the large-radius electrode is grounded.

At any applied voltage, an electric field exists in the inter-electrode space. For applied voltages less than a value referred to as the "corona starting voltage", a purely electrostatic field is present. At applied voltages above the corona starting voltage, the electric field in the vicinity of the small-radius electrode is large enough to produce ionization by electron impact. Between collisions with neutral molecules, free electrons are accelerated to high velocities and, upon collision with a neutral molecule, their energies are sufficiently high to cause an electron to be separated from a neutral molecule. Then, as the increased number of electrons moves out from the vicinity of the small-radius electrode, further collisions between electrons and neutral molecules occur. In a limited high electric field region near the small-radius electrode, each collision between an electron and a neutral molecule has a certain probability of forming a positive molecular ion and another electron, and an electron avalanche is established. The positive ions migrate to the small-radius electrode and the electrons migrate into the lower electric field regions toward the large-radius electrode. These electrons quickly lose much of their energy and, when one of them collides with a neutral electronegative molecule, there is a probability that attachment will occur and a negative ion will be formed. Thus, negative ions, along with any electrons which do not attach to a neutral molecule, migrate under the influence of the electric field to the large-radius electrode and provide the current necessary for the precipitation process.

Figure 1a is a schematic diagram showing the region very near the small-radius electrode where the current-carrying negative ions are formed. As these negative ions migrate to the large-radius electrode, they constitute a steady-state charge distribution in the inter-electrode space which is referred to as an "ionic space charge". This "ionic space charge" establishes an electric field which adds to the electrostatic field to give the total electric field. As the applied voltage is increased, more ionizing sequences result and the "ionic space charge" increases. This leads to a higher average electric field and current density in the inter-electrode space.

Figure 1b gives a qualitative representation of the electric field distribution and equipotential surfaces in a wire-plate geometry which is most commonly used. Although the electric field is very nonuniform near the wire, it becomes essentially uniform near the collection plates. The current density is very nonuniform throughout the inter-electrode space and is maximum along a line from the wire to the plate.

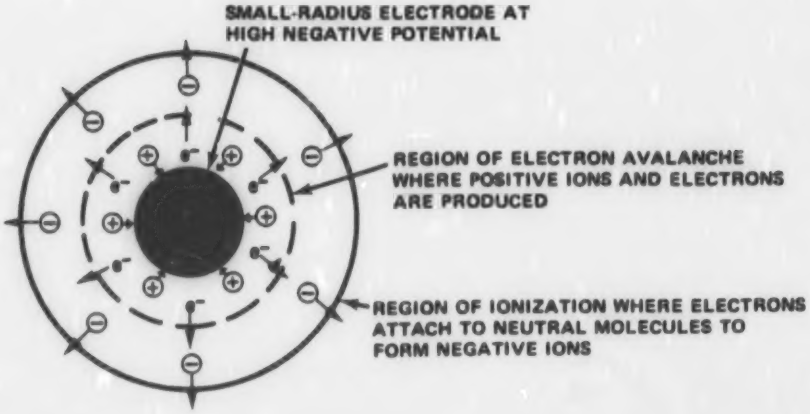
SMALL-RADIUS ELECTRODE AT HIGH NEGATIVE POTENTIAL
REGION OF ELECTRON AVALANCHE WHERE POSITIVE IONS AND ELECTRONS ARE PRODUCED
REGION OF IONIZATION WHERE ELECTRONS ATTACH TO NEUTRAL MOLECULES TO FORM NEGATIVE IONS

Figure 1a. Region near small-radius electrode.

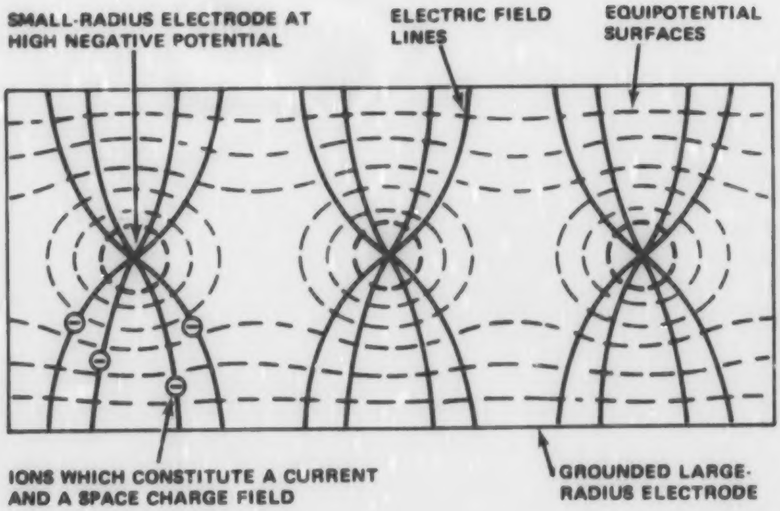
SMALL-RADIUS ELECTRODE AT HIGH NEGATIVE POTENTIAL
ELECTRIC FIELD LINES
EQUIPOTENTIAL SURFACES
IONS WHICH CONSTITUTE A CURRENT AND A SPACE CHARGE FIELD
GROUNDED LARGE-RADIUS ELECTRODE

Figure 1b. Electric field configuration for wire-plate geometry.

In order to maximize the collection efficiency obtainable from the electrostatic precipitation process, the highest possible values of applied voltage and current density should be employed. In practice, the highest useful values of applied voltage and current density are limited by either electrical breakdown of the gas throughout the inter-electrode space or of the gas in the collected particulate layer. High values of applied voltage and current density are desirable because of their beneficial effect on particle charging and particle transport to the collection electrode. In general, the voltage-current characteristics of a precipitator depend on the geometry of the electrodes, the gas composition, temperature, and pressure, the particulate mass loading and size distribution, and the resistivity of the collected particulate layer. Thus, maximum values of voltage and current can vary widely from one precipitator to another and from one application to another.

Particle Charging

Once an electric field and current density are established, particle charging can take place. Particle charging is essential to the precipitation process because the electrical force which causes a particle to migrate toward the collection electrode is directly proportional to the charge on the particle. The most significant factors influencing particle charging are particle diameter, applied electric field, current density, and exposure time.

The particle charging process can be attributed mainly to two physical mechanisms, field charging and thermal charging.[8,9,10]

(1) At any instant in time and location in space near a particle, the total electric field is the sum of the electric field due to the charge on the particle and the applied electric field. In the field charging mechanism, molecular ions are visualized as drifting along electric field lines. Those ions moving toward the particle along electric field lines which intersect the particle surface impinge upon the particle surface and place a charge on the particle.

Figure 2 depicts the field charging mechanism during the time it is effective in charging a particle. In this mechanism, only a limited portion of the particle surface $(0<\theta<\frac{\pi}{2})$ can suffer an impact with an ion and collisions of ions with other portions of the particle surface are neglected. Field charging takes place very rapidly and terminates when sufficient charge (the saturation charge) is accumulated to repel additional ions. Figure 3b depicts the electric field configuration once the particle has attained the saturation charge. In this case, the ions circumvent the particle. In Figures 2 and 3, the arrows indicate the direction of the force acting on the ions.

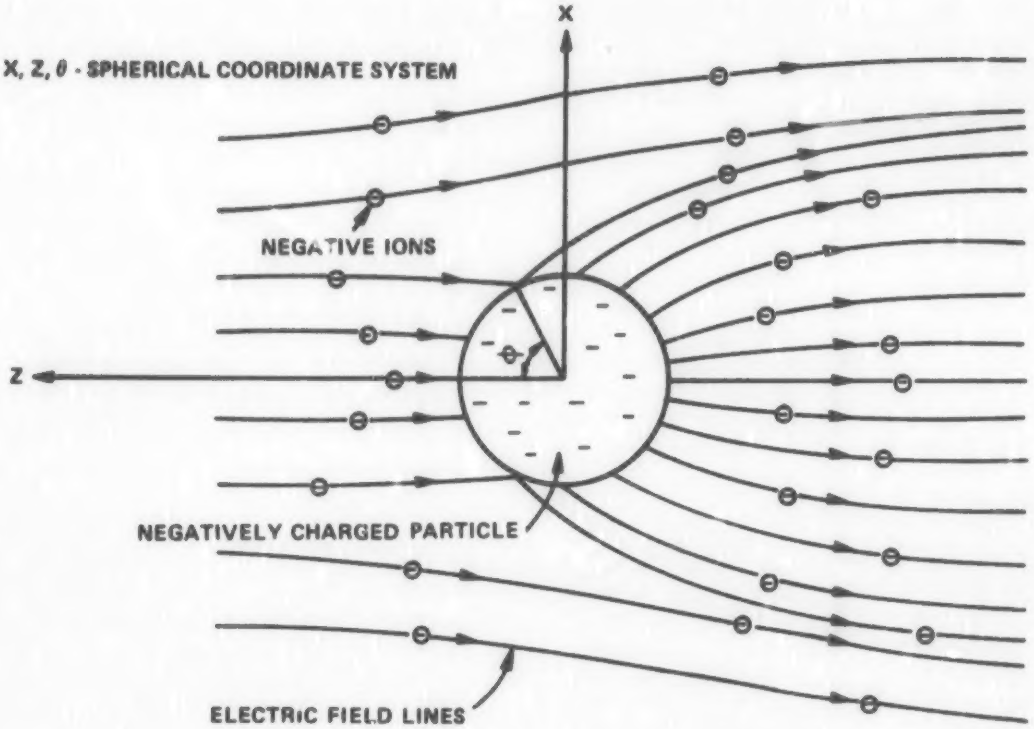
X
X, Z, θ - SPHERICAL COORDINATE SYSTEM
NEGATIVE IONS
Z
NEGATIVELY CHARGED PARTICLE
ELECTRIC FIELD LINES

Figure 2. Electric field configuration during field charging

Theories based on the mechanism of field charging agree reasonably well with experiments whenever particle diameters exceed about 0.5 μm and the applied electric field is moderate to high. In these theories, the amount of charge accumulated by a particle depends on the particle diameter, applied electric field, ion density, exposure time, ion mobility, and dielectric constant of the particle.

(2) The thermal charging mechanism depends on collisions between particles and ions which have random motion due to their thermal kinetic energy. In this mechanism, the particle charging rate is determined by the probability of collisions between a particle and ions. If a supply of ions is available, particle charging occurs even in the absence of an applied electric field. Although the charging rate becomes negligible after a long period of time, it never has a zero value as is the case with the field charging mechanism. Charging by this mechanism takes place over the entire surface of the particle and requires a relatively long time to produce a limiting value of charge.

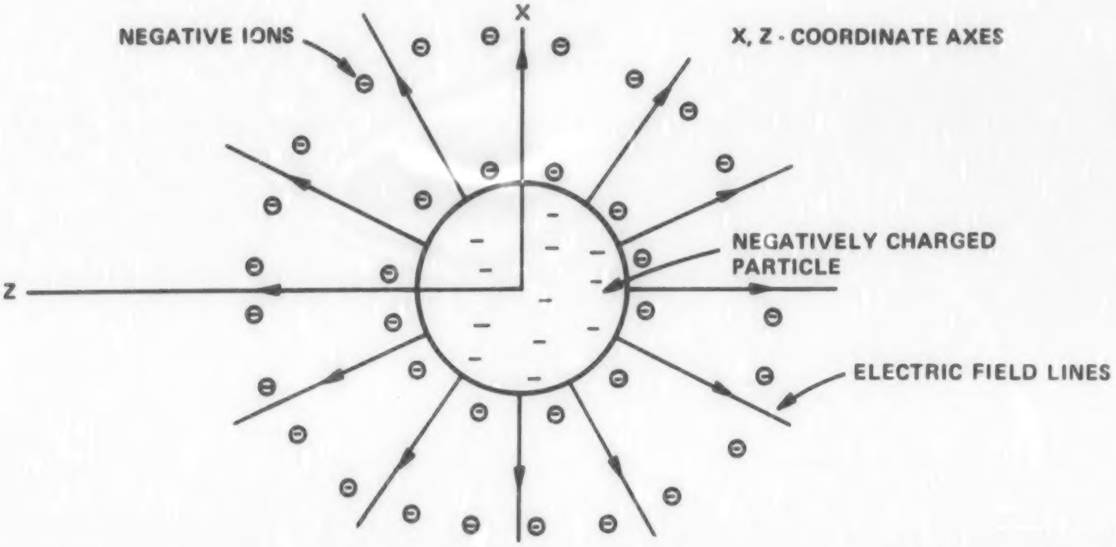
NEGATIVE IONS
X
X, Z - COORDINATE AXES
NEGATIVELY CHARGED PARTICLE
Z
ELECTRIC FIELD LINES

Figure 3a. *Electric field configuration and ion distribution for particle charging with no applied field.*

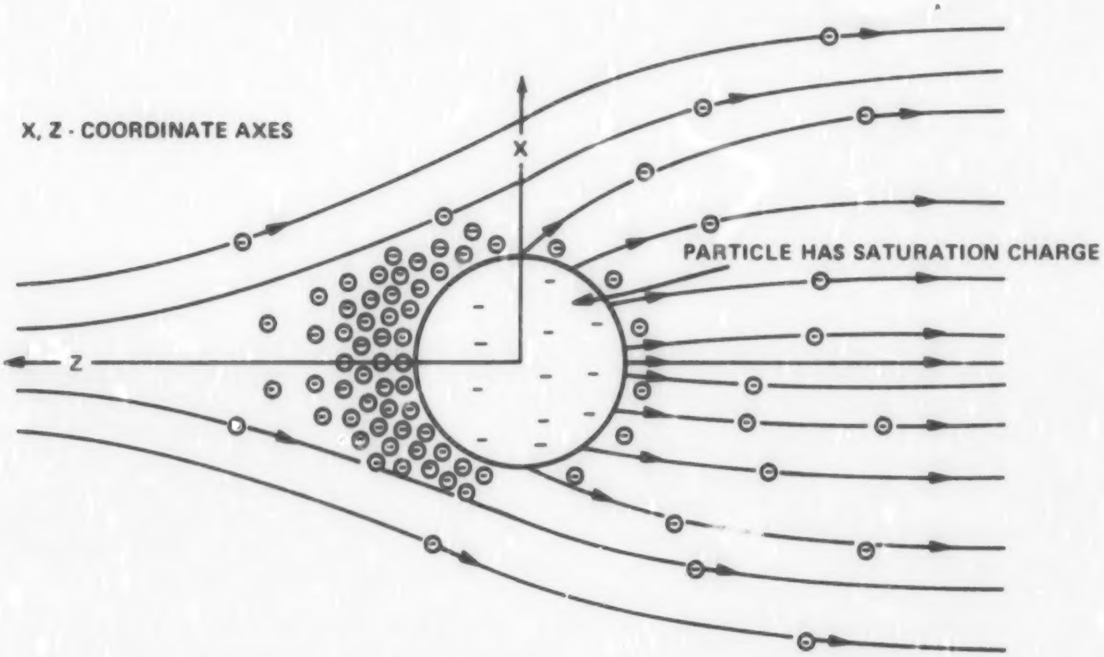
X, Z - COORDINATE AXES
X
PARTICLE HAS SATURATION CHARGE
Z

Figure 3b. *Electric field configuration and ion distribution for particle charging in an applied field after saturation charge is reached.*

Figure 3a depicts the thermal charging process in the absence of an applied electric field. In this case, the ion distribution is uniform around the surface of the particle and each element of surface area has an equal probability of experiencing an ion collision. Thermal charging theories which neglect the effect of the applied electric field adequately describe the charging rate over a fairly broad range of particle sizes where the applied electric field is low or equal to zero. In addition, they work well for particles less than 0.2 µm in diameter regardless of the magnitude of the applied electric field.

Figure 3b depicts the thermal charging process in the presence of an applied electric field after the particle has attained the saturation charge determined from field charging theory. The effect of the applied electric field is to cause a large increase in ion concentration on one side of the particle while causing only a relatively small decrease on the other side. Although the ion concentration near the surface of the particle becomes very nonuniform, the net effect is to increase the average ion concentration, the probability of collisions between ions and the particle, and the particle charging rate.

In thermal charging theories, the amount of charge accumulated by a particle depends on the particle diameter, ion density, mean thermal velocity of the ions, absolute temperature of the gas, particle dielectric constant, and the applied electric field. The effect of the applied electric field on the thermal charging process must be taken into account for fine particles having diameters between 0.1 µm and 2.0 µm. Depending most importantly on the applied electric field and to a lesser extent on certain other variables, particles in this size range can acquire values of charge which are 2-3 times larger than those predicted from either the field or the thermal charging theories. For these particles, neither field nor thermal charging predominates and both mechanisms must be taken into account simultaneously.

In most cases, particle charging has a noticeable effect on the electrical conditions in a precipitator. The introduction of a significant number of fine particles or a heavy concentration of large particles into an electrostatic precipitator significantly influences the voltage-current characteristic. Qualitatively, the effect is seen by an increased voltage for a given current compared to the particle-free situation. As the particles acquire charge, they must carry part of the current but are much less mobile than the ions. This results in a lower "effective mobility" for the charge carriers and, in order to obtain a given particle-free current, higher voltages must be applied to increase the drift velocities of the charge carriers and the ion densities.

The charged particles, which move very slowly, establish a "particulate space charge" in the inter-electrode space. The distribution of the "particulate space charge" results in an electric field distribution which adds to those due to the electrostatic field and the ionic field to give the total electric field distribution. It is desirable to determine the space charge resulting from particles because of its influence on the electric field distribution, especially near the collection plate where, for the same current, the electric field is raised above the particle-free situation. In addition, the "particulate space charge" is a function of position along the length of the precipitator since particle charging and collection are a function of length.

Particle Collection

As the particle-laden gas moves through a precipitator, each charged particle has a component of velocity directed toward the collection electrode. This component of velocity is called the electrical drift velocity, or migration velocity, and results from the electrical and viscous drag forces acting upon a suspended charged particle. For particle sizes of practical interest, the time required for a particle to achieve a steady-state value of migration velocity is negligible and, near the collection electrode, the magnitude of this quantity is given by:[11]

$$w_p = \frac{qE_p\,C}{6\pi a\mu}\,, \qquad (1)$$

where

w_p = migration velocity near the collection electrode of a particle of radius a (m/sec),

q = charge on particle (coul),

E_p = electric field near the collection electrode (volt/m),

a = particle radius (m),

μ = gas viscosity (kg/m-sec),

C = Cunningham correction factor, or slip correction factor[12]

$= (1 + A\lambda/a)$, and

where

$A = 1.257 + 0.400 \exp(-1.10\, a/\lambda)$, and

λ = mean free path of gas molecules (m).

If the gas flow in a precipitator were laminar, then each charged particle would have a trajectory which could be determined from the velocity of the gas and the migration velocity. In this case, the collection length required for 100% collection of particles with a known migration velocity can be calculated. For cases where turbulence exists, a laminar flow calculation is of interest only because it establishes the best possible collection efficiency for a given collection length.

In industrial precipitators, laminar flow never occurs and, in any collection mechanism, the effect of turbulent gas flow must be considered. The turbulence is due to the complex motion of the gas itself, electric wind effects of the corona, and transfer of momentum to the gas by the movement of the particles. Average gas flow velocities in most cases of practical interest are between 0.6 and 2.0 m/sec. Due to eddy formation, electric wind, and other possible effects,the instantaneous velocity of a small volume of gas surrounding a particle may reach peak values which are much higher than the average gas velocity. In contrast, migration velocities for particles smaller than 6.0 μm in diameter are usually less than 0.3 m/sec. Therefore, the motion of these smaller particles tends to be dominated by the turbulent motion of the gas stream. Under these conditions, the paths taken by the particles are random and the determination of the collection efficiency of a given particle becomes, in effect, the problem of determining the probability that a particle will enter a laminar boundary zone adjacent to the collection electrode in which capture is assured.

Using probability concepts and the statistical nature of the large number of particles in a precipitator, an expression for the collection efficiency can be derived[13] in the form:

$$\eta = 1 - \exp\left(-A_p w_p / Q\right), \qquad (2)$$

where

η = collection fraction of the particle size under consideration,

A_p = collection area (m^2),

w_p = migration velocity near the collection electrode of a particle of radius a (m/sec), and

Q = gas volume flow rate (m^3/sec).

The simplifying assumptions on which the derivation of Equation (2) is based are:

(1) The gas is flowing in a turbulent pattern at a constant, mean forward-velocity.

(2) Turbulence is small scale (eddies are small compared to the dimensions of the duct), fully developed, and completely random.

(3) Particle migration velocities are small compared with the gas velocity.

Experimental data[14] under conditions which are consistent with the above assumptions demonstrate that Equation 2 adequately describes the collection of monodisperse aerosols in an electrostatic precipitator under certain idealized conditions.

In industrial precipitators, the above assumptions are never completely satisfied but they can be approached closely. With proper design, the ratio of the standard deviation of the gas velocity distribution to the average value can be made to be 0.25 or less so that an essentially uniform, mean forward-velocity would exist. Although turbulence is not generally a completely random process, a theoretical determination of the degree of correlation between successive states of flow and between adjacent regions of the flow pattern is a difficult problem and simple descriptive equations do not presently exist for typical precipitator geometries. At the present, for purposes of modeling, it appears practical and plausible to assume that the turbulence is highly random. For particles larger than 10 μm diameter, the turbulence does not dominate the motion of these particles due to their relatively high migration velocities. Under these conditions, Equation 2 would be expected to under-predict collection efficiencies. The practical effect in modeling precipitator performance will be slight, however, since even Equation 2 predicts collection efficiencies greater than 99.6% for 10 μm diameter particles at relatively low values of current density and collection area [i.e., a current density of 10 nA/cm^2 and a collection area to volume flow ratio of 39.4 $m^2/(m^3/sec)$].

Removal of Collected Material

In dry collection, the removal of the precipitated material from the collection plates and subsequent conveyance of the material away from the precipitator represent fundamental steps in the collection process. These steps are fundamental because collected material must be removed from the precipitator and because the buildup of excessively thick layers on the plates must be prevented in order to ensure optimum electrical operating conditions. Material which has been precipitated on the collection plates is usually dislodged by mechanical jarring or vibration of the plates, a process called rapping. The dislodged material falls under the influence of gravity into hoppers located below the plates and is subsequently removed from the precipitator.

The effect of rapping on the collection process is determined primarily by the intensity and frequency of the force applied to the plates. Ideally, the rapping intensity must be large enough to remove a significant fraction of the collected material but not so large as to propel material back into the main gas stream. The rapping frequency must be adjusted so that a larger thickness which is easy to remove and does not significantly degrade the electrical conditions is reached between raps. In practice, the optimum rapping intensity and frequency must be determined by experimentation. With perfect rapping, the sheet of collected material would not reentrain, but would migrate down the collection plate in a stick/slip mode, sticking by the electrical holding forces and slipping when released by the rapping forces.

DESCRIPTION OF THE MATHEMATICAL MODEL

Ideal Calculation of Particle Collection Efficiency

The mathematical model uses the exponential-type relationship given in Equation 2 to predict the collection fraction, $\eta_{i,j}$ for the i-th particle size in the j-th increment of length of the precipitator. Thus, Equation 2 is applied in the form:

$$\eta_{i,j} = 1 - \exp\left(-w_{i,j} A_j/Q\right) , \qquad (3)$$

where $w_{i,j}$ (m/sec) is the migration velocity of the i-th particle size in the j-th increment of length, A_j (m^2) is the collection plate area in the j-th increment of length, and Q is the gas volume flow rate (m^3/sec).

In order to determine the migration velocities for use in Equation 3, the electrical conditions and the particle charging process must be modeled. The electrical conditions are calculated by a technique developed by McDonald et al.[15] In this numerical technique, the appropriate partial differential equations which describe the electrodynamic field are solved simultaneously and subject to the boundary conditions existing in a wire-plate geometry. The procedure yields the voltage-current curve for a given wire-plate geometry and determines the electric potential and electric field distributions for each point on the curve. The effect of "particulate space charge" on the electrical conditions is estimated by using an "effective mobility" which is determined by reducing the ionic mobility by an appropriate factor.[16] Comparisons of the predictions of this technique with available experimental data show that the agreement is within 15%.

Particle charge is calculated from a unipolar, ionic-charging theory formulated by Smith and McDonald.[17] In this theory, particle charge is predicted as a function of particle diameter, exposure time, and electrical conditions. The theory accounts simultaneously for the effects of field and thermal charging and accounts for the effect of the applied electric field on the thermal charging process. The agreement between the results predicted by the theory and experimental data for cases where electron-charging can be ignored is within 25% over the entire range of data which are available and is within 15% for practical charging times in precipitators. The theory agrees well with experimental data on the charging of fine particles where particle charging is difficult to describe physically and mathematically.

The collection fraction (fractional efficiency) η_i for a given particle size over the entire length of the precipitator is determined from

$$\eta_i = \frac{\sum_j \eta_{i,j} N_{i,j}}{N_{i,1}} , \qquad (4)$$

where $N_{i,j}$ is the number of particles of the i-th particle size per cubic meter of gas entering the j-th increment. The quantity $N_{i,j}$ can be written in the form:

$$N_{i,j} = N_{i,j-1} \exp \left(^{-}w_{i,j-1} A_{j-1}/Q\right) , \qquad (5)$$

where $N_{i,1} = N_{i,o}$, the number of particles of the i-th particle size per cubic meter of gas in the inlet size distribution which is expressed in the form of a histogram.

The overall mass collection efficiency η for the entire polydisperse aerosol is obtained from:

$$\eta = \sum_i \eta_i P_i , \qquad (6)$$

where P_i is the percentage by mass of the i-th particle size in the inlet size distribution.

Methods for Estimating Nonideal Effects

In the preceding section, a basis for calculating ideal collection efficiencies has been developed. In this section, the nonidealities which exist in full-scale electrostatic precipitators will be discussed and calculation procedures for estimating the effects on predicted collection efficiencies will be briefly described. The nonideal effects of major importance are: (1) gas velocity distribution, (2) gas sneakage, and (3) particle reentrainment.

Nonidealities will reduce the ideal collection efficiency that may be achieved for a precipitator operating with a given specific collecting area. Since the model is structured around an exponential-type equation for individual particle sizes, it is convenient to represent the effect of the nonidealities in the model as correction factors which apply to the exponential argument. These correction factors are used as divisors for the ideally calculated migration velocities. The resulting "apparent" migration velocities are empirical quantities only and should not be interpreted as an actual reduction in the migration velocities in the region of space adjacent to the collection electrode.

Although it is widely known that a poor velocity distribution results in a lower than anticipated efficiency, it is difficult to formulate a mathematical description for gas flow quality. White[18] discusses nonuniform gas flow and suggests corrective actions. Preszler and Lajos[19] assign a figure-of-merit based upon the relative kinetic energy of the actual velocity distribution compared to the kinetic energy of the average velocity. This figure-of-merit provides a measure of how difficult it may be to rectify the velocity distribution but not necessarily a measure of how much the precipitator performance would be degraded.

It is possible to develop an approach to estimating the degradation of performance due to a nonuniform velocity distribution based upon the velocity distribution, the ideal collection efficiencies, and the exponential-type collection equation.[5] In this approach, it is assumed that Equation 2 applies to each particle size with a known migration velocity and that the specific collecting area and size of the precipitator are fixed.

For any practical velocity distribution and efficiency, the mean penetration obtained by summation over the point values of velocity will be higher than the penetration calculated from the average velocity. If a migration velocity for a given particle size is calculated based upon the mean penetration and Equation 2, the resulting migration velocity will have a value lower than the value necessary to obtain the same mean penetration from a summation of point values of penetration. The ratio of the migration velocity determined by the summation of point values of penetration to that determined by Equation 2 is a numerical measure of the performance degradation caused by a nonuniform velocity distribution. An expression for this ratio may be obtained by setting the penetration based on the average velocity equal to the corrected penetration obtained from a summation of the point values of penetration and solving for the required correction factor, which will be a divisor for the migration velocity given in Equation 2.

Whether the correction factor obtained from the above procedure correlates reasonably well with statistical measures of velocity nonuniformity is yet to be established. A limited number of traverse calculations which have been performed seem to indicate a correlation between the correction factor and the normalized standard deviation of the velocity traverse. Based upon a pilot plant study,[19] the following empirical relationship between the correction factor F_i, the normalized standard deviation of the velocity distribution σ_g, and the ideal collection efficiency η_i for the i-th particle size under consideration has been obtained:[5]

$$F_i = 1 + 0.766\ \eta_i \sigma_g^{1.786} + 0.0755\ \sigma_g \ln (1/1-\eta_i). \qquad (7)$$

In simulating the performance of a particular precipitator, the preferred procedure would be to obtain the relationship $[F_i = F_i\ (\eta_i, \sigma_g)]$ between F_i, η_i, and σ_g for the conditions to be simulated from a velocity traverse at the entrance to the precipitator. If this can not be done, Equation 7 can be used, but only in the sense of obtaining a rough estimate of the effects of a given nonuniform velocity distribution.

Gas sneakage occurs when gas bypasses the electrified regions of an electrostatic precipitator by flowing through the hoppers or through the high voltage insulation space. Sneakage can be reduced by frequent baffles which force the gas to return to the main gas passages between the collection plates. If there were no baffles, the percent sneakage would establish the minimum possible penetration because it would be the percent volume having zero collection efficiency. With baffles, the sneakage re-mixes with part of the main flow and then re-bypasses in the next unbaffled region. The limiting penetration due to sneakage will therefore depend on the amount of sneakage gas per section, the degree of re-mixing, and the number of baffled sections.

If the simplifying assumption is made that perfect mixing occurs following each baffled section, then an expression for the penetration P_{N_S} of a given particle size from the last baffled section which is corrected for gas sneakage can be derived[5] in the form

$$P_{N_S} = [S + (1-S)\ (1-\eta_i)^{1/N_S}]^{N_S}\ , \qquad (8)$$

where S is the fractional amount of gas sneakage per baffled section and N_s is the number of baffled sections. Estimations based on Equation 8 indicate that, for high efficiencies, the number of baffled sections should be at least four and the amount of sneakage should be held to a low percentage. With a high percentage of sneakage, even a large number of baffled sections fails to help significantly.

Gas sneakage factors B_i can be defined in the form of divisors for the effective, or length-averaged, migration velocities in the exponential argument of Equation 2. The factors B_i are obtained by taking the ratio of the effective migration velocity w_e under ideal conditions to the "apparent" value w_e' under conditions of gas sneakage so that

$$B_i = \frac{w_e}{w_e'} = \frac{\ln (1-\eta_i)}{\ln P_{N_s}} = \frac{\ln (1-\eta_i)}{N_s \ln [S + (1-S)\ (1-\eta_i)^{1/N_s}]} \quad . \qquad (9)$$

The foregoing estimation of the effects of gas sneakage is a simplification in that the sneakage gas passing the baffles will not necessarily mix perfectly with the main gas flow and the flow pattern of the gas in the bypass zones will not be uniform and constant. Equation 8 has been formulated to help in designing and analyzing precipitators by establishing the order of magnitude of the problem. Considerable experimental data will be required to evaluate the method and establish numerical values of actual sneakage rates.

Particle reentrainment occurs when collected material is dislodged from the collection plates and reenters the main gas stream. This can be caused by several different effects and, in certain cases, can severely reduce the collection efficiency of a precipitator. Causes of particle reentrainment include: (1) the action of the flowing gas stream on the collected particle layer, (2) rapping which propels collected material into the inter-electrode space, (3) sweepage of dust from hoppers caused by poor gas flow conditions, air inleakage into the hoppers, or the boiling effect of rapped material falling into the hoppers, and (4) excessive sparking which dislodges collected material by electrical impulses and disruptions in current, which is necessary to provide the electrical force which holds the material to the collection plate.

Although it is difficult to quantify the complex mechanisms associated with particle reentrainment, the effect of this nonideal condition on precipitator performance can be estimated if some simplifying assumptions are made. If it is assumed that a fixed fraction of the collected material of a given particle size is reentrained and that the fraction does not vary with length through the precipitator, an expression can be derived which is identical in form to that obtained for gas sneakage:[5]

$$P_{N_R} = [R + (1-R)(1-\eta_i)^{1/N_R}]^{N_R} \quad , \tag{10}$$

where P_{N_R} is the penetration of a given particle size corrected for reentrainment, R is the fraction of material reentrained, and N_R is the number of stages over which reentrainment is assumed to occur.

Since Equations 8 and 10 are of the same form, the effect of particle reentrainment can be expected to be similar to the effect of gas sneakage, provided that a constant fraction of the material is reentrained in each stage. It is doubtful that such a condition exists, since precipitators frequently use different rapping programs on different sections, agglomeration occurs during collection, different holding forces and spark rates exist in different sections, and the gas flow pattern changes throughout the precipitator. However, until sufficient data on rapping losses PER SECTION as a function of particle size can be accumulated, Equation 10 may be used to estimate the effect of particle reentrainment on precipitator performance.

Gas sneakage and particle reentrainment effects are estimated in the mathematical model by reducing the ideally calculated migration velocities by combined correction factors B_i'. From input values of the number of stages over which losses are assumed to occur, the B_i' are determined from the ideal collection fraction for each particle size.

In summary, the mathematical model takes into account the nonideal effects of nonuniform gas velocity distribution, gas sneakage, and particle reentrainment by reducing the ideally calculated migration velocities w_i by the correction factors F_i and B_i'. "Apparent" migration velocities w_i' are determined from:

$$w_i' = \frac{w_i}{F_i \cdot B_i'} \quad . \tag{11}$$

Using the w_i', the corrected fractional collection efficiencies are calculated from Equation 2.

EFFECT OF FACTORS INFLUENCING PRECIPITATOR PERFORMANCE

Voltage and Current

Figure 4 shows voltage-current characteristics obtained from measurements taken from a precipitator installed on a copper reverberatory furnace at Plant A. The precipitator has two electrical sections in the direction of gas flow. Power set C drives the inlet section and power sets A and B drive the outlet section. The

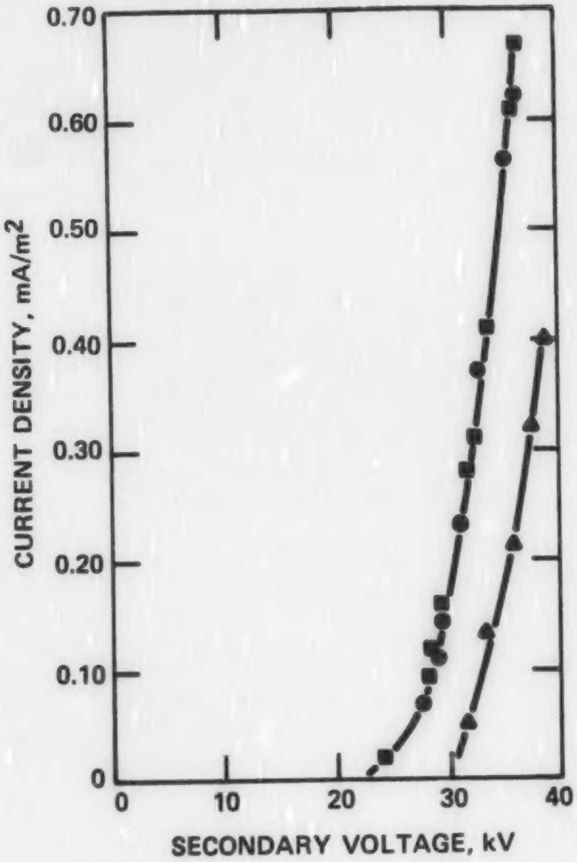

Figure 4. Voltage-current characteristics for Plant A.

effect of the inlet mass loading and particle size distribution is evidenced in the shift of the voltage-current curve to higher currents for a given voltage as particles are removed from the gas stream. The particle size distribution for this installation is shown in Figure 5 up to a particle diameter of 10 μm as determined from measurements made with cascade impactors. Extrapolation of the experimental particle size measurements indicates that the size distribution has a mass median diameter (MMD) of approximately 20 μm and a geometric standard deviation (σ_p) of approximately 3.0. Other pertinent data concerning Plant A are given in Table 1.

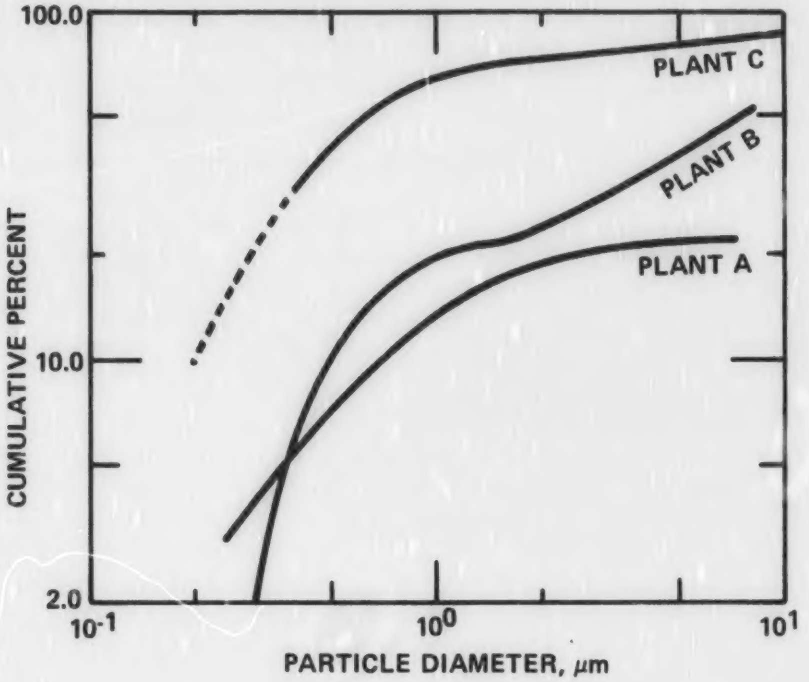

Figure 5. Inlet particle size distributions.

By using the data discussed above and the mathematical model, the relative effect of changes in voltage and current on precipitator performance can be determined. Figure 6 shows a curve for overall mass collection efficiency versus current density as predicted by the model with no corrections for nonideal effects. The curve was obtained by keeping the current densities the same in both electrical sections up to 0.40 mA/m^2 and using an appropriate average value of current density above this value. This curve demonstrates the importance of operating the precipitator at the highest possible values of voltage and current.

Specific Collecting Area

An important parameter which influences the performance of a precipitator is called the specific collecting area (SCA) and is defined as the ratio of the total collection area to the total gas volume flow. In effect, changes in SCA result in changes in the treatment time experienced by the particles. Figure 6 shows the effect of SCA on the overall mass collection efficiency. This curve was generated using the conditions from Plant A. Although the voltage-current characteristics will change with changes

TABLE 1. DATA FOR PRECIPITATORS AT THREE DIFFERENT PLANTS

	Plant A	Plant B	Plant C
Geometry of ESP			
Plate-to-plate spacing (cm)	22.9	25.4	30.5
Wire-to-wire spacing (cm)	22.9	15.2	15.0
Effective wire diameter (cm)	0.268	0.397	0.554
Total plate area (m^2)	3696.0	5049.0	2733.0
Total length (m)	5.49	6.86	5.49
Electrical Operating Conditions			
No. of electrical fields || gas flow	2	3	3
Applied voltage (kV) - 1	38.5	52.0	48.0
- 2	37.5	44.1	48.0
- 3	--	46.1	52.0
Average current density (nA/cm^2) - 1	30.1	9.4	17.0
- 2	61.3	25.3	38.0
- 3	--	29.0	52.0
Gas Conditions			
Average gas velocity (m/sec)	0.92	0.68	0.68
Average gas volume flow (m^3/sec)	70.95	63.1	44.15
Average gas temperature (°K)	616.1	443.9	310.6
Average gas viscosity (10^{-4} poise)	2.8	2.4	1.9
Particulate Conditions			
Inlet mass loading (gm/m^3)	0.32	0.57	0.09
Inlet mass median diameter (μm)	∿20.0	∿8.0	∿0.6
Inlet geometric standard deviation	∿3.0	∿3.0	∿17.0

in SCA, it was assumed that they remained constant as shown in Figure 4 in order to obtain trends.

The SCA provides the most flexible variable in designing a precipitator. It has no physical limitations and can be increased indefinitely. As is also the case with current density, increases in SCA will eventually lead to a leveling off of the efficiency curve due to the exponential nature of the collection mechanism.

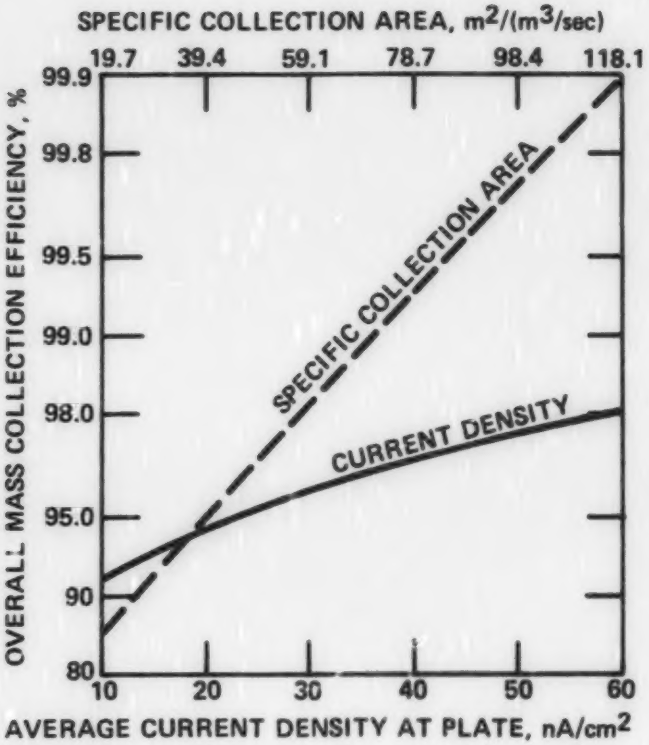

Figure 6. Effects of specific collection area and current density on overall mass collection efficiency.

Particle Size Distribution

The distribution of the various particle sizes entering a precipitator influences the electrical operating conditions and the overall mass collection efficiency. Normally, the distribution of particulate emissions from industrial sources can be approximated by a log normal distribution. This type of distribution can be characterized by the mass median diameter and the geometric standard deviation, and the effect of both parameters on precipitator performance must be considered. The MMD provides a representative size for the distribution and σ_p provides a measure of the dispersion of the distribution.

Figure 7 shows the effects that particle size distribution can have on precipitator performance. These curves were generated using the conditions for Plant A. Although the particle size distribution will influence the voltage-current characteristics, it was assumed that they remained constant as shown in Figure 4

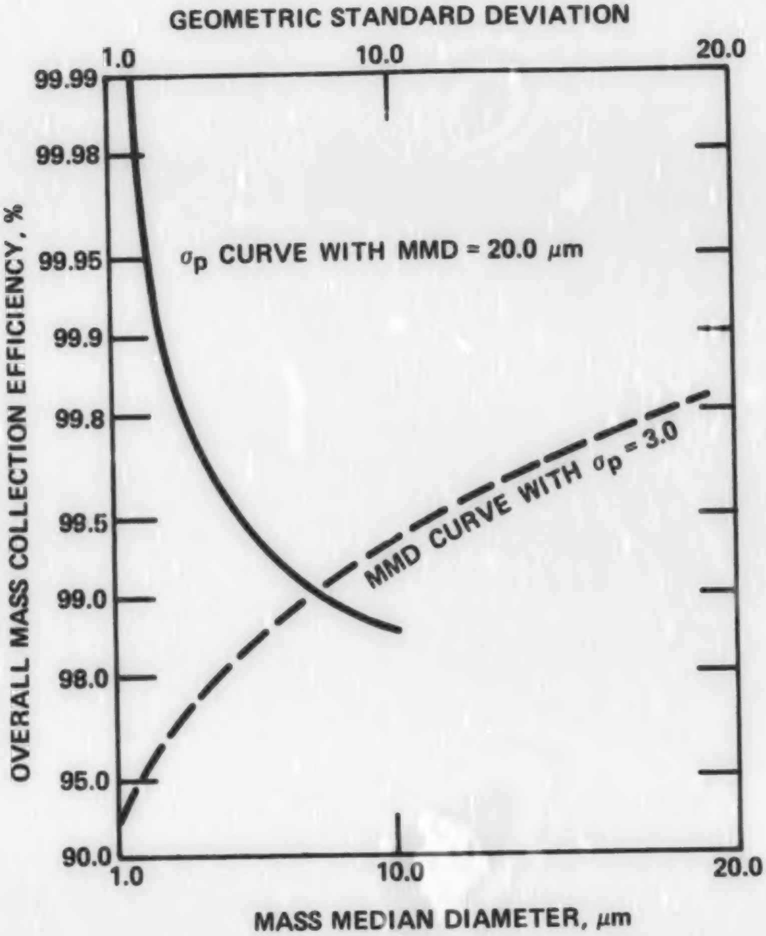

Figure 7. Effect of particle size distribution on overall mass collection efficiency.

in order to obtain trends. The curves were obtained by varying the MMD and keeping σ_p fixed at 3.0 in one case and varying σ_p and keeping the MMD fixed at 20.0 μm in the other case. The results show that, in general, precipitator performance will increase with increasing values of MMD. However, even with a relatively large MMD of 20.0 μm, precipitator performance can be significantly reduced for large values of σ_p.

Resistivity

In many instances, the useful operating current density in a precipitator is limited by the resistivity of the collected particulate layer. If the resistivity of the collected particulate layer is sufficiently high, dielectric breakdown of the layer will occur at a value of current density which in most cases is undesirably low. Depending on the applied voltage, the breakdown of the collected particulate layer will result in either a condition of sparking or the formation of stable back corona from points on the particulate layer. Excessive sparking and back corona are detrimental to precipitator performance and should be avoided.

Figure 8 shows an experimentally determined relationship between maximum allowable current density and resistivity.[20] It points out the severe drop in current density as the resistivity increases over the range 0.5 - 5 x 10^{11} ohm-cm. Figure 9 shows the effect of resistivity on overall mass collection efficiency. The curve in Figure 9 was generated by using the conditions for Plant A and Figure 8. The curve shows that the performance of a precipitator is very sensitive to the value of resistivity.

Nonideal Effects

The effects on precipitator performance of nonuniform gas velocity distribution, gas sneakage, and particle reentrainment are shown in Figure 10. The curve of overall mass collection efficiency versus the normalized standard deviation of the gas velocity distribution was generated using the conditions for Plant A, Equation 7, and assuming no gas sneakage or particle reentrainment. The curve of overall mass collection efficiency versus gas sneakage or particle reentrainment or a combination of both was generated using the conditions for Plant A, Equation 9, and $\sigma_g = 0.25$.

The curves shown in Figure 10 point out the importance of careful mechanical design and optimization of gas flows and rapping programs. Nonideal effects can seriously degrade the performance of a precipitator and must be minimized in order to obtain high collection efficiencies.

COMPARISON OF MODEL PREDICTIONS WITH FIELD TEST DATA

At present, only a very limited amount of data from the nonferrous metals industry is available in a form which can be comprehensively compared with the predictions of the mathematical model. Since the existing data represent first experiences in extensive field testing to characterize precipitator performance in this industry, the data were obtained at times under unexpected

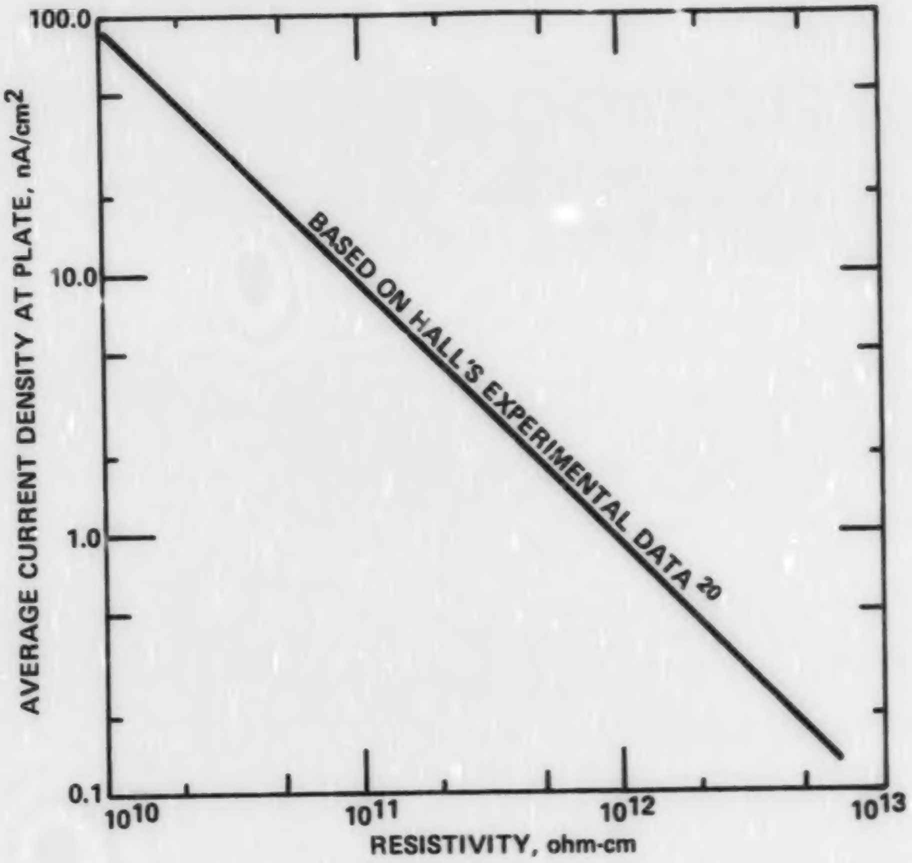

Figure 8. Experimentally determined effect of resistivity on allowable current density in a precipitator.

conditions which could prejudice the results. Unavailability of representative sampling ports, clogging of impactors, impactor leaks, inadequate sampling times, changes in fuel in the process from which the emissions occur, and the possible formation of condensibles within the precipitator are some of the unexpected conditions which have influenced the data and make interpretation of the results difficult. Thus, comparisons of model predictions with existing field test data may not be conclusive.

Table 1 contains data which were obtained for full-scale precipitators located at three different plants. Figure 5 shows the measured inlet size distributions at these installations. Plants A and B had a dry precipitator installed on a copper

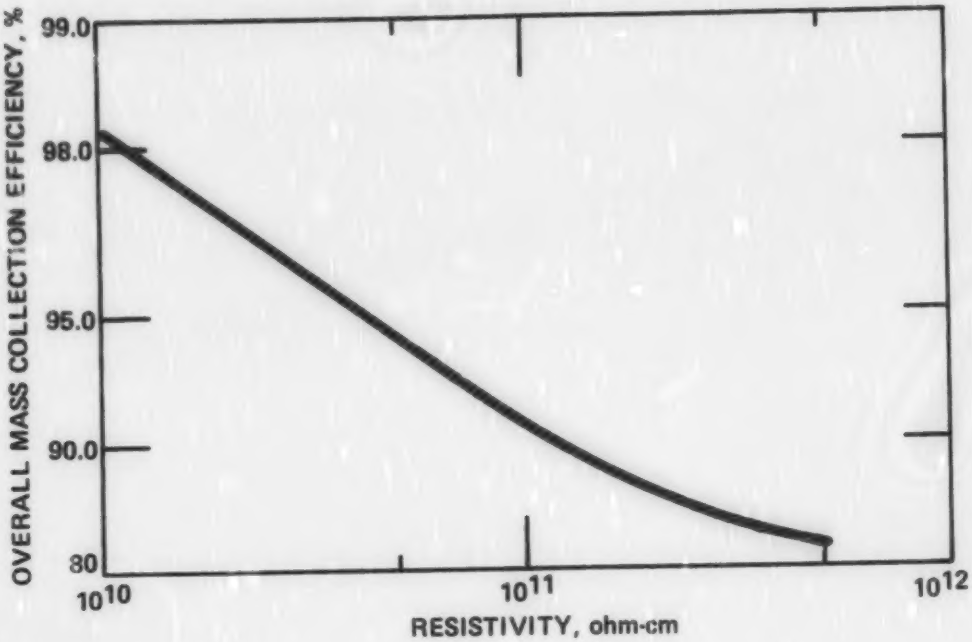

Figure 9. Effect of resistivity on overall mass collection efficiency.

reverberatory furnace and the inlet particle size distributions were measured by using modified Brink cascade impactors. Plant C had a wet precipitator collecting fume from an aluminum pot line and the inlet particle size distributions were measured by using Andersen cascade impactors. Overall mass collection efficiencies were obtained from inlet and outlet mass train measurements. The data in Table 1 and Figure 4 were used in the model simulations.

Figures 11, 12, and 13 show theoretically calculated and experimentally measured fractional efficiencies for Plants A, B, and C. The theoretical curves have not been corrected for nonideal effects. In making comparisons, it is seen that the trend is for the theory to predict efficiencies below the measured values for a portion of the fine particle size range and to predict efficiencies well above the measured values for the larger particles. The agreement can be increased for the larger particles by taking into account nonideal effects which would lower the theoretical efficiencies. However, for the fine particle size range, the lack of agreement must be attributed to certain fundamental mechanisms which are presently either inadequately modeled or unmodeled. Some of these mechanisms include the

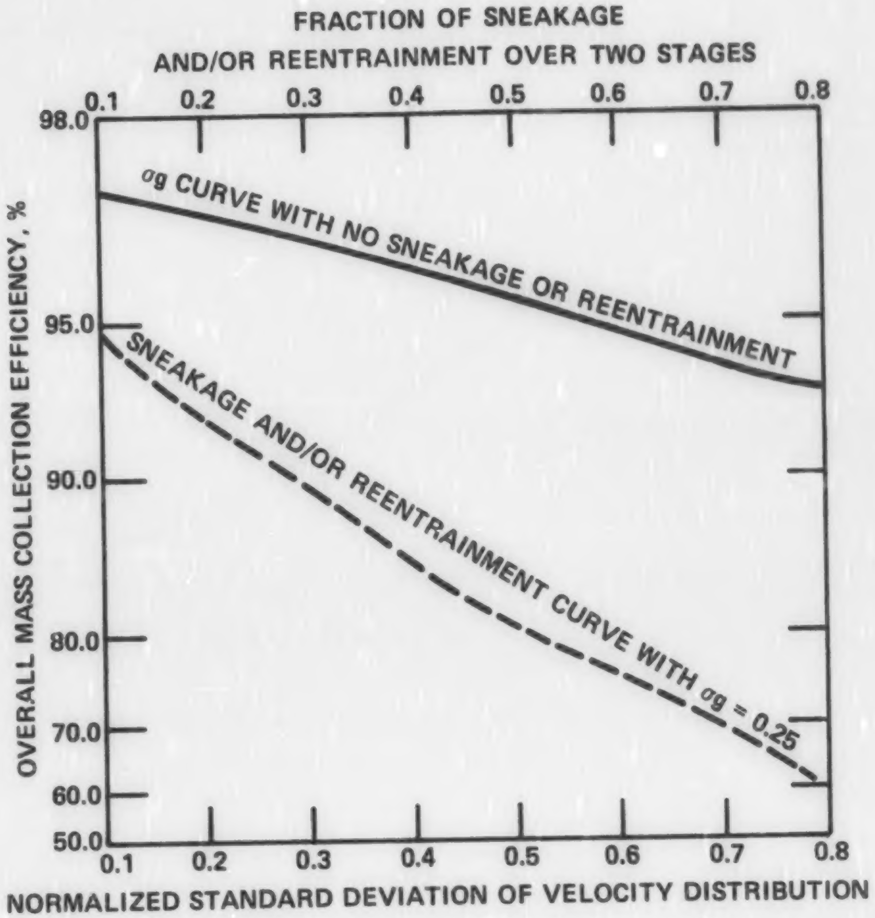

Figure 10. Effects of nonideal conditions on overall mass collection efficiency.

effects of the flow field, particle concentration gradients, and particle charging near corona wires. Research programs are in progress to better describe these mechanisms which are difficult to treat mathematically. Due to compensating effects, the overall mass collection efficiencies predicted by the model for Plants A, B, and C of 96.8, 91.3, and 98.9%, respectively, show better agreement with the measured values of 96.7, 90.0, and 98.0%, respectively.

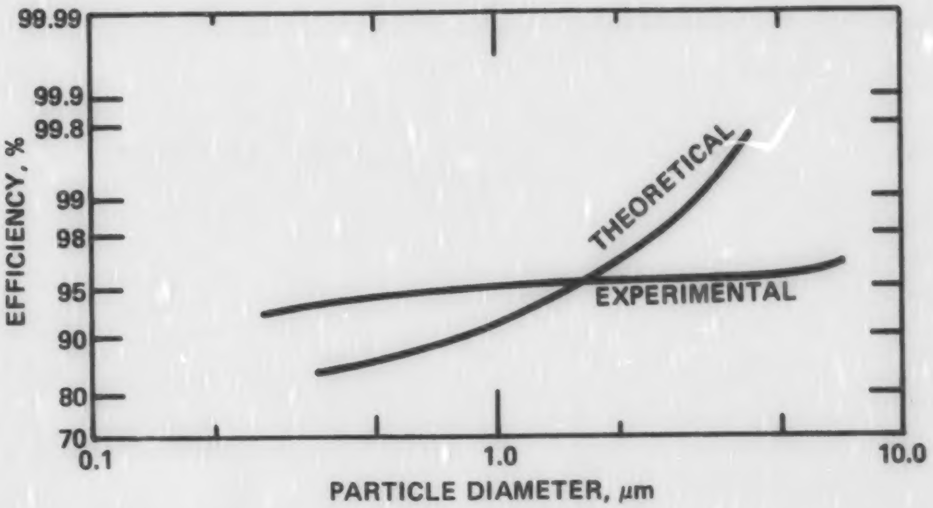

Figure 11. Theoretical and experimental fractional efficiencies for Plant A.

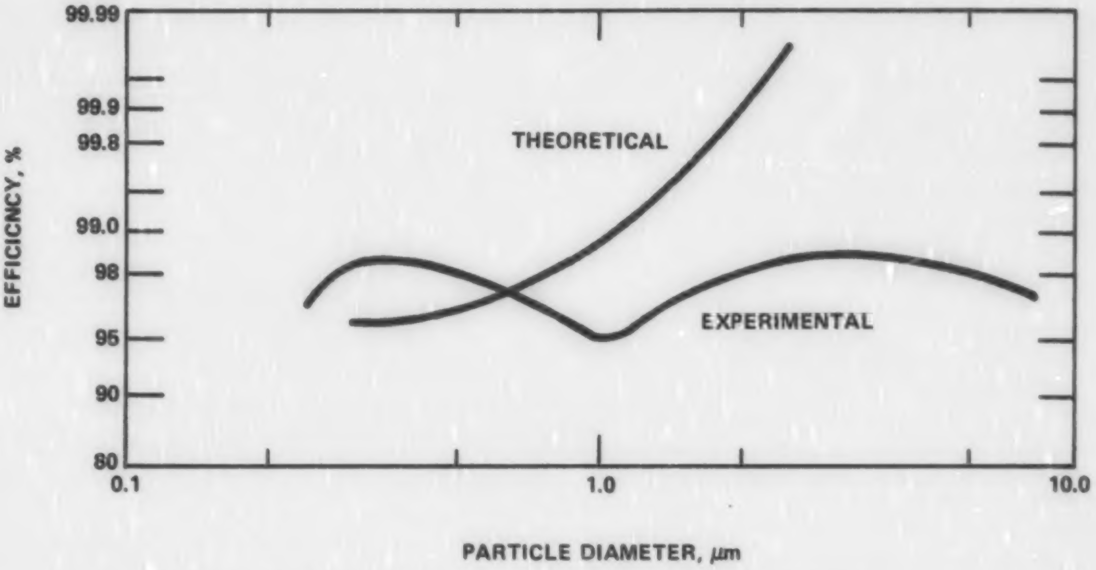

Figure 12. Theoretical and experimental fractional efficiencies for Plant B.

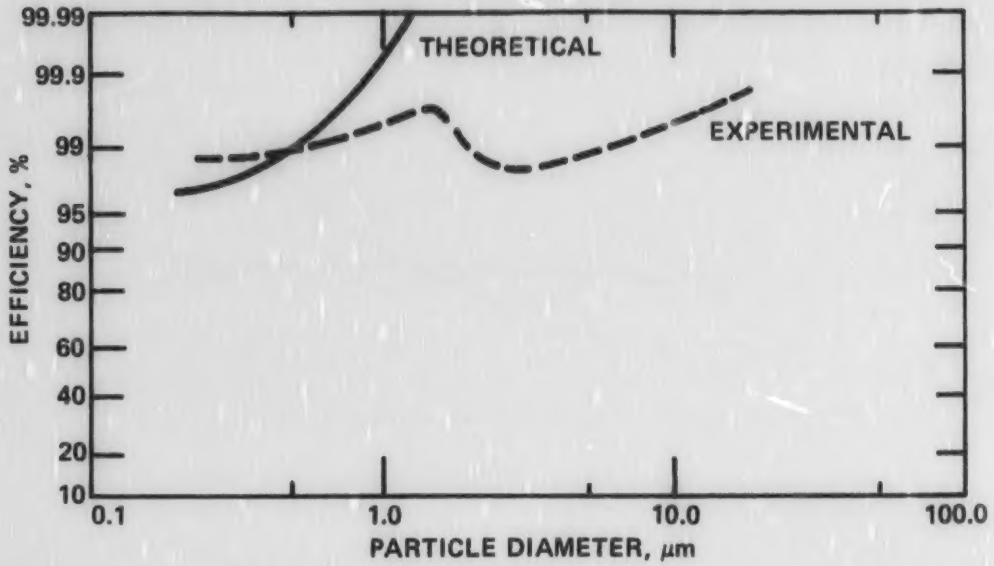

Figure 13. Theoretical and experimental fractional efficiencies for Plant C.

CONCLUSIONS

In its present form, the mathematical model for electrostatic precipitation provides a basis for indicating performance trends caused by changes in specific collecting area, electrical conditions, and particle size distribution. Current density, applied voltage, and particle size distribution are the most important variables in the calculation of particle collection efficiencies for a given specific collecting area. Procedures, based on simplifying assumptions, can be used to estimate the effects of nonuniform gas flow, gas sneakage, and particle reentrainment.

Comparisons of model predictions with field data obtained from full-scale precipitators collecting emissions from nonferrous metallurgical processes show that the theoretical fine particle collection efficiencies are less than the measured values. This discrepancy must be attributed to certain fundamental mechanisms which are presently either inadequately modeled or unmodeled. Some of these mechanisms include the effect of the flow field, particle concentration gradients, and particle charging near corona wires.

REFERENCES

1. Oglesby, S., Jr., and G.B. Nichols. A Manual of Electrostatic Precipitator Technology: Part II, Application Areas. APTD 0611, National Air Pollution Control Administration, Cincinnati, OH, 1970. NTIS PB 196381. pp. 324-345.

2. White, H.J. Industrial Electrostatic Precipitation. Addison-Wesley, Reading, MA, 1963. pp. 10-27.

3. Danielson, J.A. Air Pollution Engineering Manual. 2nd ed., Air Pollution Technical Information Center, U.S. Environmental Protection Agency, Research Triangle Park, NC, 1973. NTIS PB 225132/OAS. p. 138.

4. White, H.J. Reference 2, pp. 1-2.

5. Gooch, J.P., J.R. McDonald, and S. Oglesby, Jr. A Mathematical Model of Electrostatic Precipitation. EPA-650/2-75-037, U.S. Environmental Protection Agency, Research Triangle Park, NC, 1975. NTIS PB 246188/AS.

6. Gooch, J.P., and J.R. McDonald. Mathematical Modelling of Fine Particle Collection by Electrostatic Precipitation. AIChE 1976 Air Symposium Volume (to be published).

7. Gooch, J.P., and J.R. McDonald. Mathematical Modelling of Fine Particle Collection by Electrostatic Precipitation. In: Conference on Particulate Collection Problems in Converting to Low Sulfur Coals. EPA-600/7-76-016, U.S. Environmental Protection Agency, Research Triangle Park, NC, 1976. NTIS PB 260498/AS.

8. Pauthenier, M., and M. Moreau-Hanot. Charging of Spherical Particles in an Ionizing Field. J. Phys. Radium [7] 3:590-613, 1932.

9 White, H.J. Particle Charging in Electrostatic Precipitation. Trans. Amer. Inst. Elec. Eng. Part 1 70:1186-1191, 1951.

10. Hewitt, G.W. The Charging of Small Particles for Electrostatic Precipitation. Trans. Amer. Inst. Elec. Eng. Part 1 76:300-306, 1957.

11. White, H.J. Reference 2, p. 157.

12. Fuchs, N.A. The Mechanics of Aerosols. Macmillan, New York, 1964. Chap. 2.

13. White, H.J. Reference 2, pp. 166-170.

14. White, H.J. Reference 2, pp. 185-190.

15. McDonald, J.R., W.B. Smith, H.W. Spencer, and L.E. Sparks. A Mathematical Model for Calculating Electrical Conditions in Wire-Duct Electrostatic Precipitation Devices. J. Appl. Phys. 48(6):2231-2246, 1977.

16. Oglesby, S., and G.B. Nichols. A Manual of Electrostatic Precipitator Technology: Part I, Fundamentals. APTD 0610, National Air Pollution Control Administration, Cincinnati, OH, 1970. NTIS PB 196380. pp. 57-66.

17. Smith, W.B., and J.R. McDonald. Development of a Theory for the Charging of Particles by Unipolar Ions. J. Aerosol Sci. 7:151-166, 1976.

18. White, H.J. Reference 2, pp. 238-293.

19. Preszler, L., and T. Lajos. Uniformity of the Velocity Distribution Upon Entry into an Electrostatic Precipitator of a Flowing Gas. Staub Reinhalt. Luft (in English) 32(11):1-7, 1972.

20. Hall, H.J. Trends in Electrical Energization of Electrostatic Precipitators. Presented at Electrostatic Precipitator Sympos., Birmingham, Alabama, Paper I-C, February 23-25, 1971.

PAPER 6

STUDIES OF PARTICLE REENTRAINMENT RESULTING FROM ELECTRODE RAPPING

JOHN P. GOOCH
SOUTHERN RESEARCH INSTITUTE

AND

WALTER PIULLE
ELECTRIC POWER RESEARCH INSTITUTE

INTRODUCTION

Collection of particulate matter by the electrostatic precipitation process consists of three separate operations: (1) particle charging, (2) particle collection, and (3) removal and disposal of the collected material. In ideal circumstances, all material collected on the grounded electrodes would be transported to a collection hopper without reentrainment into the gas stream. While this ideal situation is approached in the collection of liquid particles, the process of removing dry particulate from collecting electrodes is usually accompanied by a significant re-introduction of the collected material into the flue gas. This paper discussed particle reentrainment caused by rapping of the collection electrodes in conventional wire-plate electrostatic precipitators.

The purpose of an electrode rapping system is to provide an acceleration to the electrode which is sufficient to generate inertial forces in the collected dust layer that will overcome those forces holding the dust to the electrode. A successfully designed rapping system must provide a proper balance between electrode cleaning and minimizing emissions resulting from rapping reentrainment. As part of an overall program to gain a better understanding of the electrostatic precipitation process, measurements with the objective of quantifying and size-characterizing losses due to electrode rapping have been conducted on one pilot scale and several full-scale electrostatic precipitators. Although these measurement programs were conducted with fly ash produced from coal combustion, the results allow an examination of the qualitative effects of rapping reentrainment on overall and fractional collection efficiency, and thus are of interest in the electrostatic collection of other dusts with differing properties.

BACKGROUND

Dust Layer Behavior

Forces which hold precipitated particles to collection electrodes and adjacent particles are complex and can be influenced by a number of variables. The dust layer as a whole is held to the collection surface by electrical forces and by cohesive and van der Waals forces between the collection plate and the particles comprising the dust layer. Penney and Klingler[1] have studied the electrical forces holding the dust layer, and have presented the following relationship concerning the electrostatic force which acts upon the dust layer as a whole:

$$F = \tfrac{1}{2}\varepsilon_0 \left[E^2 - \left(\frac{j\rho\varepsilon_1}{\varepsilon_0} \right)^2 \right]$$

where

F = force per unit area (a positive force pulls the dust from the electrode)

ε_0 = permittivity of free space

ε_1 = permittivity of dust layer

ρ = resistivity of dust

E = potential gradient in the gas adjacent to the dust surface

In most practical applications, the electrical forces are in the direction that forces the dust layer on to the collection surface. In the case of low resistivity dusts, however, negative forces can develop, as indicated in Figure 1.

Tassicker[2] has developed an elemental theory of dust removal which considers only the tensile strength of the dust layer and the acceleration normal to the plate. This relationship states that the dust layer will be removed when

$$a > \frac{P}{\delta \ell} = \frac{P}{M/A}$$

where

a = acceleration normal to the plate

P = tensile strength of the dust layer

δ = bulk density of the dust

ℓ = dust layer thickness

M/A = mass per unit area

Thus, the acceleration must be greater than the ratio of dust layer tensile strength to the mass per unit area. The effect of time interval between raps is indicated by consideration of the relationship between mass per unit area and the collection time

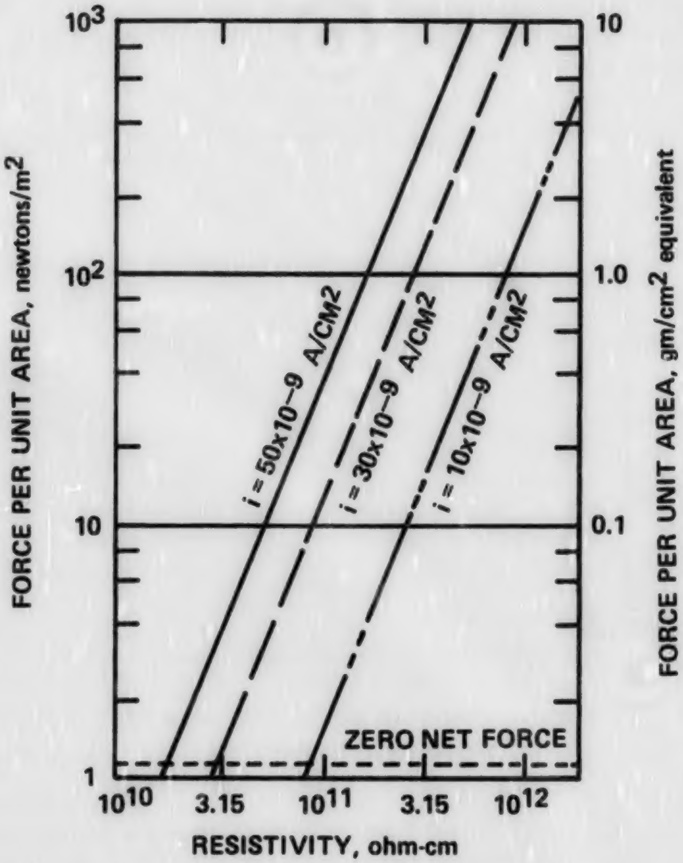

Figure 1. Relationship between the electrical attractive force and resistivity of the dust layer for a range of current densities.

between raps. As collection time between raps is increased, the mass per unit area is increased, and the acceleration required for removal is decreased.

Sproull[3] has conducted a series of experiments which illustrate the effect of dust composition, corona forces, accelerations, and temperature on the removal of dust layers from collection electrodes. Figure 2 presents some of Sproull's data to illustrate the relative effects of these parameters as a function of the maximum shear acceleration of the collecting electrodes in multiples of "g". A comparison of these curves indicates that, under the conditions of the experiments, the cement dust was more difficult to remove than fly ash, even though the particle size distributions of the two dusts were similar, presumably as a result of differences in composition. It is also clear that the electrical holding force was acting to retain the dusts on the collection electrode surface. Similar data were obtained for acceleration perpendicular to the electrode plate produced by a "normal" rap. Lower values of acceleration were required for removal of difficult to remove dust with normal rapping than was the case for shear rapping.

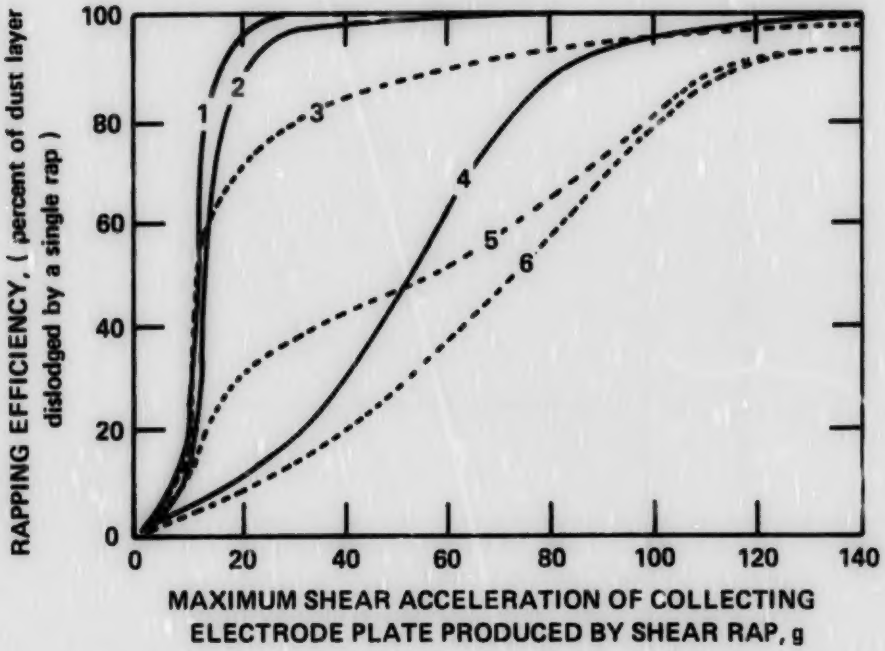

Figure 2. Shear (parallel) rapping efficiency for various precipitated dust layers having about 0.2 grams of dust per square inch as a function of maximum acceleration in multiples of "g". Curve (1) fly ash, 70 to 300°F, power off. Curve (2) fly ash, 300°F, power on. Curve (3) cement kiln feed, 70°F, power off. Curve (4) cement kiln feed, 200 or 300°F, power on. Curve (5) fly ash, 70°F, power on. Curve (6) cement kiln feed, 70°F, power on.

Figure 3 (also from Sproull) illustrates the effect of temperature on the removal efficiency of a precipitated layer of copper ore reverberatory furnace dust. These data indicate that the net holding force on the dust layer decreases with increasing temperature until softening or partial melting occurs, excluding the cases in which the dust temperature falls below the dew point of the surrounding gases.

Particle reentrainment is influenced by factors concerning the design and operation of the precipitator as well as the physical and chemical properties of the dust. White[4] has summarized the particle properties and precipitator design factors which affect reentrainment and these are presented in Figure 4. Although hopper design and ash removal system operation do not influence the manner in which particles are directly reentrained, as a result of rapping, improper operation of the ash removal system can increase emissions through hopper boil-up resulting from rapping or as a result of gas circulation through the hoppers.

Sproull[5] has reported that optimum rapping conditions are achieved when the collected dust layer is permitted to accumulate to a reasonable thickness and then rapped with sufficient intensity

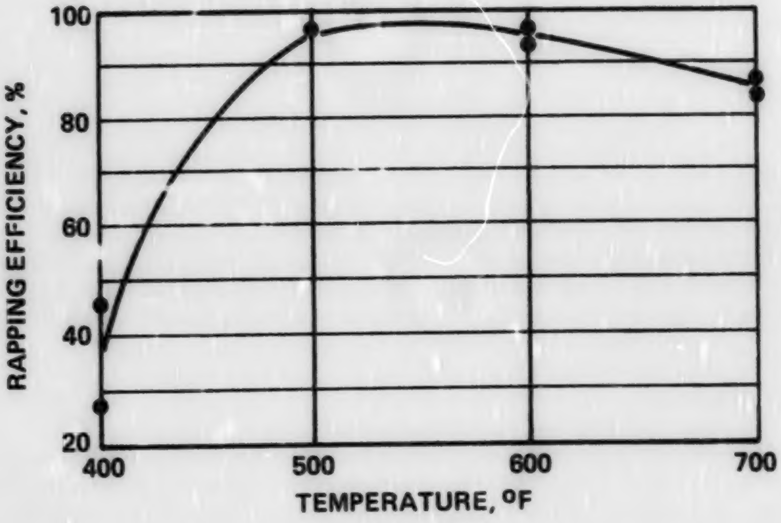

Figure 3. Rapping efficiency for a precipitated layer of copper ore reverberatory furnace dust, rapped with a ballistic pendulum having an energy of 0.11 foot-pound, at various temperatures.

PARTICLE PROPERTIES

1. SIZE DISTRIBUTION
2. SHAPE
3. BULK DENSITY
4. ADSORBED MOISTURE AND OTHER VAPORS
5. ENVIRONMENT–GAS TEMPERATURE AND COMPOSITION
6. RESISTIVITY

PRECIPITATOR FACTORS

1. GAS VELOCITY
2. GAS-FLOW QUALITY
3. COLLECTING ELECTRODE CONFIGURATION AND SIZE
4. ELECTRICAL ENERGIZATION
5. RAPPERS: TYPE, NUMBER, AND AMPLITUDE
6. HOPPER DESIGN
7. AIR IN LEAKAGE INTO HOPPERS OR PRECIPITATOR PROPER
8. DUST REMOVAL SYSTEM DESIGN AND OPERATION
9. SINGLE STAGE OR TWO STAGE

Figure 4. Particle properties and precipitator design factors which affect reentrainment.

to progress down the plate in a slip-stick mode. This procedure has the advantage of resulting in the deposition of only a portion of the dust on the lower portion of the collecting plate into the hoppers at any one time. These circumstances would minimize the disturbance of previously deposited dust since the velocity of the falling layer would be relatively low.

The foregoing considerations illustrate that it is desirable to vary both rapping intensity and rapping interval in order to optimize the performance of a dust removal system. Since the mass rate of dust collection varies with length through a precipitator, it follows that rapping frequency variations between the inlet and exit fields would be expected to yield the best rapping conditions. If a precipitator consists of four fields in the direction of gas flow and exhibits a no-reentrainment efficiency of 99%, the rate of build up in the first field would be about 30 times that in the outlet field, again neglecting reentrainment effects. However, the optimum rapping intervals for these fields would not be expected to correspond to the dust collection rate ratios.

Methods of Rapping

The types of rappers which are employed in industrial precipitators may be classified in two categories: impulse types and vibrator types. The following descriptions include the most commonly employed configurations:[6]

Electromagnetic solenoid single impact--These rappers consist of a plunger which is lifted by energizing the solenoid. On release of the plunger by de-energizing the coil, it falls under the influence of gravity against an anvil which transmits the rap through a rod to the electrodes to be cleaned.

Single impact motor driven cams--The mechanism consists of a motor driven shaft extending horizontally across the precipitator. Cams are located along the shaft which raise small hammers by handles. When the rotating cam reaches the end of its lobe, the hammer swings downward and strikes an anvil located on the end of a single collecting electrode. Rapping control is limited to adjustment of operating time and shaft speed.

Single impact motor driven swing hammers--The mechanism consists of a shaft extending horizontally across the precipitator between banks of collecting electrodes. The shaft is oscillated by a motor driven mechanical linkage, and hammer heads are connected to the shafts by spring leaf arms. The hammers strike anvils attached to the ends of collecting plates near the bottom. The impact can be varied by adjusting the arc of the hammer.

Single impact mechanical rappers--This system consists of a drive shaft extending across the precipitator. The rotation of the shaft actuates swing hammers which fall under gravitational force and strike the support structure of the electrodes.

Air Vibrators--The major components are a reciprocating piston in a sleeve type cylinder. The vibrator assembly is fastened directly to the end of a rapper rod which transmits the rapping energy to the electrodes.

Eccentrically unbalanced motor vibrators--These mechanical vibrators consist of an electric motor with adjustable cam weights mounted on a shaft. When operated, the eccentrically positioned cam weights set the entire assembly into vibration. The motor is mounted directly on the rapper shaft which transmits the generated vibration to the electrodes.

Electromagnetic vibrators--These vibrators consist of a balanced spring-loaded armature suspended between two synchronized electromagnetic coils. When energized, the armature vibrates at line frequency. The vibrating energy is transmitted through a rapper rod to the electrodes.

Previous Work

Spencer[7] has briefly summarized published work concerning rapping emissions and their dependence on certain rapping parameters. By increasing the time interval between raps, Plato[8], Schwartz and Lieberstein[9], and Nichols, Spencer, and McCain[10] have all observed improvements in performance of full-scale precipitators. Sproull[5] conducted a study of rapping on a large fly ash precipitator using a triboelectric meter of the type described by Prochazka (a "Konitest" meter). This device uses electrical charge generation by the particle-surface contact as a measure of particulate concentration. Tests at various rapper intensities and rapping intervals were made to adjust the precipitator for optimum conditions. The results indicated rapping intervals should be adjusted for the installation under study such that the inlet field is rapped 3 or 4 times as frequently as the third or last field. Sproull concluded that, contrary to the results of the investigations previously mentioned, that overall rapping emissions could be reduced by lessening the rap intervals for this particular installation. Sproull also found that reducing the rapping intensity was beneficial in reducing rapping emissions.

Francis[11] has developed an expression which gives the penetration of a given particle size as a function of the no-reentrainment efficiency and the number of stages over which the reentrainment is assumed to occur. This expression is based on the assumptions that (1) a constant fraction of the particle size under consideration collected in each section would be reentrained in each successive section, and (2) the reentrained material is perfectly mixed in the gas stream following rapping. While these assumptions are unlikely to be accurate in most circumstances, the expression is of interest in that it indicates the qualitative effects of sectionalization and reentrainment on collection efficiency. The development of the expression is as follows:

Let R = fraction of mass of a given particle size that is reentrained

η = collection fraction of a given particle size obtained with no reentrainment for total collection area

η_j = collection fraction per section for a given particle size

$= 1 - (1-\eta)^{1/N_R}$

N_R = number of stages over which the reentrainment is assumed to occur

P_j = penetration from section j

Then the penetration from section 1 is given by

$$P_1 = R\eta_j + 1-\eta_j$$

and from section 2

$$P_2 = R\eta_j P_1 + (1-\eta_j)\, P_1$$

$$= P_1[R\eta_j + (1-\eta_j)]$$

$$= [R\eta_j + (1-\eta_j)]^2$$

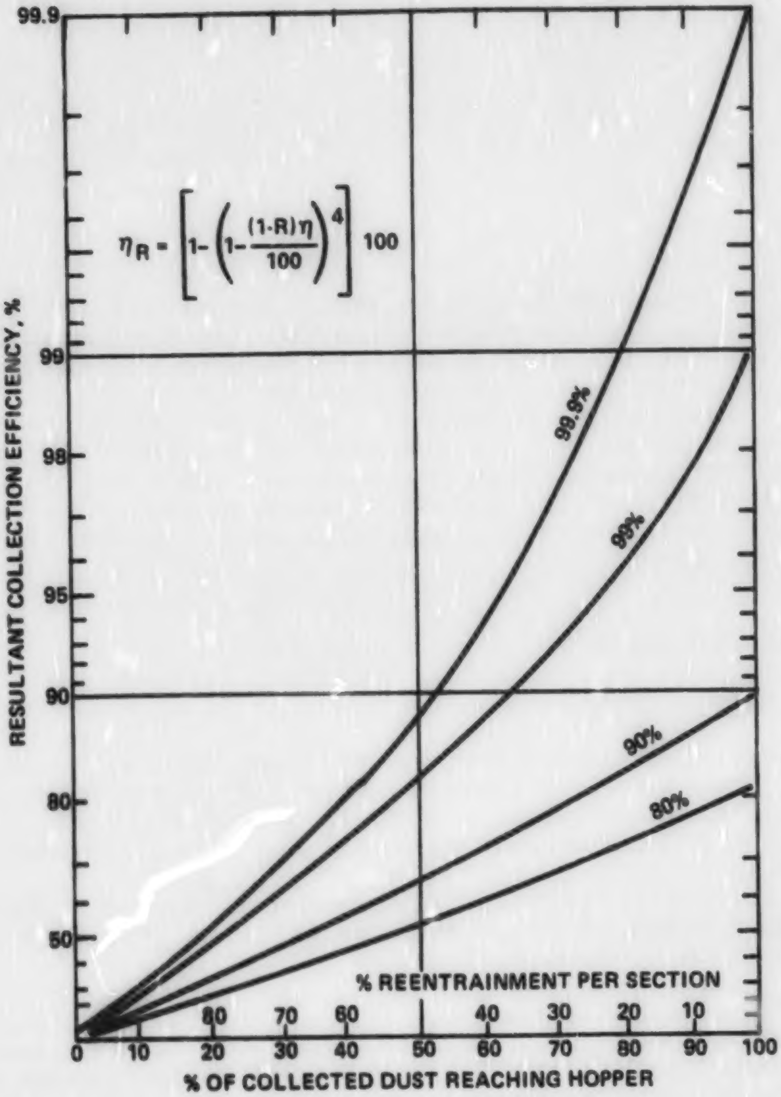

Figure 5. Effect of reentrainment on the efficiency of a four-section precipitator designed for a no-reentrainment efficiency as indicated for a monodisperse particulate.

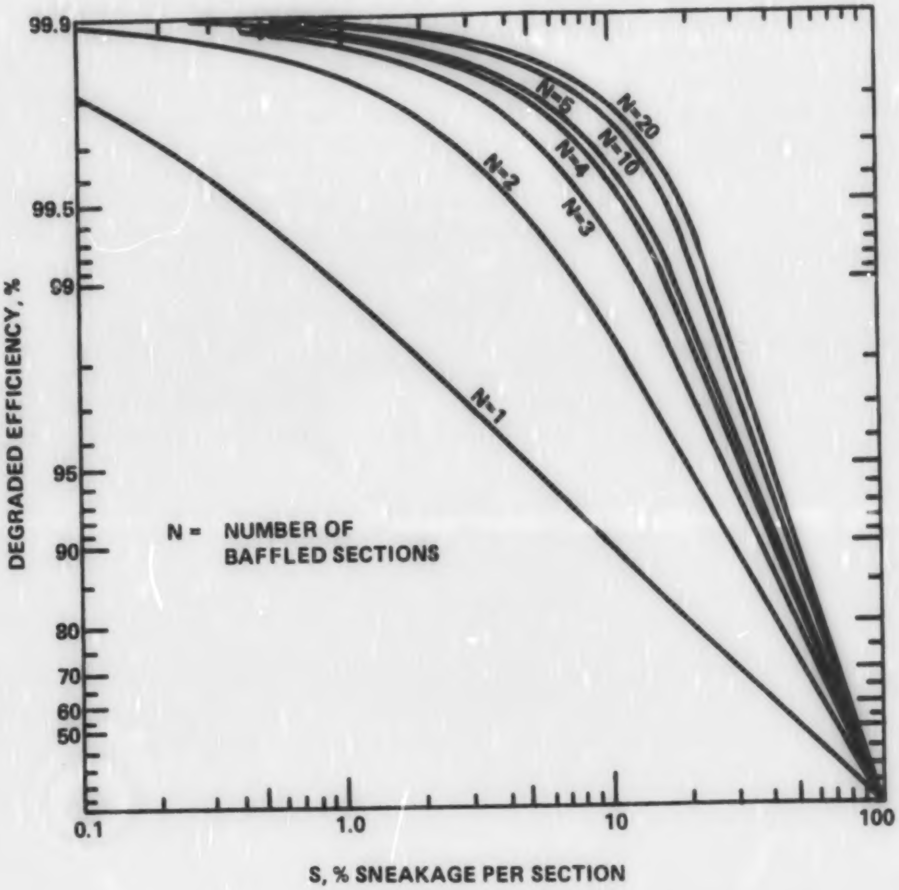

Figure 6. Degradation from 99.9% efficiency with reentrainment.

were about 1 meter from the plane of the outlet baffles, and only one lane of the precipitator was sampled. Both outlet mass trains were modified to consist of two systems: one of which was used to measure emissions between raps and the other was used to measure emission during raps. Each outlet sampling probe consisted of a 2.5 cm pipe, to the end of which two 47 mm Gelman filters with 1.25 cm nozzles pointed 110° apart were attached. Separate copper tubes were run to each filter from a three-way valve. The valve was used to connect the appropriate filter to the metering box. Sampling rates at each traverse point were based on velocity traverses made prior to the sampling.

One of the two filters on each of the two outlet probes was designated the between rap sampler and the other the rapping puff sampler. After stable conditions were obtained, the between rap sampling systems were started. Before rapping the plates, sampling was discontinued and the probes were rotated so that both nozzles on each probe pointed downstream. The dust feed was turned off, and after a clear flue was obtained, the second filter was rotated into the gas stream. Sampling was resumed and the plates were rapped. When dust had settled, sampling with this second set of filters was discontinued and the nozzles to the filters were again pointed downstream. The dust feed was then turned on and the sampling was resumed again with the between rap system.

Data obtained with the between rap system were handled in the usual manner and were used to calculate steady-state mass emission rates. Data from the second set, or "rap" set of filters were used to calculate emission rates from the rapping puffs independently of the between-rap emissions. These emission rates were calculated from

$$E_p = \frac{M_p A_s N_H}{A_N N_s}$$

where

E_p = emission rate from rapping puffs

M_p = mass collected by the filter while sampling the flue gas during rapping

A_s = cross sectional area of precipitator sampled by the probe

A_N = cross sectional area of nozzle

N_H = number of raps per hour

N_s = number of raps sampled

The emission rates between raps and from raps were combined to obtain the overall hourly emission rate.[7]

For the full-scale precipitator installation one would expect to be able to measure rapping reentrainment simply by obtaining data with either a mass train or an impactor sampling system, with a rapping system energized and subsequently deenergized and then comparing these measurements. However, it was found that during the test program at the first installation (Plant 1) the sensitivity of the electrostatic precipitator to changes in resistivity and other process variables could overshadow the differences in total emissions caused by energizing and deenergizing the rappers. The variation in precipitator performance caused by the resistivity and other process variable changes made it impossible to determine rapping reentrainment losses from a direct comparison of data obtained one day with rappers in the normal mode and rappers deenergized on subsequent days.

In order to minimize this difficulty, a revised sampling strategy was adopted for the remaining installations. This strategy consisted of sampling with mass trains and impactors dedicated to designated "rap" and "no rap" periods. Data with a rapping system energized and deenergized were obtained by traversing selected ports with dedicated sampling systems in subsequent thirty-minute periods on the same day. This procedure, while necessarily distorting the frequency of the rapping program being examined, minimized the effects of resistivity and other process variable changes.

The use of this sampling strategy leads to two possible procedures for calculating the fraction of losses attributable to rapping reentrainment. The first procedure calculates the ratio of emissions obtained with rappers off to rappers on and subtracts it from unity. The emissions data utilized in this procedure were obtained during the time in which alternating sampling periods for rap and no rap sampling trains were employed. The second procedure consisted of subtracting the mass emissions obtained with the rappers deenergized from those of the previous day with normal rapping, and dividing by the emissions obtained with the rappers operating normally. It could be argued that if the alternating on-and-off procedure for sampling did not distort the results obtained, and if there were no other variations in parameters affecting the precipitator performance, that data obtained from the "rap" period should be approximately equal to that obtained during periods in which the rappers were operating in a normal fashion. In this paper we have calculated percentage of rapping emissions using both of these procedures.

Particle Sizing--

Three size selective sampling systems were used in the measurement programs, two of which were real time extractive systems (a large particle system and a fine particle system) while the third (cascade impactors) provided time integrated *in situ* data. The large particle (diameter range 0.6-2.0μm) extractive system was employed only for outlet measurements to provide qualitative information on the relative fractions of the emissions that could be attributed to rapping losses in the precipitator. In addition, this system also provided data on particulate concentration changes with time.

The fine particle system (0.01 μm to 0.3 μm) was employed at both the inlet and outlet of the full-scale precipitators for purposes of providing fractional efficiency data and to give quantitative information on the contribution of rapping, if any, to emissions in this particle size range.

Description of Installations

Pilot Scale Precipitator--

The pilot scale rapping tests were conducted on a nearly full scale pilot precipitator owned and operated by FluiDyne Engineering. Figures 7 and 8 illustrate the features of the test facility. This pilot unit effectively represents one electrical section in a full-scale precipitator. The plate height is 6 meters, and the plate length is 2.7 m. The total collecting area is 167 m^2, and wire to plate spacing is 11 cm. In the original design, the plates were constructed from expanded metal. For this rapping reentrainment study, three of these plates were replaced to provide two lanes with solid plates on each side of the lane. Outlet sampling was confined to the lanes with solid plates. The plate rappers are of the single shot pneumatic type. The rapper weight is supported in a cylinder by low pressure compressed air. When a rap is desired, a signal to a solenoid valve pressurizes the other side of the cylinder and forces a weight down on top of a rod that transmits the force to a plate support beam.

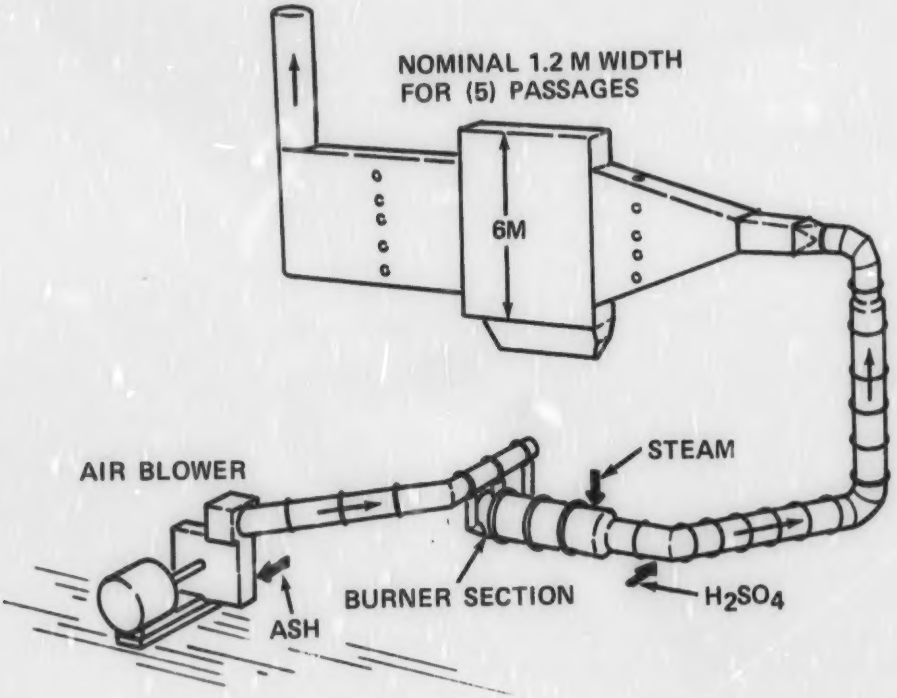

Figure 7. Near full scale pilot precipitator at FluiDyne Engineering.

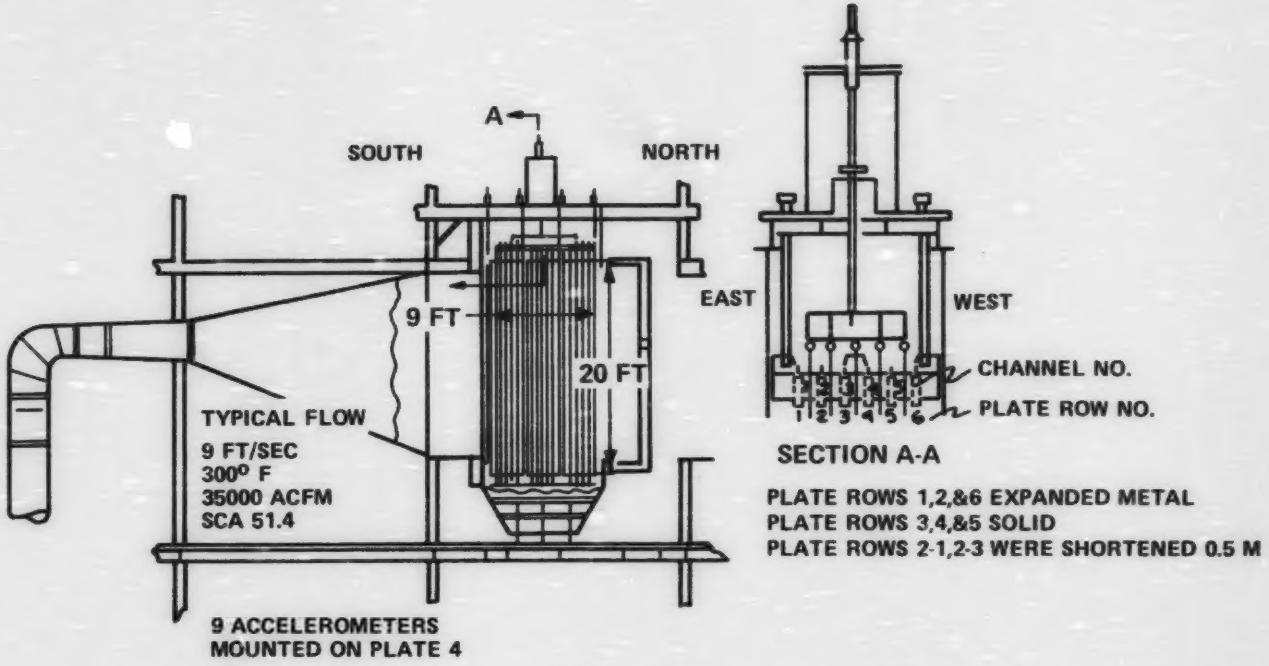
A
SOUTH
NORTH
9 FT
20 FT
EAST
WEST
CHANNEL NO.
PLATE ROW NO.
1 2 3 4 5 6
TYPICAL FLOW
9 FT/SEC
300° F
35000 ACFM
SCA 51.4
9 ACCELEROMETERS
MOUNTED ON PLATE 4
SECTION A-A
PLATE ROWS 1,2,&6 EXPANDED METAL
PLATE ROWS 3,4,&5 SOLID
PLATE ROWS 2-1,2-3 WERE SHORTENED 0.5 M

Figure 8. FluiDyne pilot precipitator.

Dust feed is supplied from a dust dispersion system which has an adjustable feed capability. Three oil burners are available to heat the gas stream to the desired temperature level. A water injection system consisting of three atomization nozzles each with a capacity of eleven liters of water per minute, is available to supply the desired humidity. The water is atomized by compressed air and is vaporized by the burners that heat the system gas flow to the design temperature.

Full-Scale Precipitators--

Plant 1--The first electrostatic precipitator tested under the EPRI program was a retrofit unit manufactured by Lodge-Cottrell Division of Dresser Industries and consists of six fields in the direction of gas flow. The first and second fields each have 57,600 ft^2 of collecting area while the third through the sixth fields have 72,000 ft^2 of collecting area, for a total of 403,200 ft^2. This gives a specific collection area of 504 ft^2/1000 cfm for the design volume of 800,000 acfm. Each field has two double half wave transformer rectifiers. The precipitator has 12 in. plate spacing, operates at approximately 300°F and is connected to the boiler and stack by two inlet and two outlet ducts. A mechanical collector which constituted the previous ash removal system precedes the precipitator. The precipitator employs a drop hammer type of rapping system in which two plates are rapped simultaneously. Under normal operation the first two fields are rapped six times per hour, the third and fourth fields are rapped three times per hour and the fifth and sixth once per hour.

Plant 2--The second cold-side ESP tested was manufactured by SF-Carborundum Company and consists of six physically divided chambers. The test program was conducted on the #5 chamber of the precipitator. Each chamber of the precipitator has 44 lanes and five electrical fields in the direction of gas flow. Each electrical field is 10.5 ft long and has a total collection area of 37,879 ft^2. The precipitator has 9.75 in. plate spacing, and spiral discharge electrodes with a radius of 0.049 in. Tumbling hammers are used to rap both the collecting plates and high voltage discharge frames. The rapping frequencies for the collecting electrodes in the five fields in the direction of gas flow are 10, 5, 5, 2 and 1 per hour, respectively. The precipitator operates at 190 to 250°F and was designed to handle 2.33 million acfm at 250°F, which results in a design specific collection area of 487.6 ft^2/1000 acfm. However, as in the case of Plant 1, the actual measured SCA on the tested chamber was higher than design, i.e., 589 ft^2/1000 acfm.

Plant 3--The hot-side ESP tested was a retrofit Research Cottrell unit which was designed, installed and operated in series with an existing cold-side precipitator. Data for the test series were obtained only on one-half of the hot-side unit. The precipitator is designed with four parallel chambers for gas flow, and separate ducts transport gas to and from the four chambers. A gas-tight partition divides the precipitator into two separate sides, and in each of the two sides, the eight sections are supplied with power from four transformer-rectifier sets in the direction of gas glow. Each chamber contains 39 parallel gas passages, which consist of pairs of plates 30 ft high x 9 ft long for a total length in the direction of gas flow of 36 ft. Plate-to-plate spacing is 9 inches, and the discharge wires are 0.109 inch in diameter.

Total plate area is 336,960 ft^2, and the design gas flow is 1,250,000 acfm, which results in a design-specific collecting area of 270 ft^2 per 1000 acfm. However, total gas flow for the two chambers tested was about 430 kacfm, which resulted in an SCA of approximately 400 ft^2/1000 acfm. This value is in accordance with data published by others for the same installation.[12] The precipitator rapping system employs solenoid activated plate rappers, with each plate rapper activated either once or twice every two minutes.

Results and Discussion

Pilot-Scale Tests--

Table 1 presents a summary of results obtained from the experiments on the Fluidyne Pilot Unit. These results indicate that rapping emissions decreased with increasing time between raps. Figure 9 shows the effect of rapping interval on efficiency. The percentage of the collected dust removed from the collecting electrode also increased with increased time between raps, as Figure 10 illustrates. These results are consistent with the theory of dust removal which indicates that the product of the normal plate acceleration and the dust surface density must be greater than the tensile strength of the layer.

TABLE 1. RESULTS FROM PILOT-SCALE RAPPING EXPERIMENTS

Type of test	Plate acceleration G's x,y,z axis	Rap intervals, min	Gas velocity, m/sec	Avg. plate current density, nA/cm^2	Total penetration, %	Penetration due to rapping reentrainment, %
Rap	11 16 15	12	0.87	23.3	11.4	53
Rap		32			7.6	32
Rap		52			6.1	18
Rap		150			6.9	25
No Rap		--			5.2	--

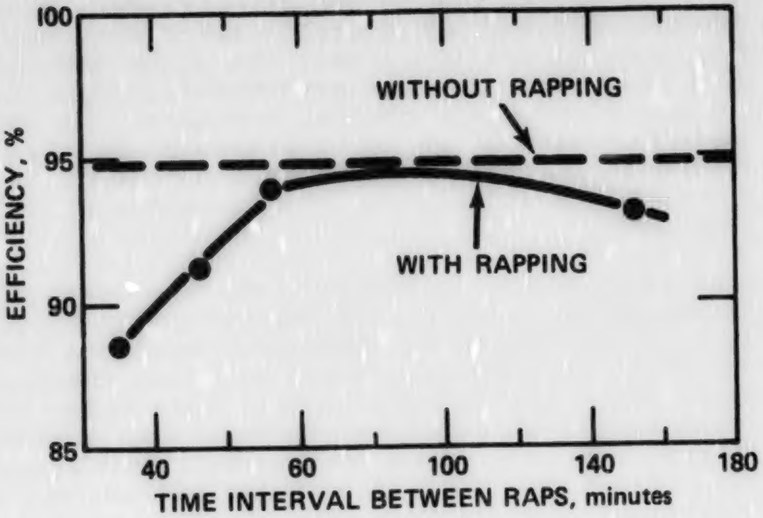

Figure 9. Average efficiencies for FluiDyne pilot precipitator for various rapping intervals.

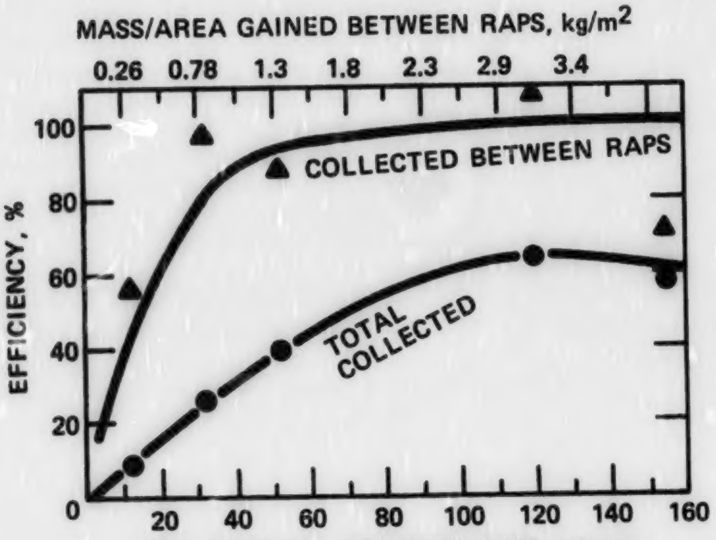

Figure 10. Dust removal efficiency versus the time interval between raps.

Figure 11 presents particle size distribution of rapping puffs for the indicated rapping interval. These data suggest that thicker dust layers produce larger reentrained particles upon rapping. An inspection of the impactor substrates at the outlet sampling locations 2 and 3 revealed that the majority of the large particles in the rapping puffs were agglomerates. Producing relatively large agglomerates instead of individual particles is desirable because the larger agglomerates are recollected faster than discrete particles or smaller agglomerates.

Observations of the rapping process in a pilot unit at SRI with motion pictures (32 frames/sec) showed that the dust was not removed in the ideal slip-stick mode described earlier. Instead, the dust layer fractured along lines of discontinuity in the dust surface. The separate sheets of dust appear to fall without recollection and tend to break up as they encounter other falling sheets and patches of unremoved dust. In both the Fluidyne and SRI pilot plants, it was evident that "boil-up" from the hoppers comprised a significant portion of the reentrainment. The measurement of the vertical distribution of the rapping loss at the Fluidyne pilot unit indicated that 82% of the rapping emission occurred in the lower 32% of the precipitator. This effect was apparently due to both hopper boil-up and gravitational settling of the reentrained material. Figure 12 illustrates the vertical stratification as a function of particle size. All of the particle size bands show a decrease in concentration with increasing distance from the bottom baffle.

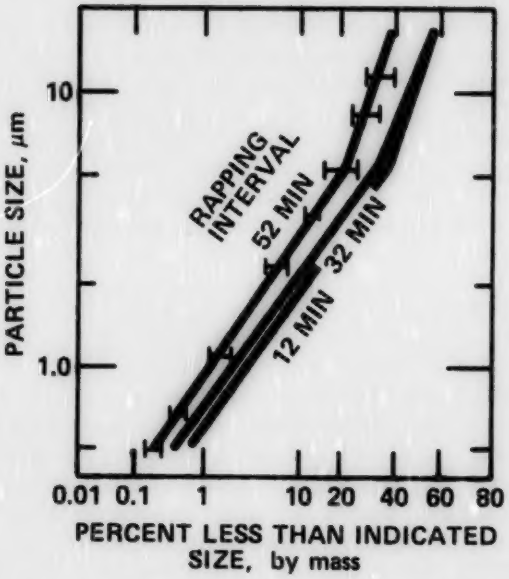

Figure 11. Cumulative percent distribution for rapping puffs, rapping intervals of 12, 32, and 52 minutes from FluiDyne tests.

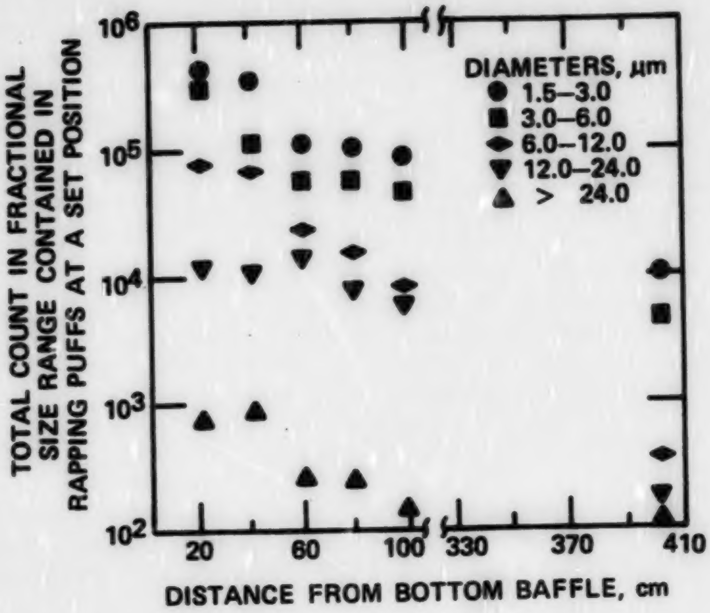

Figure 12. Spatial distribution of particles in rapping puff.

Full-Scale Tests--

Table 2 provides a summary of results from test programs conducted on the three electrostatic precipitator installations. The installations were characterized by relatively high overall mass efficiency, and rapping losses as a percentage of total emissions ranged from 20 to 30% for the cold side units to over 80% for the hot side precipitator. The difference in rapping losses between the hot side unit and the cold side unit is probably due both to reduced dust adhesivity at high temperatures and the radically different rapping sequence philosophy of the manufacturers.

Figure 13 contains the collection efficiency as a function of particle size at Plant 1 for sampling periods in which the rapping system was energized and deenergized. Due to the previously discussed difficulty with process variations at this location, data from the large particle real-time system were used to estimate the collection efficiency for particles greater than 0.5 µm. Figure 14 presents analogous data from Plant 2, with the exception that the rap and no rap data were obtained with the alternating sampling plan described in an earlier section. Fractional efficiency data with the rapping system operating normally are given in Figure 15. For particles larger than about 1.0 µm diameter, the fractional efficiency data for the "normal" and rap sequence data sets indicate reasonable agreement.

TABLE 2. SUMMARY OF PRECIPITATOR TEST RESULTS

Plant	SCA, ft^2/kacfm	Load, MW	Gas flow, kacfm	Temp, °F	Precipitator efficiency %, normal rap interval	Total outlet emissions, lb/10^6 Btu	% Emissions due to rapping		In-situ resistivity, ohm-cm	Portion of ESP tested
							rap-no rap[a] rap	normal-no rap[b] normal		
1	560	135	720	306	99.92	0.0015	-	31[c]	1.4×10^{11}@290°F	Total
2	589	508	321	223	99.85	0.0142	34	22	5.5×10^{11}@221°F	1/6[d]
3	403	271	427	635	99.64	0.0370	83	82	3.2×10^{10}@630°F	1/2[d]

[a] From tests conducted with rapper system on and off alternately.

[b] From tests conducted with normal rapper operation and rapper off.

[c] Estimated from large particle optical sizing system.

[d] Due to the large size of the precipitators involved and to retain cost effectiveness, only a portion of the precipitators were selected for testing.

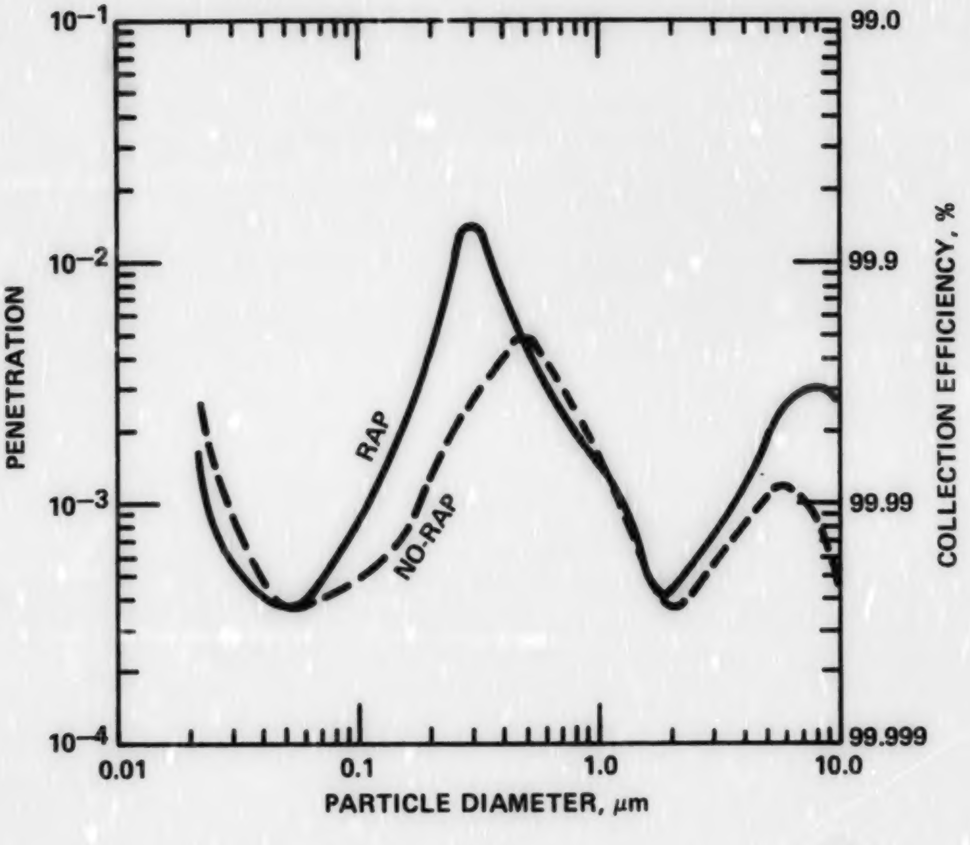

Figure 13. Normal rapping and no rapping results for Plant 1 (cold-side). SCA = 560 ft^2/kacfm.

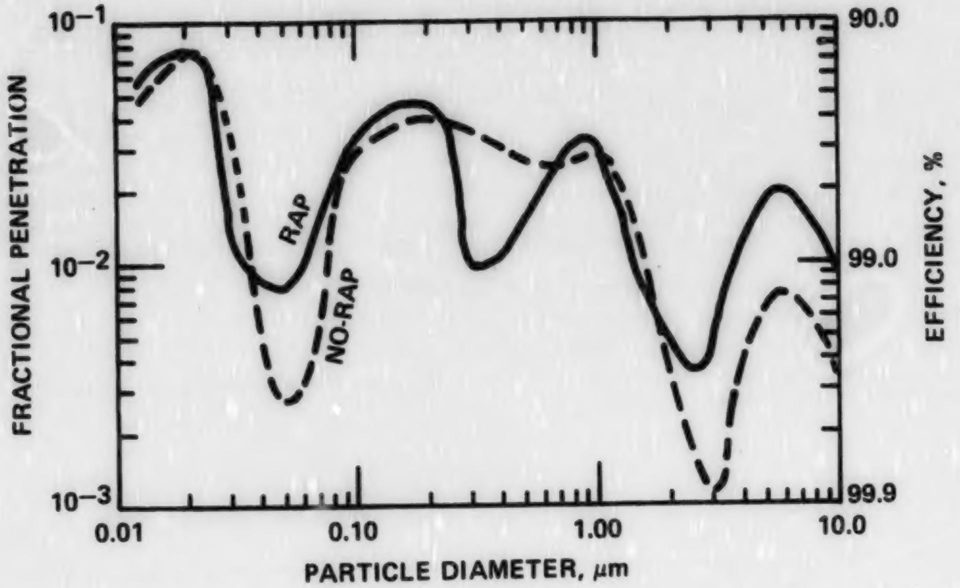

Figure 14. Rappers on and rappers off results for Plant 2 (cold-side). SCA = 589 ft^2/kacfm.

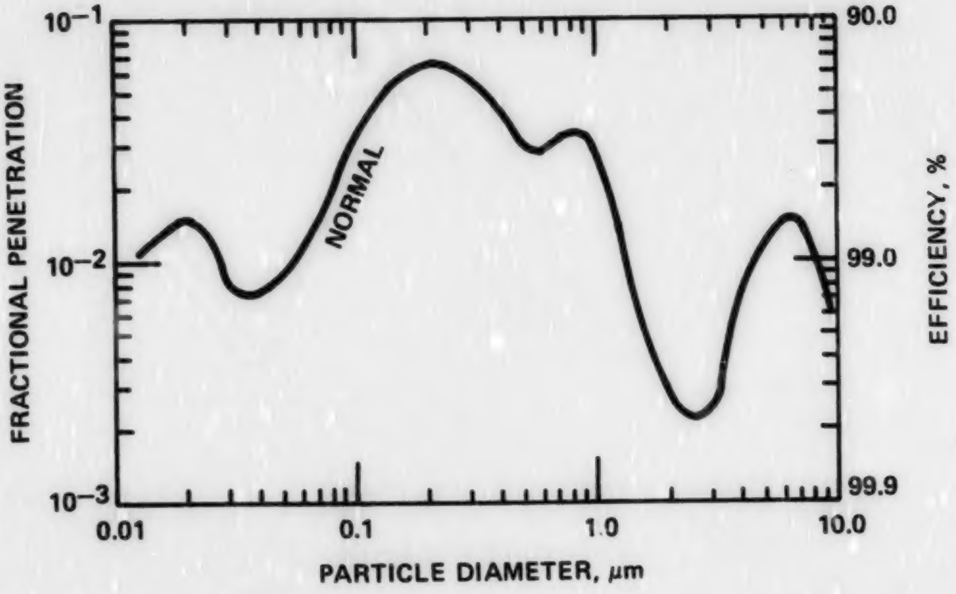

Figure 15. Normal rap sequence fractional efficiency results for Plant 2 (cold-side). SCA = 589 ft^2/kacfm.

The fractional efficiency data sets for the hot-side unit are presented in Figures 16 and 17. The normal and rap sequence data sets again show reasonable agreement for sizes greater than about 1.0 µm. The cause of the apparently higher penetrations for the sub-tenth micron particles during the normal sequence test period is not known. From all of these locations, it is apparent that rapping losses occur for the most part in the larger particle sizes, primarily as particles larger than 2.0 µm diameter. Thus, it appears that rapping reentrainment does not cause a significant change in fine particle emissions. However, the rapping losses for both the hot and cold side precipitators provide a major contribution to the overall penetration, and illustrate that significant improvement in overall mass collection efficiency may be possible by optimization of the rapping system design and operation.

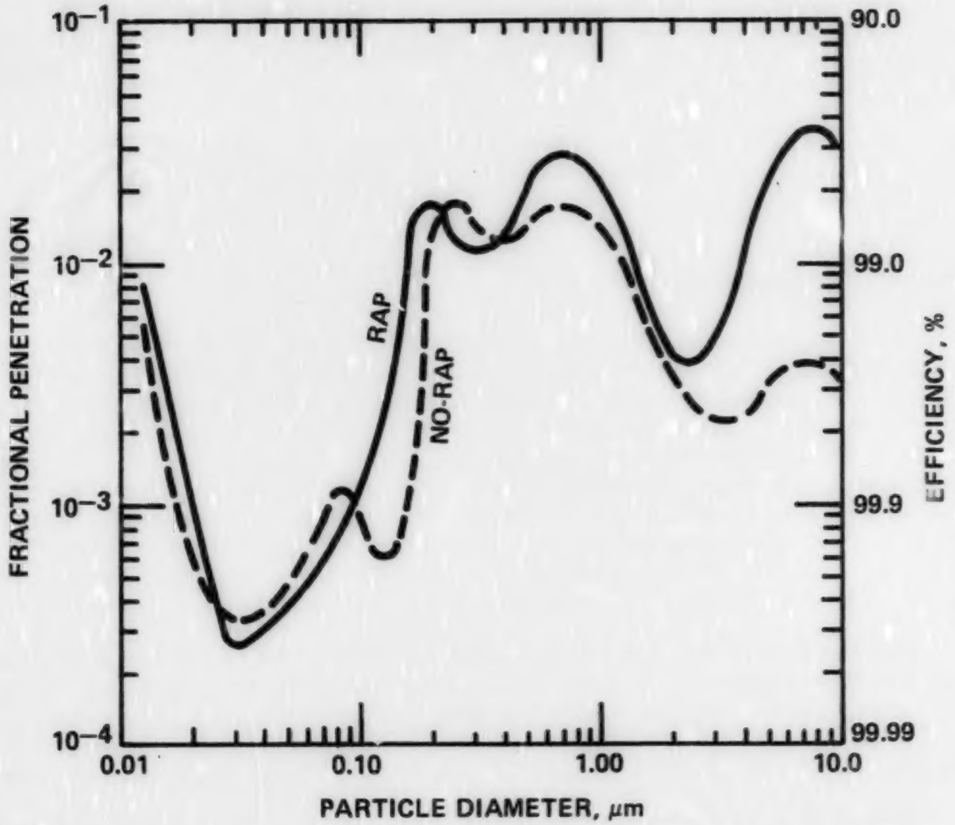

Figure 16. Rappers on/rappers off results for Plant 3 (hot-side).

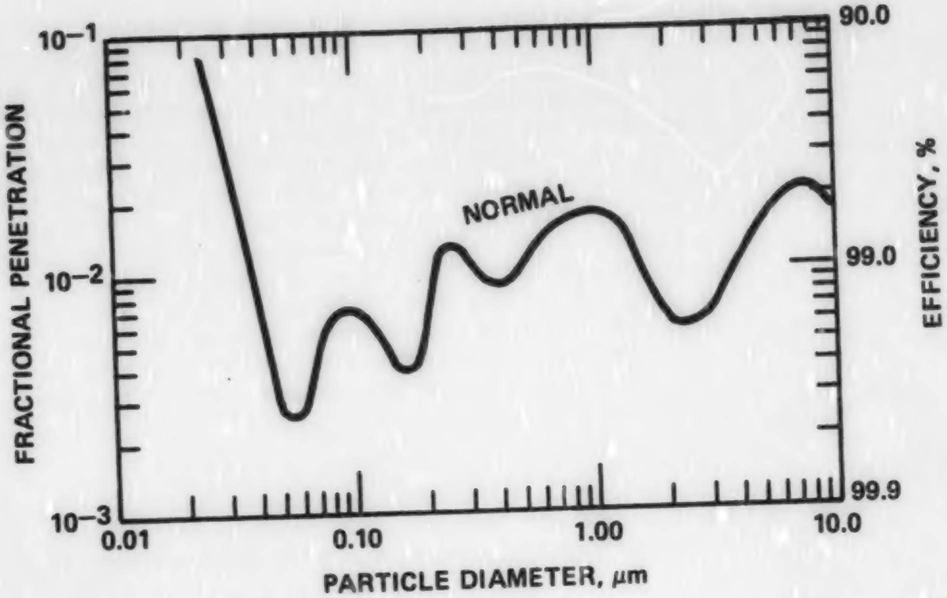

Figure 17. Normal rap sequence fractional efficiency results for Plant 3 (hot side). SCA = 403 ft^2/kacfm.

SUMMARY AND CONCLUSIONS

The electrical forces holding collected dust on collecting electrodes are a function of the electrical operating conditions in the precipitator and the dust resistivity. Negative forces can result for low resistivity dust. Other forces are complex and can be influenced by a number of variables. The efficiency of removal by rapping is influenced by the type of dust, plate acceleration, electrical holding forces, and environmental conditions. For full-scale precipitator installations, rapping emissions are affected by gas velocity, plate accelerations, sectionalization, temperature, and rapping intervals.

Measurement of rapping reentrainment on full-scale precipitators has indicated that the contribution of rapping to total mass emissions can be significant. However, for the installations tested thus far, particle size measurements have shown that rapping does not significantly increase fine particle emissions.

The potential benefits that may be derived from optimizing the rapping procedures at a given installation may be defined by conducting outlet mass and/or opacity measurements with a properly designed test program. The program should allow the determination of the differences in emissions caused solely by energizing the rapping system. If these measurements indicate a substantial difference, then the rapping system should be examined to determine whether an optimization program is practical. Other factors which should be examined include hopper design, ash handling system operation, and gas flow quality in the precipitator.

ACKNOWLEDGEMENTS

The work described in this paper was funded by the Industrial Environmental Research Laboratory of the Environmental Protection Agency at Research Triangle Park, N.C., and the Electric Power Research Institute.

REFERENCES

1. Penney, G.W., and E.H. Klingler. Contact Potentials and Adhesion of Dust. Trans. Amer. Inst. Elec. Eng. Part I 81:200-204, 1962.

2. Tassicker, O.J. Aspects of Forces on Charged Particles in Electrostatic Precipitators. Dissertation, Wollongong University College, University of New South Wales, Australia, 1972.

3. Sproull, W.T. Fundamentals of Electrode Rapping in Industrial Electrical Precipitators. J. Air Pollut. Contr. Assoc. 15:50-55, 1965.

4. White, H.J. Industrial Electrostatic Precipitation. Addison-Wesley, Reading, MA, 1963.

5. Sproull, W.T. Minimizing Rapping Losses in Precipitators at a 2000 Megowatt Coal-Fired Power Station. J. Air Pollut. Contr. Assoc. 22:181-186, 1972.

6. Oglesby, Sabert, Jr., G.B. Nichols, and J.P. Gooch. Electrostatic Precipitation. Decker, in press.

7. Spencer, H.W. A Study of Rapping Reentrainment in a Nearly Full Scale Pilot Electrostatic Precipitator. EPA-600/2-76-140, U.S. Environmental Protection Agency, Research Triangle Park, NC, 1976.

8. Plato, H. Rapping of Collecting Plates in Electrostatic Precipitator. Staub Reinhalt. Luft (in English) 29:22-30, August 1969.

9. Schwartz, L.B., and M. Lieberstein. Effect of Rapping Frequency on the Efficiency of an Electrostatic Precipitator at a Municipal Incinerator. In: Proc. Fourth Ann. Environ. Eng. Sci. Conf., March 4-5, University of Louisville, KY.

10. Nichols, G.B., H.W. Spencer, and J.D. McCain. Rapping Reentrainment Study. Report SORI-EAS-75-307 to Tennessee Valley Authority, TVA Agreement TV 36921A, 1975.

11. Gooch, J.P., and N.L. Francis. A Theoretically Based Mathematical Model for Calculation of Electrostatic Precipitator Performance. J. Air Pollut. Contr. Assoc. 25:108-113, 1975.

12. Gooding, Charles H., Joseph D. McCain, and Diane H. Sommever. Comparative U.S./U.S.S.R Evaluation of a Hot-Side Electrostatic Precipitator. EPA-600/2-77-002, U.S. Environmental Protection Agency, Research Triangle Park, NC, 1977.

PAPER 7

VOLTAGE-CURRENT DATA FROM ELECTROSTATIC PRECIPITATORS UNDER NORMAL AND ABNORMAL CONDITIONS

SHERMAN M. BANKS
JACK R. McDONALD
SOUTHERN RESEARCH INSTITUTE

AND

LESLIE E. SPARKS
INDUSTRIAL ENVIRONMENTAL RESEARCH LABORATORY-RTP
ENVIRONMENTAL PROTECTION AGENCY

INTRODUCTION

Electrostatic precipitation occurs when a charged particle in a gas stream, under the influence of an electric field, impacts and adheres to a collection surface and is thus removed from the gas stream. The relationship of the voltages applied to a precipitator to effect this particle collection and the resultant currents may be analyzed and, coupled with knowledge of other relevant parameters, gives insight into the operation and expected performance of the precipitator. It is the purpose of this paper to explain how a voltage-current relationship is obtained and how the various shapes of the V-I curves are interpreted. The specific relationships discussed here refer to a dry-wall, single-stage, wire-duct precipitator. The conclusions may, in general, be applied to other geometries.

VOLTAGE RELATIONSHIPS

The voltage applied to a precipitator performs two functions. Corona generation provides the ions which charge the particles. The voltage also produces an electric field distributed throughout the precipitator which serves a threefold purpose: (1) the electric field is an important factor in the charging of particles, (2) the charged particles tend to drift along the field lines toward the collection plates, and (3) the field at the collection plates provides an external force assisting in holding the collected particles.

When a small radius electrode is raised to a sufficiently high electrical potential, the electric field near the electrode becomes strong enough to create a corona discharge. A corona may be formed by either positive or negative voltages. A negative corona is generally used in electrostatic precipitation because (1) it produces higher sparking voltage and current, and (2) it is generally more stable than a positive corona.[1] Figure 1 shows the relationships of voltage and current for both positive and negative coronas under equivalent conditions.

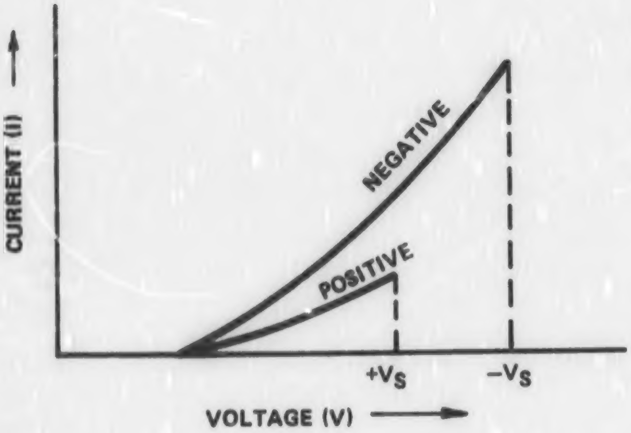

Figure 1. Voltages and currents for positive and negative coronas. After White.[1]

In a negative corona discharge, free electrons near the discharge electrode are accelerated to a high velocity and collide with gas molecules. These collisions produce positive ions and more free electrons. In the region near the electrode where the electric field is large enough, these electrons are also accelerated and have more collisions in an avalanche type process. Some photons are released producing the characteristic corona glow. Outside of this avalanche region the free electrons attach themselves to electronegative gases which become negative ions. These negative ions impact the particles in the gas stream which thus become charged. Under the influence of the electric field the particles migrate toward the collection electrode.[2]

In order to collect particles the voltage applied to the precipitator must be at least high enough to cause the corona to start. The critical field at the surface of the discharge electrode for the onset of the corona is given by a semi-empirical relation by Peek[3] for concentric cylinder geometry:

$$E_c = 30am\delta\left(1 + 0.3\sqrt{\frac{\delta}{a}}\right) \qquad (1)$$

where E_c = corona onset field in kV/cm

a = radius of the discharge electrode in cm

m = a roughness factor for the discharge electrode, usually $0.5 \leq m \leq 1.0$

$\delta = \frac{T_0}{T} \cdot \frac{P}{P_0}$

T_0 = standard absolute temperature (273°K)

P_0 = standard absolute pressure (760 mm mercury)

T and P are the actual absolute temperature and pressure for which δ is to be calculated.

The voltage required to generate the critical electric field for that geometry has been shown to be:[2]

$$V = 30am\delta\left(1 + 0.3\sqrt{\frac{\delta}{a}}\right)\ln\frac{b}{a} \qquad (2)$$

where V = the applied voltage in kV

b = the radius of the outer electrode in cm.

These relationships may be used for estimating E_C and V for parallel plate geometries using b = the plate to wire spacing in cm.

CURRENT RELATIONSHIPS

The measured current in a precipitator is practically zero when the applied voltage is below the level required for corona initiation, V in Equation (2). When a negative corona is generated and current flows, the copious electrons supplied by the avalanche process are generally attached to the electronegative gases in the inter-electrode region. The current carriers outside the corona region comprise a space charge consisting of ions, particles, and possibly electrons. These carriers have a mobility associated with them ranging from the highly mobile electrons to the relatively sluggish particles. Ignoring the contribution to the current of the free electrons, the current density at the collection electrode can be expressed by:[4]

$$J_T = E_0 q_i b_i + E_0 q_p b_p = E_0 q_t b_e \quad \mathrm{A/m^2} \qquad (3)$$

where J_T = total current density - $\mathrm{A/m^2}$

E_0 = average electric field - V/m

q_i = charge on ions - $\mathrm{coul/m^3}$

b_i = ion mobility - $\mathrm{m^2/(volt\text{-}sec)}$

q_p = charge on particles - $\mathrm{coul/m^3}$

b_p = particle mobility - $\mathrm{m^2/(volt\text{-}sec)}$

q_t = total charge - $q_i + q_p$

b_e = effective mobility of ions and particles - $\mathrm{m^2/(volt\text{-}sec)}$

With no particulate in the gas stream and with sufficient voltage applied to produce a negative corona, the total current will depend upon the mobility of the gas ions and their number density. As the number density of fine particles increases, a larger portion of the total charge transferred is carried by the less mobile particles. This space charge effect results in a reduction in current for a given voltage below the current seen with no particulate in the gas stream.

CIRCUIT CONCEPTS

The electrical equivalent circuit of a precipitator is shown in Figure 2.[5]

where V = voltage applied in volts

I = total conventional current flow in amperes

C_p = equivalent precipitator capacitance in farads

R_G = effective resistance of the inter-electrode gap in ohms

C_D = effective capacitance of the dust layer in farads

R_D = effective resistance of the dust layer in ohms.

The voltage normally applied to a precipitator is either half-wave or full-wave rectified 60 Hertz ac. Neglecting for a moment the effects of C_D and R_D, the capacitor, C_p, charges on the increasing portion of the voltage waveform and discharges on the decreasing portion. The current from the discharging capacitance flows through the resistance R_G tending to maintain the peak voltage applied. There is an exponential decay of this voltage dependent on the time constant of the R_GC_p circuit. This time constant is given by:[6]

$$T = R_GC_p \text{ seconds} \tag{4}$$

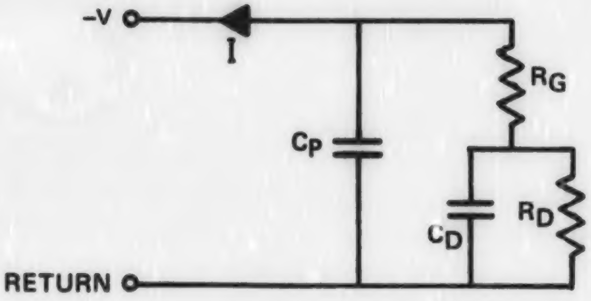

Figure 2. Electrical equivalent circuit of a precipitator electrode system with a dust layer. After Oglesby and Nichols.[5]

where T = time in seconds for the waveform to decrease to approximately 37% of its peak value after the voltage is removed

R_G = equivalent resistance of the inter-electrode region in ohms

C_p = equivalent capacitance of the electrode system in farads.

The current, I, will flow in the return leg of the circuit only during the charging of the capacitor. During the remainder of the cycle, the current supplied to R_G is the discharge current from C_P. These relationships are shown in Figure 3. In this example T is assumed to be greater than 8 milliseconds or 1/2 cycle of the line voltage.

Normally the effective impedance presented by the parallel combination of C_D and R_D is negligible compared to the impedance of R_G. Thus, the time domain response of the precipitator is determined by the combination of C_P and R_G. However, this is not true when the dust layer is in a breakdown condition and possibly exhibiting back corona. The breakdown may effectively short out the dust layer and a portion of R_G thereby reducing the time constant, T, and increasing the current, I. This change in time constant may be monitored on an oscilloscope presentation of the voltage waveform and used to support evidence that breakdown of the dust layer is occurring.

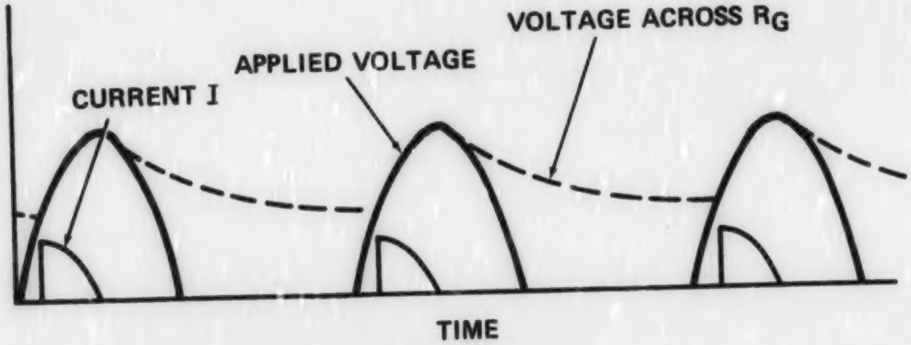

Figure 3. Voltage-current relationship in an ideal capacitor/resistor parallel combination.

The voltages and currents in a precipitator are most often measured by the installed power set instrumentation as root-mean-square (rms) or effective values. The capacitances and resistances vary slowly with time so that the equivalent circuit of a precipitator in normal operation can be approximated as a pure resistance across the terminals of a DC source. The voltage-current relationship is simply V = RI where R is the effective value of the resistance in ohms, V is in rms volts, and I is in rms amperes. An actual precipitator departs from the ideal in that R is a non-linear function of the current. The graphical presentation of precipitator voltage versus secondary current is not the straight line generated with an ideal resistance, but generally curved and referred to as a V-I curve.

V-I CURVE MEASUREMENT TECHNIQUES

The practical measurement of V-I curves entails the direct measurement of power set secondary voltages and currents. Today, most precipitator manufacturers install secondary kV and current (milliamp) meters on each transformer/rectifier (T/R) set. These readings may be used directly when taking V-I data. However, in the instances when there is no secondary kV meter or greater accuracy is required, calibration with known voltage dividers and an accurate voltmeter may be necessary.

The secondary voltage meter calibration involves inserting a known resistive voltage divider in parallel across the high voltage bus section of the precipitator and taking comparative readings with the DC KV meter installed on the power set controller. The installation of this device is shown schematically at point number 1 in Figure 4.

Most power set manufacturers install in the return leg of the secondary circuit a resistance, on the order of 50 ohms or less. The entire precipitator secondary current passes through this resistance. The voltage developed is proportional to the current and a meter calibrated to read current detects this voltage. Other manufacturers may place a current meter with very low impedance across this resistor and allow all the precipitator current to pass through the meter. The resistor is in the circuit to prevent isolating the power set if the meter is removed from the circuit. Figure 4 also shows the relation of these components to the remainder of the system, at point number 2.

In order to calibrate the secondary current meter it must first be determined whether the meter is a voltage or current sensing device. If this cannot be determined from the precipitator operation and maintenance manual, a test must be made. If it is a voltage detecting type current meter, a volt meter placed across the resistor will read within a few percent of the same voltage whether the T/R set current meter is attached or not. If

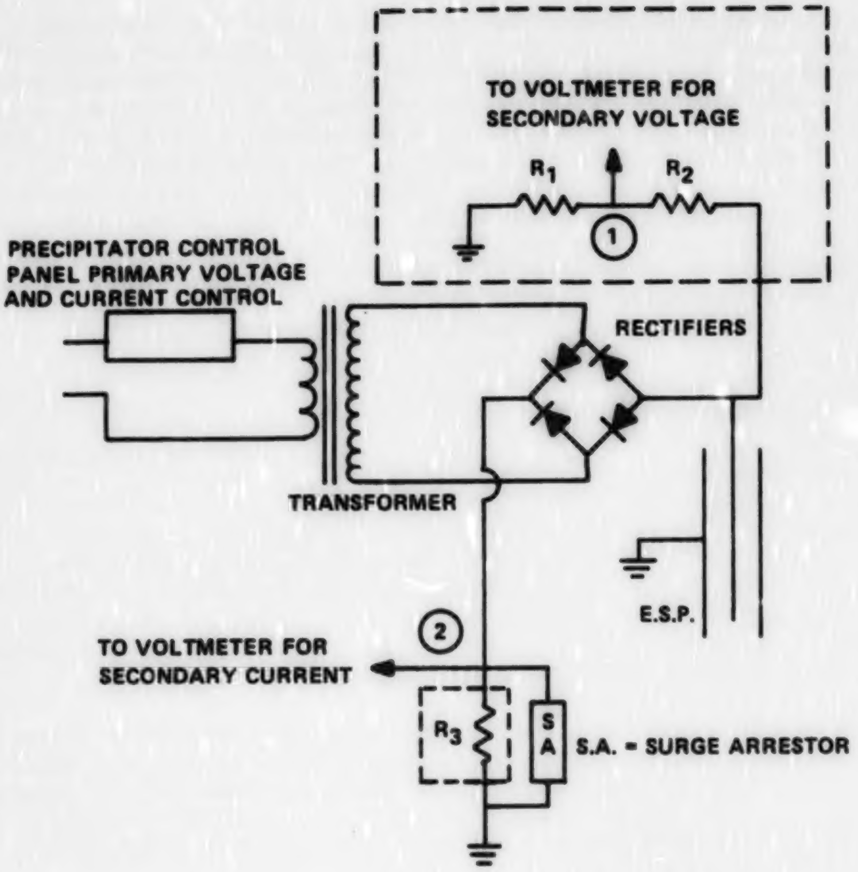
TO VOLTMETER FOR
SECONDARY VOLTAGE
R_1
R_2
①
PRECIPITATOR CONTROL
PANEL PRIMARY VOLTAGE
AND CURRENT CONTROL
RECTIFIERS
TRANSFORMER
E.S.P.
②
TO VOLTMETER FOR
SECONDARY CURRENT
R_3
S
A
S.A. = SURGE ARRESTOR

Figure 4. Voltage divider network for measuring precipitator secondary voltages and currents.

the measured voltage is low with the T/R set meter in the circuit, the T/R set meter is a current sensing device. Calibrating a voltage sensing type meter requires accurately measuring the resistance of the resistor, out of the circuit, and recording the voltages for various currents. Then apply Ohm's law and compare the calibrated currents with the meter readings. If the set has a current sensing meter, insert a calibrated current meter of appropriate capacity in series with the meter to be calibrated and measure various currents, comparing the two readings.

Figure 5 is a facsimile of a data sheet used to collect data from which voltage-current relationships may be plotted. In the general heading, information is recorded which will identify the test, the power supply (T/R Set), the plate area fed by the power set, and the determined calibration factors for the voltage and current. Data is taken as the manual set control is gradually increased until some current flow is detected. This is recorded as the corona starting voltage. Subsequent points are taken by increasing the control for some increment of current and recording the meter readings at that point. Readings are taken until some limiting factor is reached. This factor is recorded on the right-hand side of the data sheet and is usually excessive sparking or a current or voltage limitation of the power set.

The columns as shown in Figure 5 usually completed for each point include those labeled PRIMARY VOLTS, PRIMARY AMPS, DCKV T/R SET METER, DCMA T/R SET METER, SPARK RATE, and DC VOLTS VOLTAGE DIV. At a later time the DCMA correction factor is applied to the T/R set meter reading and the DCMA CORR. column is completed.* The DCKV CORR. column is completed by multiplying the DC VOLTS VOLTAGE DIV. column by the voltage divider multiplier. The last two columns are completed by dividing the DCMA CORR. by the appropriate collecting area in square feet or square centimeters and applying a multiplicative factor of 10^{-3}. A plot is then made on linear graph paper of the DCKV CORR. vs $\mu A/ft^2$ or nA/cm^2 depending on the experimental requirement.

A typical voltage-current curve is shown in Figure 6. Voltage is plotted linearly along the horizontal axis and current density linearly along the vertical axis. Current density at the collection plate is used rather than total current supplied to give a basis for comparison. This curve was obtained with 2.67 mm diameter wires in a laboratory scale precipitator.

THEORETICAL V-I CURVES

A numerical method has been developed[7] which will allow the calculation of voltage-current characteristics in wire-duct geometries. The method, based upon the numerical technique suggested by Leutert and Böhlen[8], accounts for the effect of space charge

---

*On a dual half-wave installation where the voltage is measured on one independent HV bus but the current is the sum of both sections, the secondary current must also be multiplied by the ratio of the plate area of the section under test to the total plate area in order to approximate the secondary current in that power supply leg.

POWER SET
VOLTAGE-CURRENT CURVE DATA SHEET
DATE/TIME________ T/R SET NO. _______ COLLECTING AREA __________
VOLTAGE DIV. MULT. __________
T/R SET DCMA CORRECTION__________

PRIMARY VOLTS	PRIMARY AMPS	DCKV T/R SET METER	DCMA T/R SET METER	SPARK RATE	DCMA CORR.	DC VOLTS VOLTAGE DIV.	DCKV CORR.	$\mu A/f^2$	NA/ cm^2

TERMINAL POINT
DETERMINED BY:
(CIRCLE ONE)

1. SPARKING
2. SEC. CURRENT LIMIT
3. SEC. VOLTAGE LIMIT
4. OTHER
____

COMMENTS:

Figure 5. Sample V-I curve data sheet.

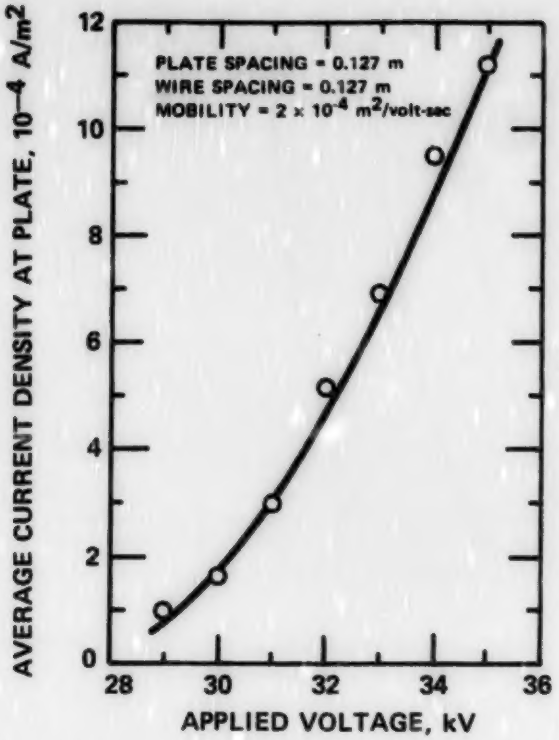

Figure 6. Typical voltage-current curve derived experimentally in a laboratory wire-duct precipitator. After McDonald.[7]

and is applicable over the entire range of current and voltage where sparkover does not occur. It has been used to demonstrate the effects of precipitator geometry and the lowering of the effective mobility of the charge carriers due to particulate space charge effects. Curves generated with this technique will be used in the following paragraphs to illustrate the theoretical influence on the V-I curves caused by varying certain parameters.

Figure 7 shows the theoretical dependence of the V-I curves on wire radius, a. The wire sizes vary from 0.127 mm radius to 5.8 mm radius. Note the shift directly to the right of each curve.

Figure 8 shows the effect of p[illegible] spacing on the V-I curves, as the plate spacing is varied from [illegible] 2 m to 0.508 m. The corona starting voltages stay nearly the same, but the slopes of the V-I curves decrease.

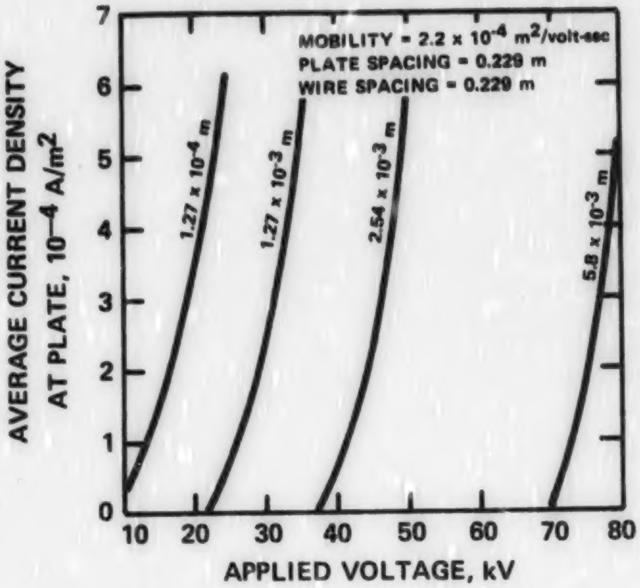

Figure 7. Theoretical curves showing the effect of wire size on voltage-current characteristics.

Figure 9 shows the effect of wire-to-wire spacing. As the spacing is increased from 0.098 m to 0.503 m the V-I curves tend to shift to the left. However, there is also a variation in the slope of the curves which is due to the interaction of the fields created by the individual wires. This suggests that there exists for a given plate-to-plate spacing and wire diameter some "optimum" wire-to-wire spacing.

Another geometrical factor is the plate area per power set, since the sparkover voltage depends on this quantity. In a clean electrode system, as voltage is increased, the current follows a typical V-I relationship until the average electric field in the inter-electrode region exceeds the field strength of the gas. If the sparkover voltage for one corona wire is V, then the sparkover voltage for n identical corona wires is:[9]

$$V_n = V_i - \frac{1}{b} \log_e n \text{ volts} \qquad (5)$$

where b is an empirical constant on the order of one. This can be related to plate area by substituting for n the value of (total plate area)/(plate area per corona wire). The graphical relationship is shown in Figure 10, with V_i = 50 kV and various values of b.

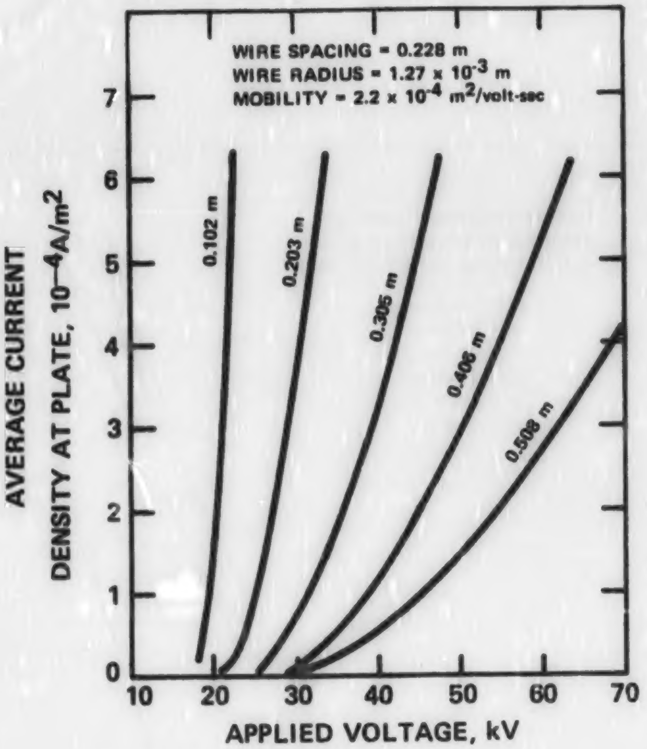

Figure 8. Theoretical curves showing the effect of plate-to-plate spacing on voltage-current characteristics.

Misalignment problems in the electrode geometry are usually manifested in reduced sparking voltages. This generally can be detected by comparison of the V-I curves of the unit under investigation with the curves produced by adjacent fields across the gas flow or with V-I curves obtained previously under normal conditions.

The particle size distribution of the dust at the inlet to a precipitator is one of the most important parameters affecting the electrical operation of a particular installation. The more particles in the submicron range, the lower will be the effective mobility of the space charge. Figure 11 illustrates the theoretical effect on the voltage-current relationship of various effective mobilities.[10] As the mobility decreases the current density for a given voltage decreases also. Thus total current is suppressed by large numbers of fine particles in the dust load. As the gas stream proceeds through the precipitator, more and more particles are collected and the space charge effect is lessened. That is, the effective mobility increases in successive precipitator electrical sections from inlet to outlet. This is illustrated in Figure 12. Section Number 1 is the inlet field.

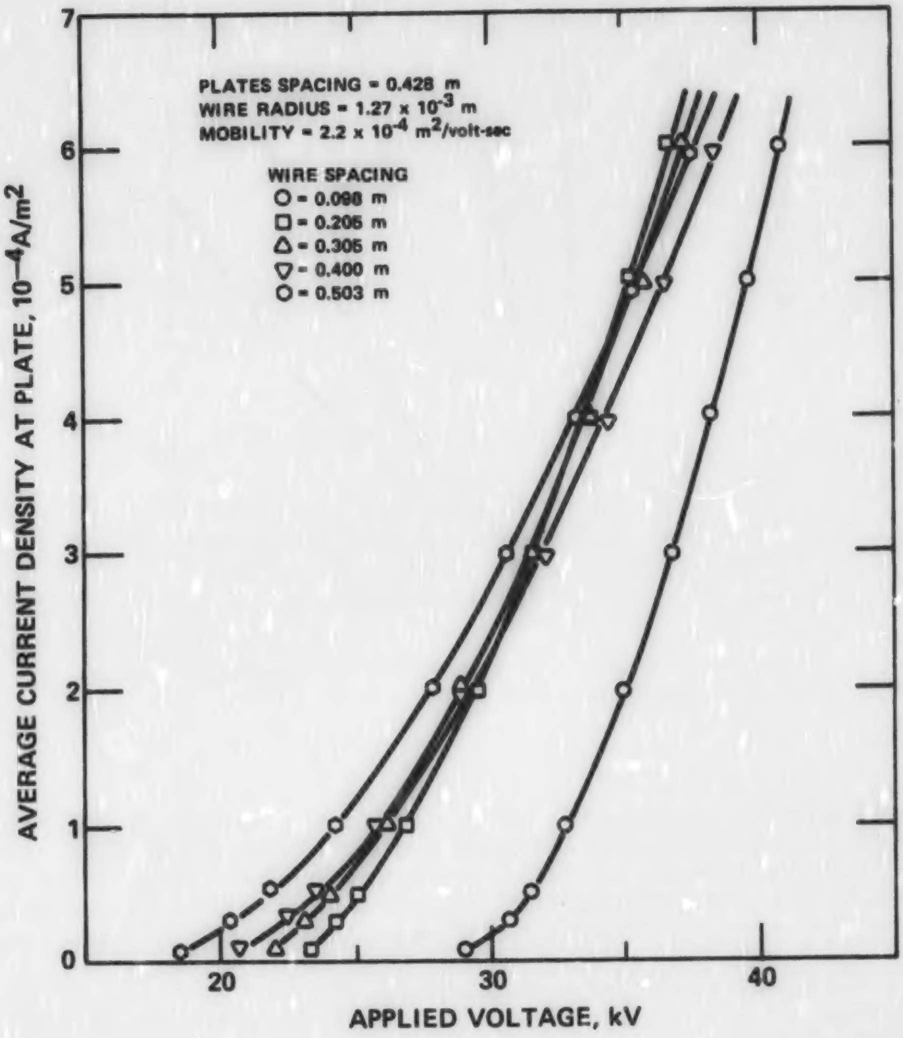

Figure 9. Theoretical curves showing the effect of wire-to-plate spacing on voltage-current characteristics.

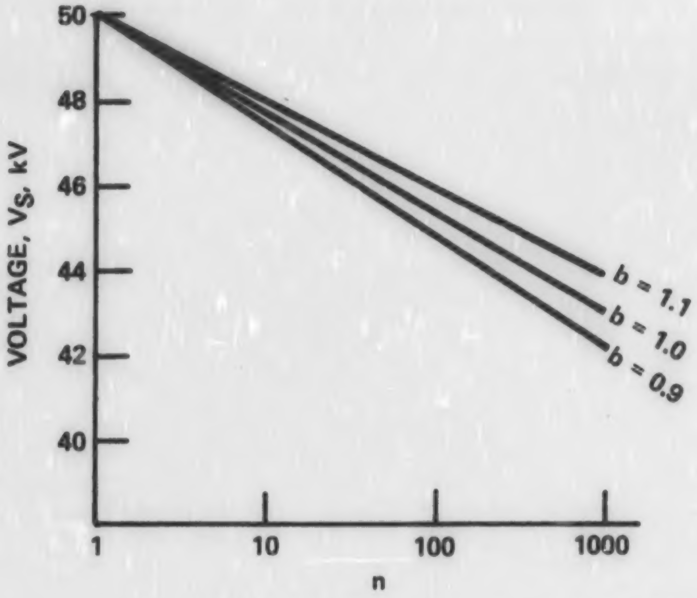

Figure 10. *Sparking voltage as a function of number of corona wires.*

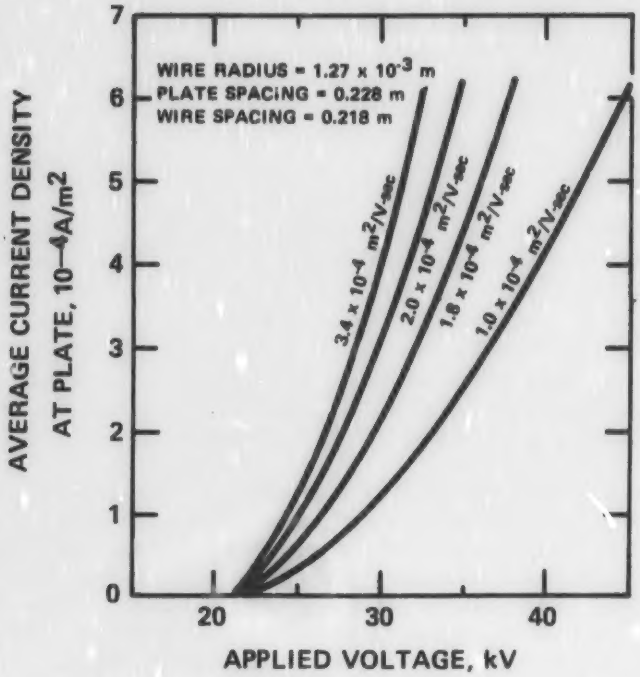

Figure 11. *Theoretical curves showing the effect of effective mobility on voltage-current characteristics.*

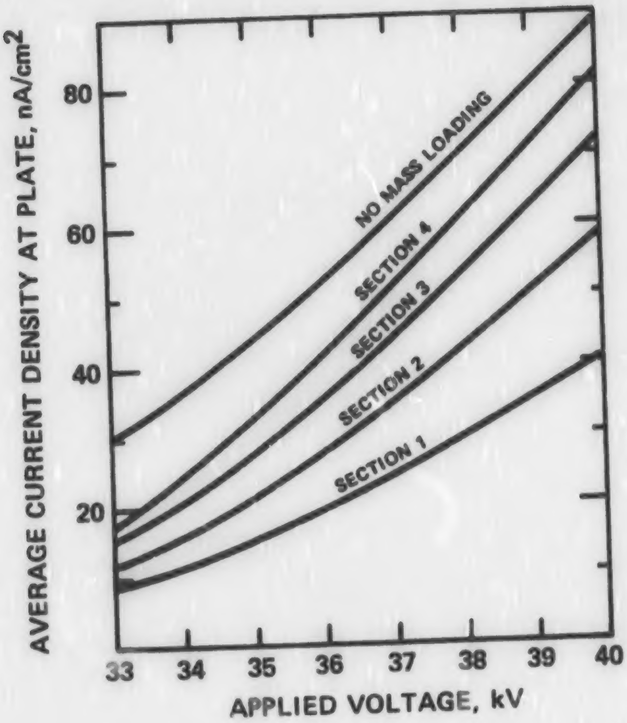

Figure 12. Theoretical voltage-current curves for a specific collection area of 59.1 $m^2/(m^3/sec)$.

In some installations dust may build up on the corona wires. This may manifest itself as a change in the V-I curve position from an airload baseline. Mistakenly it may be attributed to a change in the space charge resulting from some process change. However, dust buildup shifts the V-I curves directly to the right, similar to a change in corona wire size. A change in mobility resulting from a change in the space charge would rotate the curves with essentially the same corona starting voltage.

The sparkover voltage of a gas is proportional to the factor δ as was shown in Equation 2. In general higher temperature and lower pressure tend to lower the sparkover voltage for a given geometry. Most precipitators operate at or near atmospheric pressure so that the δ factor is mostly dependent on temperature. Figure 13 illustrates the decrease in sparking voltage with increasing temperature and the resultant increase in current from the increased mobility of the charge carriers.[11]

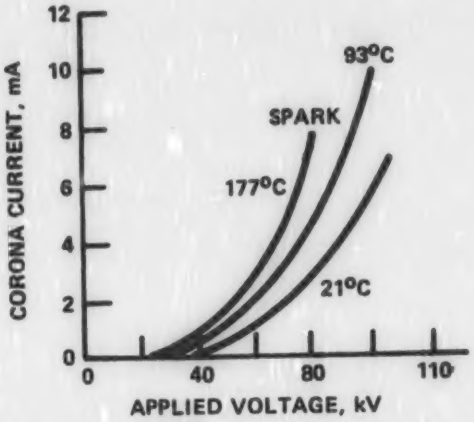

Figure 13. Effect of temperature on negative corona in air. After White.[11]

Generally clean plate curves have been considered to this point. However, when a dust layer is deposited on the collection plates, the curves are somewhat modified from the clean plate relationship as shown in Figure 14.[12] This relationship between current and voltage can be thought of as inserting a non-linear impedance in series with the non-linear impedance of the inter-electrode region. No significant departure from the clean plate V-I curve is seen until the resistivity of the dust, ρ, approaches 10^{10} ohm-cm. Then the curves begin to show a rotation to the right with decreased currents for the same applied voltages and decreased sparkover voltages. The decreased currents are caused by the increase in the effective circuit impedance.

The relationship

$$E = j\rho \tag{6}$$

where E = electric field in V/cm

j = current density in A/cm^2

ρ = resistivity in ohm-cm

describes the formation of an electric field in the dust layer. An uneven current density distribution in the dust layer causes an uneven field. When the localized field in the dust layer exceeds the field strength of the dust, a breakdown of the gas in the interstitial regions may occur. The point at which the breakdown occurs becomes a low impedance path and the current density becomes even greater. A localized glow (sometimes referred to as

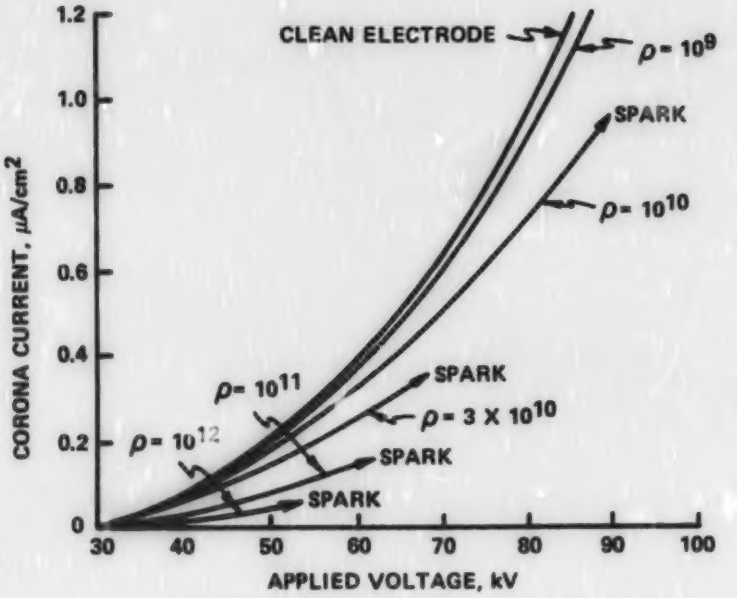

Figure 14. Theoretically calculated effect of resistive dust layer on d-c current-voltage curves for laboratory pipe precipitator. After White.[13]

back corona) may form as the breakdown becomes more intense with increasing voltage. Streamers may also form from the dust layer and may propagate across the inter-electrode region. Since the dielectric strength of the dust is generally smaller than the dielectric strength of the gas, sparking with dust-covered electrodes occurs at a lower voltage than with clean electrodes. Under conditions of back corona in a dust layer with a resistivity of 10^{11} ohm-cm, the spark could be confined to the dust layer and would not propagate across the inter-electrode region. The result would be a large increase in current for a slight increase in voltage starting at the theoretical sparking voltage and possibly crossing the clean plate V-I curve before sparking.[13]

Figure 15 displays data collected in a laboratory study by White[14] which shows more practically the effect of resistivity on the voltage-current relationship in a precipitator. This data was collected under experimentally controlled conditions and only the resistivity of the dust layer has been varied. Note that even the curve with dust resistivity of 10^{10} ohm-cm shows a significant reduction in the sparkover voltage. The curve with dust resistivity of 2.5×10^{11} ohm-cm shows evidence of electrical breakdown in the dust and possibly back corona due to the steep slope of the curve and the higher currents for a given voltage than the curve with clean electrodes.

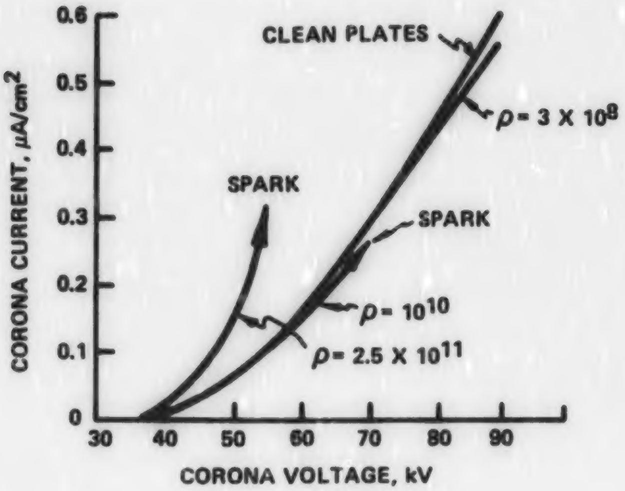

Figure 15. Corona current-voltage distortions caused by resistive dust layers on ground plates; d-c voltage. After White.[12]

Spencer[15] goes into great detail discussing back corona and the relationship with resistivity. In summary, when back corona does exist, the dust layer is breaking down electrically and positive ions are being generated. These positive ions are drawn toward the discharge electrode and add to the total current in the precipitator. They tend to cancel the space charge and may actually charge some particles positively. The consequences of severe back corona are (1) loss in charging and collecting efficiency of the entering dust load with a concomitant reduction in overall precipitator collection efficiency, and (2) higher reentrainment of the previously collected dust.

An accumulation of a thin tenacious layer of dust on the collection plate is inevitable. The resultant voltage drop across the dust layer is given as:

$$V = j\rho t \tag{7}$$

where V = voltage in volts

j = current density in A/cm^2

ρ = resistivity in ohm-cm

t = thickness of the layer in cm.

If there is no resistivity problem in the unit, there will be no appreciable change in the V-I curves, since V would be so small as to be insignificant. However, as the thickness and/or the resistivity increases, the electric field in the layer increases, reducing the electric field in the inter-electrode region available for the charging and collection of particles. This is seen on the V-I curves as a shift to the right, giving higher voltages required for the same current densities. There would also be a slight modification caused by the effective shortening of the plate-to-wire spacing. The net result would be a lower operating voltage and current with the buildup of a high resistivity dust layer on the plates.

For a given inlet dust load, an increase in the ratio of collecting area to gas volume treated, the specific collecting area (SCA), will obviously increase the efficiency of the precipitator. This increase in SCA may be accomplished most easily on a coal-fired boiler by a decrease in the boiler load, if the gas temperature is held relatively constant. The gas temperature should remain stable to prevent any change in dust resistivity. This decrease in load will give a lesser gas volume through the precipitator and thus the particles will have a greater residence time. The net effect of an increase in SCA, whether accomplished by lowering the gas volume or increasing the plate area, is to reduce the current suppression due to space charge effects. This is reflected in the V-I curves in Figure 16. The first section of the unit with an SCA of 19.7 $m^2/(m^3/sec)$ is shown to be affected the most from the space charge effect. The fourth section of that unit shows little improvement over the first section of the higher SCA unit. However, the fourth section of the higher SCA unit begins to closely approach the theoretical V-I curves obtained with no mass loading. In practice, it is usually difficult to reduce load and have temperature remain a constant. Since resistivity is strongly dependent on temperature, for certain high temperature precipitators, any relative increase in performance due to increased current density may be offset by a degradation due to an increased resistivity.

ACTUAL V-I CURVES

V-I curves and data are presented in the following paragraphs which serve to illustrate several of the theoretical points already presented. The data is primarily from precipitators treating the effluents from coal-fired boilers; however some data is presented from precipitators servicing the gases at two copper smelters.

Figure 17 shows two V-I curves taken at the outlet fields of two precipitators, one high temperature, about 300°C, and the other low temperature, about 150°C, neither of which had any apparent malfunctions. The difference in the V-I curves that should be seen due to the variation in temperature is offset somewhat because of a difference in the discharge electrode diameter. However, the

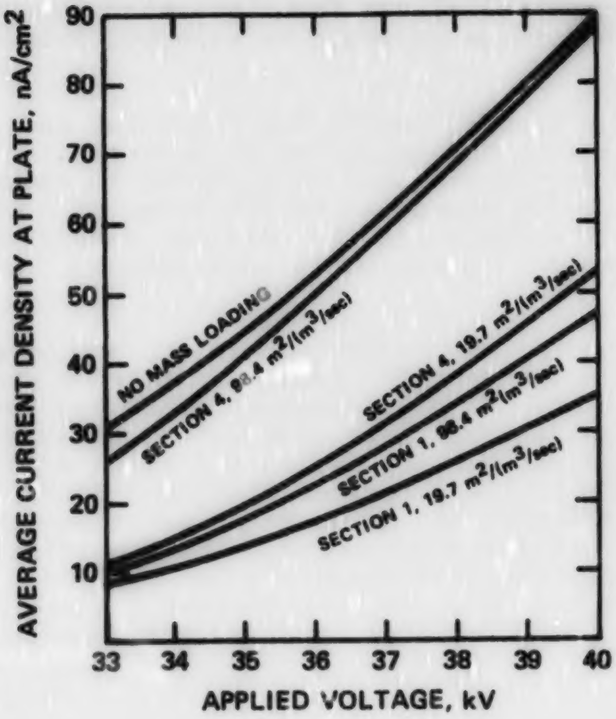

Figure 16. *Comparison of theoretical voltage-current curves for different specific collection areas.*

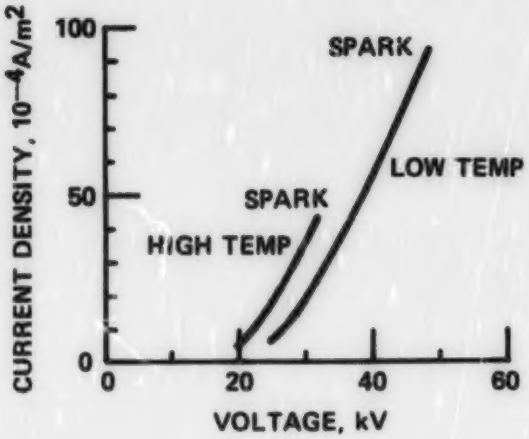

Figure 17. *Comparison of normal hotside and coldside precipitator V-I curves.*

high temperature curve exhibits a lower sparking voltage and higher current for a given voltage as would be expected from the temperature difference.

Figure 18 shows the V-I curves for the inlet and outlet of a low temperature precipitator operating on a dust with a measured ρ of 10^{12} ohm-cm. This dust would be expected to cause a case of severe back corona. The steepness of the slope of each curve with a slight increase in voltage and the foldback displayed is evidence that an electrical breakdown is occurring in the dust layer.

The precipitator on the reverberatory furnace of a copper smelter, Smelter A, was recently studied. It had a geometry essentially identical to that of precipitators whose V-I curves have already been presented. The plate spacing was 0.229 m, the corona wire size was 2.7 mm, it had a moderate SCA of 52 $m^2/(m^3/sec)$, and the operating temperature was between 315°C and 370°C. The inlet particle size distribution had more larger particles than expected, having a mass median diameter measured to be significantly greater than 10 μm. The dust load was about 1 x 1^{-3} kg/DSCM. The V-I curves presented in Figure 19 are for the two fields, inlet and outlet. The inlet operating at a lower current density than the outlet is normal and explained in terms of a space charge effect due to the inlet mass loading.

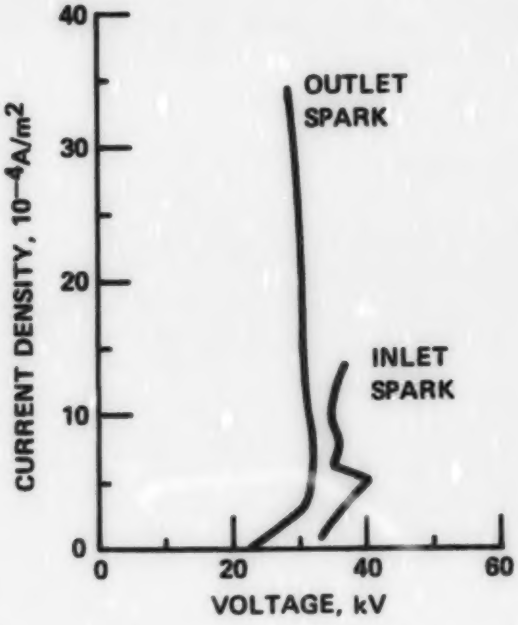

Figure 18. V-I curves from inlet and outlet fields on coldside precipitator servicing high resistivity dust.

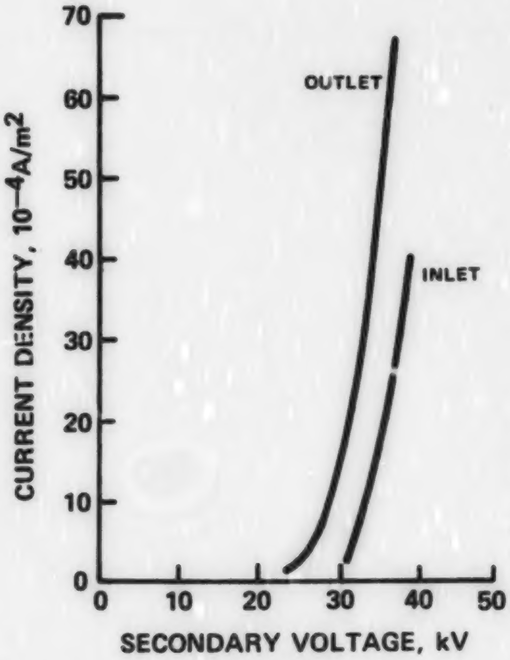

Figure 19. Voltage-current characteristics of the inlet and outlet fields of the precipitator servicing the effluent from the copper reverberatory furnace at smelter A.

The precipitator at another copper smelter, Smelter B, also servicing the effluent from a reverbatory furnace, was examined recently on two separate occasions. The discharge electrodes in this precipitator were square, 4 mm on a side. The unit had 0.254 m plate-to-plate spacing, design SCA of 35.6 $m^2/(m^3/sec)$, and operating temperature of approximately 280-350°C. The furnace at Smelter B during test No. 1 was being fired by a mixture of gas and oil. During test No. 2 only oil was used. The apparent rotation in the curves seen in Figure 20 may be attributed to an increased space charge and subsequent lowering of mobility due to the difference in fuel mixture. The shift to the right of Smelter B curves with respect to Smelter A may be due to the different discharge electrodes.

The curves from Smelter A and the two sets of curves from Smelter B are an indication of the variations that may be encountered throughout metallurgical industries. Each individual case must be studied quite closely. All the process variables should be taken into consideration before accurate interpretations may be made from the V-I curves.

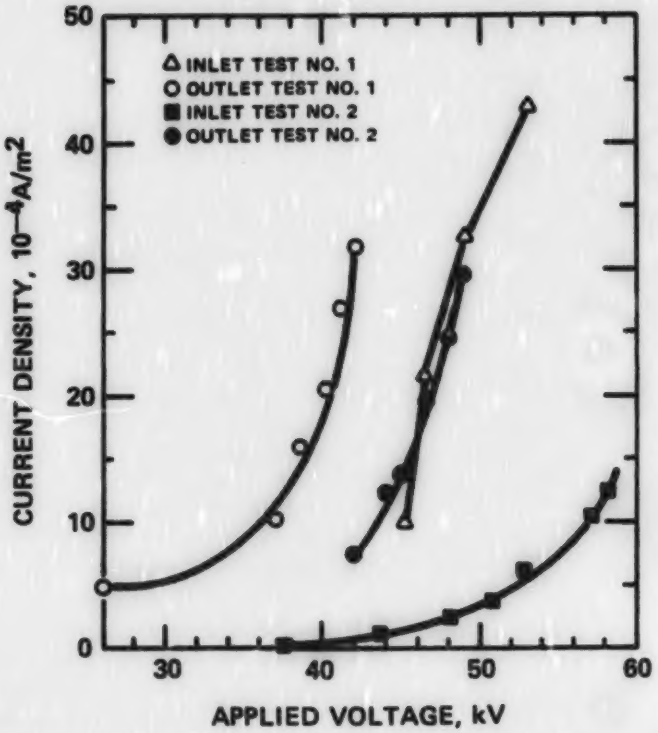

Figure 20. V-I curves for inlet and outlet fields, copper reverberatory furnace on two separate tests at smelter B.

REFERENCES

1. White, H.J. The Role of Corona Discharge in the Precipitation Process. Elec. Eng. 71:67-73, 1952.

2. Oglesby, S., Jr., and G. Nichols. A Manual of Electrostatic Precipitator Technology Part I - Fundamentals. APTD 0610, National Air Pollution Control Administration, Cincinnati, OH 1970. NTIS PB 196380. p. 27.

3. Peek, F.W., Jr. Dielectric Phenomena in High Voltage Engineering. 3rd ed., McGraw Hill, New York, 1929.

4. Gooch, J.P., J.R. McDonald, and S. Oglesby, Jr. A Mathematical Model of Electrostatic Precipitation. EPA-650/2-75-037, U.S. Environmental Protection Agency, Research Triangle Park, NC, 1975. NTIS PB 246188/AS. 162 pp.

5. Reference 2, p. 251.

6. Reference 2, p. 254.

7. McDonald, J.R. Mathematical Modelling of Electrical Conditions, Particle Charging, and the Electrostatic Precipitation Process. Ph.D Dissertation, Auburn University, Auburn, AL, 1977. 186 pp.

8. Leutert, G., and B. Böhlen. The Spatial Trend of Electric Field Strength and Space Charge Density in Plate Type Electrostatic Precipitators. Staub Reinhalt. Luft (in English) 32(7):27-33, 1972.

9. White, H.J. Industrial Electrostatic Precipitation. Addison-Wesley, Reading, MA, 1963. p. 222.

10. Reference 7, p. 63.

11. Reference 9, p. 106..

12. White, H.J. Resistivity Problems in Electrostatic Precipitation. J. Air Pollut. Contr. Assoc. 24(4):314-338, 1974.

13. Reference 2, p. 117.

14. Reference 12, p. 325.

15. Spencer, H.W. Electrostatic Precipitators: Relationship Between Resistivity, Particle Size, and Sparkover. EPA-600/2-76-144, U.S. Environmental Protection Agency, Research Triangle Park, NC, 1976. NTIS PB 257130/AS. 68 pp.

PAPER 8

PARTICLE CHARGING IN AN ELECTRICAL CORONA AND ASSOCIATED PROBLEMS

DUANE H. PONTIUS
WALLACE B. SMITH
SOUTHERN RESEARCH INSTITUTE

AND

JAMES H. ABBOTT
INDUSTRIAL ENVIRONMENTAL RESEARCH LABORATORY-RTP
U.S. ENVIRONMENTAL PROTECTION AGENCY

INTRODUCTION

In the electrostatic precipitation process, particle charging mechanisms are described in terms of the forces which drive ions toward the surface of a particle against the repulsion arising from the static charge which resides on the particle. The particle charging process occurs in a physical system consisting of several components, including, in general, particles of various sizes and states of charge, gas molecules, ions, and free electrons. Forces arising from the effects of diffusion and the applied electric field produce movement of each component in the system, resulting in a very broad distribution of velocities. Diffusion produces average speeds which are easily calculated by application of the kinetic theory for each component of the system.[1] Drift velocities depend upon the electric field strength, charge and aerodynamic effects.[2,3]

Figure 1 illustrates component velocities as a function of the negative logarithm of the mass. The particle diameters indicated on the graph are based on a density of 2.2 g/cm^3. The diffusional or thermal velocities lie along a straight line in this graph. Although the thermal velocities are large for ions and small particles, the associated motion is random, and therefore does not contribute directly to deposition of particles on the collecting surfaces in a precipitator. Diffusion forces are quite important, however, in the process of attaching ions to particles.

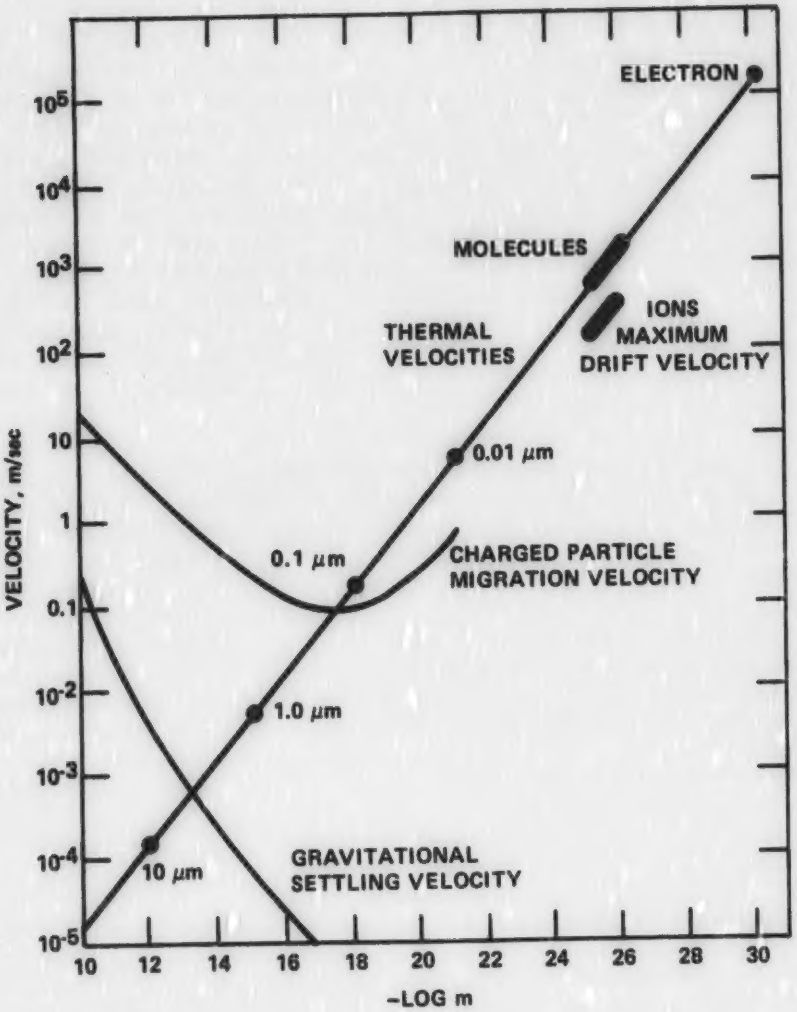

Figure 1. Typical velocities associated with ions, molecules and particles in an electrostatic precipitator.

Directed motions of ions and particles in an electric field are indicated by the drift and migration velocities shown in Figure 1. The curve representing gravitational settling is included for completeness in the system description.

If a charge is brought close enough to a particle, an attractive force will exist between the two, regardless of the charge already residing on the particle. This effect occurs as a result of the rearrangement of the charge on the particle, caused by the electric field of the external charge. It is usually treated theoretically in terms of an induced image charge, with polarity opposite in sign to that of the external charge.[4] The range of the attractive force in the absence of an applied field is indicated by the graph in Figure 2, in which an attractive force is represented as a negative quantity. When an ion moves toward a particle with sufficient energy to approach to within the range of the attractive force, the ion attachment process is essentially accomplished, because the attractive force increases very rapidly as the distance from the particle decreases.

Since the diffusion velocities of ions are, in general, much greater than the drift velocity arising from the effect of an applied electric field, it might be expected that diffusion effects always dominate the charging process. But thermal velocities are random, and the associated mean free paths between collisions among molecules and ions are very short -- of the order of 0.01 μm. On the other hand, the presence of an electric field produces a directed ion velocity and also modifies the local field in the vicinity of each particle. In practice, both diffusion and field effects are important to the theory of particle charging. Among the various theories advanced, approaches have been made on the basis of field effects alone, diffusion effects alone, and combinations of the two.

CHARGING THEORIES

The total charge applied to a particle as a result of diffusion effects is[5]

$$q = \frac{akt}{e^2} \ln\left(\frac{1 + a\bar{v}\pi e^2 Nt}{2kt}\right) \qquad (1)$$

where

a = particle radius
k = Boltzmann constant
T = absolute temperature
$\bar{V}$ = mean molecular velocity
N = ion concentration
t = time interval
e = electron charge.

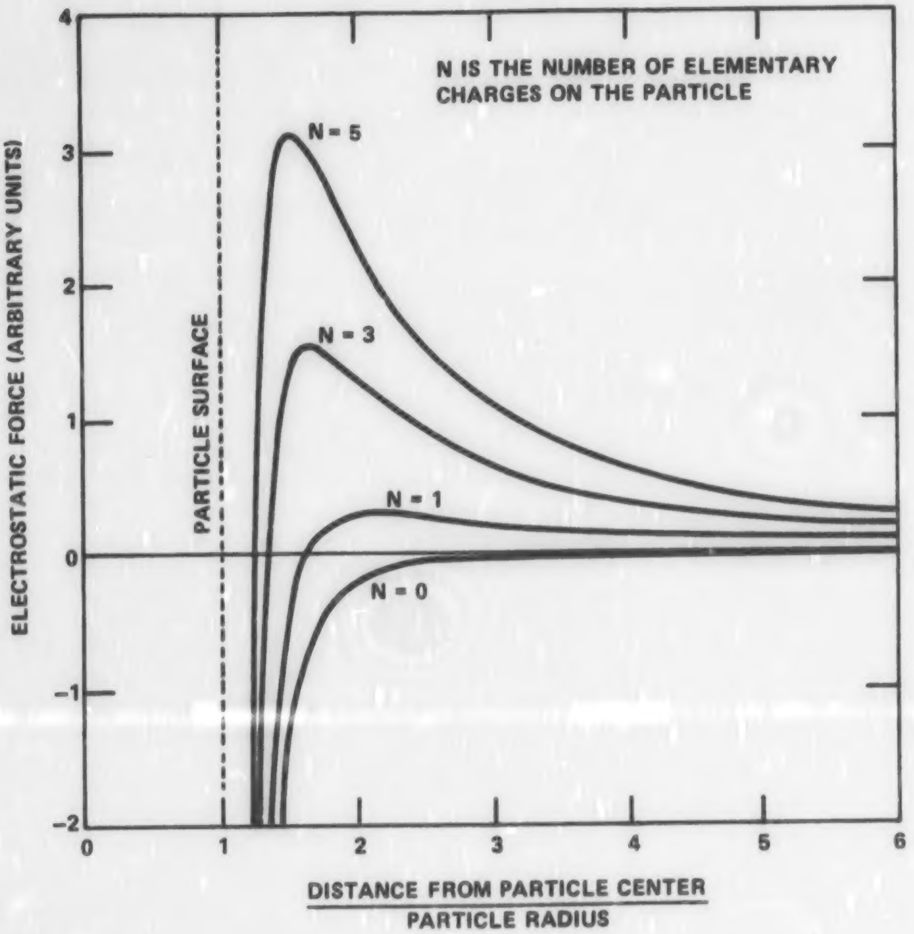

Figure 2. Electrostatic force between an ion and its image charge as a function of the distance between the particle and the ion. A positive value of force indicates repulsion.

Equation 1 does not depend on an applied electric field. The thermal energy kT and the diffusion velocity $\bar{v}$ determine the charging rate. This expression has been verified experimentally for particles smaller than approximately 0.2 μm in diameter. For larger particles this theory does not agree well with the experimental data. Charging theories for larger particles must, therefore, take into account the effects of the applied electric field.

Where the effects of an electric field dominate the charging process, the total charge accumulated by a particle having a radius a is[6]

$$q = \left(1 + 2\,\frac{K-1}{K+2}\right) Ea^2 \left(\frac{\pi Nte\mu}{1+\pi Nte\mu}\right). \tag{2}$$

In this expression

K = dielectric constant of the particle
E = applied electric field strength
μ = ion mobility.

Diffusion effects are ignored in this theory. Consequently, Equation 2 agrees well with experimental results only for particles larger than approximately 2 μm in diameter.

Various theories have been developed in attempts to combine effects of field and diffusion in the charging process. Currently in use at Southern Research Institute is the theory of Smith and McDonald,[7] which predicts the charging rate of particles on a statistical basis. Charging is principally attributed to the thermal motion of the ions. The electric field acts to enhance the probability of ion attachment by modifying the ion distribution in the neighborhood of a particle.

MEASURED EFFECTS OF CHARGING PARAMETERS

Figures 3 through 6 show the effects of various parameters on the charging process.[8] In Figure 3, experimental data are presented for particles ranging from 0.2 to 8.0 μm in diameter. Each curve corresponds to a given value of electric field strength, and the product Nt of the ion density and particle residence time in the charging region is held constant at 1.0×10^{13} sec/m^3 for all three curves. The charge per particle increases approximately as the square of the particle diameter for the larger sizes, where field charging dominates.

The effects of varying the product Nt are illustrated in Figure 4 for 2.0 μm diameter particles. The solid lines represent the theory of Smith and McDonald. The increase in accumulated charge per particle is relatively gradual after the initial sharp rise from zero.

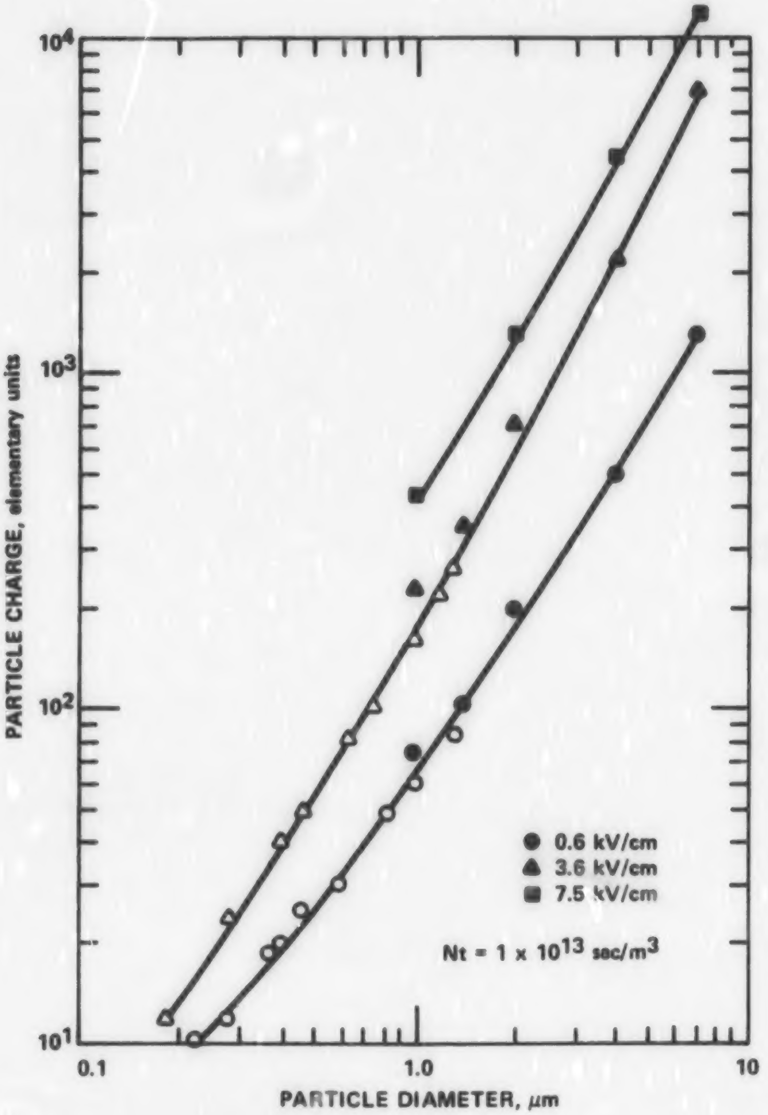

Figure 3. Particle charge versus diameter for DOP aerosols. The open symbols are Hewitt's data.[9] *The solid lines are the theory of Smith and McDonald.*[7]

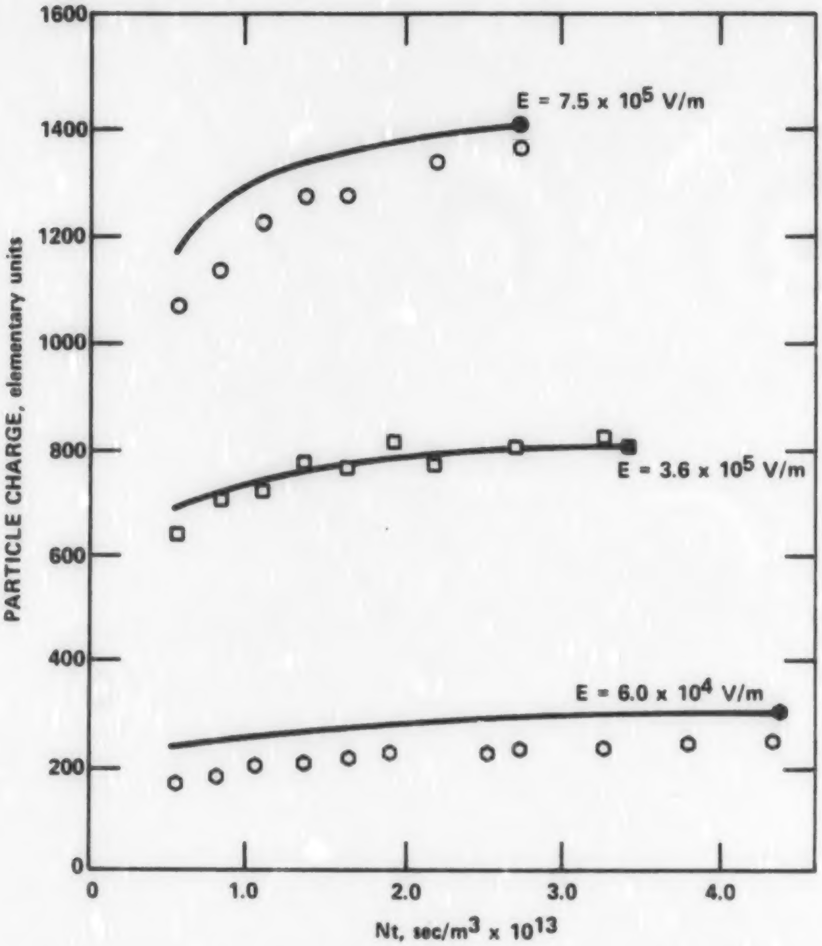

Figure 4. Comparison of experimental and theoretical values of particle charge for a 2.0 μm diameter DOP aerosol. The solid lines are the theory of Smith and McDonald.[7]

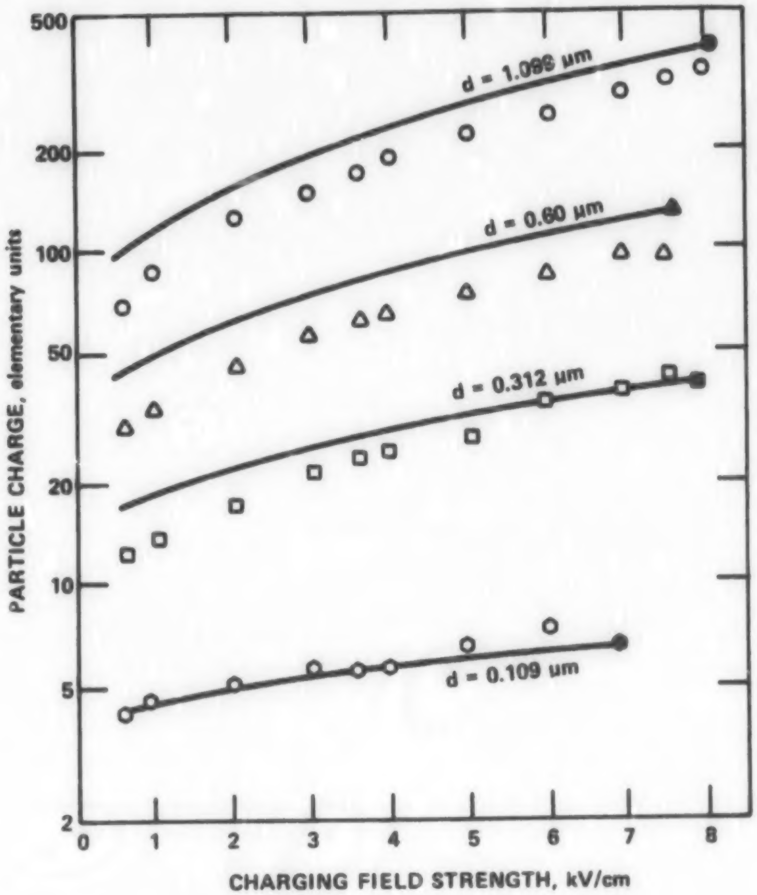

Figure 5. Number of charges per particle as a function of charging field strength for polystyrene latex particles of four different diameters. Nt product held constant at 1.0×10^{13} sec/m^3. Solid lines show the theory of Smith and McDonald.[7]

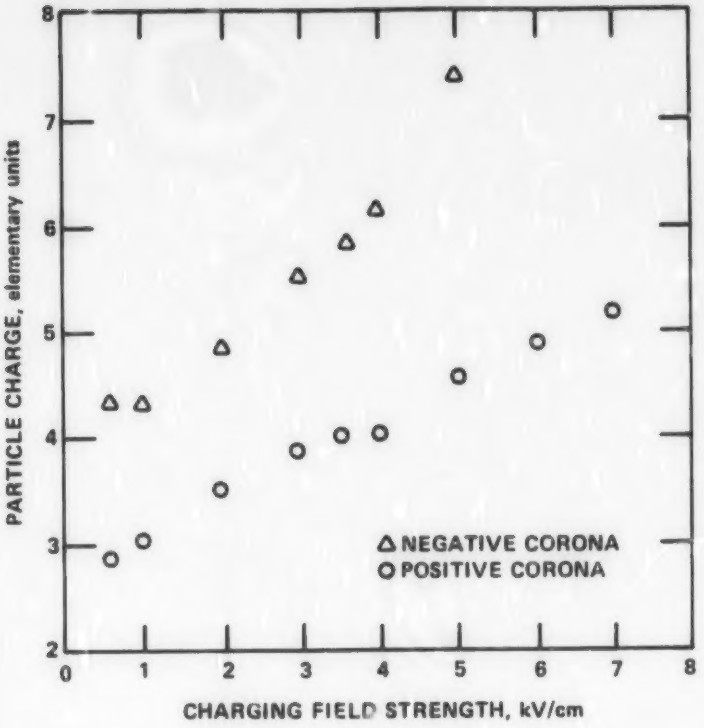

Figure 6. Comparison of positive and negative corona charging for 0.109 μm polystyrene latex spheres. For both sets of data Nt is 5.0 x 10^{12} sec/m^3.

Thus, for a fixed value of ion density, corresponding to a steady electrical operating condition, 2.0 μm particles will take on charge rapidly at first, after which the charge will approach a saturation value asymptotically. This behavior is generally followed when the field charging mechanism dominates.

Figure 5 shows the relationship between particle charge and electric field strength for four different particle sizes. The Nt product is 1.0 x 10^{13} sec/m^3. As in Figure 4, the solid lines represent calculated values based on the theory of Smith and McDonald.[7] Increased field strength has a more pronounced effect on charging for larger particles. For the smaller particles, charging is dominated by the diffusion mechanism, which is independent of electric field strength.

Experiments have shown that the polarity of the ion field has a strong effect on the charging rate. A comparison of charge per particle as a function of electric field strength for positive and negative corona is presented in Figure 6. The calculated value of Nt was 5.0×10^{12} sec/m^3 for these data. The enhanced charging associated with the condition of negative corona is generally attributed to the presence of free electrons in the charging region.

PROBLEMS ASSOCIATED WITH PARTICLE CHARGING

Theoretical considerations indicate that effective particle charging can be achieved by providing a prescribed electric field strength and ion density. In practice, however, conditions may arise which prevent the ideal charging conditions from being met. Two important problem areas are those related to the collection of particulate materials having high resistivity, and the presence of large number densities of fine particles.

High Resistivity

If the electrical resistivity of particles to be collected is very high, production of useful corona current may be severely limited by the generation of a back corona from the surface of the collecting electrode. Ions resulting from back corona are opposite in polarity from the ions generated at the discharge electrode. When both positive and negative ions are present simultaneously in the space between electrodes, the competing effects of the two produce very little effective particle charging.

Precipitation of particulate material having high resistivity was recognized as a problem as early as 1912, in a copper smelter application.[8] The limitation on current density caused by the presence of high resistivity particles affects both the diffusion charging and the field charging mechanisms, since both depend strongly upon ion density in the charging region.

Back corona arises from electrical breakdown across a layer of material deposited on the collection electrode. Electrical breakdown is, characteristically, a localized phenomenon which tends to cause a convergence of current toward the breakdown site, with a concomitant enhancement of the local electric field. The resulting increase in the electric field strength may be sufficient to develop a corona discharge at the point of breakdown in the particulate layer. Thus, ions may be injected into the charging region from the collecting electrode as well as from the discharge electrode, resulting in degradation of particle charging effectiveness.

The criterion for the onset of back corona may be expressed in terms of Ohm's law as applied to the condition of maximum permissible current density j_{max} for a given particulate resistivity ρ,

$$j_{max} = \frac{E_b}{\rho} , \qquad (3)$$

where E_b is the electrical breakdown field strength associated with the deposited particulate layer. If, for example, the resistivity is 10^{12} ohm cm and E_b is a typical value of about 10^4 V/cm, then the maximum permissible current density at the collection electrode is 10^{-8} A/cm^2 (9.3 μA/ft^2). Increasing the corona current beyond the onset of back corona in an electrostatic precipitator results in a rapid decline in efficiency because of the loss of charging effectiveness.

The external symptoms of back corona normally include an increase in current, because additional carriers are injected into the system from the passive electrode. Since Equation 3 is independent of the thickness of the particulate layer, it does not require a large accumulation of high resistivity material to cause back corona.

A number of different techniques have been used in attempts to control the effects of back corona. Methods based on altering the resistivity of the particulate material include addition of chemical conditioning agents and control of the temperature at the collection electrodes in a precipitator. In some instances, improvement in performance may be achieved by dividing a precipitator into sections, each with its own power supply. Onset of back corona depends on the peak value of corona current density at the passive electrode, rather than on the average current density. Thus, the optimum operating condition is that which provides the most uniform current density possible.

Space Charge Effects

Charging theories, in general, are based on the assumption that each particle may be considered independently, in that the ion density in the neighborhood of a particle is not affected by the proximity of other particles. This assumption loses validity, however, where the number density of particles approaches or exceeds that of the ions. If, for an extreme example, there are twice as many particles as ions passing through a given region per unit time, at least half of the particles must be completely uncharged when they emerge from the region.

For smaller relative number densities of particles, the results are less obvious, but the effects on the conduction properties of a corona system may be important. From the elementary theory of electrical conduction, the current density j in any region of space may be written as the sum of the contributions due to each carrier species, as

$$j = \sum_k N_k q_k \bar{v}_k \, , \tag{4}$$

where N_k is the number density of the kth species of charge carrier, q_k is the charge per carrier, and $\bar{v}_k$ is the average drift velocity of the carrier on the electric field. For a simple two-component system consisting of a single ion species and a monodisperse aerosol, Equation 3 becomes

$$j = N_i q_i \bar{v}_i + N_p q_p \bar{v}_p . \tag{5}$$

The subscripts i and p refer to the ions and particles, respectively. Under usual conditions the first term on the right-hand side of Equation 5 dominates the current, and only a very small part of the current is carried by charged particles. As particle charging proceeds, N_i in Equation 5 decreases while the product $N_p q_p$ increases. Ion drift velocities are, typically, hundreds of times greater than particle velocities. Thus, the charging process increases the coefficient of the larger velocity while decreasing the coefficient of the slower component, resulting in an overall reduction in the sum. If there are enough particles in the system to take on a significant fraction of the ions present, a measurable decrease in corona current will be observed.

The electric field in the space between electrodes in a corona system depends not only upon the applied voltage, but also upon the distribution of charge in that space. The charge residing on the relatively very slowly moving particles is essentially stationary compared with the charge associated with the free ions. Thus, under heavy particulate loading with fine particles, a virtually static space charge tends to build up in the conduction region. This charge has the same polarity as the corona discharge electrode, and hence it tends to depress the electric field strength near the discharge electrode. The field strength may become sufficiently reduced that a corona discharge can no longer be sustained.

Space charge effects are usually associated with the presence of fine particles. For a given mass loading, the number density of particles is inversely proportional to the cube of the particle diameter. The charge per particle under a fixed set of conditions increases no more rapidly than the square of the particle diameter. Thus, the total amount of charge attached to a particle in the charging region is approximately in inverse proportion to the particle diameter.

The space charge problem is quite fundamental in nature. Because it depends only upon the relative number densities of ions and particles, it can be alleviated only by designing the corona system to provide a sufficiently large ion density, or by diluting the number density of the particles before the gas stream enters the charging region.

REFERENCES

1. Leighton, R.B. Principles of Modern Physics. McGraw-Hill, New York, 1959. 795 pp.

2. Knutson, E.O., and K.T. Whitby. Aerosol Classification by Electric Mobility: Apparatus, Theory and Applications. J. Aerosol Sci. 6:443-451, 1975.

3. Viehland, L.A., and E.A. Mason. Gaseous Ion Mobility in Electric Fields of Arbitrary Strength. Ann. Phys. 91:499-533, 1975.

4. Jackson, J.D. Classical Electrodynamics. Wiley, New York, 1962. 641 pp.

5. Arendt, P., and H. Kallmann. The Mechanism of Charging of Cloud Particles. Z. Phys. 35:836-897, 1935.

6. Pauthenier, M., and M. Moreau-Hanot. Charging of Spherical Particles in an Ionizing Field. J. Phys. Radium [7] 3:590-613, 1932.

7. Smith, W.B., and J.R. McDonald. Development of a Theory for the Charging of Particles by Unipolar Ions. J. Aerosol Sci. 7:151-166, 1976.

8. White, H.J. Resistivity Problems in Electrostatic Precipitation. J. Air Pollut. Contr. Assoc. 24(4):315-338, 1974.

9. Hewitt, G.W. The Charging of Small Particles for Electrostatic Precipitation. Trans. Amer. Inst. Elec. Eng. Part 1 76:300-306, 1957.

PAPER 9

ADVANCED ELECTROSTATIC COLLECTION CONCEPTS

DENNIS C. DREHMEL
INDUSTRIAL ENVIRONMENTAL RESEARCH LABORATORY
ENVIRONMENTAL PROTECTION AGENCY

INTRODUCTION

The conventional approach in using electrostatics for abatement of particulate emissions is to collect charged particles in an electric field that also is responsible for the presence of ions which charged the particles. Alternatives to this approach involve precharging the particles and subsequent collection of the charged particles in a separate device. This collection device may use electrostatic forces or may introduce a collecting medium such as water droplets or a filter.

Possible electrostatic collection concepts are given in Table 1. Details for these concepts are given below. In general, the entries in Table 1 reflect the three major categories of collection mechanisms; that is, electric field effects, scrubbing, and filtration. In the case of the latter two, the combination of electrostatic effects with the conventional mechanisms permits enhanced performance of the new device as compared with conventional devices of the same type. It was the possibility of enhanced performance that was the stimulus for EPA's involvement in developing advanced electrostatic collection concepts. After 4 years' work under eight contracts and grants, many of the projects have produced conclusive results and the remainder continue to indicate potential success. This paper summarizes the progress made in developing advanced electrostatic collection concepts.

ELECTROSTATIC COLLECTION WITH DROPLETS

The use of water droplets in an electrostatic collection device will differ according to whether the drops are charged or not and whether there is an ambient electric field. The case of

TABLE 1. ELECTROSTATIC COLLECTION CONCEPTS

Name	Collection by means of	EPA activity
Two stage precipitator	Electric fields	C. 68-02-2114, Southern Research Institute
Electric curtain	AC electric fields	G. 803047, University of Illinois
Electrostatic scrubbing	Electric fields and water droplets	C. 68-02-0250, Massachusetts Institute of Technology C. 68-02-1345, TRW, Inc.
Charged droplet scrubbing	Water droplets	G. 803278, University of Washington G. 80493
Electrostatic fiber beds	Filter fibers	G. 801581, Battelle Northwest
Electrostatic effects in fabric filters	Filter fabric	G. 803020, Carnegie-Mellon

no ambient field with the drops charged to an opposite sign to that of the particles is the usual configuration for a charged droplet scrubber (CDS). The scrubber consists of three chambers: (1) a corona discharge section for particle charging; (2) a spray chamber which introduces oppositely charged droplets; and (3) a mist eliminator.

A second case is one in which there is no ambient field and the drops are not charged. This case may be called an electrostatically augmented scrubber (EAS) and consists of two sections: a corona discharge section and a conventional scrubber.

A third case, which does not use a precharging section as other devices in this section do, is one with an ambient field and charge on the drops imposed by the electric field. In this device, referred to as a charged droplet precipitator (CDP), there is only one chamber where the water is introduced into the middle from nozzles at high voltage. The drops leave the nozzle with a charge and are accelerated to the walls by the electric field.

Either through development programs as noted above or through field tests, an electrostatic device of each type has been tested and results are shown in Table 2. The CDS tested is the University of Washington electrostatic scrubber.[1] The scrubber was tested on a coal fired boiler side stream at 1655 to 1802 Am^3/hr and on an electric arc steel furnace side stream at 1754 to 3031 Am^3/hr. Performance of this scrubber is greatly influenced by the water to gas ratio. At the coal fired boiler site, doubling the ratio from 0.32 to 0.76 l/Am^3 halved the overall penetration from 3.9 to 1.9 percent. The power consumption was approximately 13 $W/(m^3/min)$ and the residence time was 8 seconds.

The EAS tested is the Air Pollution Systems electrostatic scrubber.[2] This scrubber consists of a venturi scrubber with an electrode placed upstream to do the precharging. The test aerosol was redispersed TiO_2 with a mass median diameter of 1 μm and a geometric deviation of 2.2. Since the scrubber is primarily a venturi, an important consideration is the pressure drop, which was 43 cm WC for the system including a cyclone entrainment separator. Summing the power consumption for the pressure drop and the ionizer, the total energy requirement was 80 $W/(m^3/min)$.

The CDP tested is the TRW charged droplet scrubber which was demonstrated on a coking oven battery exhaust.[3] The test unit had a capacity of 31,000 m^3/hr at a gas flow rate of 1.83 m/s with a residence time of 3 seconds. The scrubber operated with a low water rate of less than 0.14 l/Am^3 (1 gal./1000 acf). The total power consumption was 28-42 $W/(m^3/min)$. During the demonstration testing it was found that the TRW unit could be operated with very infrequent wall wash and that the efficiency was highest under this condition.

TABLE 2. COMPARISON OF ELECTROSTATIC DROPLET CONCEPTS

Concept	Unit Tested	Overall Efficiency, Percent	Water to Gas Ratio, l/Am^3	Percent Efficiency at	
				0.5 μm	1.0 μm
CDS	U. of Washington electrostatic scrubber	98.1 - 99.5[a]	0.76 - 0.77	99	97.5
CDS	U. of Washington electrostatic scrubber	96.4 - 98.6[b]	2.23 - 2.29	95	97
EAS	APS electrostatic scrubber	83 - 97[c]	1.44	96	90
CDP	TRW charged droplet	93.5[d]	0.11 - 0.13	90	85 - 95

[a] At a coal fired boiler.

[b] At an electric arc furnace.

[c] Total pressure drop is 43 cm WC

[d] Pooled data with no wall wash.

In comparing the performance of these concepts, it is important to note that water consumption rates can differ by an order of magnitude and power consumption by a factor of 2. All concepts provide high overall collection efficiencies and high efficiencies in removing the 0.5 μm diameter particle. It has been noted previously that penetrations range from 30 to 53 percent for 0.5 μm particles in conventional scrubbers.[4] Since penetrations for the 0.5 μm particle through the advanced electrostatic collection devices range from 1 to 10 percent, these concepts have demonstrated significantly enhanced performance. It is possible to increase the pressure drop in a venturi scrubber to decrease the penetration of 0.5 μm particles to 10 percent. The pressure drop required can be estimated by Calvert's equation 5.3.6-12 in the Scrubber Handbook.[5] The energy requirement for a venturi scrubber to collect 90 percent at a 0.5 μm particle size is 325 W/(m^3/min). This is an order of magnitude higher than the 28-80 W/(m^3/min) reported for the same performance with electrostatic droplet concepts.

ELECTROSTATIC COLLECTION WITH FILTERS

The use of filters with electrostatics will vary according to whether the filter uses fibers or a fabric as the collector. If it is a fiber collector, precharging the particles will enhance the collection efficiency. If it is a fabric collector, precharging the particles will change the nature of the deposited cake and correspondingly lower the pressure drop and may improve the collection efficiency.

The first case, referred to as an electrostatic fiber bed (EFB), was studied by Battelle Northwest.[6] Figure 1 shows the test apparatus. Three aerosols were studied: NH_4Cl, Na_2O, and MgO. All three aerosols had mass median diameters of less than 1 μm. The freshly generated particles were drawn first through a charge section and then through the fiber bed. The fiber beds had a void fraction of 0.96, were 15 or 30 cm thick, and were composed of stainless steel, polypropylene, or Teflon. Performance of the polypropylene beds is shown in Figure 2. Using a 30 cm bed, one can maintain a collection efficiency greater than 95 percent for bed velocities less than 1 m/s. The pressure drop through the clean bed was less than 1 cm WC.

The second case, that of precharging particles before a fabric filter or electrostatically augmented filter (EAF), has been studied by Carnegie-Mellon.[7] The filter was a 10 cm ID by 30 cm long bag made of woven material such as polypropylene without antistatic treatment. The aerosol was a silica dust charged either by impingement against a tungsten carbide surface or by corona discharge. The bags were pulse-jet cleaned. At an air-to-cloth ratio of 6, the EAF had a pressure drop of 6.4

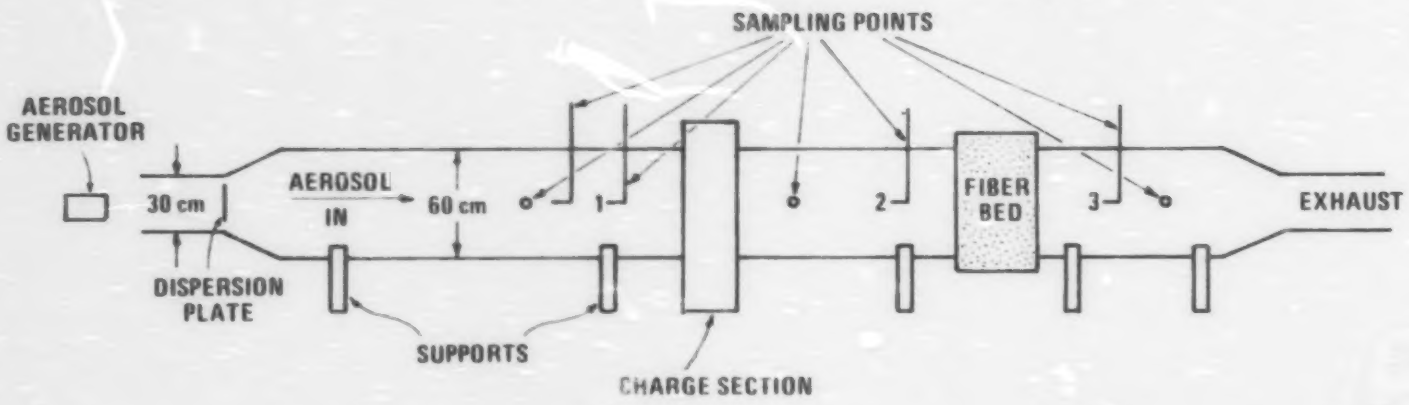
SAMPLING POINTS
AEROSOL GENERATOR
30 cm
AEROSOL IN
60 cm
1
2
FIBER BED
3
EXHAUST
DISPERSION PLATE
SUPPORTS
CHARGE SECTION

Figure 1. Electrostatic fiber bed schematic.

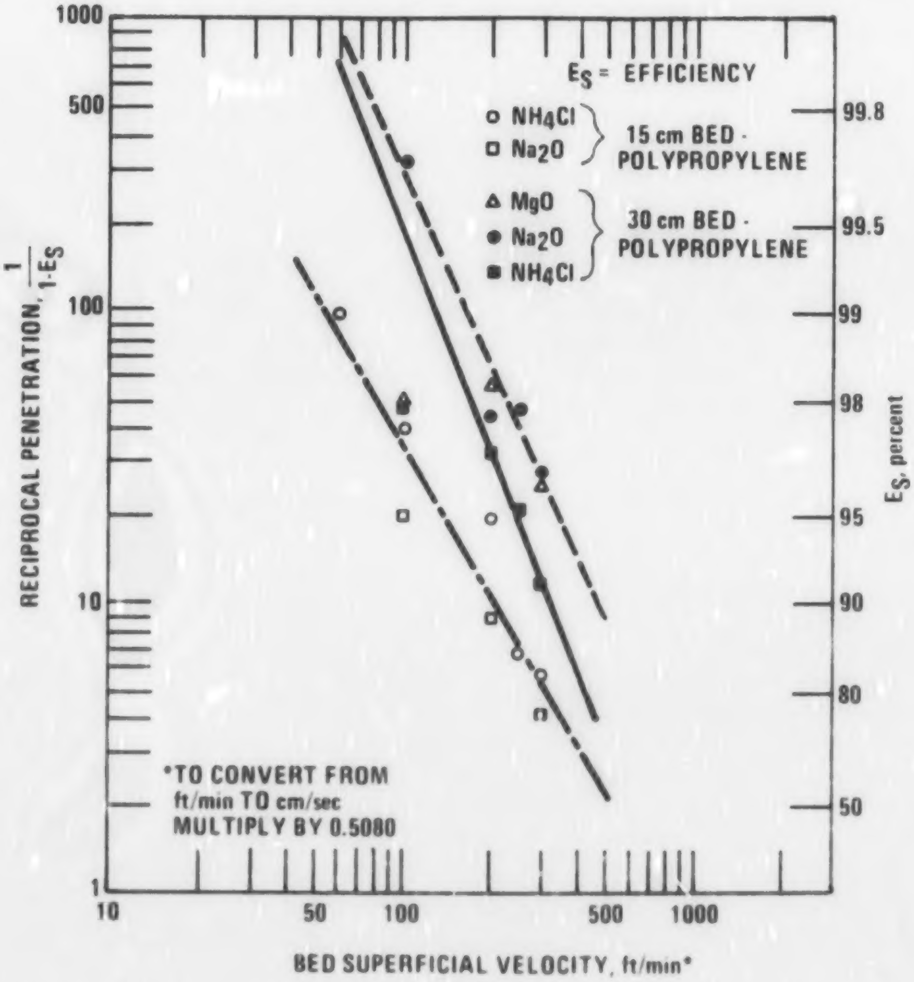

Figure 2. Fiber bed performance.

cm WC; a comparable bag without precharged particles had a pressure drop of 16.5 cm WC. Similar results have been reported by American Precision Industries, Inc.[8] Testing their EAF called the APITRON, American Precision Industries reports a reduction in pressure drop from 10 cm WC for a conventional filter to approximately 1 cm WC for the APITRON maintaining the same filtration rate on a steel furnace fume. If the pressure drop is the same for both filter types, the APITRON may be operated at a filtration rate 4 times greater. Since electrostatically augmented filters have demonstrated significant reductions in pressure drop at the same filtration rate (or significant improvements in filtration rate at the same pressure drop in conventional filters), this concept also has proven enhanced performance with electrostatics.

ELECTROSTATIC COLLECTION WITH AC FIELDS

In a recently completed study, the University of Illinois determined the feasibility of collecting charged particles with AC fields.[9] The device is called an electric curtain and is shown in Figure 3. The vertical plane of parallel rods is to act as a barrier to charged particles. The rods have a high voltage AC field and neighboring rods are either 180 or 120 degrees out of phase. Charged particles approaching the rods see a force sufficient to suspend them against gravity. However, in tests with fly ash particles, the highest air velocity against which the electric curtain could prevent penetration was approximately 1 cm/sec. This performance is no better than that for a conventional fabric filter. Under special circumstances this concept may have advantages but it appears that the electric curtain does not provide hoped-for enhanced performance.

CONCLUSIONS

Of the advanced electrostatic collection concepts studied, those employing water droplets or filters have demonstrated enhanced performance while that employing AC fields has not. Electrostatic collection with water drops shows high removal efficiencies for 0.5 μm particles which are difficult to capture. Electrostatic collection with filters shows the potential for operation at either lower pressure drops or higher filtration rates.

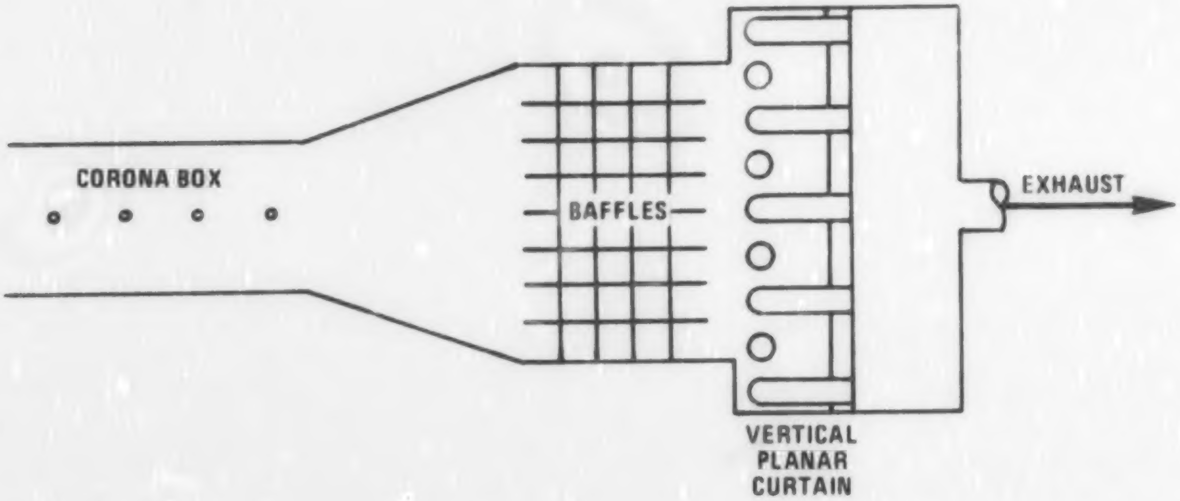

Figure 3. Electric curtain.

REFERENCES

1. Pilat, M.J., *et al*. Fine Particle Control with the UW Electrostatic Scrubber. Presented at the 2nd Fine Particle Scrubber Symposium, May 2-3, 1977, New Orleans, LA.

2. Calvert, S., *et al*. APS Electrostatic Scrubber Evaluation. EPA-600/2-76-154a, U.S. Environmental Protection Agency, Research Triangle Park, NC, 1976. NTIS PB 256335/AS.

3. Krieve, W.F., and J.M. Bell. Charged Droplet Scrubber for Fine Particle Control: Pilot Demonstration. EPA-600/2-76-249b, U.S. Environmental Protection Agency, Research Triangle Park, NC, 1976. NTIS PB 260474/AS.

4. Abbott, J.H., and D.C. Drehmel. Control of Fine Particle Emissions. Chem. Eng. Progr. 72(12):47-51, 1976.

5. Calvert, S., *et al*. Wet Scrubber System Study, Volume I. Scrubber Handbook. EPA-R2-72-111a, U.S. Environmental Protection Agency, Research Triangle Park, NC, 1972. NTIS PB 213016.

6. Reid, D.L., and L.M. Browne. Electrostatic Capture of Fine Particles in Fiber Beds. EPA-600/2-76-132, U.S. Environmental Protection Agency, Research Triangle Park, NC, 1976. NTIS PB 260590/AS.

7. Penney, G.W. Using Electrostatic Forces to Reduce Pressure Drop in Fabric Filters (to be published). Work performed under Grant No. 803020.

8. Helfritch, D.J., and T. Ariman. Electrostatic Filtration and the APITRON. Presented at the EPA/NSF New Concepts Symposium, April 20-22, 1977, Notre Dame, IN.

9. Yen, A., *et al*. Electric Curtain Device for Control and Removal of Fine Particles. EPA-600/2-77-055, U.S. Environmental Protection Agency, Research Triangle Park, NC, 1977. NTIS PB 266094/AS.

PAPER 10

PERFORMANCE OF A WET ELECTROSTATIC PRECIPITATOR IN AN ALUMINUM PROCESSING FACILITY

JOHN P. GOOCH
JOSEPH D. McCAIN
SOUTHERN RESEARCH INSTITUTE

AND

LESLIE E. SPARKS
INDUSTRIAL ENVIRONMENTAL RESEARCH LABORATORY-RTP
ENVIRONMENTAL PROTECTION AGENCY

INTRODUCTION

This paper presents the results obtained from a performance test conducted for the U.S. Environmental Protection Agency by Southern Research Institute on a wet electrostatic precipitator collecting fume from horizontal stud Soderberg (HSS) aluminum reduction cells. The objectives of the test series were (1) to determine the fractional and overall particulate collection efficiency of the electrostatic precipitator and (2) to compare the measured performance of the precipitator with that projected from a mathematical model.

At the reduction plant, wet precipitators are installed both with and without spray towers prior to the precipitators. Because the occurrence of condensation within the precipitator itself confuses the interpretation of the data, it was decided to conduct the test series on a unit which is preceded by two spray towers, to minimize this effect. The spray towers treat exhaust gas from 28 pots with an alkaline solution which cools the gas from about 105°C (220°F) to about 38°C (100°F). Figure 1 shows the arrangement of the wet precipitator, scrubbers, sampling locations, and a schematic of the liquor flow through the system given by Bakke.[1]

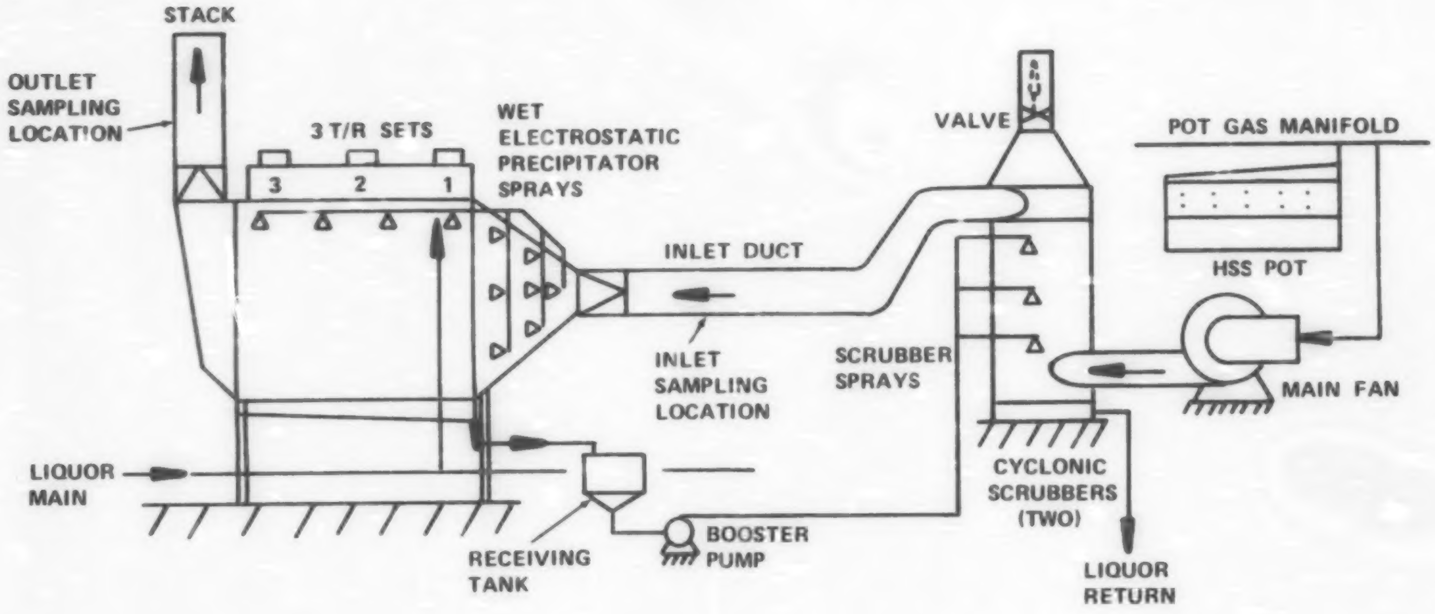
STACK
OUTLET SAMPLING LOCATION
3 T/R SETS
3
2
1
WET ELECTROSTATIC PRECIPITATOR SPRAYS
INLET DUCT
INLET SAMPLING LOCATION
LIQUOR MAIN
RECEIVING TANK
BOOSTER PUMP
SCRUBBER SPRAYS
VALVE
CYCLONIC SCRUBBERS (TWO)
LIQUOR RETURN
POT GAS MANIFOLD
HSS POT
MAIN FAN

Figure 1. Schematic of primary emission control system.

Horizontal stud Soderberg cells are of the "self-baking" type, in that the carbon electrode is baked within the cell. The effluent from the cell therefore contains hydrocarbons volatilized from the binders used to make the anode. Other constituents include HF gas, which results from hydrolysis of fluoride salts, particulates of vaporized bath materials, and alumina, cryolite, and other dusts entrained from the bath crust. During the course of the test period, routine operations were in progress on the cells which supply the scrubber-precipitator system. These operations include the breaking of the crust in each cell at approximately 2 hr intervals, and anode maintenance operations known as "pin and channel pulls" and "flex raises". The anode maintenance and the crust breaking are performed on the cells on an individual basis. Thus the effect of the individual operations on the total particulate concentration entering the wet precipitator is somewhat damped.

DESCRIPTION OF THE WET ELECTROSTATIC PRECIPITATOR

The wet electrostatic precipitator on which this test series was conducted is a wire and plate design with three electrical sections in series in the direction of gas flow. Plate-to-plate spacing is 30.5 cm (1 ft), and each collecting electrode is 1.83 m (6 ft) long and 7.52 m (25 ft) high. Thus, the total parallel plate collecting electrode length is 5.48 m, or 18 ft. Each electrical set powers 28 gas passages. Figures 2 and 3, taken from the manufacturer's literature, illustrate the overall precipitator arrangement and the electrode design, respectively. The total parallel plate collecting area is 2343 m^2(25,200 ft^2), and the "transverse baffles", which are perpendicular to the gas flow, provide additional collecting electrode area. The effective collecting area provided by these baffles was estimated as 390 m^2(4200 ft^2), resulting in a total collection area of 2732 m^2 (29,400 ft^2). Average specific collecting area during the test series was therefore 62 $m^2/(m^3/sec)$, or 315 $ft^2/(1000$ cfm). Electrode irrigation is provided by sprays at the precipitator inlet and above the collection plates. The sprays provide a mist which is collected along with the particulates in the flue gas, and the electrode cleaning is accomplished by the coalescence and subsequent downward flow of the collected spray droplets. The sprays are operated continuously, except for those installed near the precipitator outlet, which are operated only periodically. These spray nozzles were not in operation during the test program.

Table 1, provided by the manufacturer,[1] summarizes the specifications for the wet precipitator installation. The irrigating fluid is a high pH sodium-based liquid which is returned to clarifiers and a cryolite recovery plant. Plant personnel reported that the cryolite recovery system is essentially a closed liquid loop, which results in a solids content of about

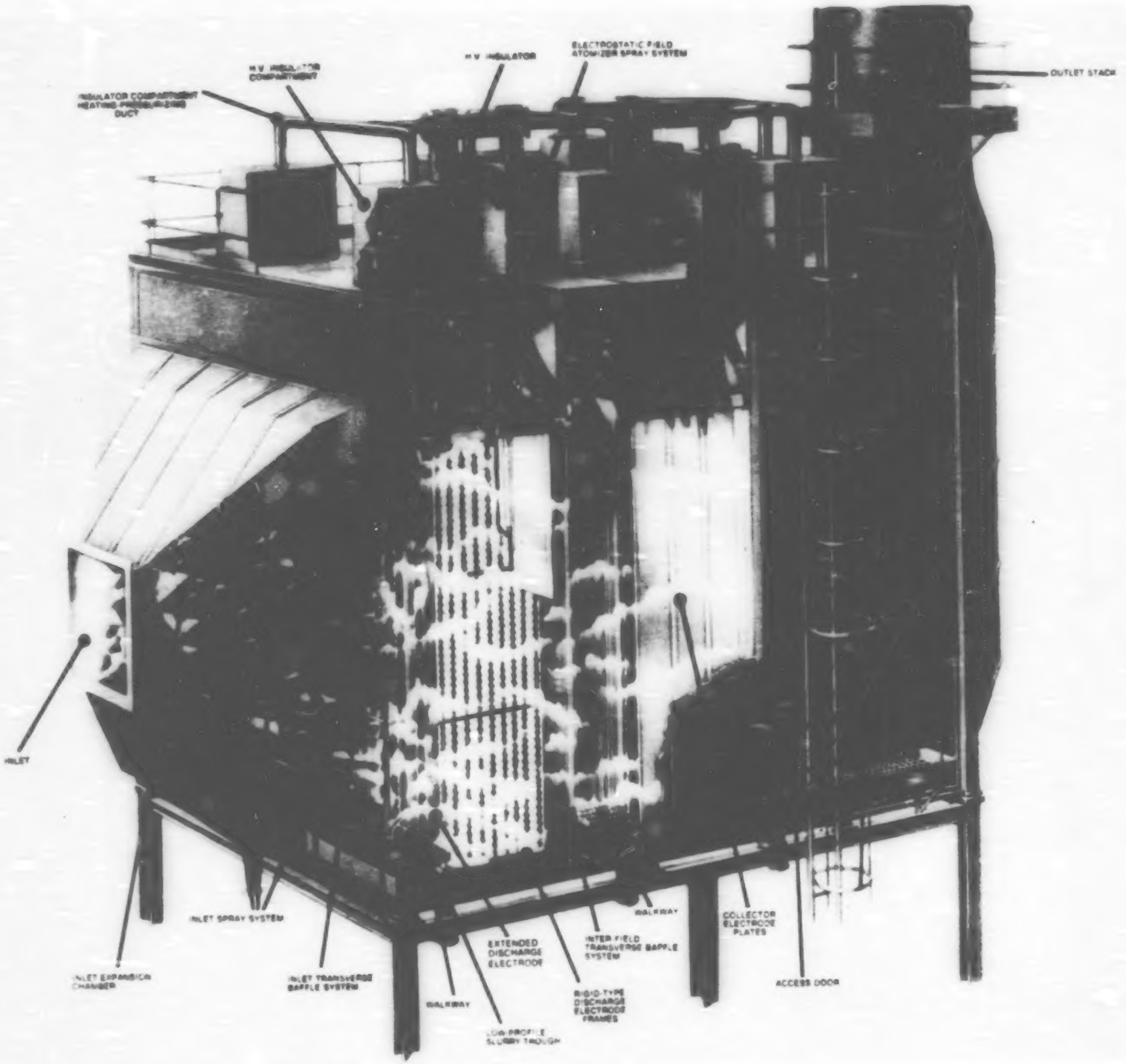
INSULATOR COMPARTMENT HEATING-PRESSURIZING DUCT
H.V. INSULATOR COMPARTMENT
H.V. INSULATOR
ELECTROSTATIC FIELD ATOMIZER SPRAY SYSTEM
OUTLET STACK
INLET
INLET EXPANSION CHAMBER
INLET SPRAY SYSTEM
INLET TRANSVERSE BAFFLE SYSTEM
WALKWAY
LOW-PROFILE SLURRY TROUGH
EXTENDED DISCHARGE ELECTRODE
RIGID-TYPE DISCHARGE ELECTRODE FRAMES
INTER FIELD TRANSVERSE BAFFLE SYSTEM
WALKWAY
COLLECTOR ELECTRODE PLATES
ACCESS DOOR

Figure 2. Wet electrostatic precipitator.

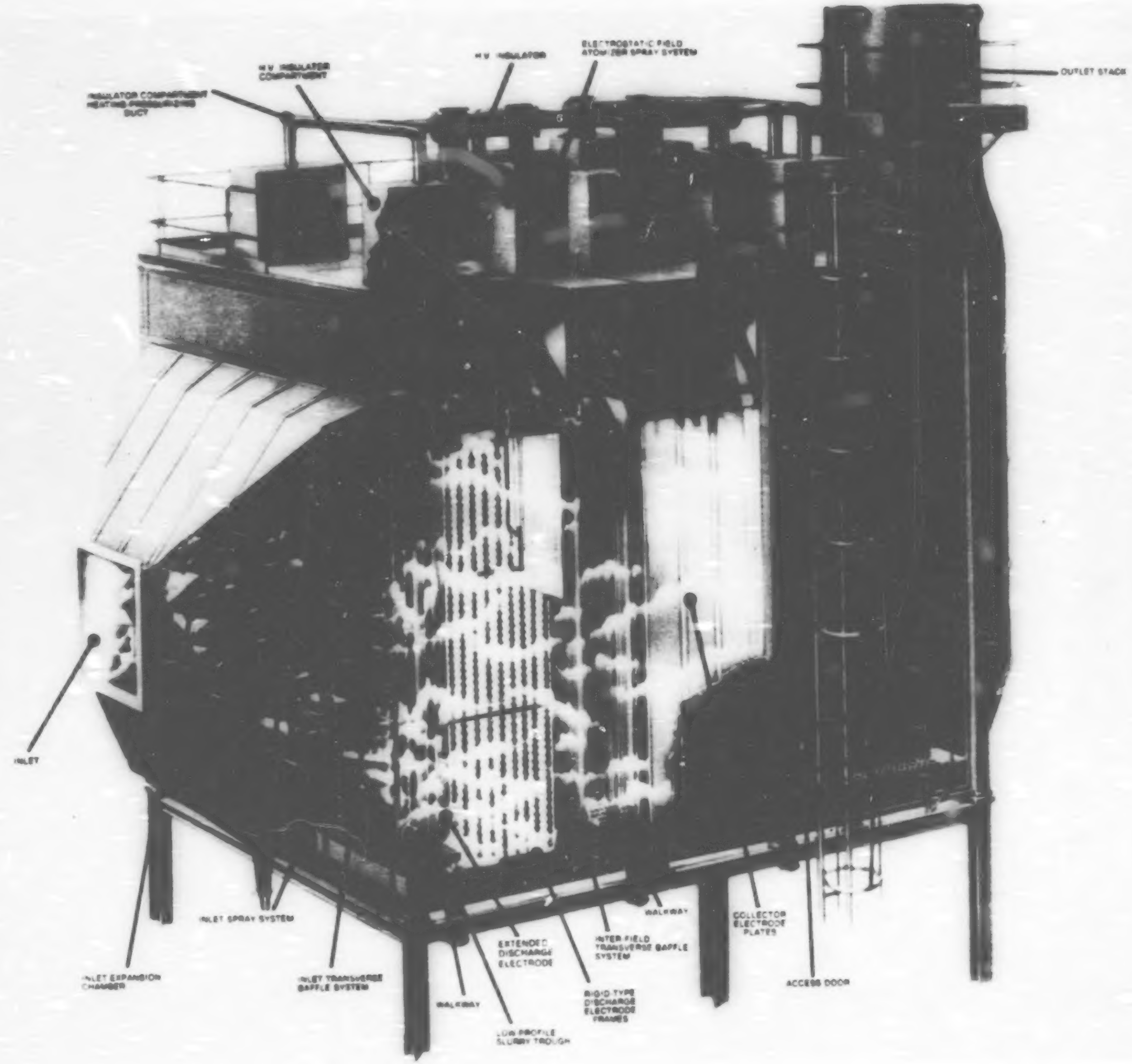
INSULATOR COMPARTMENT HEATING-PRESSURIZING DUCT
H.V. INSULATOR COMPARTMENT
H.V. INSULATOR
ELECTROSTATIC FIELD ATOMIZER SPRAY SYSTEM
OUTLET STACK
INLET
INLET SPRAY SYSTEM
INLET EXPANSION CHAMBER
INLET TRANSVERSE BAFFLE SYSTEM
WALKWAY
EXTENDED DISCHARGE ELECTRODE
LOW PROFILE SLURRY TROUGH
RIGID TYPE DISCHARGE ELECTRODE FRAMES
INTER-FIELD TRANSVERSE BAFFLE SYSTEM
WALKWAY
COLLECTOR ELECTRODE PLATES
ACCESS DOOR

Figure 2. Wet electrostatic precipitator.

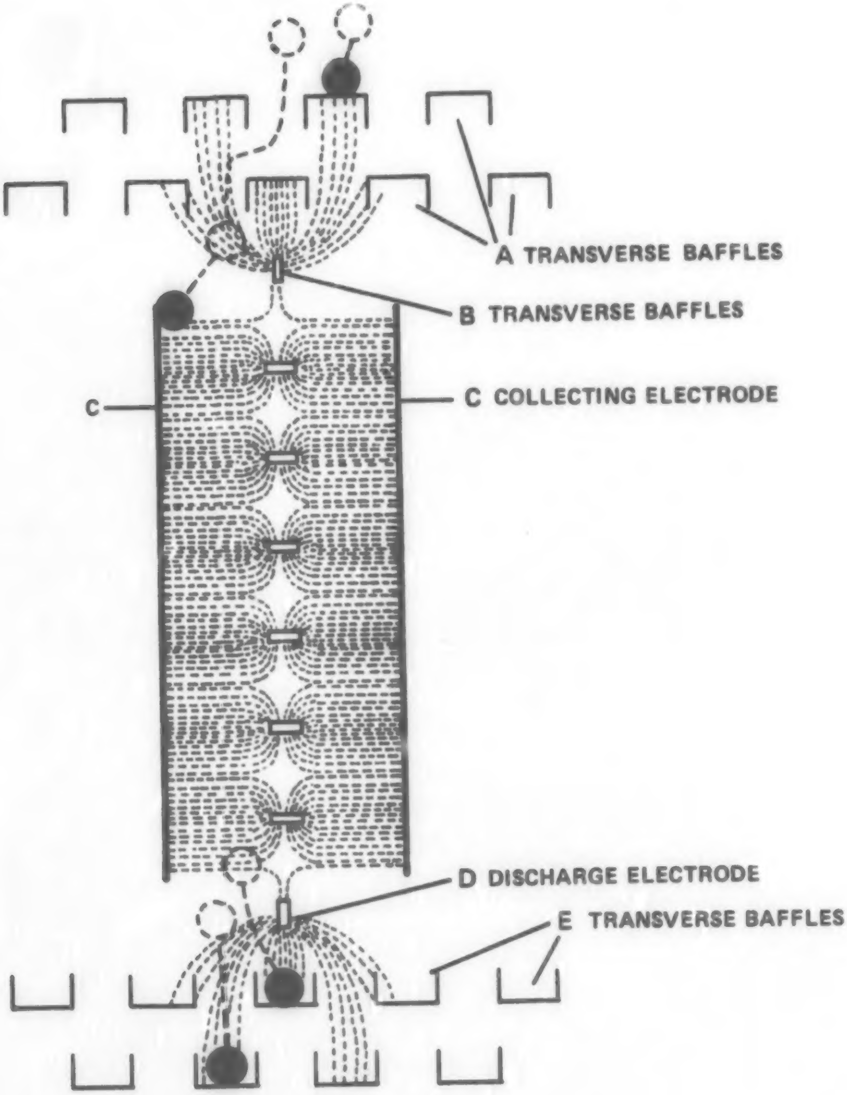
A TRANSVERSE BAFFLES
B TRANSVERSE BAFFLES
C
C COLLECTING ELECTRODE
D DISCHARGE ELECTRODE
E TRANSVERSE BAFFLES

Figure 3. Schematic of electrode arrangement.

5% by weight being returned to the wet ESP/scrubber system. Liquor flow through the wet ESP during the test program was constant at 31.5 l/sec (500 gal./min), which gives a liquid to gas ratio of about 0.7 l/m^3 (5.3 gal./1000 ft^3). Liquor temperature, based on measurements reported by plant personnel, ranges from 32°C (90°F) to 40°C (104°F), and is usually 34°C (94°F) to 35°C (95°F). No significant temperature drop has been observed in the liquor loop across the precipitator.

TABLE 1. SUMMARY OF SPECIFICATIONS FOR THE WET ELECTROSTATIC PRECIPITATORS[1]

Gas flow	100,000 scfm, or 47.2 m^3/sec, at standard conditions
Inlet temperature to scrubbers	121°C
Inlet temperature to WESP	38.1°C - 43.7°C
Total particulate inlet loading (solids and condensables, excluding water)	0.05 gr/scf, or 0.114 g/m^3, at standard conditions
No. of electrostatic fields	3
Liquor flow rate at 60 psi (4.14×10^6 dynes/cm^2)	500 gpm or 31.5 l/sec
Liquor pH	7-10
Outlet loading for an inlet loading of 0.05 gr/scf (0.114 g/m^3) or less	0.003 gr/scf, or 0.0069 g/m^3, at standard conditions
Minimum collection efficiency for outlet loadings greater than 0.003 gr/scf (0.0069 g/m^3)	95%
Face velocity	2.38 ft/sec, or 0.726 m/sec
Maximum pressure drop	1 in. WG, or 2.54 cm WG
Treatment time	10.1 sec
Housing material, hot rolled MS, thickness	3/16 in., or 0.476 cm

(continued)

TABLE 1 (continued)

Collection plates, hot rolled MS, thickness	10 gauge
Discharge electrodes, flatbars MS	1 in. x 1/8 in., or 2.54 cm x 0.318 cm
Piping materials	PVC
Spray nozzles, SS 316, type	Full cone
No. of transformer/rectifiers	3
Rectifier type	Silicon
Wave form	Full
Minimum output per T/R set	60 kV, 1000 mA
Primary voltage	480 V, 60 Hz
Voltage and spark rate control	Manual and automatic

ELECTRICAL CONDITIONS

Voltage and current readings were obtained from the panel meters of the precipitator periodically during the test program. At the conclusion of the test program, voltage-current curves were obtained for the unit with the spray system operating normally. The secondary voltage-current relationships are given in Figure 4, along with the range of operation that was observed for each electrical set during the test program. The difference between the voltage-current curves and the operating ranges is a result of the fact that, in normal operation, the power supplies are operating under automatic control with a certain spark rate, whereas the V-I curves were obtained by manually increasing the applied voltage until sparking occurred. The plant personnel were operating the power supplies at a spark rate which was believed to maximize the time-averaged electric field.

The V-I curve for the first electrical set is shifted toward high voltages for a given current when compared with readings from the other electrical sets. This behavior is often observed and is a reflection of the higher space charge density contributed by the higher particulate loadings which exist in the inlet field. Although the third field operates at a relatively high current, the average current density for all three sets was only about 30 nA/cm^2. The current density limitation was imposed by sparking, since the electrical resistivity of the particulate is not a factor in the wet mode of operation.

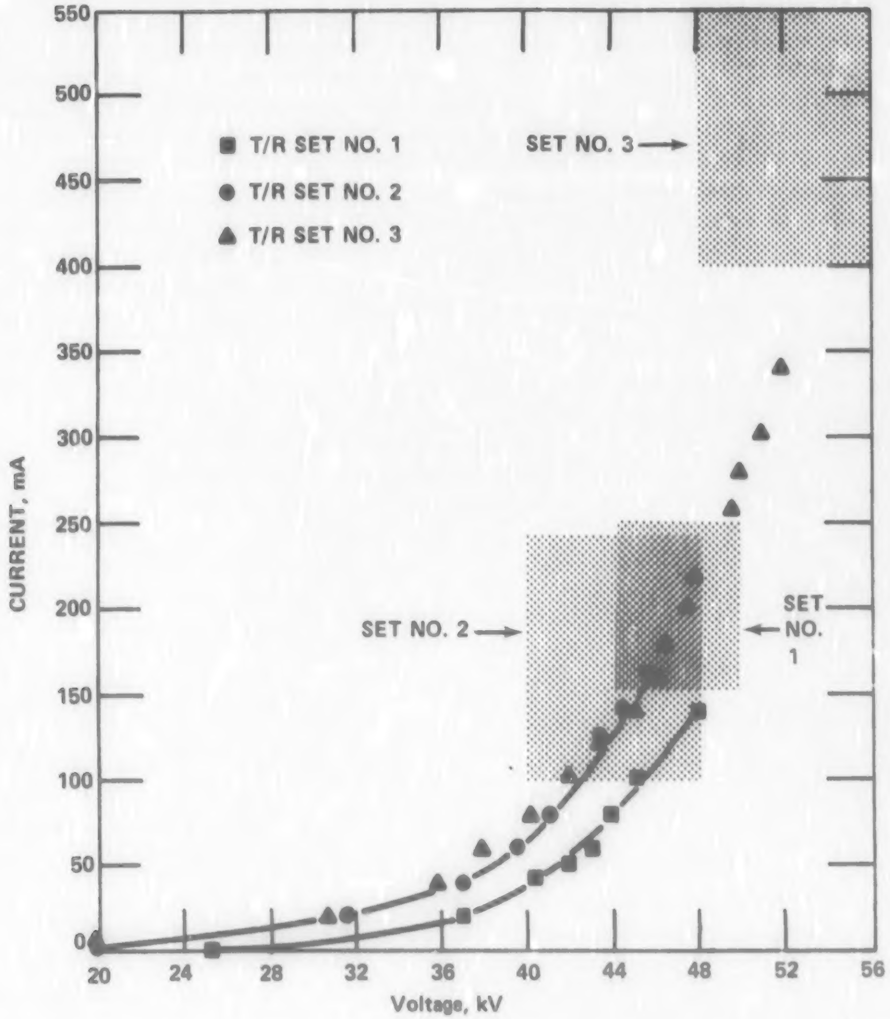

Figure 4. Voltage-current relationship (Manual Control) (points and lines) and operating ranges (Automatic Control) (shaded).

MEASUREMENT TECHNIQUES

Particle Size Measurements

Particle size and concentration measurements were conducted using the following methods: (1) diffusional techniques using condensation nuclei counters and diffusion batteries for determining concentration and size distribution on a number basis for particles having diameters less than approximately 0.2 μm, (2) optical techniques for determining concentrations and size distributions for particles having diameters between approximately 0.3 μm and 1.5 μm, and (3) inertial techniques using cascade impactors for determining concentrations and size distributions on a mass basis for particles having diameters between approximately 0.25 μm and 5.0 μm. A detailed description of these measurement techniques is given elsewhere;[2] therefore, only a brief discussion will be given in this paper.

For optical and diffusional measurements, extensive dilution of the gas stream being sampled is usually required because of the limitations imposed by the useful ranges of both the optical counter and condensation nuclei counter. Dilution ratios ranging from zero to 20 were used at the outlet, and from 30 to 90 at the inlet. As a general practice, checks of the linearity of particle count with dilution changes are performed to determine whether any anomalies resulting from condensation or other phenomena are occurring within the measurement system.

Due to limitations imposed by equipment availability, it was not possible to obtain simultaneous measurements at the precipitator inlet and outlet with the optical and diffusional instruments. However, the particulate concentrations were sufficiently stable to enable meaningful fractional efficiency data to be derived by first obtaining inlet data, and subsequently moving the equipment to the outlet to obtain the outlet data.

The optical particle counter was calibrated with polystyrene latex spheres. The indicated diameters of the particulate in the stack gas can differ from the true diameters because of the effect of refractive index differences on results obtained from the particle counter. In order to check the diameter obtained for this effluent, the diffusion batteries were used as sedimentation chambers, and particle diameters obtained from calculated sedimentation rates were compared with the indicated optical particle diameters. This comparison indicated fair agreement between the sedimentation diameters, which are independent of refractive index, and the equivalent optical diameters.

Andersen impactors were used simultaneously at the precipitator inlet and outlet on August 20, 21, 22, and 23. Isokinetic sampling was performed at a single point for both the inlet and outlet. Due to the extremely low mass loadings at the outlet, it was necessary to operate the impactors for approximately 16 hours in order to obtain weighable quantities of particulate. Since the gas phase contains condensable hydrocarbons, gaseous fluorides, and water vapor, and is near the water vapor saturation temperature, condensation, evaporation, and chemical reaction pose potential interference problems for impactor mass measurements. In an effort to determine the order of magnitude of some of these potential interferences, two Andersen impactor "blank" runs were made with a filter prior to the impactors. The blank runs gave an estimate of the weight loss or gain which could be expected due to reactions between the gas phase and the fiberglass substrates. Although the blank impactors were heated above the stack temperature prior to sampling, condensation occurred in the upper region of the impactor. The condensation was apparently caused by relatively short-term temperature variations in the outlet stack. For the runs used for size determinations, the impactors were heated to about 49°C (120°F) to avoid the condensation problem.

Table 2 gives the weight changes obtained from the "blank" impactor runs. No data were obtained with the first stages of the blanks due to the condensation problem. These blank changes were not significantly greater than those which may normally occur due to handling of the glass fiber substrates, and were therefore not considered to pose a serious interference problem.

TABLE 2. WEIGHT CHANGES OF ANDERSEN SUBSTRATES AFTER SAMPLING FILTERED EFFLUENT FROM WET ESP

	Sampling Time	
Stage	240 min	103 min
1	-	-
2	+0.06 mg	+0.02 mg
3	-0.04	-0.04
4	-0.02	+0.04
5	+0.08	-0.04
6	-0.12	-0.16
7	-0.08	-0.10
8	-0.12	-0.10
Average	-0.03	-0.05

Mass Loading Measurements

A modified EPA sampling train with an in-stack filter holder (the same filter used for the EPA train) was used for the mass loading measurements. The filter holder was Teflon-coated to avoid interference problems which might be caused by corrosion of metal surfaces. Mass loading determinations were conducted at the inlet and outlet simultaneously with the impactor runs. An isokinetic traverse across the stack was conducted at both the precipitator inlet and outlet through a single sampling port at each location for all but the last day of the test series. On that date, a single point mass determination was performed at the outlet. As with the Andersen impactors, it was necessary to heat the outlet filter holder to approximately 49°C (120°F) to avoid gross amounts of condensation. However, the filters were still slightly damp (both inlet and outlet), and consequently were placed in an oven at 49°C (120°F) for a few hours prior to desiccation and weighing.

RESULTS

Impactor Measurements

Tables 3 and 4 present results obtained from the Andersen impactors during the four days of testing with these devices. The outlet results are tabulated as the mass gain per stage to enable comparison with the "blank" weight changes given in Table 2. Note that the weight changes for the blanks are in general not proportional to the sampling time. Although the blank changes represent a significant fraction of the stage weights obtained during the outlet sampling, there is sufficient mass to enable meaningful conclusions to be drawn from the data. Figures 5 and 6 give the mass loadings at the inlet and outlet, respectively, on a cumulative basis, and Figure 7 gives the average inlet and outlet size distributions from the Andersen impactor data on log probability co-ordinates. No corrections were made for the blank weight changes. The mass median diameters of both inlet and outlet distributions are less than 1.0 μm. The average outlet size distribution, and all subsequent calculations involving the outlet Andersen impactor measurements, were obtained using runs 04, 05, and 06. Run 03 was discarded because it appeared to collect an anomalously low amount of mass when compared with the other three data sets.

Figures 8 and 9 are plots of dM/d log D from the Andersen impactor measurements at the inlet and outlet, respectively. Both of the distributions appear to be bimodal. The first peak occurs at about the same particle diameter for both the inlet and outlet data, but the second peak for the outlet is shifted to the left on the diameter axis. These data were used to obtain the efficiency as a function of particle diameter given in Figure 10. The midpoints were obtained from the average

TABLE 3. ANDERSEN INLET DATA

Run No.	AI-2	AI-4	AI-5	AI-7	AI-8	AI-9	AI-11	AI-12	AI-14	AI-16	AI-17	Avg.	Avg. %
Date	8/20/74	8/20/74	8/20/74	8/21/74	8/21/74	8/21/74	8/21/74	8/22/74	8/22/74	8/23/74	8/23/74		
Total Mass, mg/am^3	88.2	60.7	57.2	39.7	73.8	83.2	80.9	128.5	82.9	92.6	100.8	80.77	
Upper Size Limit, µm	Cumulative Mass, mg/am^3												
10.0	65.8	53.0	51.2	37.0	63.1	75.8	72.8	112.0	74.9	82.9	91.1	70.87	87.7
7.01	59.9	50.4	47.9	36.0	58.6	72.2	68.1	105.0	72.5	68.1	85.7	65.85	81.52
4.33	57.2	49.8	46.6	35.2	55.9	69.8	65.2	99.8	71.8	65.0	81.1	63.4	72.49
3.05	56.0	49.3	46.2	33.5	53.9	68.5	63.7	96.7	71.5	63.3	78.0	61.87	76.60
1.99	54.6	48.7	45.1	33.0	52.5	67.2	61.9	92.9	70.3	61.6	74.0	60.16	74.49
0.93	44.1	38.7	37.0	29.2	46.1	61.2	57.1	72.6	62.3	54.2	60.1	51.14	63.32
0.56	32.4	27.8	28.1	22.4	34.6	49.4	49.3	47.0	48.3	37.3	37.8	37.67	46.64
0.40	22.4	19.0	20.1	14.5	23.2	34.8	36.5	30.5	31.0	23.9	23.8	25.43	31.48

TABLE 4. ANDERSEN OUTLET DATA

Stage No.	Stack D_{50}, Upper size limit for cumulative, µm	Run Number								Avg. mg/am^3 for 04,05,06 cum.
		03		04		05		06		
		mg	mg/am^3 cum.	mg	mg/am^3 cum.	mg	mg/am^3 cum.	mg	mg/am^3 cum.	
1	10.3	0.28	0.582	0.34	0.847	0.40	0.848	0.44	0.719	0.805
2	7.2	0.14	0.570	0.26	0.824	0.32	0.820	0.34	0.691	0.778
3	4.4	0.10	0.561	0.20	0.807	0.44	0.782	0.44	0.655	0.748
4	3.1	0.10	0.552	0.26	0.748	0.44	0.744	0.32	0.628	0.707
5	2.1	0.14	0.540	0.28	0.759	0.44	0.706	0.40	0.596	0.687
6	1.0	0.08	0.533	0.46	0.719	0.22	0.687	0.40	0.563	0.656
7	0.6	0.66	0.476	1.26	0.609	1.38	0.568	1.10	0.472	0.550
8	0.4	1.00	0.389	2.18	0.418	1.94	0.400	1.58	0.343	0.387
Filter		4.46		4.78		4.62		4.18		
Total mass loading, mg/am^3			0.606		0.877		0.882		0.755	0.838

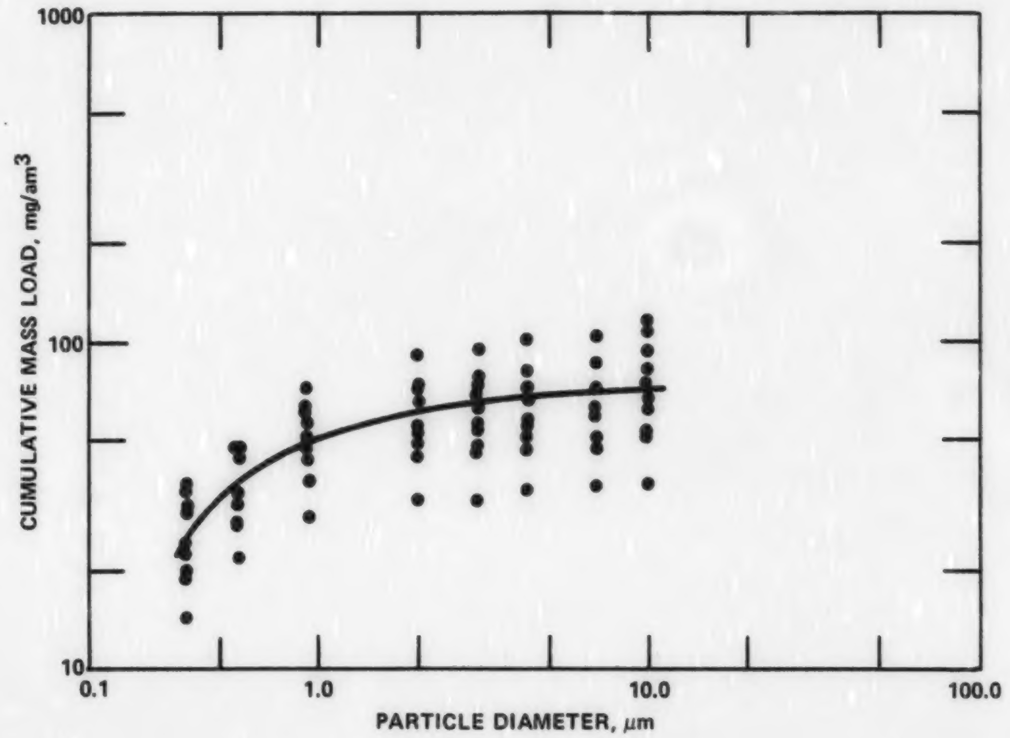

Figure 5. Cumulative mass load vs. particle diameter, at electrostatic precipitator inlet, from Andersen impactor data.

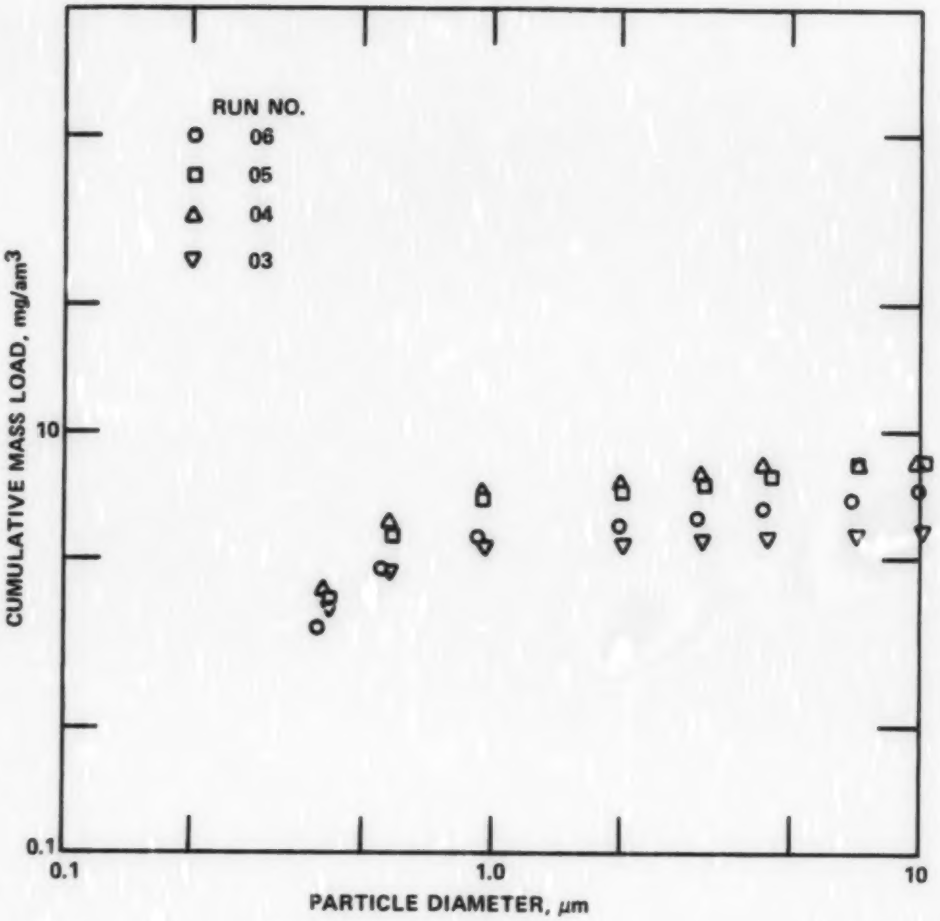

Figure 6. Cumulative mass load vs. particle diameter, at electrostatic precipitator outlet, from Andersen impactor data.

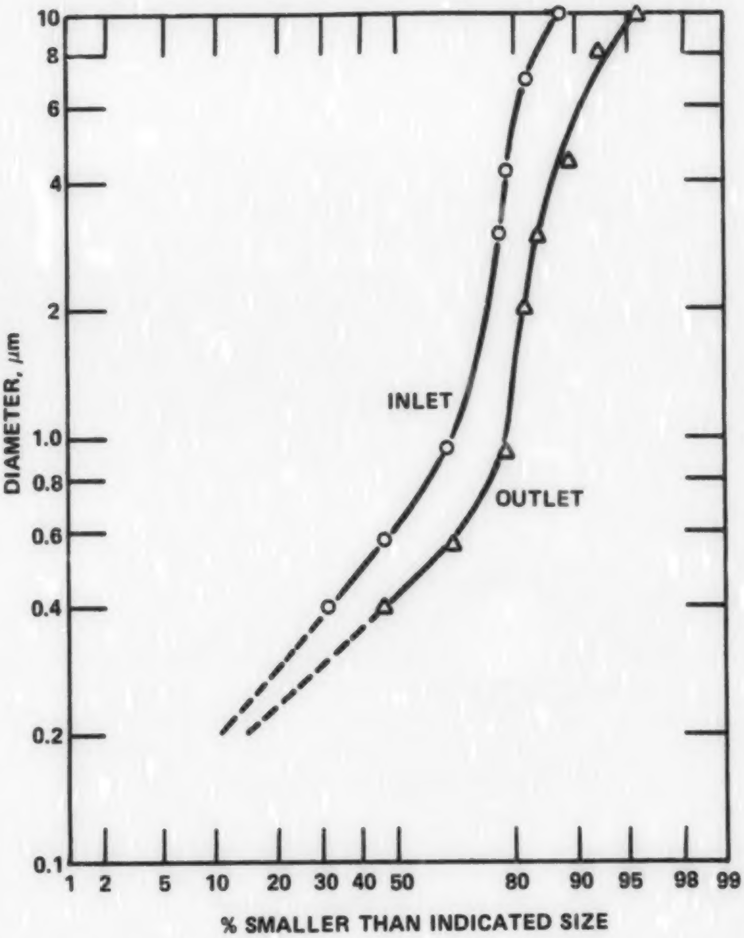

Figure 7. Particle-size distributions of particulate matter, from Andersen impactor data.

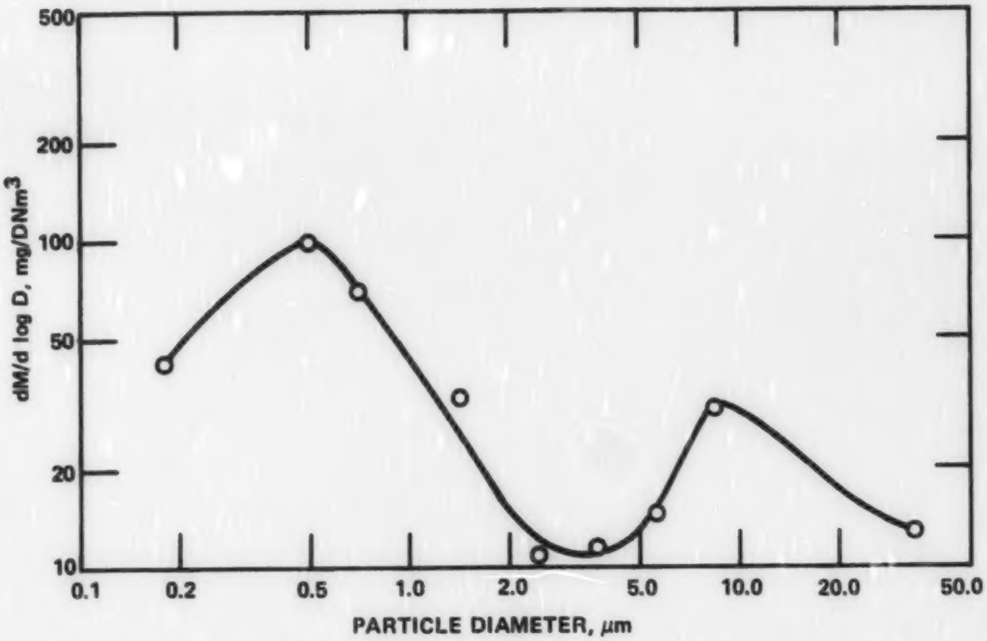

Figure 8. Inlet differential particle-size distribution.

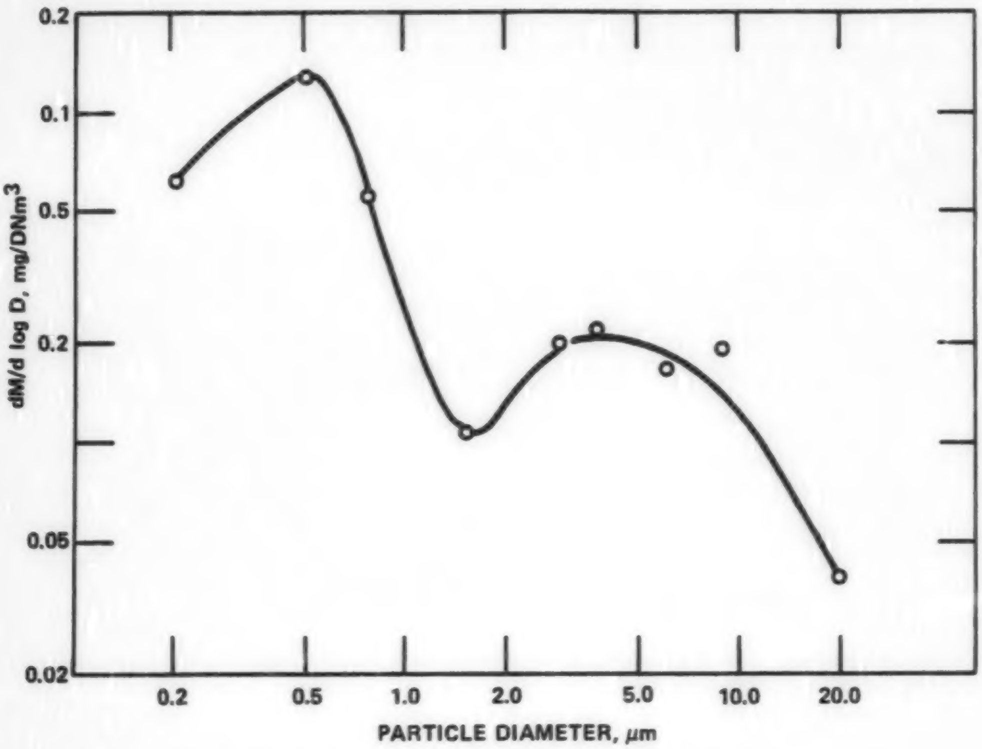

Figure 9. Outlet differential particle-size distribution.

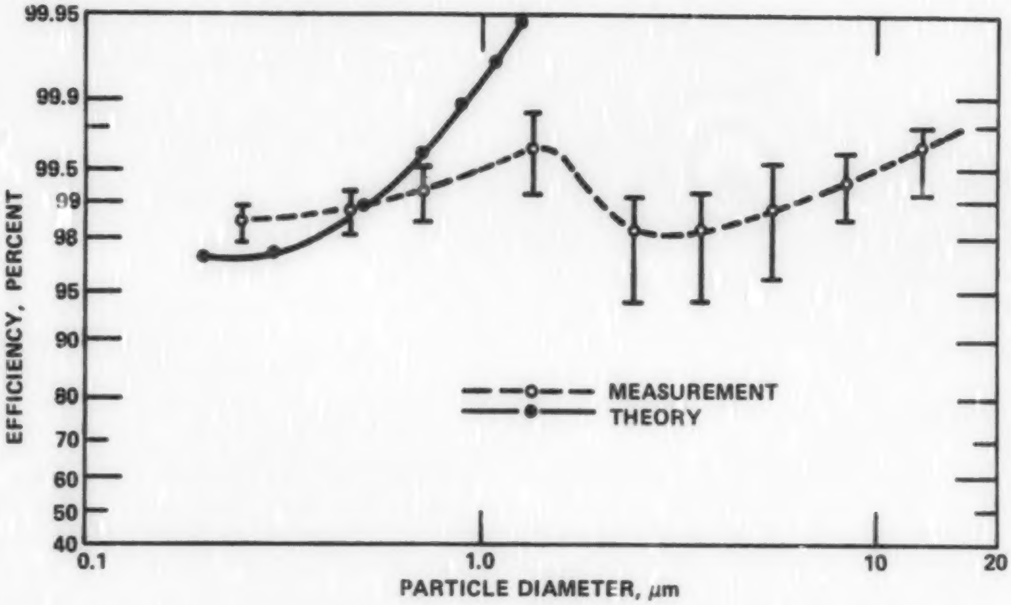

Figure 10. Fractional collection efficiency of electrostatic precipitator, from Andersen impactor data.

values of dM/d log D. The bands were obtained by: (1) calculating the standard deviation at the indicated points for the inlet and outlet data sets, (2) plotting dM/d log D values which represent plus and minus one standard deviation from the average at each particle diameter, (3) drawing curves through the points representing plus and minus one standard deviation for both inlet and outlet data sets, (4) calculating a minimum efficiency for each diameter from

$$\text{Minimum eff.} = \left[\frac{(\text{inlet average} - 1\sigma) - (\text{outlet average} + 1\sigma)}{\text{inlet average} - 1\sigma}\right]100,$$

and (5) similarly calculating a maximum efficiency from

$$\text{Maximum eff.} = \left[\frac{(\text{inlet average} + 1\sigma) - (\text{outlet average} - 1\sigma)}{\text{inlet average} + 1\sigma}\right]100.$$

These maximum and minimum values are plotted as bars in Figure 10.

The apparent decrease in efficiency which occurs between 1.4 and 2.0 μm in diameter in Figure 10 is a reflection of the second peak which occurs on Figure 9. Also plotted on Figure 10 is a curve obtained from a mathematical model of an electrostatic precipitator developed by SRI under EPA contract. These computer curves and the results obtained from the impactor data are discussed further in a subsequent section.

It should be noted that the diameters reported here for the inertial data are based on an assumed particle density of 2.0 grams/cm^3. If the true densities are lower than this value, the diameters as given should be increased by a factor equal to the square root of the ratio of the assumed density to true density.

Optical and Diffusional Measurements

Since it was necessary to obtain optical and diffusional data at different times for the inlet and outlet, source stability was investigated by obtaining particle concentration as a function of time data with the optical and diffusional sampling system at the outlet. A representative data set is shown for the condensation nuclei counter and optical particle counter in Figures 11 and 12. The CN counter and the 0.3-0.5 μm channel on the optical counter are reasonably stable, but the 0.5-0.7 μm and the 0.7-1.3 μm channels show a considerable decrease with time. However, the indicated variations are small in comparison with those observed on effluents from other metallurgical processes. These data suggest that the process was stable enough to render the nonsimultaneous measurements meaningful. Figure 13 gives the cumulative size distribution on a number basis for this test series and several other sources which have been tested by SRI with this equipment.

Fractional efficiencies were computed from the optical and diffusional data, based on inlet measurements conducted on August 20 and 21, and outlet measurements conducted on August 22 and 23. Figure 14 gives the results of these calculations, together with the inertially determined fractional efficiencies. The optical and inertial efficiency data show fair agreement over the size range 0.3 μm to about 0.7 μm.

A pronounced increase in the collection efficiency is indicated by the diffusional methods for particle sizes below 0.1 μm. This behavior is consistent with theoretical considerations and has been observed at other installations utilizing electrostatic precipitators.[4]

Mass Loading Measurements

Mass train measurements were obtained by Guardian Systems, Inc., of Anniston, Alabama, under subcontract to Southern Research Institute on August 20, 21, 22, and 23. The results of these measurements are given in Table 5. Results obtained by a local pollution control agency on October 9-10, 1973, are given for comparative purposes in Table 6. In general, fair agreement is expected between the total mass loading obtained with cascade impactors and that obtained with a mass train. A comparison of the total average mass loading obtained with the Andersen impactors at the inlet (Table 3) with the average inlet mass loading

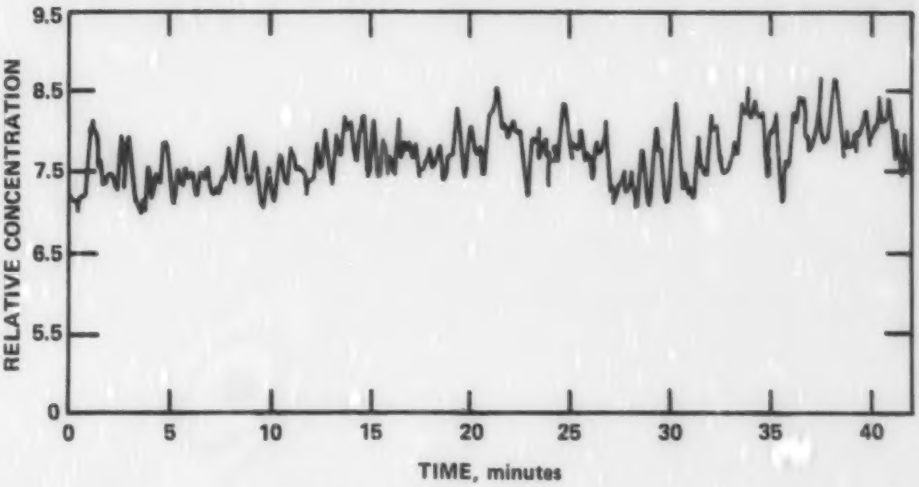

Figure 11. Relative concentration variation from condensation nuclei counter.

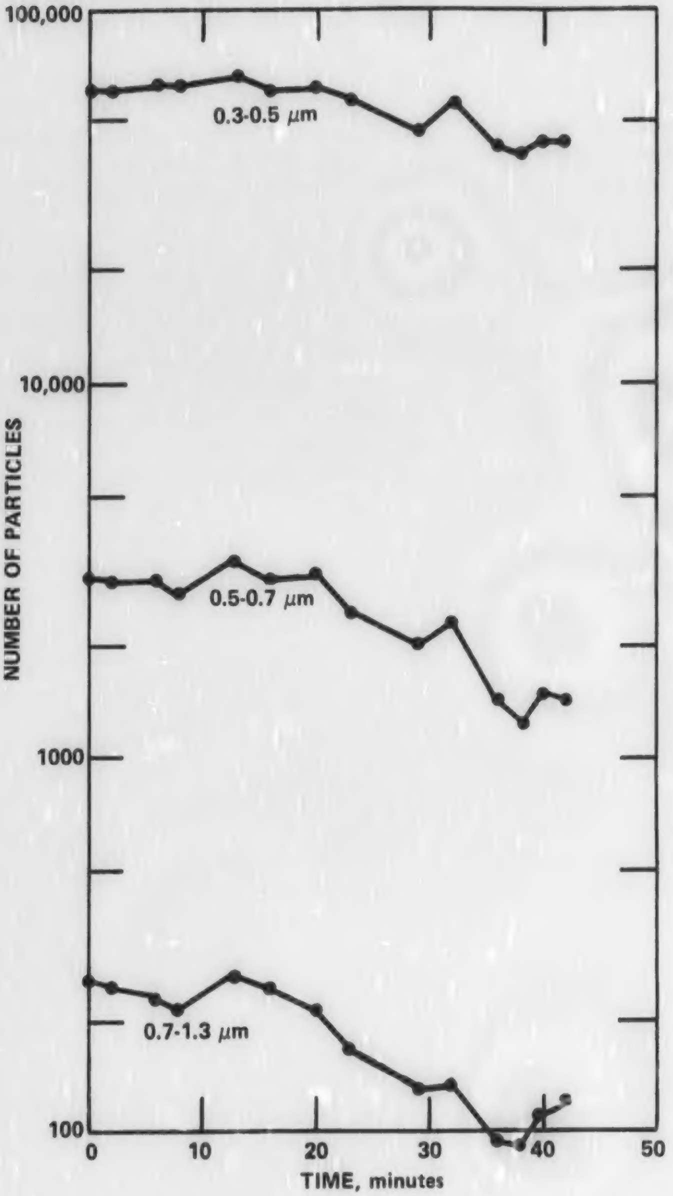

Figure 12. Relative concentration variation from optical particle counter.

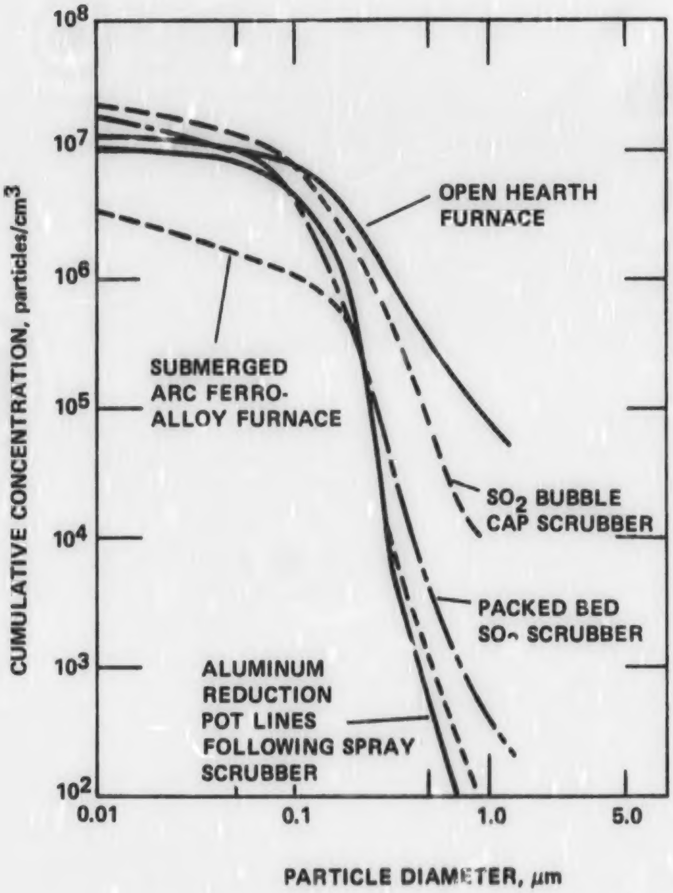

Figure 13. Cumulative size distributions on a number basis for various emissions from industrial particulate sources, as measured by optical and diffusional methods.

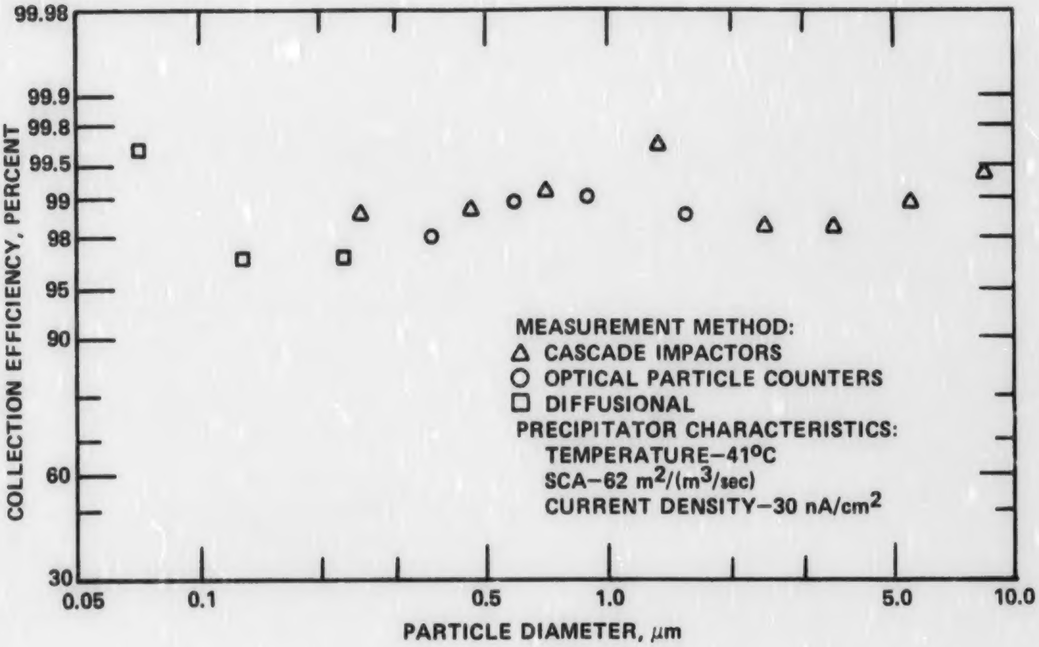

Figure 14. Measured fractional efficiencies for a wet electrostatic precipitator with the operating parameters as indicated, installed downstream of a spray type scrubber on an aluminum reduction pot line.

from Table 5 indicates that the impactors collected about 90% of the material collected by the mass train. A total average mass loading of 0.097 g/DNCM (0.0426 gr/acf) was reported by Hofer[5] from 37 tests on the outlet of one of the spray towers at this plant site. These results are consistent with those reported in Tables 3 and 5. The inlet gas flows reported in Table 5, however, are anomalously high. Possible reasons for these results are: (1) there may have been an undetected calibration error in the stack sampling system used at the inlet, and (2) the velocity profile obtained at the single port available for the mass train measurements may be non-representative of the average flow. The outlet flow rates reported in Table 5 are considered to be the correct flow rates since they show good agreement (within about 5%) with those obtained by a local pollution control agency.

In contrast to the agreement shown between mass loadings obtained with the Andersen impactors and the mass train at the inlet, severe disagreement was obtained at the outlet. The total mass obtained with a traverse using the mass train at the outlet was greater than that collected with the impactors by a ratio of approximately 5 to 1. When the mass filter was operated near the center of the stack and the sampling location used for the impactors, the disagreement was reduced to a ratio of about 3 to

TABLE 5. MASS TRAIN TEST RESULTS

	Inlet				Outlet			
Run No.	1	2	3	4	1	2	3	4[d]
Date	8/20	8/21	8/22	8/23	8/20	8/21	8/22	8/23
Sampling time, min.	300	250	280	310	376	375	375	360
H_2O, % by vol in gas	5.09	4.91	5.45	6.03	5.19	4.96	5.22	5.95
Avg. gas temp., °C	40.9	40.9	40.9	40.9	34.2[b]	38.1	38.1	38.1
Flow, ACM/sec[a]	67.2	62.5	54.9	62.5	44.6	43.5	44.4	43.9
DNCM/sec[c]	55.4	51.7	45.1	51.1	37.6	36.3	36.9	36.3
Loading, mg/ACM	89.0	94.5	95.7	100.9	4.58	4.26	3.57	1.97
g/DNCM	0.101	0.103	0.109	0.113	0.0050	0.0048	0.0338	0.0022
gr/dscf	0.0443	0.0449	0.0476	0.0494	0.00220	0.00209	0.00166	0.00098
Efficiency, %					95.03	95.34	96.51	98.02

[a] Based on traverse across one sampling port and area of 3.05 m^2 (32.85 ft^2) - see text.

[b] Based on traverse across one sampling port and area of 3.54 m^2 (38.10 ft^2).

[c] 0°C and 760 mm Hg.

[d] Obtained at a single point near the center of the stack.

1. A comparison of outlet loadings between Tables 4 and 5, however, indicates that the mass train results obtained during this test series are in fair agreement with those obtained previously by a local pollution control agency. Note that the Andersen data in Table 3 and the mass data in Table 4 show good reproducibility.

TABLE 6. RESULTS FROM TESTS CONDUCTED BY A LOCAL POLLUTION CONTROL AGENCY - OCTOBER 9 & 10, 1973

Total particulate, LVS[a]	0.0029 gr/dscf = 7.02 mg/DNCM
Total particulate, IVS[b]	0.00208 gr/dscf = 5.03 mg/DNCM
Percent water vapor	5.2%
Gas flow	99,000 acfm = 46.7 m^3/sec

[a] Low volume sampler.

[b] Intermediate volume sampler.

Reasons which have been hypothesized for the disagreement between the Andersen impactor and the mass train data are:

- The conditions in the impactor lead to evaporation of gross amounts of previously condensed hydrocarbons.
- Relatively large water droplets, containing about 5% by weight of dissolved solids, were collected by the mass filter, but not by the impactor. Evaporation of these droplets would leave a residue which could account for the greater mass observed with the mass filter.

In an effort to resolve the disagreement, the substrates from one Andersen run and the outlet filters from runs 3 and 4 of Table 4 were submitted to Southern Research Institute's Analytical Services Section for analysis with a gas chromatograph (GC). The objective of this analysis was to determine the relative volatility and approximate mass, if possible, of the hydrocarbons remaining on the filters and fiberglass substrates.

The GC results for both the filters and the substrates indicated that very little of the hydrocarbons were in the C_6 to C_{12} retention time range. The major components were eluted at times greater than that for C_{16}. It is apparent from these results that the hydrocarbons remaining on both the filters and substrates are relatively non-volatile, and therefore, the discrepancy cannot be explained by comparing the volatility and mass of the hydrocarbons remaining. It is possible, however, that if the above analyses were conducted immediately upon removal of the sampling devices from the stack, significant differences may have been observed between the hydrocarbons on the filters and substrates.

It is our conclusion that the most probable cause of the mass loading discrepancy is the collection of large water droplets containing solids by the mass filter. Such droplets would be subject to stratification in the stack, and this is qualitatively indicated by the decrease in loading which occurred when the mass train was operated at a single point. Additional work with a traverse using a sampling device designed to provide sizing information above 10 μm diameter would be required to resolve the problem.

COMPARISON OF RESULTS WITH THEORETICAL PREDICTIONS

Figure 10 presented the inertially determined fractional efficiencies and a predicted curve obtained from a theoretically based computer model of an electrostatic precipitator.[6] This mathematical model calculates theoretically expected collection efficiencies for representative particle diameters as a function of precipitator operating conditions. Predicted collection efficiencies for each particle diameter are a function of the electric field, the charge on the particle, and the ratio of collection area to gas volume flow rate.

It can be seen that fair agreement is obtained between the theoretical efficiencies and the inertially determined efficiencies over the particle diameter range 0.25-1.3 µm, but that the measured values depart drastically from the predictions at diameters larger than 1.5 µm. This apparent departure from the expected functional form may be caused by the generation of particles within the device, possibly originating from the liquid sprays or from reentrained liquid that is not captured by the outlet transverse baffles, which are considered by the manufacturer to function as an electrostatically augmented mist eliminator. It should be noted that the diameter band 0.25-1.3 µm, based on the Andersen measurements, represents 54% of the mass at the inlet and 56% of the mass at the outlet.

Since a major portion of the particulate entering the precipitator is known to consist of condensed hydrocarbons, it is of interest to consider the effect of dielectric constant on predicted collection efficiencies. The predictions shown in Figure 10 were based on the assumption that the particulate in the wet environment may be characterized by high values of dielectric constant. In order to examine the effect of low values of dielectric constant on the predicted efficiencies, the computer program for calculating particle charge used in obtaining the theoretical prediction shown in Figure 10 was employed with dielectric constants (ε) of 2 (the lowest value which might be representative of hydrocarbon droplet) and 100. The results of these calculations are presented in Table 7.

It can be seen that this range of variation of dielectric constant has a significant effect on predicted performance, with the greater effect being observed for the larger particles. Since the particulate consists of both organic and inorganic matter in a wet atmosphere, it is reasonable to expect that a major portion of the mass would exhibit a relatively high dielectric constant under these conditions.

Electrostatic precipitator performance is often described by an empirical performance parameter termed the precipitation rate parameter. The parameter is obtained by evaluating the Deutsch equation using the overall mass efficiency and the ratio of volume flow to plate area:

$$w_p = \frac{V}{A} \ln \left(\frac{100}{100-\eta}\right)$$

where

w_p = effective migration velocity

V = volumetric flow rate through the collector

A = total collecting plate area, and

η = overall collection efficiency on a mass basis.

Evaluation of this relationship using the data in Table 4 gives the results presented in Table 8. A predicted precipitation rate parameter may be obtained from the computer model based on the inlet size distribution obtained from the Andersen impactor measurements. Based on the theoretically predicted efficiencies shown in Figure 10, numerical integration over the inlet size distribution gives a total predicted penetration of 1.1% (98.9% efficiency), and predicted precipitation rate parameter of 7.3 cm/sec, which shows fair agreement with the data in Table 8. Figure 10 shows, however, that the model underpredicts fine particle collection efficiencies, and overpredicts collection for particles larger than about 0.60 μm.

COST ESTIMATES

The estimated operating power required for operation of the wet electrostatic precipitator is given in Table 9. If power costs are $0.01/kWh, the power costs would be about $27.00 per

TABLE 7. EFFECT OF DIELECTRIC CONSTANT ON PREDICTED PENETRATION[a]

Particle Diameter, μm	Penetration, % for $\varepsilon = 100$	Penetration, % for $\varepsilon = 2$
0.2	2.95	3.45
0.50	1.135	1.88
0.70	0.384	0.92
1.30	0.011	0.05
1.70	9.1×10^{-4}	0.007

[a] Smith-McDonald[3] theory used for calculating particle charge.

day of operation for the precipitator. Bakke[1] has reported that the installed flange to flange capital costs of the wet precipitator are \$1.50-\$2.00/m^3sec (\$3.00-\$4.00/cfm) based on mild steel construction. The operators reported that their total costs for installing the wet precipitators at the reduction plant would approximate \$18,000,000 or about \$3.00/m^3sec (\$6.00/cfm).

TABLE 8. PRECIPITATION RATE PARAMETERS

Run No.	Gas flow, m^3/sec	Mass Efficiency, %	Precipitation Rate Parameter, cm/sec
1	44.6	95.03	4.90
2	43.5	95.34	4.88
3	44.4	96.51	5.45
4	43.9	98.02	6.30

TABLE 9. OPERATING POWER ESTIMATED FOR WET ELECTROSTATIC PRECIPITATOR

Item	Basis	Power, kW
Power supplies	Primary meter readings	49.0
Pumping power	100 psig (6.89 x 106 dynes/cm^2) total head, 31.5 l/sec, 60% pump efficiency	36.0
Fan power	1.27 cm H_2O ΔP, 50% fan efficiency, 44.1 m^3/sec	11.0
Insulator heater power	6 kW/field, from Bakke[1]	18.0
	TOTAL	114.0 kW

REFERENCES

1. Bakke, E. The Application of Wet Electrostatic Precipitators for Control of Fine Particulate Matter. Paper presented at the Symposium on Control of Fine Particulate Emissions from Industrial Sources for the Joint U.S. - U.S.S.R. Working Group, Stationary Source Air Pollution Control Technology, San Francisco, California, January 15-18, 1974.

2. Smith, W.B., K.M. Cushing, and J.D. McCain. Particulate Sizing Techniques for Control Device Evaluation. EPA-650/2-74-102, (NTIS No. PB 240670/AS), U.S. Environmental Protection Agency, Research Triangle Park, NC, 1974. 127 pp.

3. Smith, W.B., and J.R. McDonald. Calculation of the Charging Rate of Fine Particles by Unipolar Ions. J. Air Pollut. Contr. Assoc. 25(2):168-172, 1975.

4. McCain, J.D., J.P. Gooch, and W.B. Smith. Results of Field Measurements of Industrial Particulate Sources and Electrostatic Precipitator Performance. J. Air Pollut. Contr. Assoc. 25(2):117-121, 1975.

5. Hofer, G.C. Relationship of Operating Parameters to the Efficiency of a Centrifugal Spray Tower for the Collection of Particulates Emitted from a Horizontal Spike Soderberg Aluminum Plant. Master of Science Thesis in Civil Engineering, University of Washington, 1971.

6. Gooch, J.P., and N.L. Francis. A Theoretically-Based Mathematical Model for Calculation of Electrostatic Precipitator Performance. J. Air Pollut. Contr. Assoc. 25(2):108-113, 1975.

PAPER 11

DESIGN AND FABRICATION OF A MOBILE ELECTROSTATIC PRECIPITATOR

JOSEPH L. BRUMFIELD
FRED CROWSON*
NAVAL SURFACE WEAPONS CENTER

AND

DALE L. HARMON
INDUSTRIAL ENVIRONMENTAL RESEARCH LABORATORY- RTP
ENVIRONMENTAL PROTECTION AGENCY

ABSTRACT

The particulate removal capability of any pollution control device is best evaluated in the field and under actual process stream conditions. A mobile electrostatic precipitator system has been designed, fabricated and operated for the purpose of examining the applicability of electrostatic precipitation to a broad variety of particulate emission sources. The design characteristics, fabrication problems and some preliminary field data collected with this system are presented.

INTRODUCTION

Since July 1973 the Naval Surface Weapons Center (NSWC) has assisted the Industrial Environmental Research Laboratory-Research Triangle Park of the Environmental Protection Agency (EPA) on the transfer of defense technology to help meet EPA requirements in the area of air pollution control. An immediate requirement was to formulate a program for evaluating the controllability of a broad variety of industrial sources of air pollution using a series of mobile test facilities. The expertise has already been developed by NSWC for mobile chemical removal systems, and a previous project (EPA-IAG-133(D), Task 2, July 1973) demonstrated the capability to develop a mobile wet scrubber system for air pollution control.

---

*To whom all inquiries should be addressed.

In January 1975, NSWC was selected to design and fabricate a mobile electrostatic precipitator (ESP) facility. The purpose of this unit is to determine experimentally the effectiveness of an ESP on various sources of fine particulates. Additionally, the field data obtained are used for scale-up designs or process modifications (such as chemical pretreatment) to achieve efficient removal of particulates. The primary advantage of a mobile ESP facility is that field testing will provide information under actual process conditions. Particle size and concentration, chemical composition, dust resistivity, temperature, humidity, and gaseous contaminant concentrations of any given stream can be evaluated with regard to the ESP process.

MOBILE ESP DESIGN

General Description

The mobile ESP facility is designed for the purpose of determining the effects of dust properties, plate spacing, electrode spacing, rapping and dust resistivity on ESP parameters. The entire facility is housed in two 40-foot long freight vans, a process van and a laboratory/control van. (Figure 1.) The mobile ESP system has several capabilities. Precipitation studies can be conducted at gas flows as high as 3000 acfm with a total system pressure differential up to 26 inches of water and at gas temperatures up to 1000°F. Dust particles are collected utilizing the electric field between a discharge electrode (in this case a 0.1-inch diameter wire at -50,000 volts dc) and a collection electrode (a steel plate at ground potential). The collection electrode is then vibrated to remove the dust layer to a hopper where the dust is transported by a screw conveyor to a container for analysis or disposal.

Collection efficiencies of 96% and better are possible for particles having diameters in the submicron range. The five sections of the ESP operate independently of one another and can be "rolled out" for maintenance and service. Sufficient insulation is provided to reduce skin temperatures below 140°F on all surfaces exposed to personnel.

A laboratory/control facility has 240 square feet of storage and laboratory working area. The control area contains a step-down 480/240 volt ac transformer, a motor control center for all

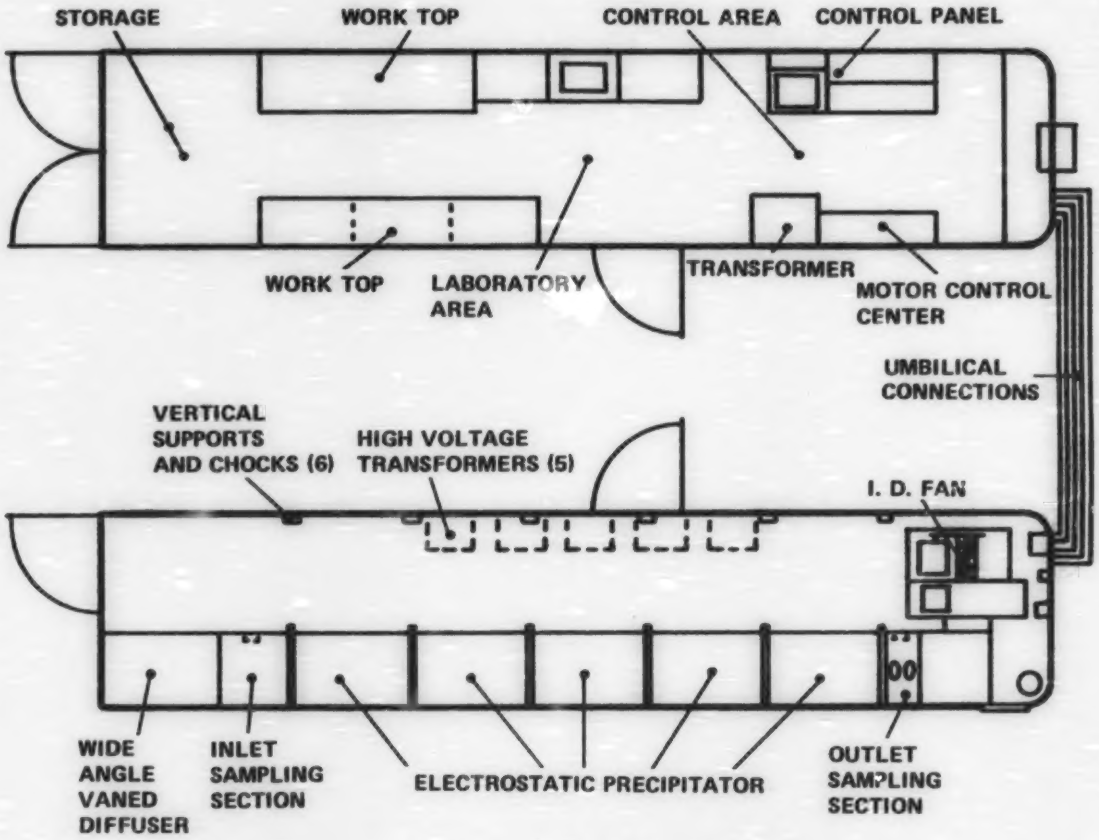
STORAGE
WORK TOP
CONTROL AREA
CONTROL PANEL
WORK TOP
LABORATORY AREA
TRANSFORMER
MOTOR CONTROL CENTER
UMBILICAL CONNECTIONS
VERTICAL SUPPORTS AND CHOCKS (6)
HIGH VOLTAGE TRANSFORMERS (5)
I. D. FAN
WIDE ANGLE VANED DIFFUSER
INLET SAMPLING SECTION
ELECTROSTATIC PRECIPITATOR
OUTLET SAMPLING SECTION

Figure 1. Plan view of mobile ESP facility.

process motors, high-voltage controllers, and a control/monitor panel. An air conditioner/heater and acoustical tile are provided for personnel comfort.

Specific Design Considerations

In accordance with EPA requests and with Southern Research Institute, Birmingham, Alabama, as consultants, the process design criteria were developed as given in Table 1.

TABLE 1. SYSTEM DESIGN PARAMETERS[a]

Operating Temperature (max.), °F	1000
Gas Flow Rate (max.), acfm	3000
Pressure Drop (total), in. WG	70
Particulate Loading, gr/scf	10
Plate Spacing, in.	10
Migration Velocity, ft/sec	0.33
Gas Velocity, ft/sec	5
Efficiency (average), %	96
Precipitator Length, ft	20
Operating Voltage (max.), kV	50
Total Current, mA/ft^2 collector	0.1
Total Power, kW/unit	2.5

---

[a] These parameters were established on principles and practices found in the Manual of Electrostatic Precipitation Technology by S. Oglesby, et al.[1]

Inlet Duct. The mobile ESP is connected to its source via 50 feet of 10.5-inch diameter, stainless steel, thin-wall tubing. This is accomplished using six 8-foot long sections and three 90° elbows connected at either end by a V-band clamp with a stainless steel C-ring seal. The duct is attached to an industrial stack using a standard-flange adapter.

Each section is equipped with six band heaters rated at 253 watts each. This power is necessary to supply heat for maintaining a maximum temperature drop of 100°F (at 1000°F initially) from the source to the ESP. This temperature maintenance will minimize resistivity change and ensure that corrosive constituents will not condense. Mineral fiber insulation (3 inches thick) and a 1-inch thick glass fiber blanket insulation are used to prevent heat loss as well as to protect personnel from hot surfaces. Aluminum sheathing covers and protects the insulation. A high-temperature cutoff switch at each section prevents stack gases with temperatures in excess of 1150°F from entering the ESP. Each duct section fully assembled weighs approximately 300 pounds and requires a minimum of two people to install.

Flow Rectification. Original designs specified a separate series of components for flow rectification. Since the inlet gas stream must be expanded and velocities are required to be uniformly distributed, an integral rectification system was desirable. Additionally, assembly time and effort could be reduced to a minimum.

The gas stream is turned and partially expanded by first entering a twin 45° vaned elbow, then through a square-to-round diffuser and in turn through a vaned 90° square elbow. Final rectification is achieved with a two-stage, wide-angle vaned diffuser in the process van. The diffuser has fixed vanes and is designed according to methods cited by O. G. Feil.[2] At either end of the step diffuser, a 1-inch mesh stainless steel wire screen with 60% openings reduces regions of high velocities. Identical screening is installed immediately after the wide-angle diffuser. This screen can be removed to clean the diffuser vanes (Figure 2).

Original designs for turning the gas flow involved adjustable vanes that could be manually oriented to compensate for irregular velocity profiles. In order to achieve a uniform profile, multiple settings and calculations would become necessary. Also, mechanical linkage for individual vanes appeared to present a reliability problem. Final design considerations dictated gas flow components with fixed turning vanes. Concern was expressed regarding dust buildup on vanes having an essentially horizontal configuration; however, since the mobile ESP is an experimental unit, vaned components can be cleaned periodically with minimum effort.

Immediately after the diffuser and prior to the first ESP section is a sampling area for obtaining velocity profiles, mass loadings and particle size distribution data. Sampling devices can be attached to 4-inch NPT fittings at five sample ports at the ESP outlet.

ESP Sections. The electrostatic precipitator is composed of five separate high voltage sections. The high voltage cable enters the ESP through a ceramic insulator assembly in the top of each section. The cable connects directly to the corona electrode frame which contains two sets of eight discharge electrode wires. The corona frame is supported at four points on its top by ceramic insulator blocks held at each end by brackets attached to threaded rods hanging from the precipitator roof.

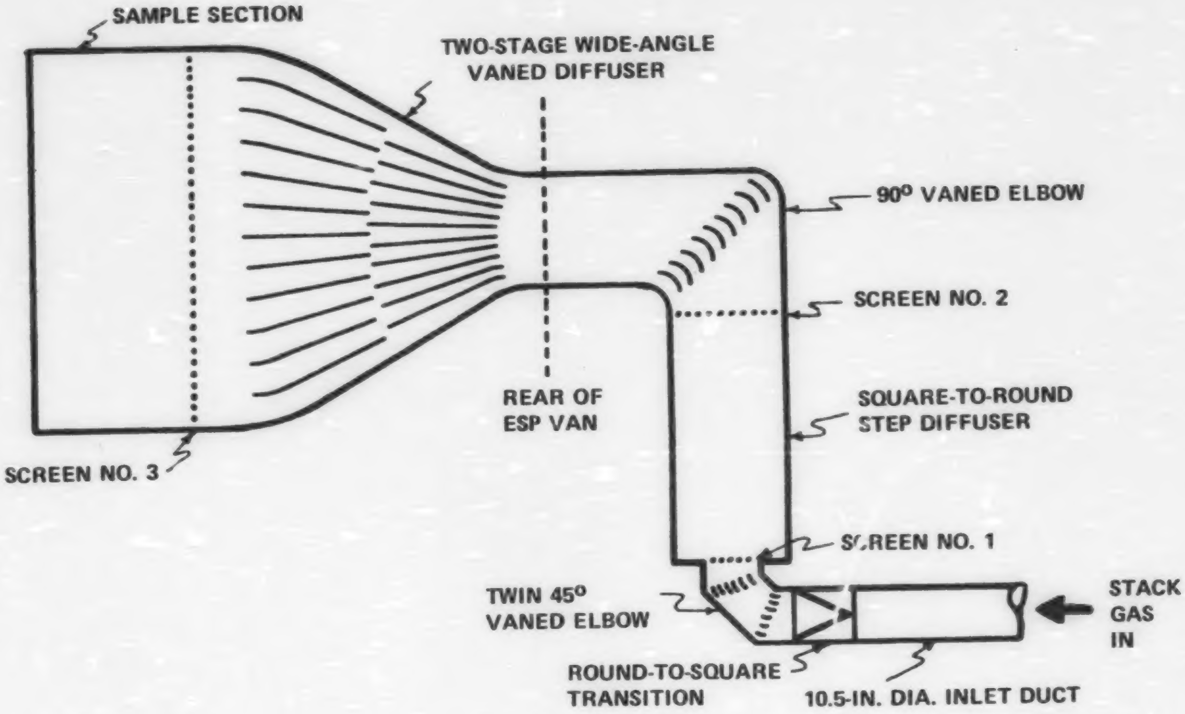
SAMPLE SECTION
TWO-STAGE WIDE-ANGLE VANED DIFFUSER
90° VANED ELBOW
SCREEN NO. 2
REAR OF ESP VAN
SQUARE-TO-ROUND STEP DIFFUSER
SCREEN NO. 3
SCREEN NO. 1
TWIN 45° VANED ELBOW
STACK GAS IN
ROUND-TO-SQUARE TRANSITION
10.5-IN. DIA. INLET DUCT

Figure 2. Flow rectification on inlet.

The collection electrode plates hang freely from slotted pipe attached to the top baffles which, in turn, are bolted to the precipitator roof. Spacer rods are used at the bottoms of each plate to keep the free end evenly spaced and aligned. The collection plates as well as the precipitator walls and roof were constructed of Cor-Ten* steel because of its abrasion resistance and high temperature properties.

Auxiliary Process Equipment. Gas flows through the precipitator up to 3000 acfm are attained using a high temperature blower mounted on the downstream side of the precipitator. The blower construction consists of Hastelloy C** for the impeller, Hastelloy X** for the hub and 316 stainless steel on all other internal parts. The blower is fully insulated and has a water-cooled jacket for high temperature operation. Approximately 30 gallons of coolant is constantly recirculated through a heat exchanger and the cooling jacket. A pressure sensor and high temperature sensor in the cooling system shut down the blower in case of low coolant flow or overheat conditions.

The collected dust is removed using solenoid actuated vibrators mounted centrally atop each precipitator section. Each vibrator is coupled directly to the collection electrode assembly by a 316 stainless steel extension rod. Frequency, intensity and cycle time can be controlled remotely from the control van.

Once the dust is vibrated free of the collection electrodes, it is collected in a trough-shaped hopper extending the full length of the precipitator. A screw conveyor then transports the dust to one end of the hopper where it is removed through a 5-inch port equipped with a positive-seal gate valve into a disposal container.

Also mounted beneath the process van are the high voltage transformer/rectifier units for providing the 50,000 volts dc operating voltage. The controller for each unit is located in the control van.

Laboratory/Control Facilities. A separate 40-foot freight van provides 240 square feet of control and analytical laboratory area. The forward quarter section contains a 480/240 volt ac step-down transformer, high voltage controllers, and a control/monitor cabinet. An air conditioner/heater and acoustical tile are provided for personnel comfort.

---

*Cor-Ten: United States Steel, 600 Grant St., Pittsburg, PA 15230.

**Hastelloy: Stellite Div., Cabot Corp., 1020 W. Park Ave,
IN 46901.

MOBILE ESP FABRICATION

Assembly Considerations

During assembly and construction of a mobile unit, certain assembly requirements must be considered. These are discussed at some length to give details of the overall operations when building such units.

Since the ESP was designed for negative pressure operation, the gas flow control valve is located in the inlet duct. The valve is situated one duct section upstream to reduce turbulent conditions immediately before the first vaned elbow. To support the transition section and the inlet end of the diffuser, a 3/8-inch steel plate is welded to the main frame of the van, replacing the aluminum-covered wooden door which is standard on all freight vans. The diffuser had to be insulated on three sides prior to installation, because of its proximity to the floor, wall and ceiling of the van. Five 4-inch NPT sampling ports were installed 12 inches apart vertically on the inlet sampling section.

To construct a sturdy precipitator structure within a lightweight freight van, approximately 25 feet of the aluminum wall had to be removed completely and replaced with 10-gage steel having 4-inch channel located 12 inches on center for structural support. The wall is welded at the base to a steel angle which is riveted to the aluminum-channel main structure of the van. The wall is welded at the top to a steel Z-beam which is riveted to the main structure of the van. Mineral fiber insulation 5 inches thick was installed and covered with 10-gage Cor-Ten steel which is anchored to the wall interior using 3/16-inch stainless steel welding studs. Interior wall sections on the fixed side were overlapped to allow for thermal expansion.

Half of the 1-3/4-inch wooden floor was removed on the side where the precipitator was to be installed. The steel I-beam main-flooring crossmembers were cut in half, down the length of the van for 30 feet. A 6-inch wide, 1/2-inch thick steel plate was welded against the cut ends of the I-beams. Another 1/2-inch plate was welded 90° to the first plate and to the tops of the I-beams forming an I-beam-within-an-angle structure. W-beams six inches thick were welded horizontally to the steel wall and to the 6-inch steel channel attached to the opposite wall to form the top main structure. T-beams 1/2-inch thick were welded vertically to the bottom angle and to the top W-beams. Horizontal T-beams, welded to the vertical T-beams at one end and to the steel wall at the other end, completed the main structure.

Precipitator door sections were fabricated of two 10-gage steel sheets with 1/2-inch stiffeners every 12 inches between the sheets and along all edges. Door sections were hung from the

W-beams using a trolley/turnbuckle arrangement. The trolleys allowed doors to slide easily in and out of the main structure and the turnbuckles provided alignment and seating adjustments. Mineral fiber insulation five inches thick covered by 10-gage Cor-Ten steel was anchored to the interior of the door sections using welding studs. Electrically actuated vibrators were mounted centrally atop each door section so that the center collection electrode plate would receive the vibration initially and the other two collection electrode plates would receive vibration from the center plate through the plate holder assembly.

The corona discharge electrode system consisted of a tubular frame constructed of 1-inch diameter stainless steel pipe bent in a U-shape. Two of these were welded together at top and bottom to form the frame. Discharge electrodes were 0.1-inch diameter 304 stainless steel wire stretched upon the frame, each wire spaced 8 inches from any other wire. The high voltage lead attached to one corner of the frame. Figure 3 illustrates the door assembly.

High voltage connections were made through mica-filled ceramic insulators mounted in the top of each door section. Originally, the high voltage cable was connected to a spherical nut which fitted into a pear-shaped corona frame holder in which the corona frame was bolted using spherical nuts on the bolts. Ceramic plugs covered all spherical nuts. The original scheme is illustrated in Figure 4.

High temperature silicone gasket material and sealant was installed in a gasket gland which ran around the main structure members of each ESP section. Additionally, bolts were used on all door sections to secure a sufficient seal on the doors.

The outlet reducer section of the ESP contained two high-temperature view-ports through which the precipitation process could be observed and reentrainment studies could be made. Additionally, three 4-inch NPT sampling ports were installed on the outlet reducer for determining outlet conditions.

An induced draft fan was used for this system. The fan was specified for high temperature operation which meant a cooling jacket and recirculating cooling system with a heat exchanger were needed. As cited previously, the fan construction was specified to be all stainless steel and Hastelloy construction internally. The fan is capable of pulling almost 6000 CFM at static pressure up to 20 inches water gauge. A 17-foot stack is mounted atop the ESP van such that any gases not removed in the ESP will not be recirculated into the process van.

To counterbalance the total load during transport, the ESP door sections are secured to the 6-inch channel on the opposite wall of the van from the main structure. A forced-air heater

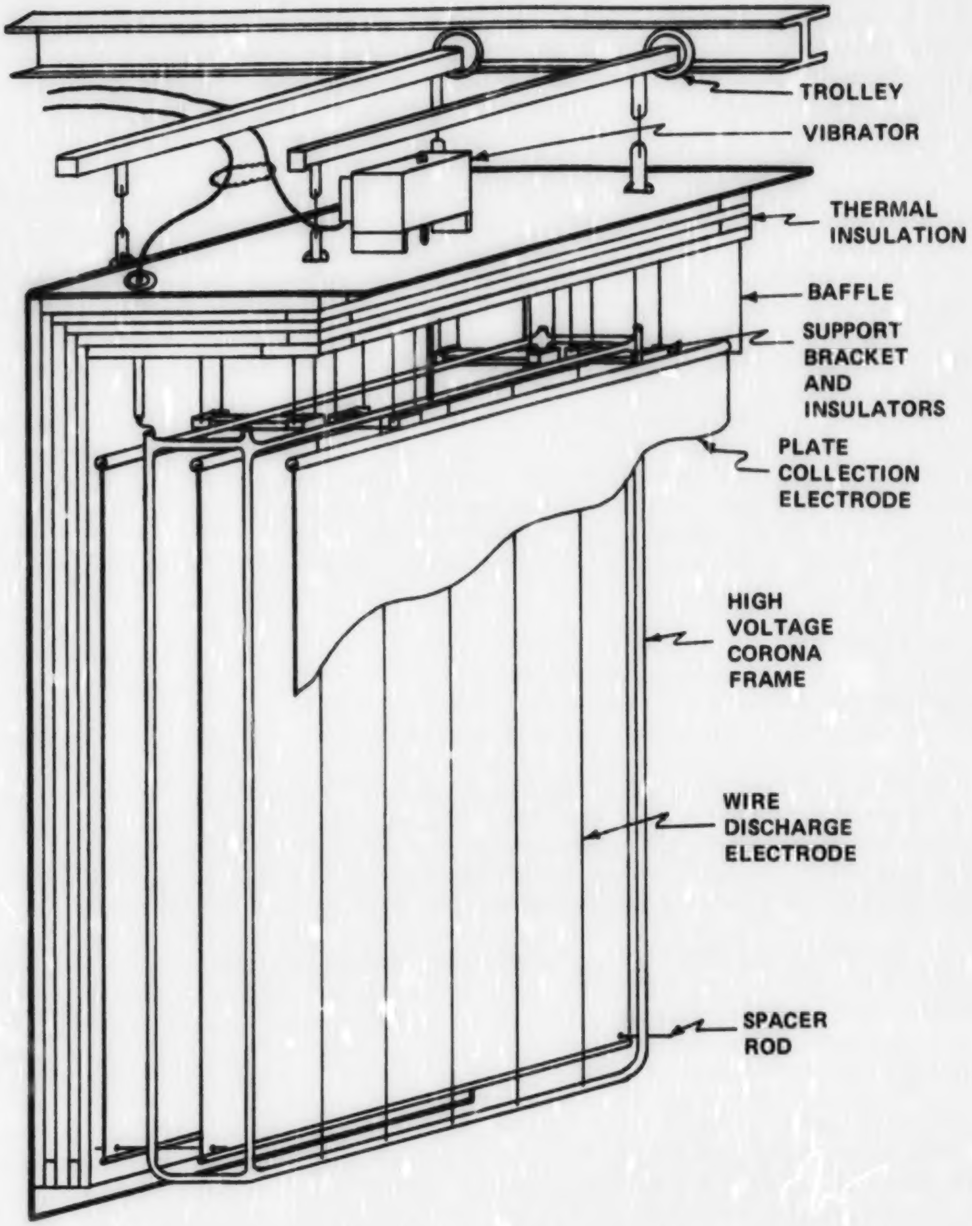
TROLLEY
VIBRATOR
THERMAL INSULATION
BAFFLE
SUPPORT BRACKET AND INSULATORS
PLATE COLLECTION ELECTRODE
HIGH VOLTAGE CORONA FRAME
WIRE DISCHARGE ELECTRODE
SPACER ROD

Figure 3. ESP section rollout.

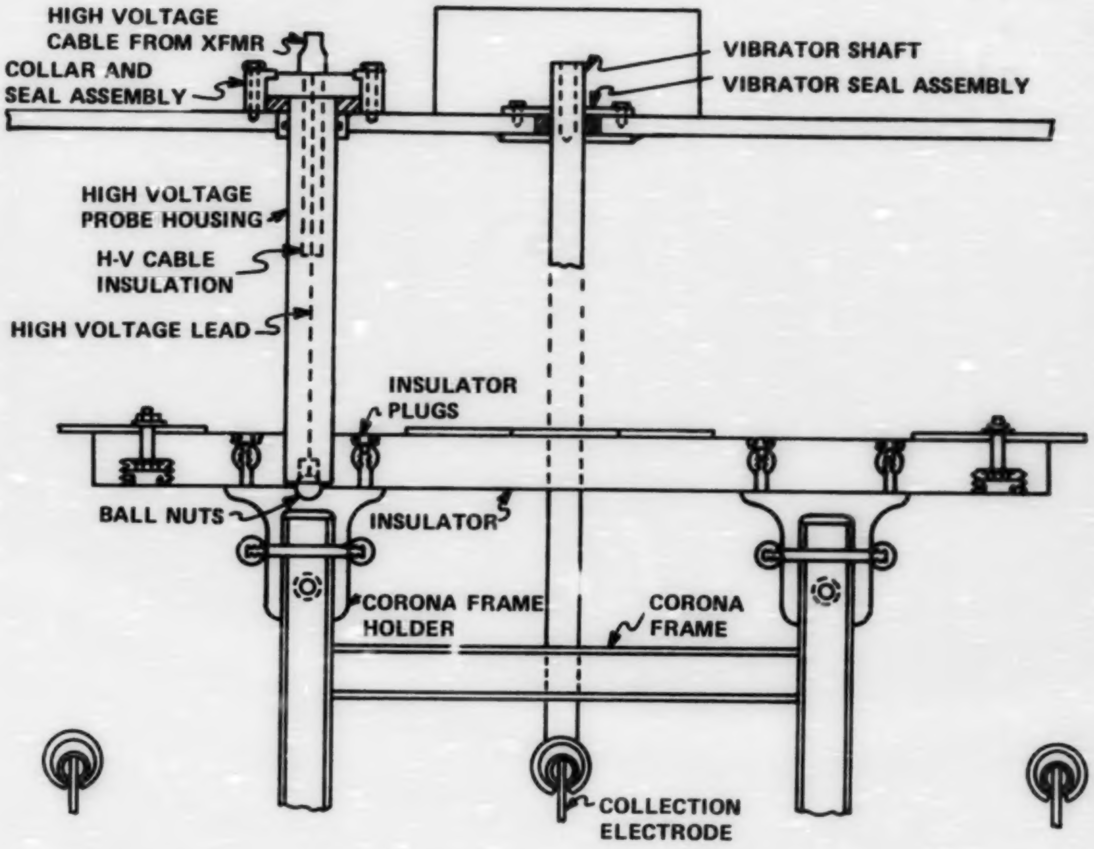
HIGH VOLTAGE CABLE FROM XFMR
COLLAR AND SEAL ASSEMBLY
HIGH VOLTAGE PROBE HOUSING
H-V CABLE INSULATION
HIGH VOLTAGE LEAD
VIBRATOR SHAFT
VIBRATOR SEAL ASSEMBLY
INSULATOR PLUGS
BALL NUTS
INSULATOR
CORONA FRAME HOLDER
CORONA FRAME
COLLECTION ELECTRODE

Figure 4. Original ESP high voltage assembly.

and an exhaust fan are provided for comfort of personnel working within the process van. All processes can be automatically controlled from the control/laboratory van and can be manually controlled within the process van.

Fabrication Problems

During fabrication, several problems occurred. A few of the "typical" problems are discussed below.

After insulating the inlet duct, a malfunction occurred in the band heater network. When power was supplied to the heater banks, a high temperature malfunction occurred. Upon disassembly, the terminal bolts were found to be rusted from allowing the inlet duct to become exposed to severe conditions of moisture. Further investigation showed mild steel bolts rather than stainless steel bolts had been used. Stainless steel bolts were installed.

The inlet duct was wired for a power input equivalent to the heater capacity necessary for a 50-foot run. Initial field tests indicated that a heating capacity for 100 feet of duct is desirable. Additionally, the inlet duct was fabricated without insulation anchors because only horizontal runs were specified. The first field test had a 60-foot run of vertical piping.

Problems also occurred in the fabrication of simple piping components. The machinist decided to construct the 90° vaned elbow according to his specifications instead of the engineering design drawings. The result was that the long side of the elbow was installed on the constricted side of the turning vanes which would have produced more turbulence than already present in the incoming gas stream. The elbow was cut along its long side and rewelded to correct the error.

During the first phase of the main structure fabrication, the two end T-beams received at the construction site were one inch too long. Both were taken to the machine shop to correct the error, returned, positioned in place, and found to be one inch too short. The "one inch" dimension had been removed from each end. The necessary modifications were made and the main structure was complete. Upon receipt and consequent installation of the inlet and outlet sampling sections, both were found to be too large overall to properly fit into the main structure openings. A custom fit of each piece was made in the field.

The outer shells of the door sections were hung in place and promptly painted with a primer coat to prevent rusting. Welding studs were installed to serve as insulation anchors. A quality control inspection afterwards resulted in replacement of all studs. Apparently, the primer paint had diffused sufficiently into the metal plate to prevent a good weld on the studs with a welding gun. The metal surface at each stud location was ground clean and studs were rewelded using a welding machine to ensure weld integrity. This procedure resulted in misalignment of the studs with the holes on the inner precipitator wall plate. A plywood template was necessary to properly locate and drill all holes in the inner walls. After all insulation and inner walls were installed, the precipitator internals were placed in position. Top baffles were bolted to the door sections and the collection electrode plates were slid into place. At this point, a significant bowing of the plates was observed. Further investigation revealed that the collection plates had been received and stored flat, instead of on edge, on the receiving floor. To make matters worse, warehouse supplies had been stored on top of the plates causing deformation across the entire plate length. Spacing bars were installed after hanging the plates in position to alleviate the misalignment. The mobile ESP was ready for shakedown testing.

INITIAL OPERATING PROBLEMS

Gas Leakage

For effective precipitator operation, the amount of ambient air leakage into the ESP should be kept to a minimum. During initial operation certain areas of the ESP assembly were discovered to contain leaks. The bearing housing on one end of the screw conveyor had not been sufficiently tightened during installation; therefore, a leak occurred at one end of the dust hopper. Proper tightening of the housing bolts remedied this situation.

Two leaks occurred due to improper welds--one on the dust hopper end and the second on an ESP door section between the top horizontal plate and the front vertical plate. In both cases, the weld had not been run to the length specified in the drawing.

A third type of leak was found in a high voltage probe assembly. Insufficient amounts of packing material in the high voltage probe collar resulted in severe air leakage through the precipitator top panel. Repacking the probe assembly alleviated this problem.

Sparking and Arcing

Initial activation of the high voltage power supplies produced electrical sparking between the wire end and the ground shielding on the power cable. To correct this situation, shielding was cut back to a minimum of 5 inches from the high voltage wire and covered with heat-shrinkable material.

The next attempt at applying the high voltage resulted in sparking from the spherical nuts through the ceramic plug covers and upward along the ceramic insulator plate to the inner top plate of the ESP door section. A 4-inch diameter hole was cut in the inner door sections directly above the corona frame holders; however, sparking still occurred along the insulator surface to an anchor stud supporting the insulator plate. A piece of 1/8-inch thick Teflon was placed between the insulator plate and the roof plate merely to see if physical spacing would increase the spark gap sufficiently to solve the problem. Negative results were obtained. A piece of 1/8-inch thick laminated mica sheet was used to replace the Teflon since mica has a higher dielectric strength than Teflon and would be more appropriate for the high-temperature design temperatures. Sparking occurred extensively. High current densities deteriorated the mica sheet lamination which allowed electrical spark penetration and resulted in arcing from the spherical nuts to the precipitator top through the mica. Apparently, the hex-shaped hole for tightening the spherical nut was causing high current densities and spark-over. The original nuts were replaced with plain spherical nuts and sparking still occurred. The spherical nuts were removed entirely and results were the same. A castable ceramic material with a relatively high dielectric strength was employed to permanently seal the counter-sunk holes containing the spherical nuts. Sparking occurred through the castable ceramic.

A total redesign of the corona frame support system was initiated. Using materials on hand, support rods, brackets and ceramic support bars were used to support the frame. Figure 5 illustrates the revised arrangement. Sparking in the top part of the door sections was eliminated using this approach.

Upon applying approximately 40,000 volts to each section, sparking occurred between sharp points and edges on both the corona frame and electrically grounded surfaces. Primarily, sparking was observed between the bottom of the corona frame and dust hopper crossmembers, and between the top of the corona frame and the support brackets. Thorough grinding, sanding and polishing of all internal surfaces prevented further sparking.

The ESP sections were operated statically for about one week. During this period, the high voltage transformer/rectifiers did not produce sufficient outputs to meet the design specifications of 50,000 volts. The units were returned to the manufacturer where outputs were increased 20%. Further static testing of the ESP demonstrated that the ceramic insulator bars absorbed moisture (contrary to specification sheets received from the manufacturer) and produced a path for sparking between the corona frame and the insulator support brackets. The insulator blocks were removed, heated and desiccated for 24 hours, and replaced in the ESP where they functioned properly throughout

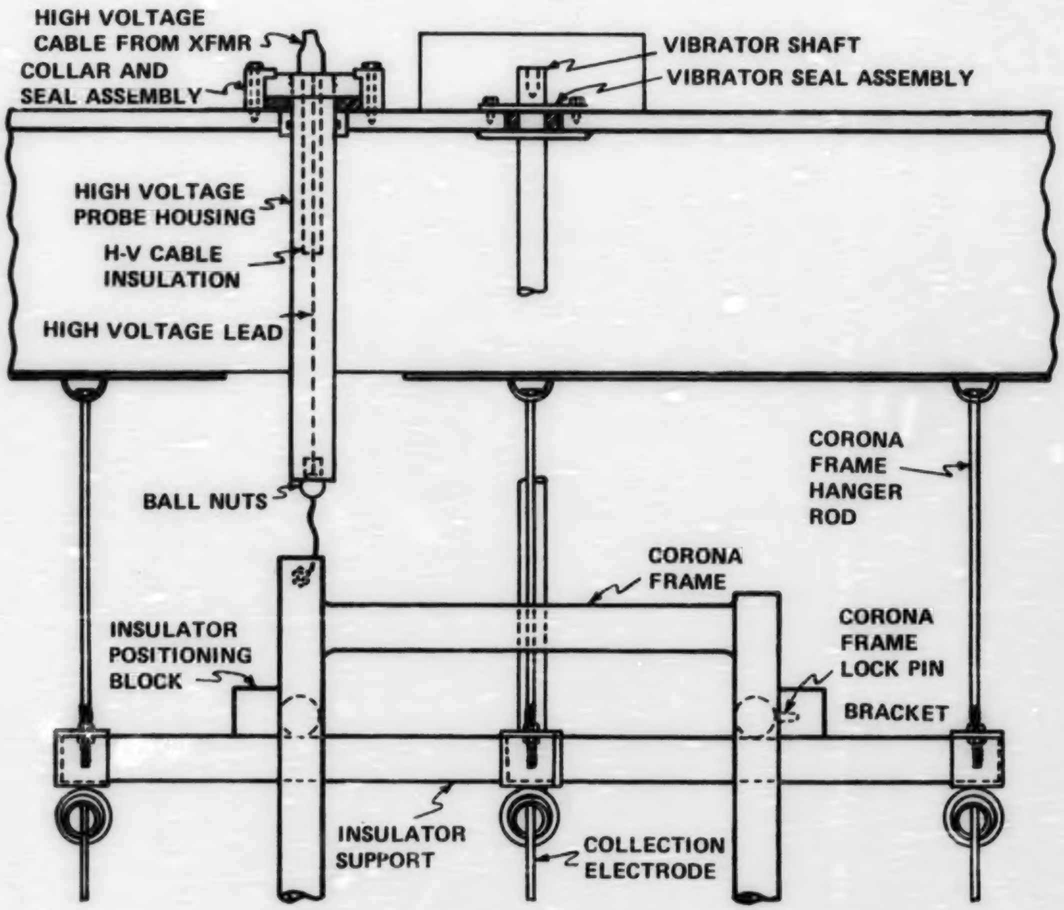
HIGH VOLTAGE CABLE FROM XFMR
COLLAR AND SEAL ASSEMBLY
VIBRATOR SHAFT
VIBRATOR SEAL ASSEMBLY
HIGH VOLTAGE PROBE HOUSING
H-V CABLE INSULATION
HIGH VOLTAGE LEAD
CORONA FRAME HANGER ROD
BALL NUTS
CORONA FRAME
INSULATOR POSITIONING BLOCK
CORONA FRAME LOCK PIN
BRACKET
INSULATOR SUPPORT
COLLECTION ELECTRODE

Figure 5. ESP high voltage assembly.

the rest of the checkout tests. Recent developments in ceramics have produced a material that appears to be more attractive for applications in humid environments. Future use of this new material on a replacement basis of the original ceramic material is anticipated.

PRELIMINARY FIELD TEST RESULTS

After in-house system checks were completed, the mobile ESP was transferred to Research Triangle Park (RTP), North Carolina, for release to the Environmental Protection Agency and subsequent field testing by Monsanto Research Corporation. Current-voltage curves were obtained on all sections and compared with those generated at NSWC. Figure 6 is a typical set of curves which illustrates that alignment on reassembly was very near the original assembly alignment.

The first set of tests on the mobile ESP was to determine its effectiveness on fly ash injected into a wind tunnel gas stream at 350°F. With a gas flow rate of 2000 acfm and an inlet mass loading of 2.0 gr/scf, a collection efficiency of 99.49% was measured using impactors. A few attempts were made at sodium conditioning using 4 percent by weight of sodium monoxide; however, no increase in efficiency was observed.

After preliminary testing at RTP, the mobile ESP was taken to Hagerstown, Maryland, where it was successfully operated on a stoker-fired boiler fueled with a mixture of coal and densified refuse. A slipstream after a cyclone separator was made to provide the ESP with a process gas stream. Gas flow rates ranged from 1500 to 3000 acfm and temperatures from 450 to 550°F. Inlet loadings were measured on the order of 0.10 to 0.25 gr/scf for particle sizes of 3 to 5 μm mean particle diameter. Collection efficiencies were calculated to range from 88 to 99%. The major problem during the first field test occurred when the precipitator was allowed to remain idle long enough to completely cool the internals. Condensation of moisture within the ESP produced sparking across the insulator blocks during start-up the following day. The blocks were removed, dried, and replaced before testing continued. Thereafter, continuous operation of the ESP prevented recurrence of this problem.

ASSESSMENT OF TESTS AND FUTURE PLANS

The mobile precipitator has been demonstrated to be highly effective on fly ash emissions in the laboratory and in the field. As cited in previous sections of this paper, certain modifications to the original mobile ESP system design were found to be necessary during various aspects of testing, such as vertical

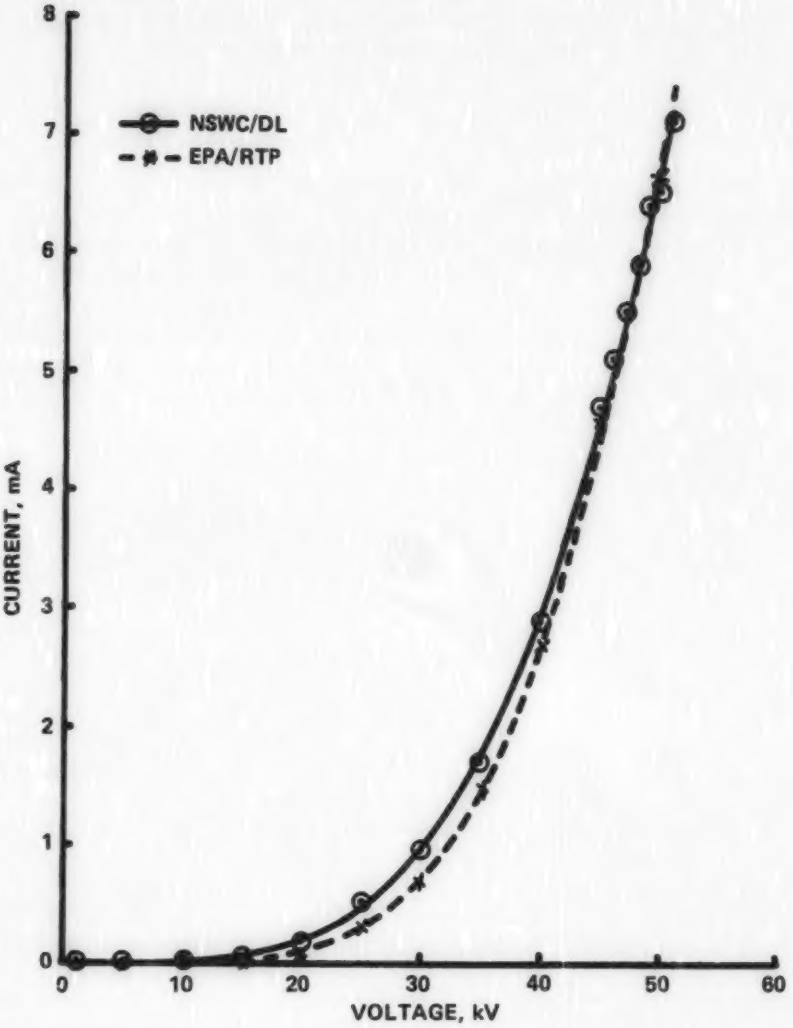

Figure 6. Clean plate curves for ESP section No. 1.

runs of duct, replacement of the insulator material, and increasing power supply output. Additional observations by the testers include items such as replacement of the high voltage probe connection, better alignment of the precipitator internals, and preheating capability of precipitator internals. Since it is difficult, if not impossible, to foresee all requirements for testing all possible emission sources, the list of modifications will probably grow from test site to test site.

REFERENCES

1. Oglesby, S., Jr., et al. A Manual of Electrostatic Precipitator Technology, Part I. Fundamentals; and Part II. Application Areas, EPA Reports APTD 0610 and 0611 (NTIS Nos. PB 196380 and 196381), Southern Research Institute, Birmingham, Alabama, August 1970.

2. Feil, O. G., Vane Systems for Very-Wide-Angle Subsonic Diffusers. J. Basic Eng. 86:759-764, 1964.

PAPER 12

FIELD TEST OF A HOT-SIDE ELECTROSTATIC PRECIPITATOR

DENNIS C. DREHMEL
INDUSTRIAL ENVIRONMENTAL RESEARCH LABORATORY
ENVIRONMENTAL PROTECTION AGENCY

AND

CHARLES H. GOODING
RESEARCH TRIANGLE INSTITUTE

ABSTRACT

This paper describes a test program that was conducted to quantify and characterize the particulate emissions from a coal-burning power plant boiler, which is equipped with a high efficiency hot-side electrostatic precipitator. The tests were conducted at Duke Power Company's Allen Steam Station in March 1976. Appropriate test equipment and procedures were used to determine the flue gas composition and velocity, total particulate mass concentration of the gas stream, particle size distribution, electrical resistivity of the particulate entering the precipitator, evidence of back corona in the precipitator, SO_2 and SO_3 concentrations in the flue gas, and chemical composition of the fuel and fly ash. The test site and test procedures are described. The results of the tests are presented and discussed.

FIELD TEST OF A HOT-SIDE ELECTROSTATIC PRECIPITATOR

Introduction

Because of the adverse effect of pollution on public health and welfare, the United States of America and the Union of Soviet Socialist Republics have independently developed pollution control methods to protect the environment from liquid, solid, and gaseous contaminants. In technology exchange, the United States and the U.S.S.R. signed a bilateral agreement pledging cooperation on environmental protection. As a part of this agreement, a working group on stationary source air pollution control was formed to define joint programs by the U.S. Environmental Protection Agency and the U.S.S.R. Research Institute of Industrial and Sanitary Gas Cleaning.

The planned cooperative programs encompass several areas of air pollution control technology, including particulate emission control. High mass-collection efficiencies are now achieved on particulate emissions from industrial processes in both countries by utilizing electrostatic precipitators, fabric filters, wet scrubbers, and novel devices. Growing concern for the health and environmental effects of fine particulate emissions (3 microns or smaller) has resulted in a need for further improvement of conventional control techniques and for the development of new techniques for fine particulate control.

In order to exchange technology on fine particulate control, a joint testing program was established. Soviet specialists would visit the U.S. to test with U.S. experts a hot-side electrostatic precipitator and U.S. experts would join Soviets to test a high efficiency scrubber in the U.S.S.R. This paper discusses the first part of that program. The hot-side electrostatic precipitator selected for the joint tests was on Unit No. 3 of Plant Allen which is part of the Duke Power Company.

Description of the Test Site and Precipitator

Allen Steam Station is located approximately 16 km (10 miles) southwest of Charlotte, N.C. Plant Allen has five coal-burning, single-reheat, steam-electric generating units. Units 1 and 2 have nameplate capacities of 165 MW each, and units 3, 4, and 5 are rated at 275 MW each. Each of the five units has a rated main steam pressure of 16.65 MN/m^2 (2,415 lbf/in.^{2}) gauge, a superheat temperature of 566°C (1,050°F) and a reheat temperature of 538°C (1,000°F).

Units 3, 4, and 5 at Allen Steam Station are identical, including the precipitator installations. Unit 3 was chosen as the test unit after consideration of maintenance outage schedules and test area access of the three units.

Commercial operation of Allen Unit 3 began in 1959. Although the unit has a nameplate rating of 275 MW, it has frequently been operated at a gross load of 300 MW or slightly greater. The gross load during the tests varied from 276 to 279 MW. The unit auxiliaries utilize approximately 6.5 percent of the generated power so that the net efficiency of Allen Unit 3 is approximately 35.9 percent (heat rate of 9,500 Btu/net kWhr). The expected thermal input to the boiler is therefore 729 MW (2,487 x 10^6 Btu/hr) at 280 MW gross electrical output. The typical coal analysis at the plant is given below.

Higher heating value	25.2 - 27.3 MJ/kg (10,850 - 11,750 Btu/lb)
Ash content	15 - 18 percent
Sulfur content	approximately 1 percent
Moisture content	6 - 9 percent

Depending on the heating value of the coal, the coal-firing rate at 280 MW ranges from approximately 96 to 104 Mg/hr (212,000 to 229,000 lb/hr). About 25 percent of the ash falls out in the dry-bottom boiler as bottom ash. The remaining 75 percent of the ash leaves the boiler with the hot flue gases. The gases flow first through the hot-side electrostatic precipitator at about 343°C (650°F), then through the air preheater where the gas temperature is lowered to approximately 138°C (280°F) by preheating the incoming combustion air. The flue gases then flow through the cold-side electrostatic precipitator before the pressure is boosted by the induced draft fan and the gases exit to the atmosphere through the 77 m (252 ft) stack.

A hot-side electrostatic precipitator was designed and installed on Unit 3 in series with the existing cold-side precipitator. Startup of the new precipitator occurred in March 1973, raising the total precipitator efficiency to better than 99 percent.

The configuration of the hot-side electrostatic precipitator is as follows. There are four parallel chambers for gas flow, and each chamber consists of four electrical sections in series. Separate ducts carry flue gases into and out of the four chambers. The two center chambers are separated internally by a gas-tight partition, dividing the precipitator into two completely separate sides. In each of the two sides, the eight sections are supplied with power from four transformer/rectifier (T/R) sets. Each of the two parallel sections that are supplied by a single T/R set is electrically isolatable. Table 1 gives additional design specifications of the hot-side electrostatic precipitator.

Ash deposits are removed from the corona wires by vibrators, which have an adjustable cycle of operation. Each vibrator is normally operated twice every half-hour with approximately a 90-second delay between the two vibration periods. Each vibration period lasts 6 seconds. Each rapper is activated at least once every 2 minutes, and some are activated twice every 2 minutes. The approximate rapping energy intensity is 32.5 J (24 ft-lbf). The collected ash falls into hoppers beneath the precipitator. It is periodically removed from the hoppers by a dry, pressurized ash-handling system and flows to a collecting tank from which it is water-sluiced to an ash-settling basin.

During the tests, operational data from the steam-electric generating unit and the electrostatic precipitator were monitored from inside the plant. In the control room from which Units 1,

TABLE 1. HOT-SIDE ELECTROSTATIC PRECIPITATOR SPECIFICATIONS

Manufacturer	Research Cottrell, Inc., Bound Brook, N.J.
Startup date	March 5, 1973
Design gas flow	590 actual m^3/s (1,250,000 actual ft^3/min)
Design gas velocity	1.81 m/s (5.94 ft/s)
Design specific collector area	53 m^2 per actual m^3/s (270 ft per 1000 actual ft^3/min)
Design efficiency	99.2%
Overall configuration	4 parallel chambers 4 electrical sections in series per chamber 39 parallel gas passages per chamber
Plates	40 plates per chamber (cold rolled steel sheets) plate height is 9.14 m (30 ft) plate length each section is 2.74 m (9 ft) for total length in direction of flow of 10.97 m (36 ft) plate-to-plate spacing is 0.229 m (9 in.) total surface area of plates is 31,305 m^2 (336,960 ft^2)
Wires	48 equally spaced wires per gas passage (handdrawn Bessemer steel with coppered surface) wire diameter is 2.77 mm (0.109 in.) wires are hanging type, placed in the center ±6.35 mm (1/4 in.) of the plate-plate space
Electrical	8 transformer-rectifier sets 16 electrically isolatable bus sections transformer rating is 96 kVA rectifier rating is 1400 mA waveform is double/half full normal power consumption is approximately 580 kW, 720 kW is maximum consumption

2, and 3 are operated, operational parameters such as electrical load, fuel flow, air flow, steam flow, and flue gas temperatures and pressures were continuously recorded on charts. The oxygen concentration of the gas was also continuously recorded in the control room and was periodically manually checked with a portable recorder at several duct sample lines.

The precipitator control panels are also in the boiler building. There are eight control panels for the Unit 3 hot-side precipitator (one for each transformer/rectifier set). Instruments on each panel continuously display the transformer primary voltage (a.c.), the transformer primary current (a.c.), the precipitator average current (d.c.), and the precipitator spark rate. These instruments were utilized in the back corona tests.

Coal samples were manually collected during the test from the hoppers located above the coal pulverizer feeders. Ash samples were collected downstream of the economizer section of Unit 3.

The identical inlet and outlet ducts of the Allen 3 electrostatic precipitators are separated by the precipitator and fly ash hoppers. The sampling ports are located on the hopper side of the ducts. Because the precipitator is divided by a gas tight seal, only two inlet and two outlet ducts were sampled. These were ducts designated B1 and B2. The eight sampling ports in each duct have an inside diameter of approximately 154 mm (6 in.). The ports are equally spaced and are 0.84 m (2 ft 9 in.) apart. The outside ports of each duct are 0.41 m (1 ft 4.5 in.) from the duct wall. The horizontal distance from the ports to the fly ash hoppers is approximately 3 m (10 ft). A beam near the inlet duct designated during these tests as B1 prevented some tests from being conducted in one port.

Two sets of sampling ports were installed for the resistivity tests. The ports were located on a horizontal segment of the hot gas duct downstream from the economizer and about 3 m (10 ft) upstream of the 90° turn which leads to the inlet test ports.

Test Procedure

The test program at Plant Allen involved the measurement of several parameters using U.S. and Soviet equipment and procedures. Replicate runs were made over a period of 8 days from March 12 through March 19, 1976, inclusive. Before each day's test began, ash was removed from the Unit 3 precipitator hoppers and boiler soot blowing was conducted. During the actual sampling both of these operations were suspended. Boiler and precipitator operating parameters were monitored at half-hour intervals during the sampling periods. Daily coal and ash samples were collected for analysis. The overall scope of the tests is summarized below:

1. The flue gas velocity and static pressure were measured at the inlet and outlet using calibrated pitot tubes supplied by both countries. Preliminary moisture and molecular weight determinations were made concurrent with the pitot traverse with U.S. equipment.

2. To determine the precipitator collection efficiency, mass sampling was conducted at the inlet and outlet using both U.S. and Soviet equipment. The standard EPA Method 5 was used at the inlet, and a hi-volume EPA Method 5 was used at the outlet.

3. Gas humidity was measured at the inlet with the U.S. equipment concurrent with the mass sampling. Flue gas molecular weight was determined from samples extracted with a separate Orsat probe attached to the mass sampling probe.

4. Particle size distributions were determined on the inlet and outlet. For the U.S. tests Brink impactors were used at the inlet and Andersen Mark III impactors were used at the outlet. Outlet samples were obtained by complete traverses of the two outlet ducts using 24 sampling points per duct. Because of a combination of short sampling times and poor inlet velocity distributions, separate inlet samples were obtained from individual ports, extracting one sample from each of four ports in each inlet duct.

5. Electrical resistivity of the fly ash particles was measured at the inlet by a U.S. method only, using a point-to-plane resistivity probe.

6. Sulfur dioxide and sulfur trioxide concentrations of the inlet gas were determined by the U.S. only (EPA Method 8).

7. Fuel analyses were performed by U.S. methods to determine the composition of ash, sulfur, hydrogen, carbon, moisture, nitrogen, and oxygen. Heating value was also determined. The collected ash samples were subjected to quantitative analysis to determine their chemical composition.

Results and Discussion

Eight separate tests were conducted using U.S. equipment. In the first six tests, U.S. equipment was used to traverse both ducts on the inlet and outlet. The only problem in the sampled areas was that the U.S. train was unable to sample port 4 of B1 on the inlet because of a physical obstruction. Test 7 was a traverse of duct B2 only, and test 8 was a traverse of duct B1 only. The precipitator collection efficiency as measured by the U.S. train averaged 99.69 percent with a standard deviation of 0.08 percent.

The inlet total mass concentration as measured by the U.S. train averaged 4,941 milligrams per actual cubic meter (mg/ACM)

[2.16 gr/acf] with a standard deviation of 319 mg/ACM. The outlet concentration as measured by the U.S. train averaged 15.06 mg/ACM (6.58 gr/1000 acf) with a standard deviation of 3.85 mg/ACM. These results show very good reproducibility with the standard deviation being less than 10 percent of the mean at the inlet and about 25 percent of the mean at the outlet.

A structural steel brace in front of port 4 on inlet duct B1 prohibited that port from being tested with U.S. equipment. For the purpose of calculations the assumption was made that the mass concentration at that port was equal to the average concentration of the particulate mass in the entire duct. However, there were two other ports in inlet duct B1 with zero gas velocity; hence, the center ports including port 4 might have had velocities somewhat higher than the average velocity, and hence, mass flow rates of dust somewhat higher than average. In fact, the preliminary velocity traverses, which did include port 4, showed it to have a velocity 22 percent higher than the average duct velocity. It is, therefore, possible that the inlet results are biased to the low side because of the uncertainty concerning port 4 in duct B1.

For the first six tests, which involved both ducts, the average inlet gas flow measured using the U.S. train was 11,440 actual cubic meters per minute (ACMM) with a standard deviation of 191 ACMM. The outlet gas flow measured by the U.S. train averaged 12,977 ACMM with a standard deviation of 212 ACMM. These results indicate increase of gas flow at the outlet averaging 13 percent more than the inlet. One possible reason for this discrepancy is air leakage into the inlet ports or into some other openings between the inlet and outlet test ports. This hypothesis is supported by the consistently higher oxygen readings measured at the outlet. Leakage from outside would also tend to dilute the particulate concentration at the outlet. Another factor which probably contributed to this discrepancy is the assumption made regarding port 4 of duct B1. If the actual velocity at port 4 were 22 percent higher than the duct average (as indicated in the preliminary velocity traverse), the actual inlet flow rate would have been about 1.4 percent higher than the value determined excluding port 4.

Particle Size Distribution

Two U.S. devices were used to determine the particle size distribution. The Brink impactor was used for U.S. inlet testing. At the outlet the U.S. Andersen Mark III impactor was used.

Results of the device used at the inlet are presented in Table 2. The mass median diameter (MMD) and geometric standard deviation (σg) estimates were obtained from best judgement fits of the data to log-cumulative distributions. Note that the inlet data are categorized by sampling location because port-to-port traverses were not possible in each day's test.

TABLE 2. RESULTS OF PARTICLE SIZING DEVICES

Inlet Tests

Date	Location	Brink	
		MMD, μm	σg
March 13	B1, Port 7	17	3.4
March 15	B2, Port 4	28	3.7
March 15	B1, Port 3	28	3.3
March 16	B1, Port 5	17	4.1
March 17	B2, Port 2	18	3.8
March 19	B2, Port 6	26	3.6

Outlet Tests

Date	Andersen	
	MMD, μm	σg
March 12	4.1	4.0
March 13	6.4	2.6
March 15	30	20
March 16	11	3.1
March 17	10	2.5
March 18	11	3.7
March 19	9.4	3.9

A summary of total particulate mass concentrations as determined with the various particle sizing devices and with the total mass devices is given in Table 3. The outlet data, especially the high concentrations of large particles obtained with the U.S. sizing device, indicate that rapping reentrainment losses in this precipitator contribute significantly to the overall emissions. Nevertheless, the overall precipitator efficiency is quite high so the effect of reentrainment losses is not critical.

Other Test Results

The results of the fly ash resistivity tests conducted with the Southern Research Institute point-to-plane probe are presented in Table 4. The average value of the resistivity during the test period was 1.9 x 10^{10} ohm-centimeters.

TABLE 3. AVERAGE PARTICULATE MASS LOADINGS BY SAMPLING DEVICE

Inlet

Device	U.S. mass train All runs	Brink
Grand average (mg/ACM)	4,942	3,244
Standard deviation (mg/ACM)	319	828
Average omitting extremes (mg/ACM)[a]	4,918	3,254

Outlet

Device	U.S. mass train All runs	Andersen
Grand average (mg/ACM)	15.06	5.47
Standard deviation	3.85	1.88
Average omitting extremes (mg/ACM)[a]	14.61	5.49

[a] The single highest and single lowest values were omitted in each case.

TABLE 4. FLY ASH RESISTIVITY RESULTS

Date	Time	Gas Temperature (°C)	Resistivity (ohm-cm)
3/13	0900-1000	347	3.5×10^{10}
	1000-1100	349	1.2×10^{10}
3/16	1445-1545	342	1.5×10^{10}
3/17	1030-1130	344	3.6×10^{10}
3/18	1030-1130	346	1.5×10^{10}
	1230-1330	345	1.4×10^{10}
	1430-1530	343	1.3×10^{10}
	1645-1745	343	1.2×10^{10}

Sulfur oxide tests were performed at the precipitator inlet ducts using the U.S. EPA Method 8 test apparatus. Six tests were performed, coinciding with the first six particulate mass tests performed on the precipitator. On a dry basis the sulfur trioxide results averaged 2.38 ppm by volume with a standard deviation of 1.91 ppm, and the sulfur dioxide concentration averaged 818.2 ppm with a standard deviation of 124.0 ppm.

Results from the chemical analysis of the combined fly ash samples are presented in Table 5. Each test sample was made up of a composite of fly ash collected from the two boilers associated with Unit 3. There is no assurance that the collected fly ash was identical in size distribution to the ash entering the precipitator. Since chemical analysis of fly ash is known to depend to some extent on the particle size, the results may not be precisely indicative of the composition of ash collected by the precipitator or of the small quantity of ash contained in the stack gas.

CONCLUSIONS

An electrostatic precipitator located on the hot side of the air preheater on Unit No. 3, Plant Allen, Duke Power Company, was tested. The precipitator has a design specific collector area of 53 m^2 per ACM or 270 ft^2 per 1000 acfm. U.S. test methods proved the precipitator to be greater than 99 percent efficient while the unit was burning 0.93-1.04% sulfur coal. The particle size distributions at the inlet had a range of mass median

TABLE 5. FLY ASH CHEMICAL ANALYSES[a]

Test No.	1	2	3	4	5	6	7	8
Loss on ignition	2.64	2.18	5.11	2.80	2.84	2.25	2.48	5.21
SiO_2	55.91	55.89	54.30	55.56	55.92	55.63	56.37	54.77
Al_2O_3	27.20	28.95	28.85	28.63	28.68	27.69	28.53	29.87
Fe_2O_3	8.41	7.90	7.21	7.60	7.77	9.17	7.67	6.23
TiO_2	1.51	1.05	0.92	1.34	1.13	1.05	0.78	0.94
CaO	1.16	1.05	0.92	1.17	1.08	1.26	1.11	1.16
MgO	0.92	0.77	0.74	0.74	0.73	0.92	0.95	0.87
Na_2O	0.46	0.49	0.45	0.50	0.47	0.52	0.51	0.47
K_2O	1.09	1.28	1.08	1.06	0.78	1.06	1.07	0.84
Li_2O	0.032	0.033	0.034	0.032	0.029	0.030	0.028	0.026
SO_3	0.40	0.15	0.16	0.20	0.25	0.14	0.20	0.26
P_2O_5	0.34	0.33	0.30	0.37	0.36	0.38	0.35	0.33
Total	100.07	100.07	100.07	100.00	100.04	100.10	100.05	100.98

[a] All results in percent of total mass.

diameter (MMD) from 17 to 28 μm using the Brink impactor. At the outlet the range of MMD was from 4.1 to 30 μm using the Andersen impactor. The greatest fractional efficiency was at 4 μm where it was 99.8 percent; it decreased to 98 percent at 0.6 μm and to 99.5 percent at 8 μm. The decline in efficiency at smaller sizes, as noted previously,[1] is part of a minimum in efficiency that is frequently observed in the mid-submicron particle size range. The decline in efficiency at larger sizes is due to rapping reentrainment losses.

REFERENCE

1. Abbot, J.H., and D.C. Drehmel. Chem. Eng. Progr. 72(12):47-51, 1976.

PAPER 13

EXPERIENCE WITH ELECTROSTATIC PRECIPITATORS AS APPLIED TO THE PRIMARY COPPER SMELTING REVERBERATORY FURNACE

GEORGE S. THOMPSON, JR.
INDUSTRIAL ENVIRONMENTAL RESEARCH LABORATORY
ENVIRONMENTAL PROTECTION AGENCY

AND

GRADY B. NICHOLS
SOUTHERN RESEARCH INSTITUTE

INTRODUCTION

The electrostatic precipitator is a well established device for the collection of particulate matter contained in industrial gas streams. The device is utilized in almost all industries where large gas volumes are encountered. The methods for obtaining electrostatic precipitators vary considerably from industry to industry. These methods range from the specification of the collection efficiency and outlet mass loadings (and occasionally a minimum collection electrode area) that is normal for the power industry to the practice of specifying the complete design that is sometimes used in the non-ferrous metals industry. Thus, there is the possibility that in some instances the responsibility for the design of the control device rests with the supplier while in others the primary responsibility rests with the user.

Southern Research Institute has been conducting research into the behavior of electrostatic precipitators over the past several years under the sponsorship of the EPA. One product of this research is the development of a computer systems model of electrostatic precipitation.[1] This systems model is to be discussed at this symposium. The industrial data that was utilized in the development of this model was primarily obtained from precipitators operating on effluent gas streams from coal-fired electric utility applications with limited inputs from the pulp and paper, cement and aluminum industries.

The EPA Industrial Environmental Research Laboratory located at Cincinnati, Ohio, has, as one area of responsibility, the control of emissions from the non-ferrous metals industry. Southern Research Institute is currently conducting a research study for this laboratory on the application of electrostatic precipitators used by this industry. The primary purposes for conducting this research are to develop a comprehensive data base of the operational characteristics of electrostatic precipitators used by this industry and to apply these data to the existing computer model established in Reference 1. This application could determine the model's usefulness in assisting in the design of control equipment for particulate matter in the non-ferrous metals industry.

Field Tests from the Primary Copper Smelting Industry

The first industry selected for study under this program was the primary copper smelting industry. Limited mass and particle size distribution measurements were conducted across electrostatic precipitators collecting particulates from the effluent gas streams from two primary copper smelting reverberatory furnaces.

The first field test, at a site designated as Plant A, served as an opportunity to evaluate the particulate test methods that had been developed and used extensively on coal-fired utility applications for use in the non-ferrous metals industry. The effluent gas stream from a copper reverberatory furnace differs sufficiently from that of a coal-fired utility that this evaluation was thought to be necessary.

The second field test was expanded significantly from the first test in an effort to obtain a larger data base for use in this research program. This test was conducted on an electrostatic precipitator operating on the reverberatory furnace off gas at Plant B.

TEST METHODS

Mass Tests

The basic purpose of this research study is to evaluate the behavior of the electrostatic precipitator. The mass tests are conducted with an ASME-type mass train with filters inserted into the flue and maintained at near stack temperatures. The test is significantly different from the EPA Method 5 test, in which the filter is maintained at a temperature of 250°F. The in-stack filter method was selected for these tests to assure that the particulate captured in the mass train actually passed through the electrostatic precipitator as a particulate rather than as a gas. This avoids the problems that would result from the condensation of constituents that appear as gases at the higher temperatures and allows observation of the precipitator's performance at its operating temperature.

Particle Size Measurements

The particle-size distribution was measured at both the inlet and outlet of the precipitator. The instruments utilized included cascade inertial impactors, five-stage cyclones, and two real time measurement systems. The inertial systems provide time-integrated size distributions, while the real-time systems provide information about the variation in particle-size distribution during the various operations of the reverberatory furnace. Detailed descriptions of the tests are given in a report prepared for the Industrial Environmental Research Laboratory entitled "Procedures Manual for Electrostatic Precipitator Evaluation" that should be currently available. Therefore, only a general discussion of the measurements will be included.

Inertial impactors normally require operation with either a substrate material or a thin layer of grease on the impactor plates to avoid particle bounce and reentrainment. The operating temperatures of reverberatory furnaces preclude the use of greases; therefore substrates were required for the operation of the inertial impactors.

There have been a number of instances where the sulfur oxides in the gas stream react with glass fiber substrates to cause weight gains on the substrate material. These reactions occur with sulfur dioxide concentrations as low as 1000 parts per million in the gas stream. Since the sulfur oxides are significantly greater in reverberatory off-gases, this problem was expected to be greater. However, preconditioning by exposure to the pre-filtered gas stream has been an acceptable method of alleviating the problem.

The particulates from the two copper reverberatory furnaces have exhibited high adhesive or cohesive characteristics. In general, bare metal substrates can be used in these installations. Specifically at Plant B, no substrate treatment was required.

Voltage-Current Relationship for Power Supplies

The behavior of an electrostatic precipitator is directly related to the operating voltages and currents. The electric field adjacent to the collection electrode is related to the applied voltage and the electrical charging characteristics of the particulate are related to the operating current density. Therefore, as a part of each test, the secondary voltage is monitored with voltage dividers and meters while the secondary current is generally obtained from the panel meters. These data serve as inputs into the precipitator analysis program.

Gas Analysis

Sulfur oxide concentrations were measured at the outlet of the precipitator at intervals during the testing period. The gas sampling system consists of a glass-lined heated sampling probe with a glass wool particulate filter, a condenser and a fritted bubbler containing a 3% hydrogen peroxide solution. A dry test meter preceded by a Drierite column was used to measure the volume of gas sampled. The condenser consists of a water jacketed glass coil maintained at a temperature between 60 and 90°C which removes the condensed sulfuric acid while passing the sulfur dioxide and water vapor. The sulfur dioxide is oxidized to sulfur trioxide and collected in the hydrogen peroxide bubbler. An acid-base titration with 0.1 normal sodium hydroxide and bromphenol blue indicator was used to determine the sulfuric acid content of each sample.

The sulfur oxide content of the gas was expected to vary considerably during the charging and operating cycle of the reverberatory furnace. Thus, an attempt was made to collect samples immediately before and after charging periods as well as during the semi-quiescent periods of the operation.

Test Results

The results of the tests conducted at two installations are summarized separately. The electrostatic precipitator description for Plant A is given below in Table 1.

TABLE 1. ELECTROSTATIC PRECIPITATOR DESCRIPTIVE PARAMETERS, REVERBERATORY FURNACE FOR PLANT A

Item	English	Metric
Collection electrode area (A)(total-2 ESP)	39744 ft^2	3692.4 m^2
Inlet set area (power set C)	19872 ft^2	1846.2 m^2
Outlet set area (power set A)	9936 ft^2	923.0 m^2
Outlet set area (power set B)	9936 ft^2	923.0 m^2
Collection electrode spacing	9 in.	0.229 m
Corona electrode diameter (round wire)	0.1055 in.	2.7 mm
Collection electrode dimension	9 ft x 24 ft	2.74 m x 7.32 m
Number of gas passages (total - 2 ESP)	46	
Gas passage length (active)	18 ft	5.49 m
Volume flow rate design (V)	150,000 acfm	70.8 m^3/sec
Design temperature	600-700°F	315-371°C
Design efficiency	96.83%	
Design precipitation rate parameter (w)	0.21 ft/sec	6.5 cm/sec
Specific collection electrode area (A/V)	265 ft^2/ 1000 cfm	52 m^2/m^3 sec

The results of the individual tests for Plant A are given in Tables 2 and 3 and Figures 1 through 3.

The operation of this electrostatic precipitator was within design specifications. The electrical measurements indicated that the operation was not limited by high resistivity and the collection efficiency was as expected. The fractional collection efficiency as shown in Figure 3 shows the characteristic and expected decrease to about 0.5 μm.

TABLE 2. MASS CONCENTRATIONS AND EFFICIENCY, PLANT A

Mass Concentration				Efficiency, %	
Inlet mg/DSCM		Outlet mg/DSCM			
Impactor	Mass Train	Impactor	Mass Train	Impactor	Mass Train
1146	1407	41	48	96.4	96.6
641	1304	21	41	96.7	96.8

TABLE 3. SULFUR OXIDE CONCENTRATIONS, PLANT A

Sampling Rate, l/min	Furnace Charge Cycle	% By Volume	
		SO_2	SO_3
3.2	after	1.0	0.024
2.9	before	0.42	0.019
2.4	after	0.73	0.018
1.9	before	0.63	0.025
1.0	after	1.7	0.067

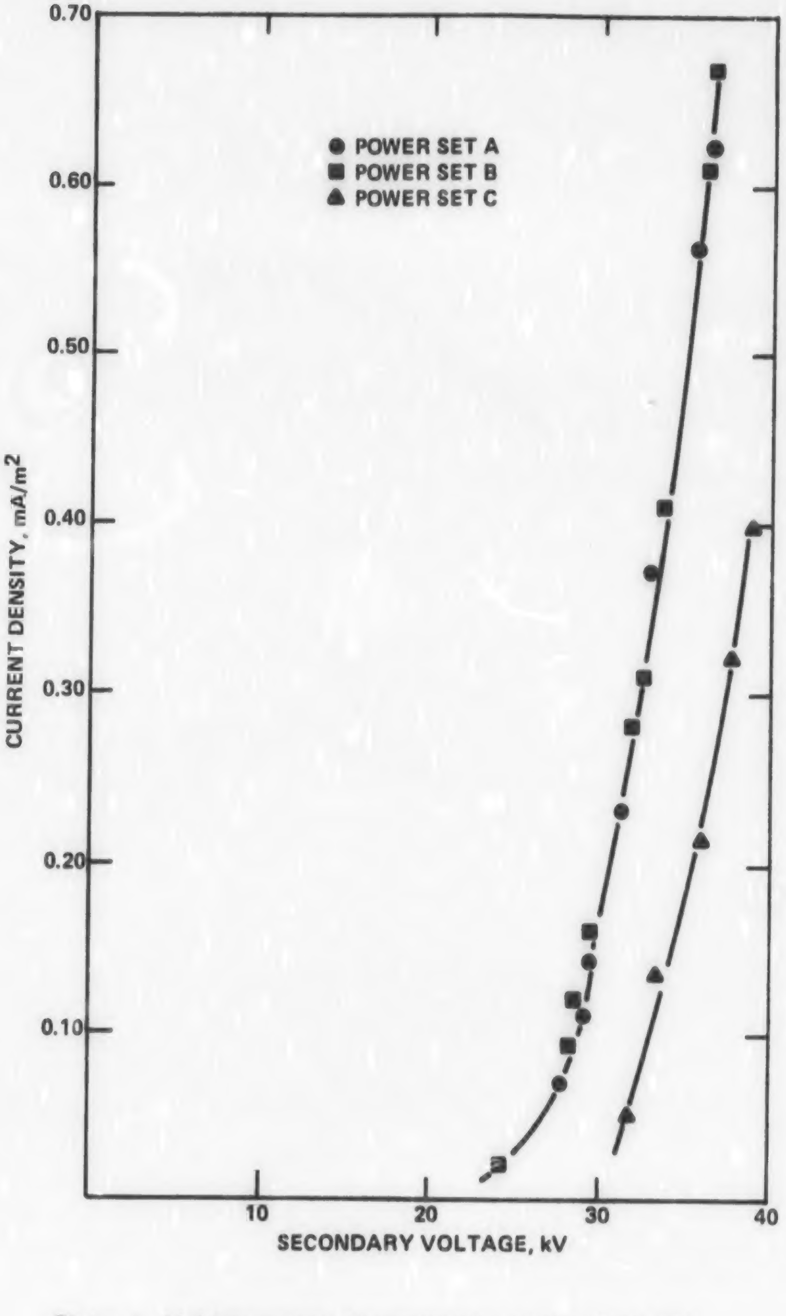

Figure 1. Voltage-current characteristics of the three ESP power sets, Plant A.

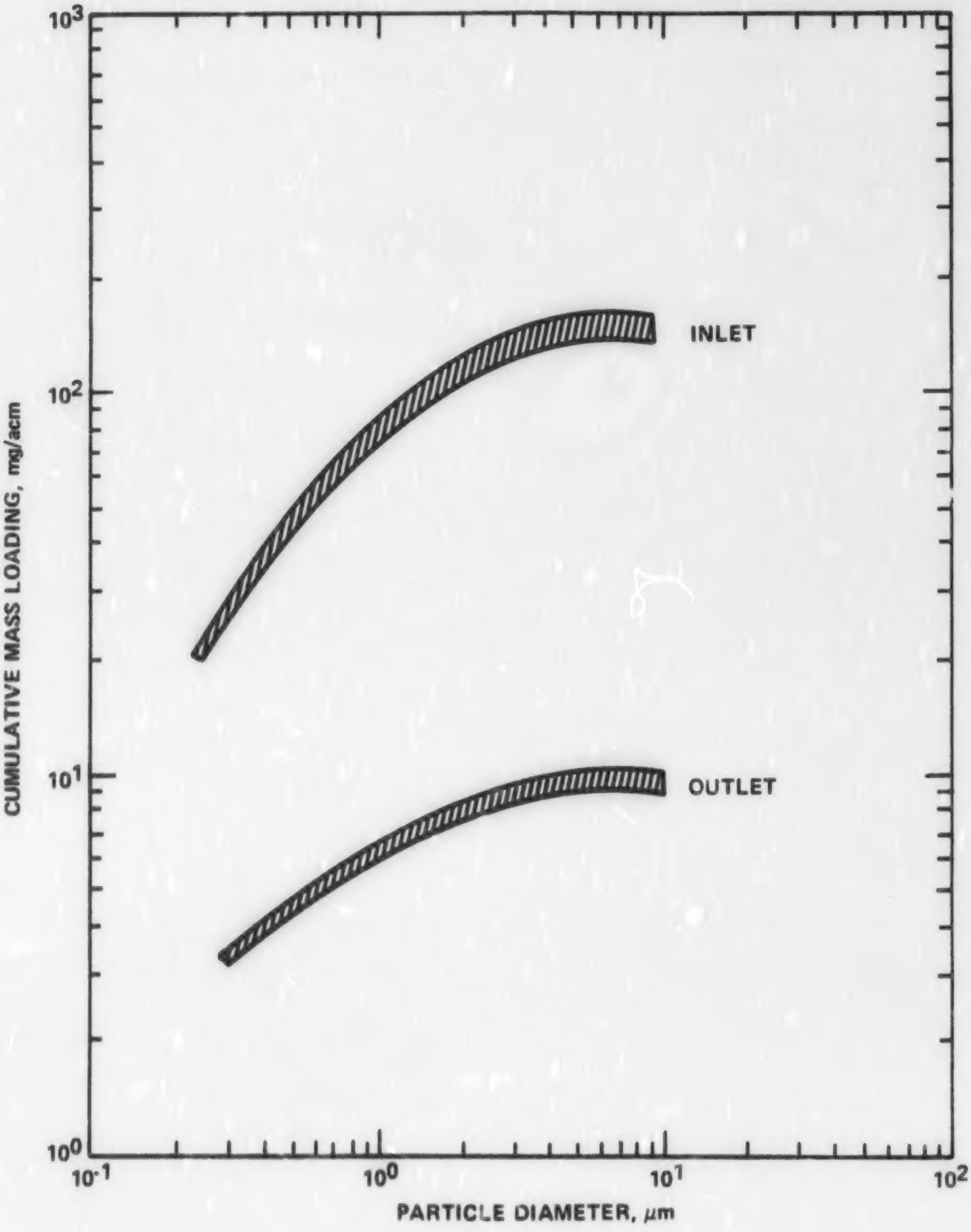

Figure 2. Average cumulative inlet and outlet mass loading vs. particle size, Plant A copper reverberatory furnace.

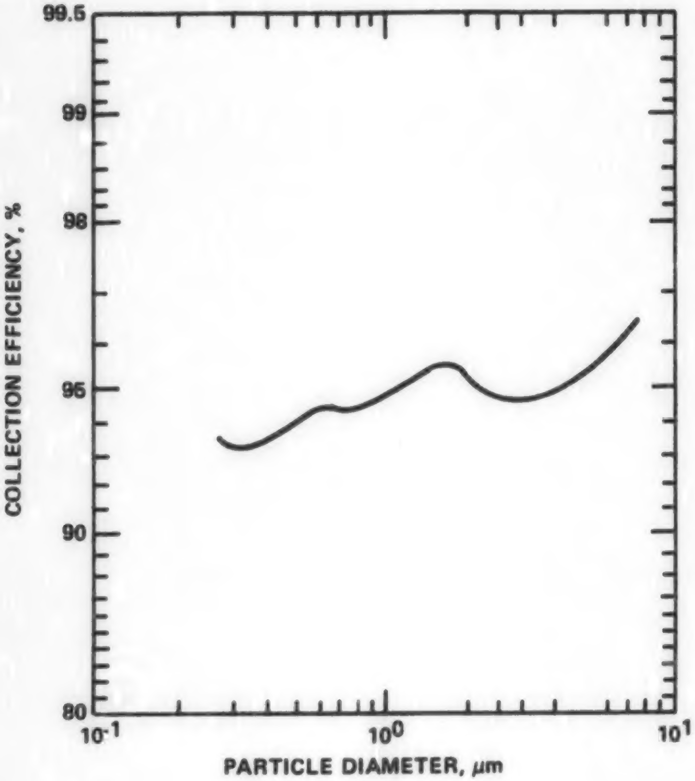

Figure 3. Fractional collection efficiency, Plant A.

The electrostatic precipitator layout and description for Plant B are given in Figure 4 and Table 4, respectively. The test results from Plant B are summarized in Tables 5 and 6 and Figures 5 and 6. This particular installation consists of several electrostatic precipitators operating in parallel as shown in Figure 4. The precipitators share a common inlet feed plenum and discharge into a common outlet duct. Therefore, it was impossible to completely define the particulate entering and leaving individual electrostatic precipitators. A second problem that leads to some difficulty is that it was not possible to determine the exact gas velocity through each unit. Therefore, only average operating parameters could be obtained.

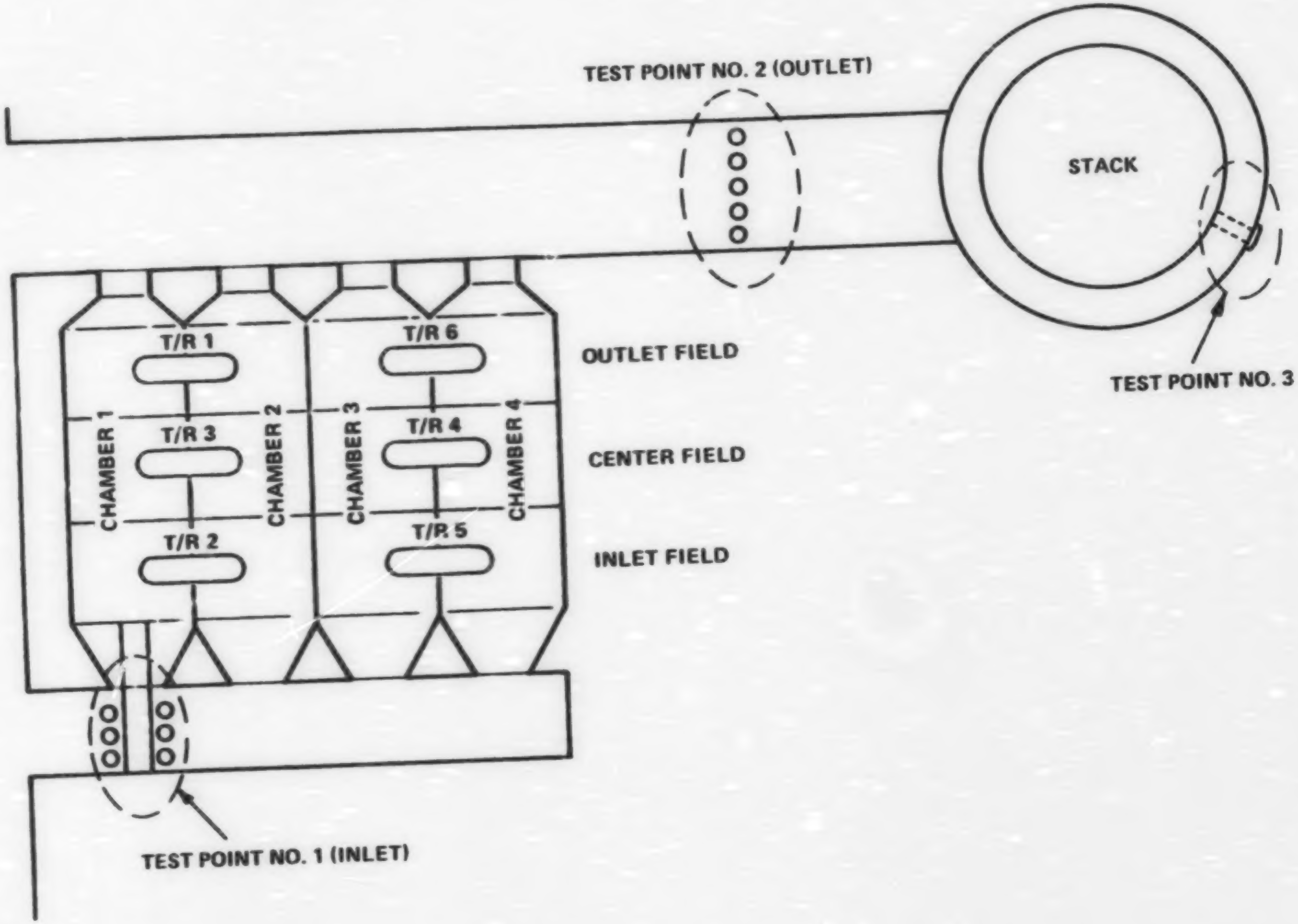
TEST POINT NO. 2 (OUTLET)
STACK
TEST POINT NO. 3
T/R 1
T/R 6
OUTLET FIELD
CHAMBER 1
T/R 3
CHAMBER 2
CHAMBER 3
T/R 4
CHAMBER 4
CENTER FIELD
T/R 2
T/R 5
INLET FIELD
TEST POINT NO. 1 (INLET)

Figure 4. Layout of the precipitator showing the sampling locations, Plant B.

TABLE 4. ELECTROSTATIC PRECIPITATOR DESCRIPTIVE PARAMETERS, PLANT B

Item	English	Metric
Collection Electrode Area	54,400 ft^2	5,044 m^2
Inlet	18,133	1,681.3
Middle	18,133	1,681.3
Outlet	18,133	1,681.3
Collection Electrode Spacing	9 in.	22.9 cm
Corona Electrode Diameter	0.109 in.	2.8 mm
Collection Electrode Dimension	7 ft 6 in. x 11 ft 4 in.	2.29 m x 3.45 m
Number of Gas Passages	160	
Gas Passage Length (Active)	22.5 ft	8.4 m
Volume Flow Rate	340,000 acfm	160 m^3/sec
Operating Temperature	~600°F	315°C
Efficiency	90%	
Specific Collection Electrode Area (A/V)	160 ft^2/1000 cfm	32 m^2/m^3 sec
Number of Electrical Sections (6 Power Supplied)	12	

TABLE 5. MASS CONCENTRATIONS AND EFFICIENCY DATA, PLANT B (IN STACK FILTERS)

Test No.	Inlet Mass, gr/dscf	Outlet gr/dscf	Efficiency, %
1	0.243	0.0225	90.7
2	0.087	0.0215	75.3
3	0.665	0.0309	95.4
4	0.597	0.1175	80.3
Avg.	0.398	0.048	87.9

Plant B also experienced difficulties with both particulate buildup within the interelectrode space and an unusually large amount of air leakage. The particulate buildup led to some electrical shorts developing in some of the power supplies and caused some delays in tests. The air inleakage causes a significant decrease in temperature and also introduces significant dilution within the gas system. These factors cause some difficulty in providing a definitive analysis of the behavior of the control device.

The emissions from Plant B were measured with both an in-stack filter and an out-of-stack filter, the latter being maintained at a nominal temperature of 250°F. The material collected at each point was chemically analyzed to determine the removal efficiency of the electrostatic precipitator operating at 260°C (500°F) for each of a number of trace elements. Table 7 indicates the results of this analysis.

Column 2 represents the removal efficiency for constituents at 500°F. Removal efficiency is defined as inlet minus outlet divided by inlet. Column 3 represents the percentage of material that appears as a particulate at 500°F to that which appears as a particulate at 250°F. Column 4 shows the percentage of material that appears as a particulate to that as particulate and gas. It is interesting to note that the electrostatic precipitator attains a reasonably high collection efficiency for all the materials that appear as particulates at 500°F, the operating temperature of Plant B's precipitator.

TABLE 6. GAS ANALYSES, PLANT B

Date	Time	Location	Flue Gas Temperature, °F	Concentration, Vol %				Concentration of SO_3, ppm
				H_2O	CO_2	O_2	SO_2	
1/12/77	9-10	Outlet	-	-	6.9	9.6	-	-
	10-12	Outlet	-	-	-	-	0.62	34
	4-5	Outlet	-	7.5	7.1	7.7	0.56	-
1/14/77	9-10	Outlet	345	-	6.5	9.5	-	-
	10-11	Outlet	-	-	7.0	9.5	0.52	24
	11-1pm	Outlet	-	-	7.1	8.7	0.57	26
	1-3	Outlet	-	-	7.8	8.2	-	-
	4-5	Outlet	-	7.8	-	-	0.53	18
1/15/77	1-2	Inlet	510	9.3	10.4	5.2	0.83	25
1/16/77	1-2	Inlet	450	9.7	9.4	7.3	Equipment failure	
Average Outlet			345	7.6	7.1	8.9	0.6	25
Average Inlet			480	9.5	9.9	6.3	0.83	25

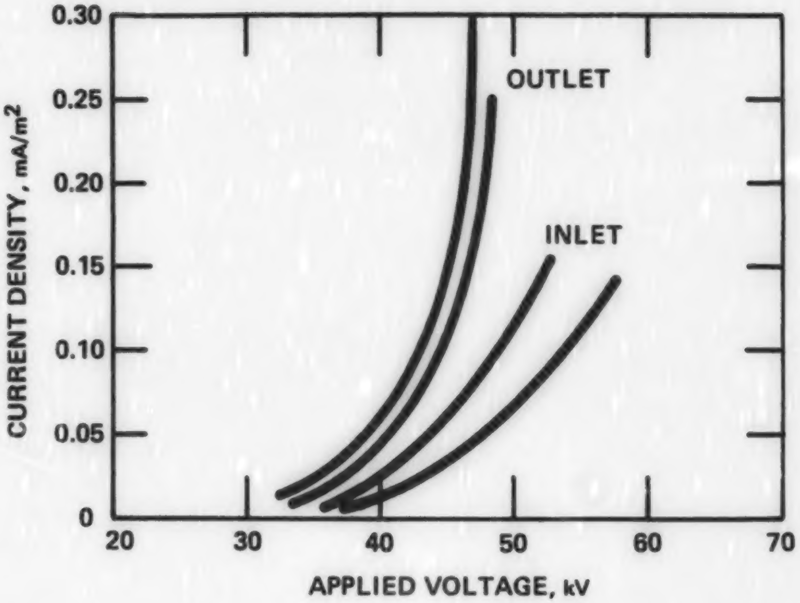

Figure 5. Voltage-current curves for an electrostatic precipitator operating on a copper reverberatory furnace.

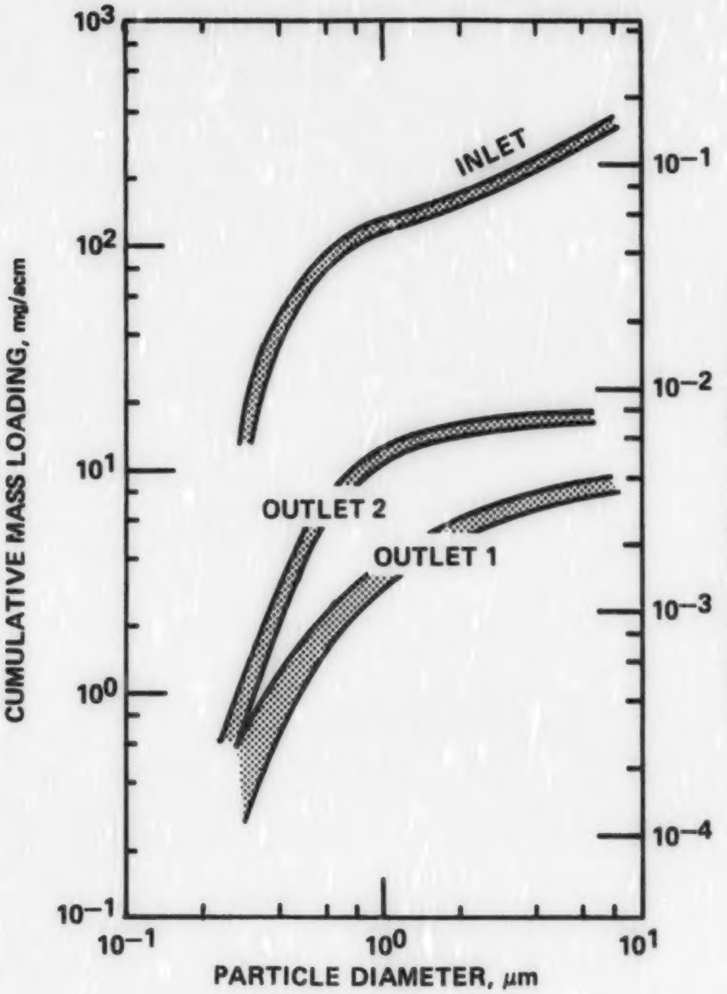

Figure 6. Average inlet particle size distribution, Plant B.

TABLE 7. REMOVAL EFFICIENCY OF SELECTED CHEMICAL ELEMENTS BY ELECTROSTATIC PRECIPITATORS AT PLANT B

Element	Percentage of particulate at 500°F caught by electrostatic precipitator	Percentage of total "available" particulate caught by electrostatic precipitator	Percentage of total element "available" as particulate
Ag	93	-	-
Al	-	-	-
As	92	98	33
Au	-	-	-
Ba	96	-	-
Cd	88	>99	>99
Co	>90	-	-
Cr	95	>99	-
Cu	98	>99	>99
F	-	-	< 2
Fe	99	>99	>99
Hg	-	-	-
Mo	94	-	>99
Ni	93	-	>96
Pb	95	>99	>99
Sb	81	>98	>95
Se	96	>99	93
V	>97	-	-
Zn	91	>99	>99

Computer Model Projections

The computer systems model was used to compute the efficiency as a function of particle size and overall mass collection efficiency. The model projection underpredicts the collection of fine particles in the 0.5 to 1 micrometer range and overpredicts the collection of large particles. This discrepancy between the model and actual performance is thought to be related to small errors in the charging equations relative to the fine particle size range and in neglecting reentrainment in the larger particle range.

The charging equations are based on peak values of the spatial average of the applied field. However, a significant fraction of the fine particles may be transported into the high field region of space adjacent to corona wires. These particles would be exposed to a higher average electric field than particles avoiding this region. Current research is aimed at better definition of the charging characteristics of particles in this region.

The reentrainment characteristics of Plants A and B should in principle be different. Plant B is equipped with flow interruption gates that are activated during rapping. The gas flow is stopped for a period of time before and after the rappers are energized. The result of the computer projection and the measured performances of these two precipitators are shown in Figures 7 and 8.

SUMMARY

These two limited tests serve as the starting point for the development of a basic engineering understanding of the behavior of electrostatic precipitators as applied to the non-ferrous metals industry. The data derived from these initial tests seem to fit into the existing electrostatic precipitator model. After a sufficient data base of performance as a function of particle size and of overall mass collection efficiency has been collected, the model can be used with a high level of confidence for assisting in the design of new electrostatic precipitator installations, as well as in evaluating the operating characteristics and performance of existing installations. The Industrial Environmental Research Laboratory will supplement this initial non-ferrous data base by testing operating electrostatic precipitators in the primary zinc, primary aluminum, and also secondary non-ferrous metals operations. Industry cooperation will be mandatory for the successful completion of this important research effort.

REFERENCE

1. Gooch, J.P., J.R. McDonald, and S. Oglesby, Jr. A Mathematical Model of Electrostatic Precipitation. EPA-650/2-75-037, U.S. Environmental Protection Agency, Research Triangle Park, NC, 1975. NTIS PB 246188/AS. 162 pp.

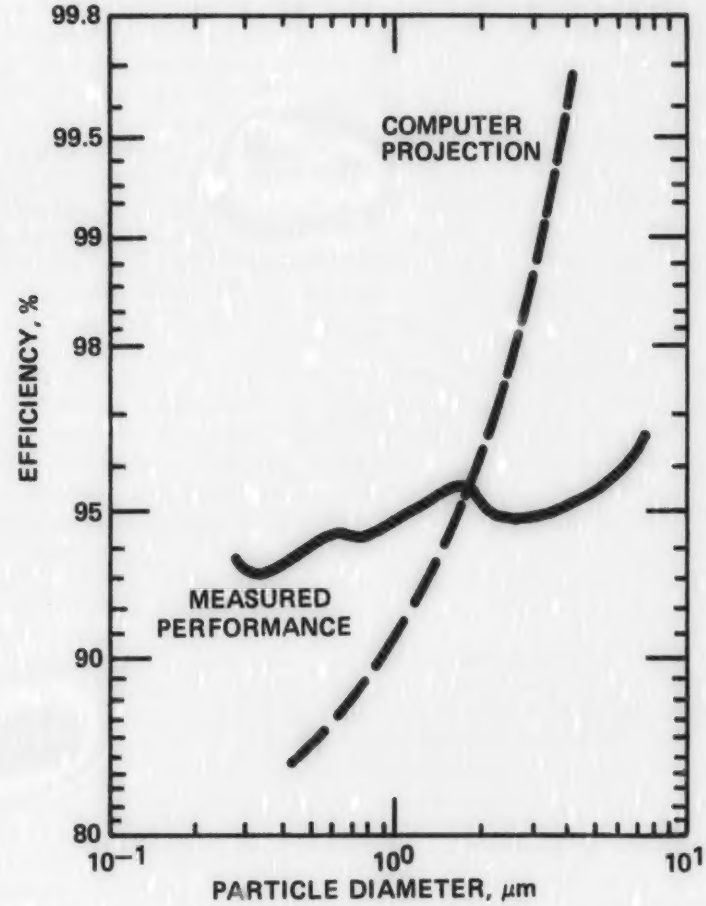

Figure 7. Measured and theoretical fractional efficiency curves for Plant A.

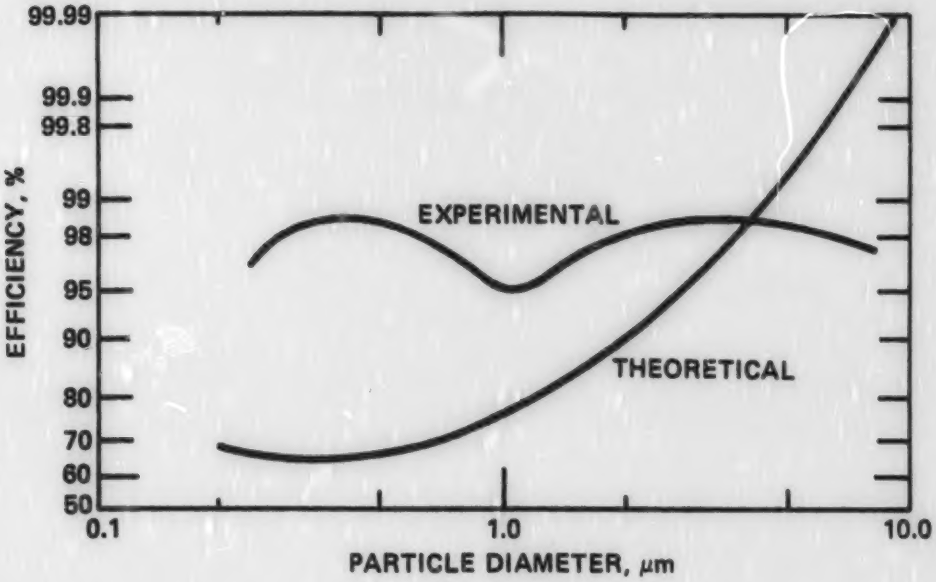

Figure 8. Computer projection compared with the measured fractional efficiency, Plant B.

METRIC CONVERSION FACTORS

To convert from:	To:	Multiply by:
lb	kg	0.454
gr/ft^3	g/m^3	2.29
ft^3/min (cfm)	m^3/sec	0.000472
$lbs/in.^2$	kg/m^2	703.
°F	°C	(°F-32) x 5/9
$ft^2/1000$ cfm	$m^2/(m^3/sec)$	0.197
in. WG	mm Hg	1.868
gallons	liters	3.785
ft	m	0.3048
in.	m	0.0254
tons	kg	908.
$in.^3$	cm^3	16.39
ft^3	m^3	0.028
gal/min	l/sec	0.0631
ft^2	m^2	0.0929
$in.^2$	cm^2	6.452
$gal/1000\ ft^3$	l/m^3	0.135
grams	grains	15.43
ft/min	cm/sec	0.508
ounces	grams	28.34
oz/yd^2	g/m^2	33.89
grains	grams	0.0647
gr/ft^2	g/m^2	0.698
lb force	dynes	44.44×10^5
lb/ft^2	g/cm^2	0.488
in. H_2O/ft/min	cm H_2O/cm/sec	5.00
Btu	calories	252